QUANTUM CHEMICAL INVESTIGATIONS OF UNIMOLECULAR AND BIMOLECULAR REACTION BARRIERS UNDER MECHANOCHEMICAL CONDITIONS

by

Gurpaul Singh Kochhar

A thesis submitted to the Department of Chemistry

In conformity with the requirements for

the degree of Doctor of Philosophy

Queen's University

Kingston, Ontario, Canada

(October, 2016)

Abstract

Mechanochemistry, i.e. the application of external forces at the molecular level, has emerged as a significant area of research in recent years. This emergence can be attributed to the development of experimental techniques such as atomic force microscopy, molecular force probes, optical and magnetic tweezers, and sonication. The application of such techniques has rendered it possible to activate chemical reactions along particular pathways. Theoretical models have been reported in the literature to account for experimental outcomes and to understand the interplay between mechanical stress and chemical reactivity. The work in this thesis uses quantum chemical calculations to examine reaction barriers, $\Delta E^{\ddagger}$'s, under mechanochemical conditions for a set of unimolecular and bimolecular reactions.

First, a code is written to predict changes in $\Delta E^{\ddagger}$'s under mechanochemical conditions. The code is used to select two atoms that a force, F, is applied along, which are termed pulling points. The predicted $\Delta E^{\ddagger}$'s are consistent with those calculated using quantum chemical methods at low values of F, in which the reactants or transition state (TS) structures are not significantly altered. The structural changes are prevented by applying constraints of varying size and chemical composition. The nature of the constraint plays a significant role in activating or deactivating a particular reaction. This result may be of value in the area of mechanoselectivity, in which the application of F can either activate or deactivate a reaction along a particular pathway.

Substituents of varying size are added to bimolecular reactions to investigate the underlying energetics associated with $\Delta E^{\ddagger}$'s under mechanochemical conditions. Increasing the sterics of the substituents increases the mechanical work contribution to the reduction in the force-dependent $\Delta E^{\ddagger}$'s

The differences in the abilities to mechanically eliminate $\Delta E^{\ddagger}$'s in unimolecular and bimolecular reactions are identified in this thesis. In unimolecular reactions, $\Delta E^{\ddagger}$ can be rendered to zero if the reactant or TS is shifted along the zero-F reaction coordinate, S_0. The $\Delta E^{\ddagger}$'s for bimolecular reactions can only be rendered to zero if there is sufficient coupling between F and other nuclear degrees of freedom in the reactants that shift the reactants along S_0 toward the TS.

Acknowledgements

I would like to acknowledge the following people and organizations for their efforts in the completion of my thesis in what follows. First and foremost, I would like to thank my supervisor Dr. Nicholas Mosey for all his guidance throughout my graduate studies. Dr. Mosey treats all his students with the utmost respect and has challenged me from day one to improve as a research scientist. The awards and publications that I have achieved throughout my Ph.D. would not be possible without Dr. Mosey's commitment to research excellence.

I would like to thank Drs. Tucker Carrington and Natalie Cann for their helpful feedback regarding my research progress. I am grateful to Dr. Igor Kozin for providing me the opportunity to work as a teaching assistance for the course CHEM 397. I had the opportunity to contribute to the development of various physical and computational labs, which has helped me in my Ph.D. research.

I would also like to thank current and past members of the Mosey research group for encouragement and valuable feedback regarding various aspects of my research. In addition, thank you to fellow graduate students Kyle Bachus, Mark Raycroft, Yaoting Zhang, Eric Keske, Ian Rupar, Brandon Moore and Prashant Agrawal. I will cherish the times we spent discussing chemistry and nonsense over whisky. I am grateful to the organizations NSERC, OGS, HPCVL, and Compute Canada for financial and computational support.

Finally, I would like to thank my entire family for all their love and support. I am grateful to my grandparents for teaching me the values of integrity, consistency, and a strong work ethic, which have helped me throughout my duration in graduate school. Thank you to my parents Harpreet Kochhar and Devinder Kochhar for supporting me my whole life and providing me the opportunity to attend university and pursue higher education. My mother, Harpreet, has always

been there for me and is my source of strength. I would certainly like to thank my brother, Manjit Kochhar, for all his support. Manjit has always been there for me when I was overwhelmed with research responsibilities and for that I am grateful.

Statement of Originality

I hereby certify that all of the work described within this thesis is the original work of the author. Any published (or unpublished) ideas and/or techniques from the work of others are fully acknowledged in accordance with the standard referencing practices.

(Gurpaul Singh Kochhar)

(October, 2016)

Table of Contents

Abstract **ii**
Acknowledgements **iv**
Statement of Originality **vi**
List of Figures **ix**
List of Tables **xiv**
List of Abbreviations **xv**

Chapter 1 Introduction **1**

1.1 Overview of mechanochemistry 1
1.2 Experimental mechanochemistry 4
1.3 Theoretical models 16
1.4 Previous theoretical studies 24
1.5 Objectives of thesis 32
References 35

Chapter 2 Methods **43**

2.1 Introduction 42
2.2 Potential energy surfaces 43
2.3 Geometry and TS optimzations 46
2.4 Vibrational frequency calculations 49
2.5 Thermodynamic and kinetic properties 52
2.6 Effect of external force on potential energy surfaces 56
2.7 Effect of external force on thermodynamic and kinetic properties 59
2.8 Energy evaluation methods 62
2.9 Density functional theory 74
2.10 Basis sets 79
2.11 Basis set superposition errors 83
References 88

Chapter 3 Predicting reaction barriers under mechanochemical conditons **94**

3.1 Introduction 91
3.2 Computing compliance matrix elements for all combinations 97
3.3 Application of code to chemical reactions 101
3.4 Force-induced instabilities 108
3.5 Summary and Future Outlook 114
References 118

Chapter 4 Altering the mechanochemical response of chemical systems through the use of constraints 121

4.1 Introduction 118
4.2 Constraints applied to reactions 121
4.3 Summary 144
References 149

Chapter 5 Effects of sterics on the contribution of mechanical work in activating mechanochemical reactions 152

5.1 Introduction 149
5.2 Reaction barriers under mechanochemical conditions 153
5.3 Summary 178
References 184

Chapter 6 Differences in the abilities to mechanically eliminate activation energies in unimolecular and bimolecular reactions 184

6.1 Introduction 184
6.2 Unimolecular reactions 187
6.3 Bimolecular reactions 193
6.4 Summary 209
References 215

Chapter 7 Conclusions and Future Work 218

References 226

List of Figures

Figure 1-1: Different ways of activating chemical reactions **3**

Figure 1-2: A general schematic of a planetary ball mill **6**

Figure 1-3: General schematics of optical and magnetic tweezers experimental setups **8**

Figure 1-4: A general schematic of an AFM experiment **9**

Figure 1-5: Mechanical activation of *trans*-3,4-dimethylcyclobutene using stiff stilbene as a molecular force probe **11**

Figure 1-6: Ring opening of cyclobutene under thermal, photochemical, and mechanical conditions **14**

Figure 1-7: A general schematic illustrating mechanochemistry at the molecular level **16**

Figure 1-8: A general schematic of the titled potential energy surface model **19**

Figure 1-9: A general schematic of the application of an external force in SMD simulations **23**

Figure 1-10: Force-modified potential energy surfaces for the ring opening of cyclobutene along conrotatory and disrotatory pathways using SMD simulations **26**

Figure 1-11: Activation energy as a function of external force for mechanical ring opening of cyclobutene along conrotatory and disrotatory pathways **27**

Figure 1-12: Snapshots of COGEF-based molecular dynamics for the ring opening of cyclobutene **28**

Figure 1-13: FMPESs obtained under COGEF conditions for the ring opening of cyclobutene along conrotatory and disrotatory pathways **30**

Figure 1-14: FMPESs obtained under EFEI conditions for the ring opening of cyclobutene along conrotatory and disrotatory pathways **31**

Figure 2-1: Potential energy surface of at carbon-carbon single bond calculated using a Morse potential **45**

Figure 2-2: Reaction scheme and potential energy surface for conversion of ozone to isozone **47**

Figure 2-3: A schematic illustrating the reaction coordinate on the Gibbs free energy surface **54**

Figure 2-4: A schematic illustrating the effect of an external force on the reaction coordinate **58**

Figure 2-5: Steps required in the EFEI method used in computational chemistry software packages **60**

Figure 2-6: Energy as a function of carbon-carbon length at several external force values **61**

Figure 2-7: Potential energy of a carbon-carbon single bond calculated using a harmonic potential and using a Morse potential **66**

Figure 2-8: Comparison of Gaussian functions and Slater functions **83**

Figure 3-1: A flowchart illustrating the code to estimate the barrier on the force-modified potential energy surface for all possible combinations of PPs in a molecule **104**

Figure 3-2: Reaction schemes considered in chapter 3 **105**

Figure 3-3: Reaction barrier versus external force for reactions **R1** to **R4** **106**

Figure 3-4: Reaction barrier versus external force for reactions **R1** and **R2** **107**

Figure 3-5: Optimized structures of the transition state at *F*=1000 pN and *F*=1500 pN for reaction **R2** **108**

Figure 3-6: Reaction barrier versus external force for reactions **R3** and **R4** **109**

Figure 3-7: Predicted structures of the reactant for reaction **R3** at *F*=0 pN, *F*=1000 pN, *F*=2000 pN **110**

Figure 3-8: Optimized structures of the reactant for reaction **R3** at *F*=0 pN, *F*=1000 pN, *F*=2000 pN **110**

Figure 3-9: Optimized structures of the reactants for reaction **R5** at *F*=1000 pN and *F*=2000 pN **111**

Figure 3-10: Potential energy as a function of pulling point distance for the configurations of the reactant in reaction **R5** at *F* =0 pN **114**

Figure 3-11: Potential energy as a function of pulling point distance for the configurations of the reactant in reaction **R5** at *F* = 1675 pN **116**

Figure 4-1: Reaction schemes considered in chapter 4 **126**

Figure 4-2: Reaction barrier versus external force for reactions **R1** to **R4** **127**

Figure 4-3: Optimized structures of the reactant for reaction **R1** at *F*= 1000 pN and *F*= 1500 pN **128**

Figure 4-4: Optimized structures of the reactant for reaction **R1** at *F*= 0 pN **128**

Figure 4-5: Reaction barrier versus external force for reaction **R1** with ring constraints of varying sizes added to the reactant and transition state structures **130**

Figure 4-6: Optimized structures of the reactant at *F* = 0pN for reaction **R1** with a 7 membered nitrogen substituted ring constraint and 7 membered oxygen ring constraint **131**

Figure 4-7: Reaction barrier versus external force for reaction **R1** with 7 membered ring constraints of varying chemical composition added to the reactant and TS structures **131**

Figure 4-8: Optimized structures of the reactant at *F* = 0 pN for reaction **R1** with constraints involving hydrogen bonding to pyrazole and coordination to a ruthenium atom **132**

Figure 4-9: Reaction barrier versus external force for reaction **R1** with no constraint, coordination to a ruthenium atom, and hydrogen bonding to pyrazole molecule **133**

Figure 4-10: Optimized structures of the reactant for reaction **R2** at *F*= 800 pN and *F*= 1000 pN **134**

Figure 4-11: Optimized geometry of the reactant for reaction **R2** at *F* = 0 pN **135**

Figure 4-12: Reaction barrier versus external force for reaction **R2** with ring constraints of varying sizes added to the reactant and transition state structures **136**

Figure 4-13: Reaction barrier versus external force for reaction **R2** with 7 membered ring constraints of varying chemical composition added to the reactant and transition state structures **137**

Figure 4-14: Reaction barrier versus external force for reaction **R2** with no constraint, coordination to a ruthenium atom, and hydrogen bonding to pyrazole molecule **138**

Figure 4-15: Optimized transition state structures for reaction **R3** at *F* = 1800 pN and *F* = 2000 pN **139**

Figure 4-16: Reaction barrier versus external force for reaction **R3** with ring constraints of varying sizes added to the reactant and transition state structures **140**

Figure 4-17: Optimized structure of the reactant for reaction **R3** with a 4 membered ring constraint at *F* = 2500 pN and *F* = 3000 pN **140**

Figure 4-18: Reaction barrier versus external force for reaction **R3** with 7 membered ring constraints of varying chemical composition added to the reactant and transition state structures **141**

Figure 4-19: Reaction barrier versus external force for reaction **R3** with no constraint, coordination to a ruthenium atom, and hydrogen bonding to pyrazole molecule **142**

Figure 4-20: Optimized structures of the reactant and TS for the competing hydrogen transfer reaction at *F* = 0 pN **143**

Figure 4-21: Reaction barrier versus external force for reaction **R4** and the competing hydrogen transfer reaction **144**

Figure 4-22: Reaction barrier versus external force for reaction **R4** and hydrogen transfer reactions with ring constraints of varying sizes added to the reactant and transition state structures **145**

Figure 4-23: Reaction barrier versus external force for reaction **R4** and hydrogen transfer reactions with 6 membered ring constraints of varying chemical composition added to the reactant and transition state structures **146**

Figure 4-24: Reaction barrier versus external force for reaction **R4** with no constraint, coordination to a ruthenium atom, and hydrogen bonding to pyrazole molecule **147**

Figure 5-1: Chemical structures of the substrates ethyl propyl ether and ethyl neopentyl ether used in the S_N2 reaction with the ethoxide anion nucleophile **155**

Figure 5-2: Reaction schemes considered in chapter 5 **157**

Figure 5-3: Reaction barrier versus external force for reactions **R1** to **R4** **158**

Figure 5-4: Optimized structures of the reactant complex and TS and changes in angle between sp^2 carbon atoms in ring and carbon-substituent bond for reaction **R1** **159**

Figure 5-5: Change in reaction barrier versus external force for reaction **R1** **160**

Figure 5-6: Contributions of the Born-Oppenheimer energy and mechanical work components to the changes in reaction barrier versus external force for reaction **R1** **161**

Figure 5-7: Pulling point distance and change in pulling point distance versus external force for reaction **R1** **162**

Figure 5-8: Optimized structures of the reactant complex and TS and changes in angle between sp^2 carbon atoms in ring and carbon-substituent bond for reaction **R2** **163**

Figure 5-9: Configurations of the transition state in reaction **R2** **164**

Figure 5-10: Change in reaction barrier versus external force for reaction **R2** **164**

Figure 5-11: Contributions of the Born-Oppenheimer energy and mechanical work components to the changes in reaction barrier versus external force for reaction **R2** **165**

Figure 5-12: Optimized structures of the reactant complex in reaction **R2** **166**

Figure 5-13: Pulling point distance and change in pulling point distance versus external force for reaction **R2** **167**

Figure 5-14: Configurations of the TS in reaction **R3** **169**

Figure 5-15: Optimized structures of the reactant complex and TS and changes in angle between sp^2 carbon atoms in ring and carbon-substituent bond for reaction **R3** **170**

Figure 5-16: Change in reaction barrier versus external force for reaction **R3** **171**

Figure 5-17: Contributions of the Born-Oppenheimer energy and mechanical work components to the changes in reaction barrier versus external force for reaction **R3** **172**

Figure 5-18: Optimized structures of complex and transition state at F = 1500 pN and F = 2000 pN and change in torsion associated with rotation around carbon-substituent bond for reaction **R3** **173**

Figure 5-19: Pulling point distance and change in pulling point distance versus external force for reaction **R3** **174**

Figure 5-20: Configurations of the transition state in reaction **R4** **176**

Figure 5-21: Optimized structures of the reactant complex and TS and changes in angle between sp^2 carbon atoms in ring and carbon-substituent bond for reaction **R1** **177**

Figure 5-22: Change in reaction barrier versus external force for reaction **R3** **178**

Figure 5-23: Contributions of the Born-Oppenheimer energy and mechanical work components to the changes in reaction barrier versus external force for reaction **R3** **179**

Figure 5-24: Optimized structures of the complex at F =2500 pN and F =3000 pN for reaction **R4** **179**

Figure 5-25: Pulling point distance and change in pulling point distance versus external force for reaction **R4** **180**

Figure 6-1: Unimolecular reaction schemes considered in chapter 6 **190**

Figure 6-2: Reaction barrier and root-mean squared differences versus external force for reactions **U1-U4** **192**

Figure 6-3: Δx_{i-j}^{RMS} versus j along S_0 for reaction **U1** using the TS at F = 3000 pN as the reference structure, i **194**

Figure 6-4: Force-induced shifts in the reactant and TS structures for reactions **U1-U4** **195**

Figure 6-5: Bimolecular reaction schemes considered in chapter 6 **197**

Figure 6-6: Reaction barrier and force-induced shifts of the reactants and TS in reactions **B1-B** **199**

Figure 6-7: Deformation energy versus zero-force reaction coordinate for reactions **B1-B5** **201**

Figure 6-8: Change in deformation energy and interaction energy with external force for reactions **B1-B5** **202**

Figure 6-9: Optimized structures of the complex and TS at F = 0 pN and F = 2000 pN in reaction **B1** **203**

Figure 6-10: Interaction energy versus zero-force reaction coordinate for reactions **B1-B5** **204**

Figure 6-11: Interaction energy versus reaction coordinates at different values of external forces for reaction **B3** and **B4** **206**

Figure 6-12: Difference in rates at which Δx_{sep} and Δx_{def} change along S_0 for reactions **B1-B5** **209**

Figure 6-13: Overlap between $\hat{\mathbf{R}}$ and $\hat{\boldsymbol{\tau}}$ for the reactant complexes in reactions **B3** and **B4** **212**

List of Tables

Table 1-1: A comparison of the force ranges applied in mechanochemical methods **15**

Table 4-1: Off-diagonal elements of **C** of the pulling point distance coupled to angles and torsions in the reactant in reaction **R1** **130**

Table 4-2: Off-diagonal elements of **C** of the pulling point distance coupled to angles and torsions in the reactant in reaction **R2** **137**

List of Abbreviations

AFM: Atomic force microscopy

APs: Attachment points

BCB: Benzocyclobutene

BSSE: Basis set superposition error

COGEF: COnstrained Geometries Simulate External Force

DFT: Density Functional Theory

EFEI: External Force is Explicitly Included

FMPES: Force-modified potential energy surface

GGA: Generalized Gradient Approximation

GTOs: Gaussian type orbitals

HF: Hartree-Fock

KS: Kohn-Sham

LDA: Local Density Approximation

MD: Molecular dynamics

MEP: Minimum energy pathway

PES: Potential energy surface

PPs: Pulling points

SCF: Self-consistent field

SMD: Steered molecular dynamics

STOs: Slater type orbitals

TF: Thomas-Fermi

TS: Transition state

TST: Transition state theory

WH: Woodward-Hoffmann

XC: Exchange-correlation

ZPVE: Zero-point vibrational energy

Chapter 1

Introduction

1.1 Overview of mechanochemistry

In chemical reactions, the conversion of reactants to products occurs along the reaction coordinate, *S*. The highest energy structure along *S* is the transition state (TS) and the energy difference between the TS and the reactants is known as the reaction barrier, $\Delta E^{\ddagger}$. The reactants must acquire sufficient energy to overcome $\Delta E^{\ddagger}$ and form products. This energy is typically provided using heat (thermochemistry), light (photochemistry), or an applied electric potential (electrochemistry). The various means of activating reactions function by applying energy to either nuclear or electronic degrees of freedom (DOFs) in a molecule in specific or non-specific ways as illustrated in Figure 1-1. Thermal activation acts on nuclear DOFs in a molecule by providing heat, which is distributed on average according to equipartition theorem. As a result, the application of heat activates a chemical reaction by exciting nuclear DOFs in a non-specific manner. In contrast to thermochemistry, in which the system remains on a particular electronic state, photochemical methods induce changes in the electronic state of the system by subjecting molecules to radiation at particular wavelengths. The irradiation of molecules promotes transitions of electrons between specific electronic states. On the other hand, electrochemical methods affect the electronic DOFs in a molecule in a non-specific manner. The application of an electric potential shifts the electronic energy levels of a reacting species in an average sense to activate processes such as electron transfer.

An alternative means of activating reactions involves subjecting molecules to external stresses or forces. This approach describes the field of mechanochemistry; however, the term mechanochemistry has not been exactly defined and has evolved over time. During prehistoric times, mechanochemistry was applied as primitive people made fire by rubbing two rocks together. In this process, the mechanical energy that arises from the friction between the two rock surfaces is converted into heat. This act, however, is regarded as a thermal process because no chemical change has occurred. Furthermore, mechanochemistry in the present day can be interpreted as applying external stresses or forces to atoms or groups in a molecule leading to a chemical change. The applied stresses perform mechanical work on the system, which induces specific changes in molecular geometry.[1–4] The mechanical work performed on the system provides energy that can be used to overcome reaction barriers that are conventionally overcome thermally. The specific details on how mechanical work is used to lower $\Delta E^{\ddagger}$'s are discussed in section 1.3. In contrast to thermochemistry, mechanochemical methods activate reactions by targeting specific nuclear DOFs in a molecule. As such, the application of external forces to specific atoms or functional groups in a molecule can be used to selectively guide systems along particular reaction pathways.[5]

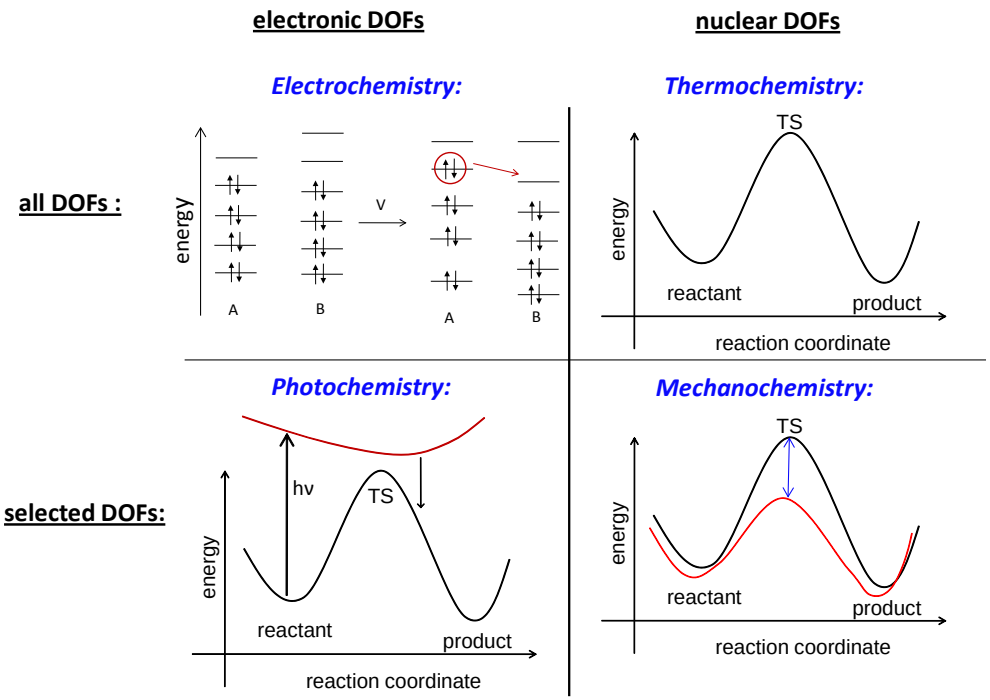

Figure 1-1. Differences in how various means of activating reactions affect the degrees of freedom (DOFs) in a molecule. Reactions activated electrochemically and thermally alter all electronic and nuclear DOFs respectively. Photochemical means of activation target specific electronic DOFs in a molecule. In mechanochemistry, reactions are activated by applying external stresses or forces to specific nuclear DOFs. The applied force performs work on the system, which lowers the reaction barrier that is typically overcome thermally.

The combined abilities of mechanochemistry to alter specific changes in molecular geometry and lower reaction barriers has prompted significant interest from an experimental and theoretical perspective.[6–10] Recent years have seen the development and application of experimental techniques that permit reactions to be activated mechanically. These techniques include grinding and milling,[11,12] optical and magnetic tweezers,[13–16] atomic force microscopy (AFM),[17–19] molecular force-probes,[7,20,21] and sonochemical methods.[22–25] These methods are discussed in detail in section 1.2. The use of these experimental techniques in practical mechanochemical efforts have demonstrated that subjecting specific groups in a molecule to external forces can activate or deactivate

reactions along particular pathways.[5,26] Several theoretical models have been reported in the literature to explain experimental outcomes as well as understand the interplay between mechanical stress and chemical reactivity.[27–29] These models are described in section 1.3 and previous theoretical studies applying such models to chemical systems are discussed in section 1.4.

1.2 Experimental mechanochemistry

The use of mechanochemistry to activate reactions in ways that fundamentally differ from thermochemistry, photochemistry, and electrochemistry suggest that the conditions required to activate reactions mechanically may be difficult to achieve through the use of these conventional experimental approaches. Mechanochemistry has been applied for millennia through grinding and milling processes. [11,12,30–32] One of the earliest published findings on using grinding and milling methods to activate chemical reactions was reported in 1820 by Michael Faraday. [33] In that study, Faraday described the reduction of silver chloride by grinding with zinc, tin, and iron in a mortar according to the mechanochemical reaction:

$$2\mathrm{AgCl} + \mathrm{M} \rightarrow \mathrm{MCl_2} + 2\mathrm{Ag} \qquad (1.1)$$

where M= (Zn, Sn, and Fe). One of the first applications of mechanically inducing an organic reaction by grinding was reported by Ling and Baker[34] towards the end of the nineteenth century. The authors in that study synthesized halogen derivatives of

quinhydrone by trituration of dry mixtures and in the presences of water or light petroleum that was used as a solvent.

During the twentieth century, mechanochemistry through grinding as well as ball milling has found many applications in the areas of solid-state chemistry and material science. [30] Throughout this period, several studies focused on investigating the effect of high pressure on phase transitions in crystals[35,36] as well as mechanical alloying using a ball mill apparatus. [37–40] The mechanical energy in a ball mill is transferred to the materials using balls, rods, and pebbles. Different types of ball mills can be classified depending on the motion of the milling body. Some of the most common types of ball mills are planetary mills, vibrational mills, and tumbling mills. [41] In planetary mills, the grinding action on the materials is achieved by a large centrifugal force that is generated from a revolving base disk and a rotating mill pot. A general schematic of the mechanical action in a planetary mill is shown in Figure 1-2. The setup consists of a planetary arm of radius, R_v, that is located at the center of the base disk. The planetary arm rotates with an angular velocity, ω_p, and the milling pot that contains the material of interest rotates in the opposite direction with an angular velocity, ω_v. In vibratory ball mills, mechanical forces are generated from the oscillatory motion of the balls used. Specifically, the oscillations of the balls inside the chamber cause shearing action, which in turn lead to the application of mechanical forces to the sample. Several factors can affect the magnitude of the forces applied including the rate of milling, the amplitude of vibration, and the mass of the milling medium. Larger forces in the vibratory ball mill can be achieved by using high frequencies and small amplitudes of vibration. [41] Tumbling ball mills are the most widely used type of mill on small and large scales. In a tumbling mill, frictional forces derived

from the rotational motion of the balls, contact areas of the colliding balls, and movement of particles within the mill are all applied to the sample.

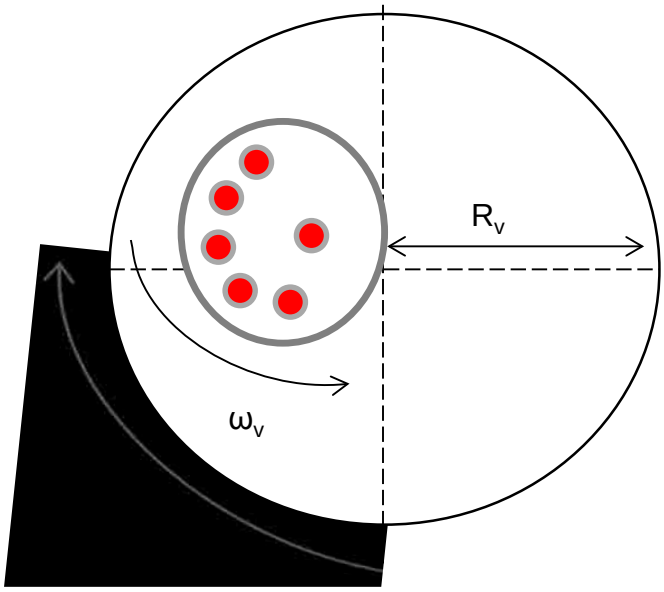

Figure 1-2. A general schematic of a planetary ball mill. The mechanical forces are generated by the revolving base disc and rotating milling pot with colliding balls (red spheres). The planetary arm of radius, R_v, rotates with an angular frequency of ω_p and the milling pot rotates in the opposite direction with an angular frequency of ω_v.

Although mechanical activation thorough grinding and milling techniques are effective for bulk scale synthesis of materials in the solid-state, they are largely non-specific in terms of the forces applied and the bonds affected. This has driven extensive research over the last decade to develop and apply mechanochemical conditions that allow stresses and forces to be subjected to specific groups in molecules in a controlled manner. The ability to subject molecules to precise forces has been made possible through developments in optical tweezers, AFM, molecular force probes, and sonication. All of these experimental techniques have emerged as powerful tools for investigating the forces and motions associated with chemical and biological systems at the molecular level.[42]

Optical tweezers have been used since the 1970's as a technique for mechanically manipulating single molecules. [14] An experiment involving optical tweezers consists of a focused laser beam and an optically transparent spherical bead. The sample is attached to the bead through a non-covalent bond. The focused laser beam exerts radiation pressure on the optically transparent spherical bead, which shifts the bead from its equilibrium position. The shifts of the bead from its equilibrium position results in a restoring force that is proportional to its displacement. The restoring force can be calculated using Hooke's law for small displacements from the equilibrium position:

$$F = -k\Delta z \tag{1.2}$$

where F is the magnitude of the restoring force, Δz is the extension of the bead from its equilibrium position, and k is the force constant. The value of the force constant depends on several factors including the steepness of the optical gradient, which is related to how tightly the laser beam is focused, the polarizability of the bead, and the intensity of the laser beam. The forces that are typically applied in experiments involving optical tweezers are on the order of magnitude of 0.1 to 100 pN.[43] Optical tweezers have found many applications in biological systems such as characterizing molecular-scale motors[44,45] and mechanically manipulating viruses and bacteria. [46]

One of the main disadvantages of using optical tweezes for mechanically manipulating single molecules arises from the presence of optical perturbations that affect the intensity of the laser beam. [43] As a result of these optical perturbations, optical tweezers are limited to highly purified samples. These issues are not present when using

magnetic tweezers to apply mechanical forces to the sample. In experiments involving magnetic tweezers, mechanical forces are applied in the same manner as described for optical tweezers; however the optically transparent spherical bead is replaced by a magnetic bead. The differences in the experimental setup between optical tweezers and magnetic tweezers are illustrated in Figure 1-3. The forces that are applied using magnetic tweezers are proportional to the gradient of the magnetic field. The magnitude of these applied forces decrease with increase in separation distance between the bead and the magnet. Magnetic tweezers have been previously used to investigate the topology of individual DNA molecules,[47,48] the stretching and unfolding proteins[49,50], and the dissociation of ligand-receptor complexes.[16,51,52] One of the main drawbacks of magnetic tweezers is that they are not as versatile as optical tweezers. This versatility can be attributed to the limited ability to manipulate the permanent magnet configuration for other applications.

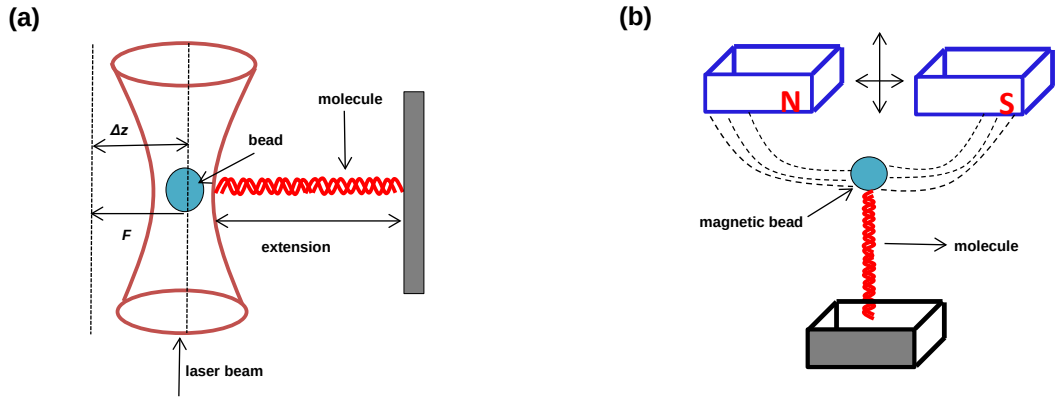

Figure 1-3. Schematics of single-molecule mechanochemical experimental methods that involve **(a)** optical tweezers and **(b)** magnetic tweezers. In experiments using optical tweezers, mechanical forces are applied through radiation pressure from a focused laser beam to a transparent spherical bead. The shift of the bead from its equilibrium positions produces a restoring force that is equal to its displacement, Δz. Magnetic tweezers apply mechanical forces using an external magnetic field onto a magnetic bead. The magnitude of the force applied is proportional to the gradient of the magnetic field.

AFM has emerged as a powerful technique for single-molecule imaging and investigating the mechanical unfolding of proteins.[53,54] In a typical AFM experiment, the molecule under study is held between a sharp tip on the cantilever and a piezoelectric scanning stage as illustrated in Figure 1-4. An external force is applied to the molecule by increasing the separation distance between the cantilever and the stage. The displacement of the cantilever from its initial position is measured from the reflection of a laser beam off the cantilever onto a position-sensitive detector. The force acting on the molecule of interest can be determined from the deflection of the cantilever and its force constant. The magnitude of the force constant depends on many factors including the material properties of the cantilever as well as its shape. Typical values for the force constant of the cantilever range from 10^1 to 10^5 pN / nm. [43]

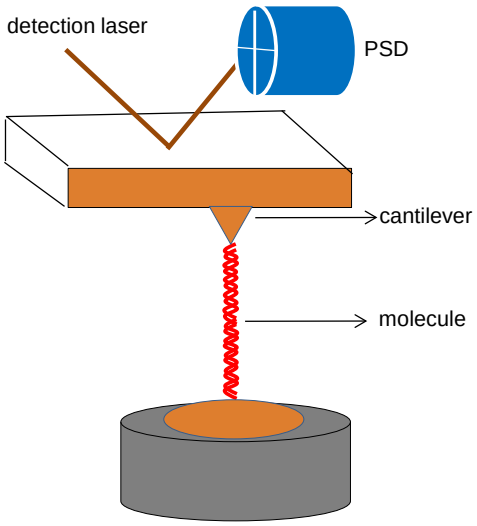

Figure 1-4. Schematic of a typical AFM experiment, which consists of a cantilever with a sharp tip that is held above the piezoelectric stage. The molecule under study is held between the tip of the cantilever and the stage. Force is applied to the molecule through the displacement of the cantilever, which is measured from the reflection of the detection laser beam onto the position-sensitive detector.

The application of optical tweezers, magnetic tweezers, and AFM has rendered it possible to subject individual molecules to precise forces. However, the single-molecule nature of these methods limits their applicability to investigate bulk samples under mechanochemical conditions. Recent advances in molecular force probes and sonication techniques have made it possible to subject a large number of molecules to precise forces.

The use of molecular force probes to activate reactions mechanically has gained considerable interest in recent years.[7,20,21] A molecular force probe is a molecule that converts light energy into mechanical energy upon a change in structure. This photochemically-induced change in structure provides mechanical force by constraining a single internuclear distance in the target molecule that is attached to the molecular force probe. A recent study by Boulatov and coworkers[20] has identified three criteria that a molecule must satisfy to be a suitable choice for a molecular force probe. First, the molecular force probe must be more structurally anisotropic than the functional group on the target molecule that it is attached to. Second, the functional groups and chemical reactions that are associated with the molecular force probe must be compatible with the target molecule. Finally, the molecular force probe should be able to apply mechanical forces without the synthesis of highly constrained molecules.[55] An example of a molecule that is suitable to be a molecular force probe in practical mechanochemical efforts is stiff stilbene. Under photochemical conditions, stiff stilbene undergoes *cis-trans* isomerization about the central C=C bond. This photo-induced structural change provides tensile forces to the target molecule. The magnitude of the applied forces can be controlled by changing the length of the linker molecules attached to the target molecule. Boulatov and coworkers[20] have used stiff stilbene as a molecular force to mechanically activate the ring

opening of *trans*-3,4-dimethylcyclobutene. as shown in Figure 1-5. Stiff stilbene was attached to the reactant structure via linker molecules consisting of approximately 16 to 20 atoms. Using a molecular force probe to mechanically activate reactions has many advantages. One of the main advantages is that bulk samples of the target molecule and molecular force probe macrocycle can be synthesized and irradiated. In addition to synthesis on the bulk scale, the magnitude and directional nature of the forces applied can be controlled using linker molecules of various sizes.

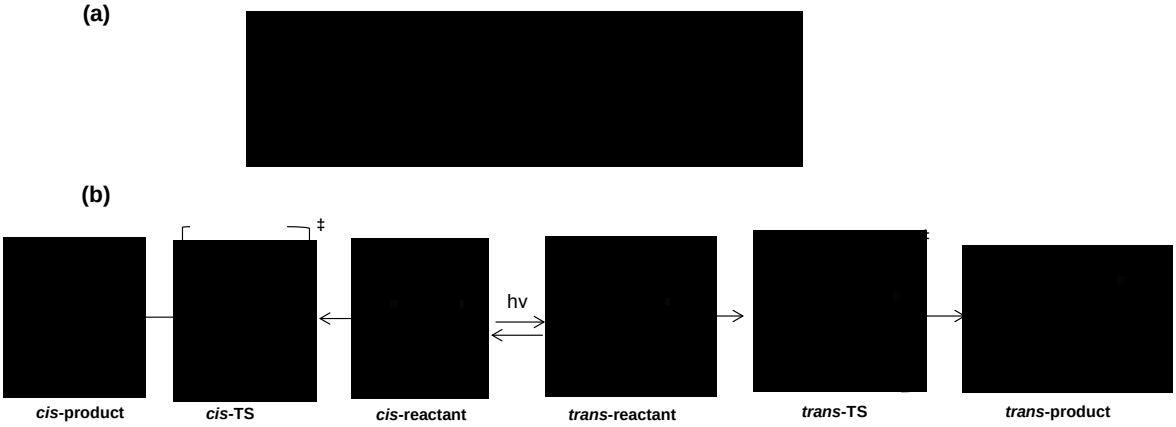

Figure 1-5. (a) Reaction scheme for the ring opening of *trans*-3,4-dimethylcyclbutane and **(b)** structures of the complexes formed by connecting the target molecule to stiff stilbene using linker molecules. The linker groups, X and Y, are of varying length and chemical composition. The force applied to the methyl groups attached to the carbon atoms of scissile bond in the reactant structure depend on the nature and length of the linker group.

Sonochemical methods have been used to subject a large number of molecules to precise forces [56,57] In a typical sonochemical experiment, sound energy is applied to agitate particles in solution. The mechanical forces do not arise from a direct interaction of the sonicator with the chemical species. Instead, external forces are applied to the molecule through acoustic cavitation.[22] Acoustic cavitation involves the formation, growth, and collapse of bubbles in a solution. The formation of cavitation bubbles

proceeds through a nucleated process, in which molecules assemble near the liquid-vapor interface.[58] The growth of cavitation bubbles can occur through various mechanisms. High intensity sound waves can be used to yield rapidly growing cavitation bubbles through inertial effects. Using lower intensity sound waves results in the growth of cavitation bubbles at a much slower rate through a process termed rectified mass diffusion. [56] Rectified mass diffusion involves the mass transfer of dissolved gas between the liquid and the bubble in the presence of an acoustic field.[59] At a certain point during the growth process, the cavitation bubble reaches a critical size in which it can efficiently absorb energy from the external ultrasonic field. The critical size of the cavitation bubble is determined by the frequency of the sound waves. The cavitation bubble cannot efficiently absorb ultrasonic energy once it exceeds the critical size, which results in the collapse of the cavitation bubble. The collapse of cavitation bubbles results in intense local heating to temperatures up to approximately 5000°C and pressures of approximately 500 atm. [23] This collapse results in shock waves, which leads to high velocity interparticle collisions and large-scale vibrations. These large-scale vibrations provide the mechanical forces that cause extension and deformation in the molecules of interest.

Sonochemical methods have been applied to study the degradation of polymers [25,60,61] and the mechanical activation of pericyclic reactions. [5,24,62] A study performed by Moore and colleagues has investigated the mechanical ring opening of benzocyclobutene (BCB) under sonochemical conditions.[5] This reaction is governed by the Woodward-Hoffmann (WH) rules, [63,64] which state that the ring opening of BCB should proceed through a conrotatory pathway when the reaction is activated thermally and a disrotatory pathway when the reaction is activated photochemically. Conrotatory ring opening refers

to both methylene groups in the carbon-carbon scissile bond rotating in the same direction whereas disrotatory ring opening refers to the methylene groups rotating in opposite directions. Based on the conservation of orbital symmetry, the thermally activated reaction is considered allowed and the photochemically activated reaction is considered forbidden. Under sonochemical conditions, the ring opening proceeds along the formally forbidden pathway. Specifically, the application of an external force to *trans*-substituents leads to the system following a conrotatory pathway whereas the application of an external force to *cis*-substituents leads to the system following a disrotatory pathway. This results in the formation of identical products in violation of the WH rules. The photochemical, thermal and mechanochemical pathways for the ring opening of BCB are illustrated in Figure 1-6.

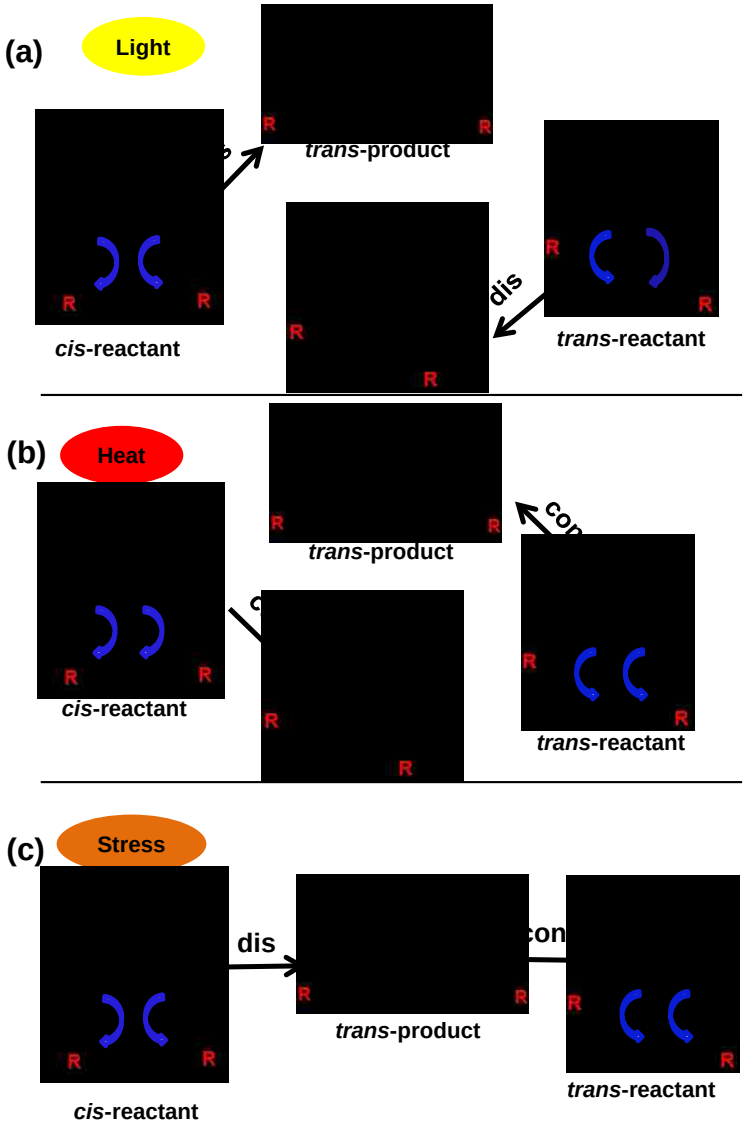

Figure 1-6. Reaction pathways for the ring opening of benzocyclobutene along the **(a)** photochemical pathway (forbidden), **(b)** thermal pathway (allowed), and **(c)** mechanochemical pathway that proceeds under sonochemical conditions. The Woodward-Hoffmann rules predict that both *cis* and *trans* benzocyclobutene follow and disrotatory pathway under photochemical conditions and a conrotatory pathway under thermal conditions. The application of mechanical stress using sonication to *cis*-substituents leads to a disrotatory ring opening whereas the application of mechanical stress to *trans*-substituents leads to a conrotatory ring opening such that identical products are formed. The R group denotes an alkane functional group and the blue arrows indicate the direction associated with the rotation of the methylene groups.

The mechanochemical methods mentioned above have gained significant interest in recent years as a means to subject molecules to precise forces in practical synthetic efforts. The force ranges that can be applied vary in each of these methods are summarized in Table 1-1. The forces applied in each of these methods are on the same order of magnitude as the forces needed to induce bond rupture.[65]

Table 1-1: A comparison of the force ranges applied in mechanochemical methods

Mechanochemical method	**Force range (pN)**
Optical tweezers	0.1 - 100
Magnetic tweezers	0.1 - 200
Atomic force microscopy	10^1 - 10^3
Molecular force probes	150 - 600
Sonication	10^1 - 10^3

Overall, the use of these mechanochemical methods in practical experimental efforts have demonstrated that applied mechanical stresses and forces can be used to activate reactions involving bond rupture and selectively guide systems along particular reaction pathways. Such phenomenon has led to the application of mechanochemistry on larger scale processes such as the development of stress sensors. [4,66] This has motivated the development and application of theoretical models to understand how reactions are activated mechanically. These models are discussed in the next section.

1.3 Theoretical models

Mechanochemistry at the molecular level can be thought of as applying an external force of magnitude F between two atoms or groups in a molecule. This is illustrated in Figure 1-7, in which F is applied between two hydrogen atoms that are attached to the carbon atoms of the scissile bond in cyclobutene.

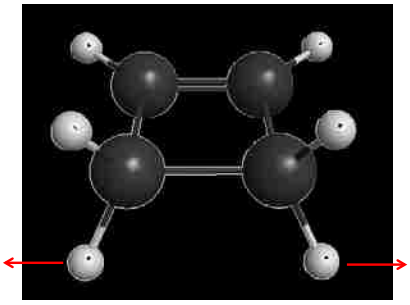

Figure 1-7. A general schematic illustrating mechanochemistry at the molecular level, in which an external force of magnitude F is applied between two hydrogen atoms in cyclobutene that are separated by a distance R. Black and white spheres indicate carbon and hydrogen atoms respectively.

The application of F to specific atoms or groups in a molecule performs mechanical work on the system in the amount $W=FR(\mathbf{q})$, where $\mathbf{q}$ represents the nuclear coordinates of the system and R is the distance between the atoms for which F is applied along. The mechanical work performed on the system modifies the potential energy surface (PES) on which the molecule moves. Specifically, F deforms molecules along a specific direction on the ground-state PES. The resulting force-modified potential energy surface (FMPES) can be expressed as:

$$E(\mathbf{q},F) = E_{\mathrm{BO}}(\mathbf{q}) - FR(\mathbf{q}) \tag{1.3}$$

where E_{BO} is the energy of the system in the absence of F on the Born-Oppenheimer PES. The evaluation of structures and other specific features of the Born-Oppenheimer PES are discussed in chapter 2 section 2.1. Structures and energetics on the FMPES can be evaluated using both qualitative and quantitative methods. Qualitative methods predict features of the FMPES and provide insights into how subjecting molecules to F affects reaction barriers without performing a large number of quantum chemical calculations. In contrast, quantitative methods rely on performing quantum chemical calculations at each value of F to calculate changes in reaction barriers and evaluate specific features of the FMPES.

1.3.1 Qualitative methods

Kauzmann and Erying[67] proposed one of the earliest models to qualitatively describe the reactivity of chemical systems under mechanochemical conditions. This model is based on extending transition state theory to examine the effect of F on $\Delta E^{\ddagger}$. This model predicts that $\Delta E^{\ddagger}$ decreases linearly with F under mechanochemical conditions. Several models have expanded on the work of Kauzmann and Erying. Bell's model[68] has been applied to qualitatively examine the effect of F on reaction rates. In Bell's model, F is applied between two atoms or groups that change in separation during the course of the reaction. It is assumed that the application of F does not change the reactant and TS structures. Given these assumptions in Bell's model, the reaction barrier on the FMPES can be evaluated using the expression:

$$\Delta E^{\ddagger}(F) = \Delta E^{\ddagger}_{BO}(0) - F\Delta R_0 \qquad (1.4)$$

where $\Delta E_{BO}^{\ddagger}$ is the barrier on the Born-Oppenheimer PES in the absence of F and ΔR_0 is the change in distance between the atoms or groups in a molecule as the system progresses from the reactant to the TS in the absence of F. Bell's model has been applied to investigate the mechanochemical response of several biological systems including the rupture of disulfide bonds in proteins, [69] force generation in actin binding protein motors, [70] and distortion of extracellular matrices in cells and tissues.[71] One of the main advantages of using Bell's model to simulate mechanochemical processes is that it only requires information of the reactant and TS structures and energies in the absence of F. As such, Bell's model correctly predicts changes in $\Delta E^{\ddagger}$ in a qualitative manner. The assumption that the reactant and TS structures are not altered with F, however limits the quantitative accuracy of Bell's model. This is because any force-induced changes in reactant or TS structures affects the underlying energetics of these species on the Born-Oppenheimer PES, which influences $\Delta E^{\ddagger}$ and the kinetics of the reaction.

The tilted PES model[72] can also be used to qualitatively describe features of the FMPES. The structural changes in the reactant and TS that arise from the application of F are accounted for in a limited manner using the tilted PES model. It is assumed that the coordinate in which F is applied is aligned exactly with the reaction coordinate in the absence of F termed zero-F reaction coordinate. The energies of the structures along the zero-F reaction coordinate are shifted upon the application of F by an amount $-FR$, where R is the distance between the atoms or groups that F is applied along at each point along the zero-F reaction coordinate. The reduction from the mechanical work term lowers $\Delta E^{\ddagger}$ relative to its value in the absence of F as shown in Figure 1-8. Furthermore, the

application of *F* alters the positions of the structures along the zero-*F* reaction coordinate. Specifically, if *F* is positive and *R* increases as the system progresses from the reactant to the TS, the reactant and TS shift closer to one another along the zero-*F* reaction coordinate. The shift in positions of the reactant and TS such that they move closer together along the zero-*F* reaction coordinate lowers $\Delta E^{\ddagger}$, which is consistent with Hammond's postulate. [73,74] Although the tilted potential energy surface model accounts for these Hammond effects, it does take into account changes in the reactant and TS structures that occur along other coordinates than the zero-*F* reaction coordinate, which are termed anti-Hammond effects. These anti-Hammond effects are significant in regards to influencing $\Delta E^{\ddagger}$'s and the reaction pathways that the system may follow.

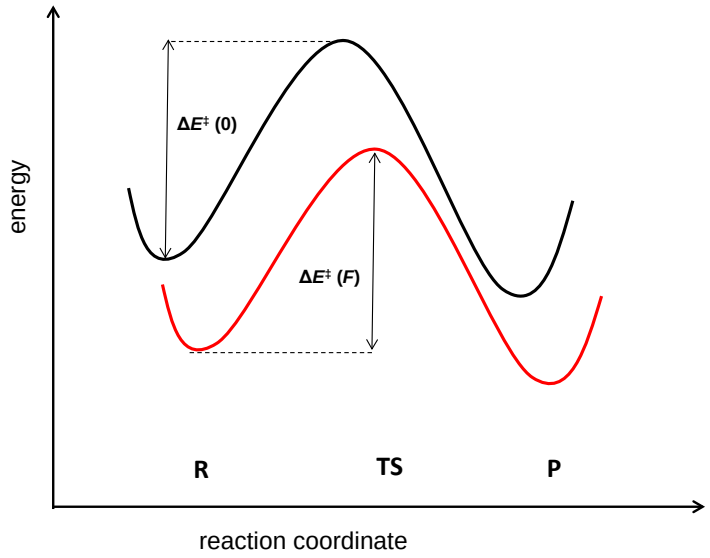

Figure 1-8. A general schematic of the tilted potential energy surface model, in which the application of *F* affects the PES on which the molecule moves. The black curve corresponds to the reaction coordinate in the absence of *F* whereas the red curve corresponds to the reaction coordinate under mechanochemical conditions that is obtained by adding *–FR* to the energies of the structures along the black curve. The labels R, TS, and P correspond to the positions of the reactant, transition state, and product respectively along the black and red curves. The $\Delta E^{\ddagger}(0)$ quantity corresponds to the reaction barrier on the zero-*F* reaction coordinate and the $\Delta E^{\ddagger}(F)$ is the reaction barrier obtained by adding *–FR* to the zero-*F* energies of the reactant and TS.

1.3.2 Quantitative methods

The force-induced anti-Hammond effects that arise from changes in the reactant and TS structures along coordinates other than the zero-*F* reaction coordinate can be described using quantitative methods. Three of the methods that have appeared in the literature are COnstrained Geometries Simulate External Force (COGEF), [28] Steered Molecular Dynamics (SMD) simulations, [29] and the External Force is Explicitly Included (EFEI). [27] COGEF techniques are used to model isometric conditions, which involve fixing a distance associated with the degree of freedom to which *F* is applied and determining the value of *F* required to maintain that distance. Such conditions can be achieved in experimental measurements such as the force-extension curves obtained in AFM in which the end-to-end distance of a molecule is fixed and the value of *F* that is required to maintain this distance is measured. Measurements of *F* at multiple values of *R* yield force-extension curves, which are useful in the context of determining the values of *F* that are required for various mechanochemical processes including the unfolding of single protein molecules[75–77] and the rupture of covalent bonds in polymers. [26,78] The COGEF technique models isometric conditions by imposing a holonomic constraint to fix the distance between two atoms in a molecule at a target value, R_0, while allowing all other atoms in the molecule to relax according to the type of calculation that is being performed. Applying the constraint to maintain a distance of R_0 between two atoms can be interpreted as subjecting the system to an external force, *F*, between these two atoms that is equal in magnitude but opposite in direction to the internal force, F_{int}, defined as:

$$F_{\text{int}} = -\frac{\partial E_{\text{BO}}}{\partial R} \tag{1.5}$$

where R represents one of the internal coordinates defining the molecular geometry and corresponds to the distance between the two atoms that are subjected to the constraint. The internal force acts along the vector connecting the two atoms that are subjected to the distance constraint. As a result, the PES on which the molecule moves is modified according to the expression:

$$E_{COGEF}(\mathbf{q}, R_0) = E_{BO}(\mathbf{q}) + F_{\text{int}} R_0 \tag{1.6}$$

where $\mathbf{q}$ represents the nuclear coordinates of the molecule, R_0 is the target distance of the PPs, E_{BO} is the energy of the structure on the Born-Oppenheimer PES, and E_{COGEF} is the energy of the structure on the FMPES obtained under COGEF conditions. The practical use of COGEF simulations has several advantages. One of these advantages is that geometric constraints are applied in chemical simulations that are not related to mechanochemistry. An example of this is constraining DOFs that are significant in exploring features of the Born-Oppenheimer PES and examining changes in free energies in molecular dynamics (MD) simulations. [79] Another advantage is that many quantum chemical software packages allow one to constrain distances or other DOFs in molecules. As such, COGEF can be used in conjunction without further modification to quantum chemical codes.

In addition to being able to model isometric conditions, COGEF methods can also be used to simulate isotensional conditions, which are also present in mechanochemical experiments. Isotensional conditions involve applying a constant external force between two atoms and allowing the distance between the atoms and the other DOFs to change in response the applied external force. Such conditions can be achieved experimentally through process such as stretching macromolecules using AFM[17] and dissociation of metal-ligand coordination complexes using sonication.[80,81] Modeling isometric conditions using COGEF requires locating different structures on the FMPES where the internal forces associated with the constrained distances are equivalent. One of the drawbacks of this approach is that locating different structures that have the same value of F_{int} typically involves performing scans over large regions of the FMPES. Therefore, methods such as SMD and EFEI are more suitable to model isotensional conditions than COGEF.

SMD simulations model isotensional conditions by attaching atoms in a molecule that are termed attachment points (APs) to a set of points in space that are external to a molecule termed pulling points (PPs). An external force, F, is applied along the vector connecting each AP to its corresponding PP as illustrated in Figure 1-9. SMD simulations have been used to study several mechanochemical processes such as the unbinding of biotin from streptavidin,[82] protein-ligand interactions,[83] and the unfolding of immunoglobulin.[84]

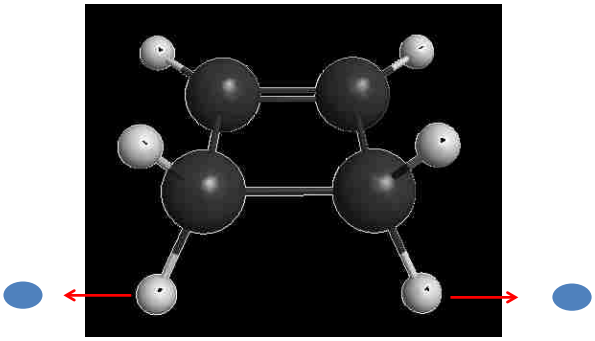

Figure 1-9. A schematic illustrating the application of an external force, *F*, in SMD simulations. In this case, two hydrogen atoms attached to the carbon atoms of the scissile bond are treated as attachment points that are each attached to an external pulling point (blue sphere). Black and white spheres represent carbon and hydrogen atoms respectively

One of the main drawbacks associated with the practical application of SMD simulations is the ambiguity with the selection of PPs. In certain cases, the positions of the PPs are defined such that they are linearly aligned with the APs as in the case of cyclobutene (Fig. 1-9). In several molecules, however the PPs may not be linearly aligned with the APs. The EFEI method is often used to overcome this issue by treating specific atoms in a molecule as the PPs rather than attaching those atoms to external PPs. Isotensional conditions are modeled in the EFEI method by applying *F* along the vector, **R**, connecting the two atoms used as PPs. As a result, the PES on which the molecule moves is modified according to the expression:

$$E_{EFEI}(\mathbf{q}, R_0) = E_{BO}(\mathbf{q}) - FR \tag{1.7}$$

where **q** represents the nuclear coordinates of the atoms in the molecule, E_{BO} is the energy of the structure in the absence of *F* on the Born-Oppenheimer PES, *R* is the distance between the PPs, and E_{EFEI} is the energy of the structure on the FMPES obtained under

EFEI conditions. In contrast to COGEF and SMD simulations, the EFEI method is not implemented in various quantum chemical software packages. However, one can modify existing quantum chemical codes to implement Eq. (1.7) as well its first and second derivatives to perform geometry optimizations and vibrational frequency calculations directly on the FMPES. This is discussed in further detail in chapter 2. The practical use of Eq. (1.7) in mechanochemical simulations requires the definition of atoms to be used as PPs, however eliminates the requirement to select directions along which F is applied, as in the case of SMD simulations. Furthermore, the application of F along the vector connecting two atoms in the molecule ensures that no net external force is added to the molecule. Despite these advantages, the EFEI method is an approximation to isotensional conditions and does not take into account any devices that are used to subject molecules to F. The EFEI method however can be interpreted as a more accurate approximation of isotensional conditions than COGEF due to the differences in the control parameters in these methods. In COGEF, the distance between the atoms subjected to F is the control variable, whereas F is the control variable in EFEI. The ability to control F in EFEI simulations has prompted several investigations into mechanochemical processes such as the rupture of covalent bonds in pericyclic reactions,[85–87] intermolecular cyclizations, [88] and the design of optical force probes.[89]

1.4 Previous theoretical studies

COGEF, SMD, and EFEI methods have been applied to investigate several mechanochemical processes including the reactivity of disulfide bonds, [69,90,91] unfolding of proteins, [82,84,92] and rupture of covalent bonds in pericyclic reactions.[29,86,87,93] The

differences in the results of the simulations performed with these methods are evident from studies of the ring opening of cyclobutene along conrotatory and disrotatory pathways. As discussed above, a previous experimental study[5] has demonstrated that sonication can be used to selectively direct the ring opening of benzocyclobutene along either the conrotatory or disrotatory pathway irrespective of the WH rules. In particular, the application of *F* to substituents attached to the carbon atoms of the scissile bond in a *trans*-configuration led to the system following a conrotatory pathway, whereas applying *F* to substituents in a *cis*-configuration resulted in the ring opening proceeding along the disrotatory pathway.

Quantum chemical calculation employing the EFEI and SMD methods yield results that are consistent with the previous sonication study of the ring opening of cyclobutene. [27,29,85] A study performed by Martinez and colleagues[29] has used SMD simulations to subject cyclobutene to external forces using hydrogen atoms attached to the carbon atoms of the scissile bond as the APs. The resulting FMPESs for applying *F* between hydrogen atoms in a *cis*-configuration and in a *trans*-configuration are shown in Figure 1-10. The plots indicate that the conrotatory and disrotatory minimum energy pathways (MEPs) were affected differently when *F* was applied between hydrogen atoms in a *cis*-configuration compared to hydrogen atoms in a *trans*-configuration. Specifically, the application of *F* between *cis*-substituents yields barrier heights along conrotatory and disrotatory MEPs that become nearly equivalent when F = 1.5 nN. The FMPES obtained from applying *F* between *trans*-substituents indicates that the barrier for the conrotatory MEP decreased with *F* whereas the barrier for the disrotatory MEP remained largely unaffected with increasing *F*. The results of this study demonstrate the ability of applied

mechanical stress to selectively guide systems along particular reaction pathways. The application of *F* between *cis*-substituents activated the formally forbidden disrotatory pathway for the ring opening of cyclobutene as in the case of the previous sonication study.[5]

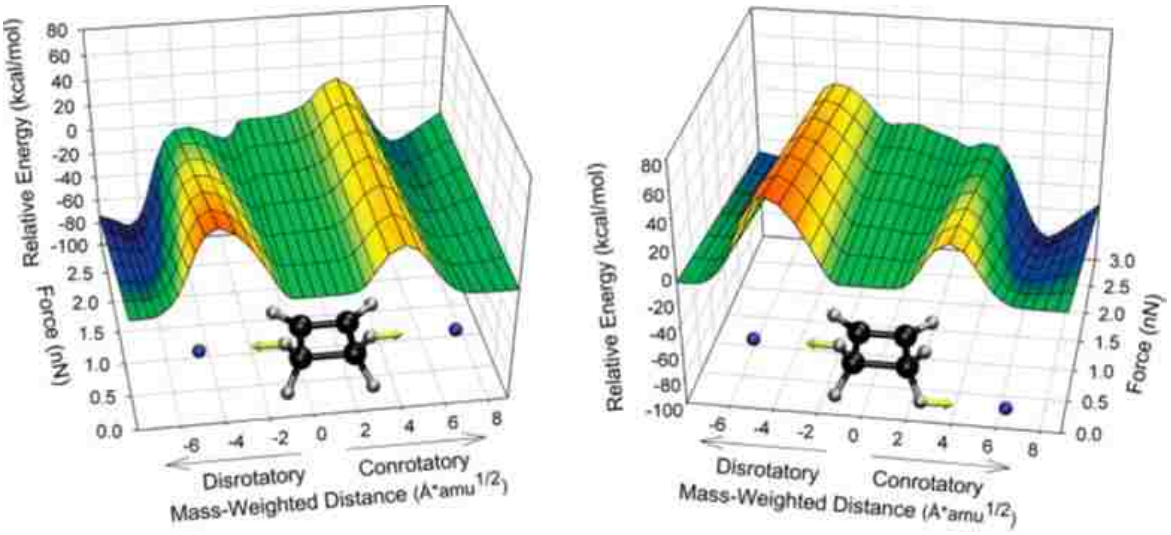

Figure 1-10. Force-modified potential energy surfaces obtained for the ring opening of cyclobutene using steered molecular dynamics simulations with *F* applied between hydrogen atoms in **(a)** *cis*-configuration and **(b)** *trans*-configuration. The disrotatory pathway decreases relative to the conrotatory pathway when *F* is applied between *cis*-substituents with the barriers for both pathways becoming nearly equivalent at 1.5 nN. The application of *F* between *trans*-substituents leads to a decrease in the conrotatory barriers whereas the barriers for the disrotatory pathway remain relatively unaffected. The blue spheres represent the external attachment points and the yellow arrows indicate the direction in which *F* is applied. The black spheres denote carbon atoms and the white spheres denote hydrogen atoms in cyclobutene. [29]

EFEI-based simulations have also shown that the application of *F* to *cis*-substituents activates the disrotatory ring opening of cyclobutene. [27,85] A study performed by Marx and coworkers[27] has shown that applying *F* to *cis*-PPs in 1,2-dimethylcyclobutene makes the conrotatory pathway disappear at values of *F* that exceed 0.75 nN. Furthermore, the disrotatory pathway becomes barrierless at values of *F* greater than 3 nN as shown in Figure 1-11.

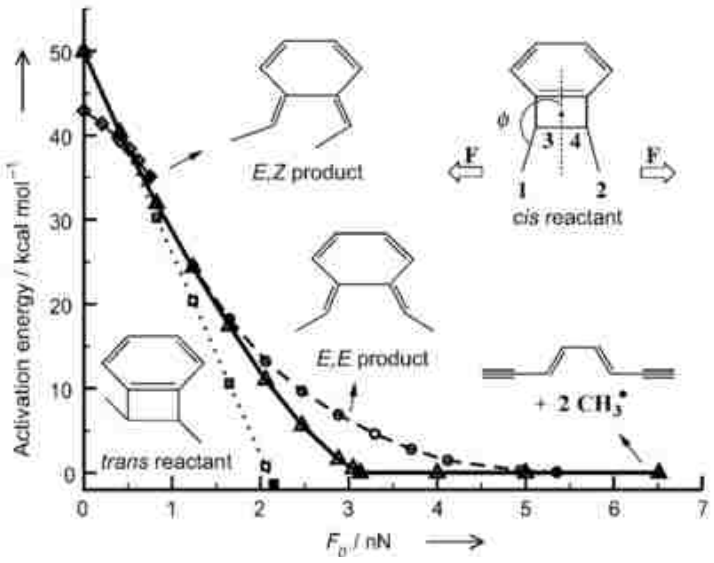

Figure 1-11. Activation energy as a function of external force, F_0, for the mechanochemical ring opening of *cis*-1,2-dimethylbenzocyclobutene ("*cis* reactant") to along conrotatory (open diamond symbols) and disrotatory (open triangle symbols) pathways. The EFEI method was used to apply F along the vector connecting the PPs labelled **1** and **2**. At F = 0.75 nN, the conrotatory pathway is rendered inaccessible and the disrotatory pathway becomes favoured. The disrotatory pathway becomes barrierless at values of F greater than 3 nN. The open square symbols and open circle symbols represent predicted barriers of the disrotatory pathway using Bell's model and the tilted potential energy surface model respectively. The *cis*-reactant dissociates at F = 6.5 nN, which is attributed to the cleavage of the C-C scissile bond (**3-4**). [27]

A study performed by Mosey and others[85] has accounted for the activation of the ring opening of cyclobutene along the disrotatory pathway by examining changes in the electronic structure. In that study, the EFEI method was used to show that the mechanical activation of a formally forbidden product according to the WH rules does not occur due to a change in electronic structure analogous to that achieved through irradiation. Instead, the disrotatory pathway is activated in two ways. First, the application of F shifts the position of the TS along the MEP towards the reactant, which reduces $\Delta E^{\ddagger}$. Second, the orbital effects dictated by the WH rules are rendered secondary to mechanical effects.

The ring opening of cyclobutene under mechanochemical conditions was also investigated using the COGEF method. [93] In that study, a distance constraint was applied between two hydrogen atoms attached to the carbon atoms of the scissile bond that were in a *cis* configuration. The distance between these atoms was increased at a rate 2.0 Å / ps during the simulation to mimic the application of *F*. A total of 20 independent MD simulations were performed with the conrotatory product formed in all cases as illustrated in Figure 1-12. This result is inconsistent with the previous sonication study, [5] SMD study, [29] and EFEI simulations. [27,85]

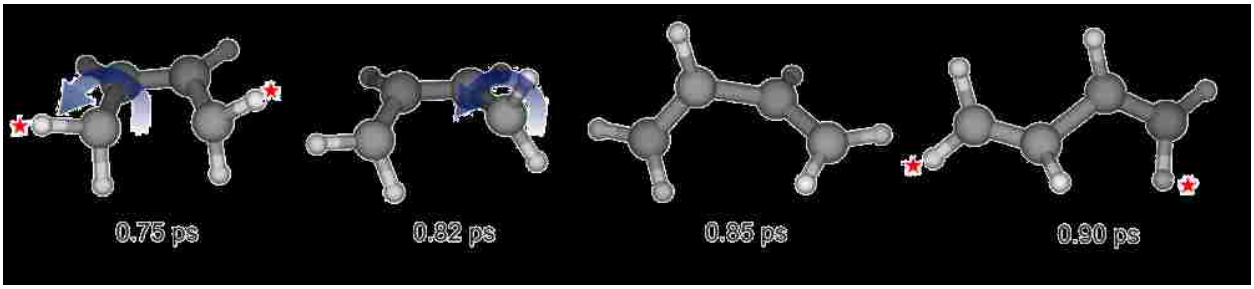

Figure 1-12. Snapshots at various times that were taken for a COGEF-based molecular dynamics simulation of the ring opening of cyclobutene. During the course of the simulation, both methylene groups rotate in the same direction yielding the conrotatory product. The grey and white spheres represent carbon atoms and hydrogen atoms respectively. The application of *F* was simulated by increasing the distance between the hydrogen atoms in a *cis*-configurations, shown using red stars, at a rate of 2.0 Å / ps. [93]

The discrepancy between the results of mechanochemical simulations of cyclobutene using COGEF versus EFEI and SMD methods has motivated further studies to understand the origin of this difference. Mosey and others[9] have attributed this discrepancy to the difference in the FMPESs obtained using COGEF and EFEI methods. In the FMPES obtained under COGEF conditions (Fig. 1-13), the system does not follow a pathway that leads to the formation of the disrotatory product. As the carbon-carbon scissile bond dissociates, which occurs at 4.3 Å (Fig. 1-13a), the methylene groups are

free to rotate and as such the system can proceed along either the conrotatory or disrotatory pathway. It is energetically favorable for the structure on the disrotatory pathway to move onto the conrotatory surface as opposed to following the pathway leading to the disrotatory product. Moreover, the authors indicated that the disrotatory product was not a local minimum on the FMPES obtained under COGEF conditions. In contrast, the FMPES obtained under EFEI conditions indicates that the disrotatory MEP can be accessed due to a reduction in $\Delta E^{\ddagger}$ relative to the conrotatory MEP. The FMPES calculated at F = 1500 pN along both conrotatory and disrotatory pathways are shown in Figure 1-14. The data show that the MEPs connecting reactants to both conrotatory and disrotatory pathways could be identified. The results of this study demonstrate that differences in the underlying FMPESs can lead to differences in the outcomes of simulations performed using these methods. Given that the EFEI method yields results that are consistent with the previous sonication study,[5] the quantum chemical calculations performed in this thesis employ the EFEI method for modeling mechanochemical conditions. SMD simulations also yield results that are consistent with the previous sonication study, [5] however they are not used because of practical limitations. Specifically, the APs defined in SMD simulations are external to the molecule and the directions to which F is applied can be somewhat ambiguous in certain cases.

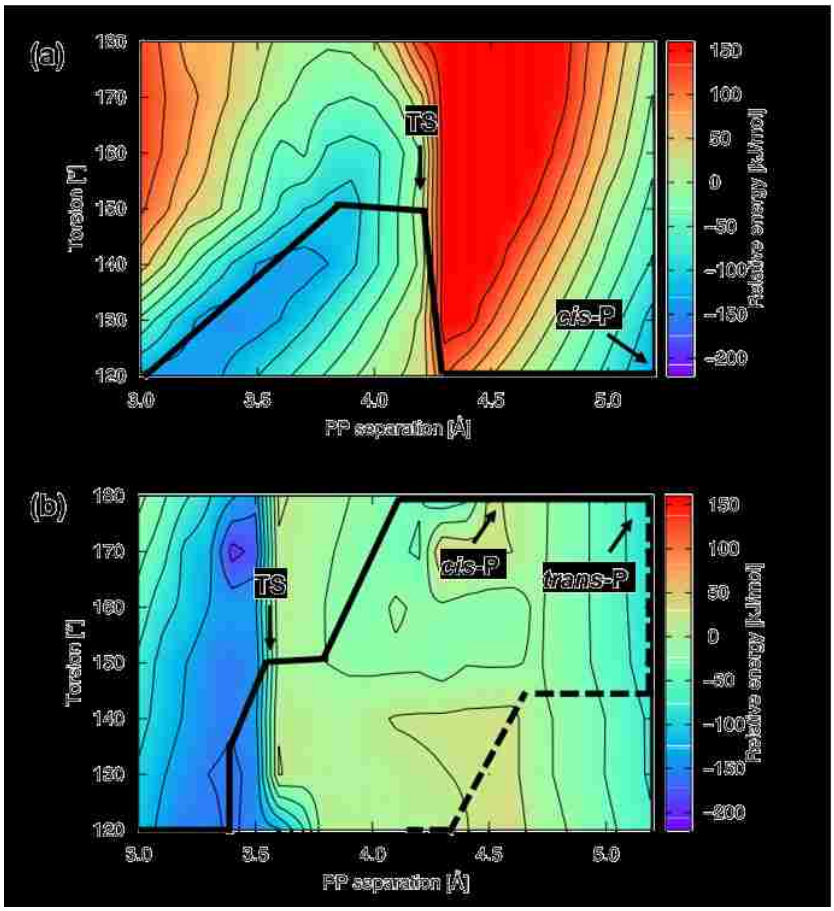

Figure 1-13. FMPESs obtained under COGEF conditions for the ring opening of cyclobutene along the **(a)** disrotatory pathway and **(b)** conrotatory pathway. The energies on the surfaces are calculated relative to a structure on the disrotatory surface with a PP separation of 3.0 Å and torsion of 180°. This torsion is calculated on the basis of the rotation of the methylene groups either in a conrotatory or disrotatory manner. Solid lines indicate the MEP on each surface. The dashed line indicates the path the system follows upon moving from the disrotatory surface to the conrotatory surface. The locations of transitions states and products are represented by labels 'TS' and 'P' respectively. [9]

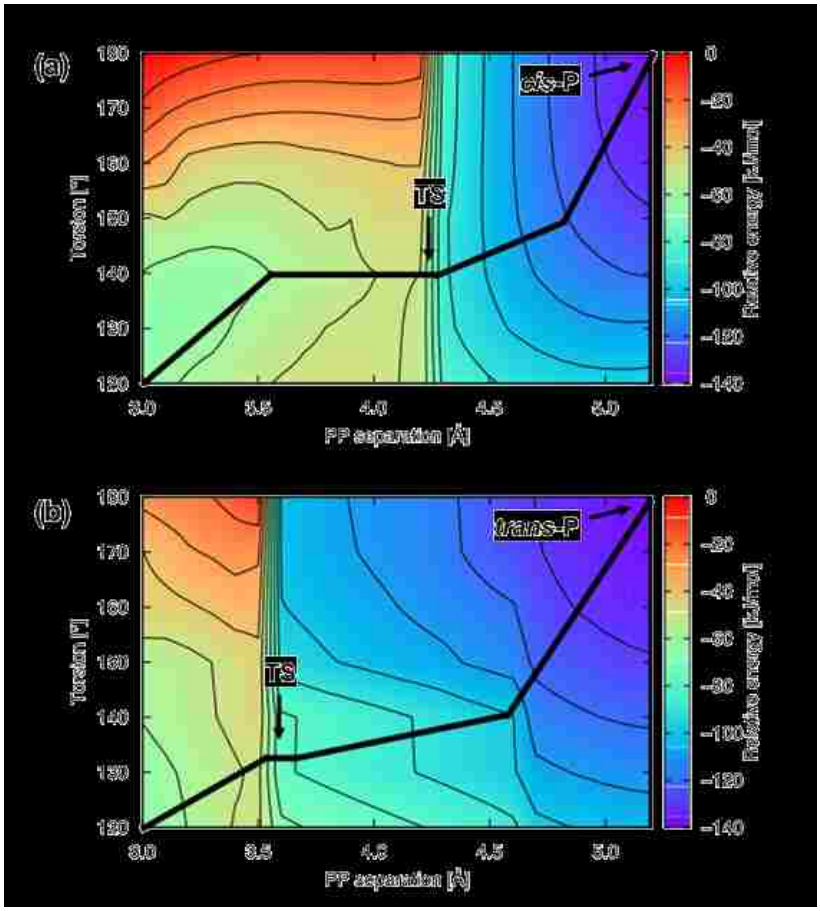

Figure 1-14. FMPESs obtained under EFEI conditions at F = 1500pN for the ring opening of cyclobutene along the **(a)** disrotatory pathway and **(b)** conrotatory pathway. The energies on the surfaces are calculated relative to a structure on the disrotatory surface with a PP separation of 3.0 Å and torsion of 180°. This torsion is calculated on the basis of the rotation of the methylene groups either in a conrotatory or disrotatory manner. Solid lines indicate the MEP on each surface. The locations of transitions states and products are represented by labels 'TS' and 'P' respectively. [9]

1.5 Objectives of thesis

Performing quantum chemical calculations employing the EFEI method directly on the FMPES can be computationally demanding, which restricts the investigation of macromolecules that are typically used in mechanochemical processes. [94] Consider a case in which one wanted to identify a set of PPs in a molecule that yield a desired mechanochemical response (e.g. reduce $\Delta E^{\ddagger}$ by the largest amount under mechanochemical conditions). In the case of the ring opening of cyclobutene, it was somewhat intuitive to select hydrogen atoms that are attached to the carbon atoms of the scissile bond as PPs because the application of F between these atoms would induce rupture of the carbon-carbon scissile bond. In several cases, however, the selection of PPs might not be as clear. Furthermore, it might be necessary to examine several combinations of PPs in a molecule to achieve a desired mechanochemical response. To accomplish this using the EFEI method, one would have to perform geometry optimization and vibrational frequency calculations (see chapter 2 for details of these calculations) of the reactant and TS at several values of F for the combinations of PPs considered. The computational expense of a geometry optimization of a structure on the FMPES is nearly equivalent to the corresponding geometry optimization of the same structure on the Born-Oppenheimer PES. However, since the number of unique combinations of PP scales as N^2, where N is the number of atoms in the molecule, it becomes computationally prohibitive to fully investigate the mechanochemical response of all possible sets of PPs within the EFEI method as the size of the molecule increases.

Bell's model and the tilted potential energy surface model are not computationally demanding in comparison to the EFEI method because geometry optimizations and

vibrational frequency calculations are required only for reactant and TS structures in the absence of *F*. These models, however do not account for changes in structure with *F*, which are necessary to fully investigate the mechanochemical response of a system. Bell's model has been extended recently to account for the force-induced changes in structure of the reactants and TS. [21,95,96] These models are described in chapter 3. The extension of Bell's model provides an estimate of $\Delta E^{\ddagger}$ on the FMPES while limiting the number of quantum chemical calculations. These methods are effective for examining the mechanochemical response for a single set of PPs, however examining all possible combinations of PPs is computationally inefficient when this model is applied in practical efforts. As such, a computationally efficient approach for applying an extended version of Bell's model[95] to reactions for all possible combinations of PPs is discussed in chapter 3.

The structural changes in the reactant and TS that result from the application of *F* may be undesirable for certain reactions because either or both of these species may be required to remain in a particular configuration for the reaction to occur. Chapter 4 focuses on developing strategies for functionalizing molecules in a manner that alters the DOFs that are affected the most from the application of *F*, and hence the mechanochemical response. These strategies include the addition of constraints consisting of rings of varying size and chemical composition to the reactant and TS structures for several unimolecular reactions. Altering the mechanochemical response of systems through the addition of constraints will assist in the rational design of molecular systems in practical synthetic efforts.

In addition to examining such force-induced structural changes, this thesis focuses on understanding how reactions are mechanically activated at the fundamental level. The

energy of a structure on the FMPES that is evaluated using Eq. (1.7) takes into account the Born-Oppenheimer energy of the structure and the mechanical work performed along the vector connecting the PPs. Chapter 5 focuses on examining the contributions of both terms on the right hand side of Eq. (1.7) to the total EFEI energy. Specifically, changes in $\Delta E^{\ddagger}$ with F are examined for a series of bimolecular reactions with substituents of varying size. The effect of the sterics of the substituent on the contributions from the Born-Oppenheimer energy and the mechanical work term to the total EFEI energy is investigated.

The results presented in chapters 3 to 5 involve examining the mechanochemical response for various unimolecular and bimolecular reactions. The changes in $\Delta E^{\ddagger}$ with F can be significantly different for unimolecular and bimolecular reactions. It is therefore of fundamental value to understand the differences in mechanical activation of unimolecular and bimolecular reactions. Chapter 6 addresses the origin of this difference by relating mechanochemical conditions to kinetic principles (e.g. Hammond effects).

References:

1. Beyer, M. K. & Clausen-Schaumann, H. Mechanochemistry: the mechanical activation of covalent bonds. *Chem. Rev.* **105,** 2921–2948 (2005).

2. James, S. L. *et al.* Mechanochemistry: opportunities for new and cleaner synthesis. *Chem Soc Rev* **41,** 413–447 (2012).

3. Rosen, B. M. & Percec, V. Mechanochemistry: A reaction to stress. *Nature* **446,** 381–382 (2007).

4. Black, A. L., Lenhardt, J. M. & Craig, S. L. From molecular mechanochemistry to stress-responsive materials. *J Mater Chem* **21,** 1655–1663 (2011).

5. Hickenboth, C. R. *et al.* Biasing reaction pathways with mechanical force. *Nature* **446,** 423–427 (2007).

6. Ribas-Arino, J. & Marx, D. Covalent Mechanochemistry: Theoretical Concepts and Computational Tools with Applications to Molecular Nanomechanics. *Chem. Rev.* **112,** 5412–5487 (2012).

7. Lenhardt, J. M. & Craig, S. L. Mechanochemistry: Force probes in a bottle. *Nat. Nanotechnol.* **4,** 284–285 (2009).

8. Seidel, C. A. M. & Kühnemuth, R. Mechanochemistry: molecules under pressure. *Nat. Nanotechnol.* **9,** 164–165 (2014).

9. Kochhar, G. S., Heverly-Coulson, G. S. & Mosey, N. J. in *Polymer Mechanochemistry* (ed. Boulatov, R.) **369,** 37–96 (Springer International Publishing, 2015).

10. Tian, Y., Kucharski, T. J., Yang, Q.-Z. & Boulatov, R. Model studies of force-dependent kinetics of multi-barrier reactions. *Nat. Commun.* **4,** 1-10 (2013).

11. Friščić, T. *et al.* Real-time and in situ monitoring of mechanochemical milling reactions. *Nat. Chem.* **5,** 66–73 (2012).

12. Içli, B. *et al.* Synthesis of Molecular Nanostructures by Multicomponent Condensation Reactions in a Ball Mill. *J. Am. Chem. Soc.* **131,** 3154–3155 (2009).

13. Wang, M. D., Yin, H., Landick, R., Gelles, J. & Block, S. M. Stretching DNA with optical tweezers. *Biophys. J.* **72,** 1335–1346 (1997).

14. Ashkin, A. Acceleration and Trapping of Particles by Radiation Pressure. *Phys. Rev. Lett.* **24,** 156–159 (1970).

15. Moffitt, J. R., Chemla, Y. R., Smith, S. B. & Bustamante, C. Recent Advances in Optical Tweezers. *Annu. Rev. Biochem.* **77,** 205–228 (2008).

16. De Vlaminck, I. & Dekker, C. Recent Advances in Magnetic Tweezers. *Annu. Rev. Biophys.* **41,** 453–472 (2012).

17. Kreuzer, H. J., Payne, S. H. & Livadaru, L. Stretching a Macromolecule in an Atomic Force Microscope: Statistical Mechanical Analysis. *Biophys. J.* **80,** 2505–2514 (2001).

18. Kersey, F. R., Yount, W. C. & Craig, S. L. Single-molecule force spectroscopy of bimolecular reactions: system homology in the mechanical activation of ligand substitution reactions. *J. Am. Chem. Soc.* **128,** 3886–3887 (2006).

19. Duwez, A.-S. *et al.* Mechanochemistry: targeted delivery of single molecules: *Nat. Nanotechnol.* **1,** 122–125 (2006).

20. Yang, Q.-Z. *et al.* A molecular force probe. *Nat. Nanotechnol.* **4,** 302–306 (2009).

21. Huang, Z. & Boulatov, R. Chemomechanics with molecular force probes. *Pure Appl. Chem.* **82,** 931-951 (2010).

22. Suslick, K. S. Sonochemistry. *science* **247,** 1439–1445 (1990).

23. Suslick, K. S., Hammerton, D. A. & Cline, R. E. Sonochemical hot spot. *J. Am. Chem. Soc.* **108,** 5641–5642 (1986).

24. Colarusso, P. & Serpone, N. Sonochemistry II.—Effects of ultrasounds on homogeneous chemical reactions and in environmental detoxification. *Res. Chem. Intermed.* **22,** 61–89 (1996).

25. Koda, S. Ultrasonic degradation of water-soluble polymers. *Polymer* **35,** 30–33 (1994).

26. Davis, D. A. *et al.* Force-induced activation of covalent bonds in mechanoresponsive polymeric materials. *Nature* **459,** 68–72 (2009).

27. Ribas-Arino, J., Shiga, M. & Marx, D. Understanding covalent mechanochemistry. *Angew. Chem. Int. Ed.* **48,** 4190–4193 (2009).

28. Beyer, M. K. The mechanical strength of a covalent bond calculated by density functional theory. *J. Chem. Phys.* **112,** 7307-7312 (2000).

29. Ong, M. T., Leiding, J., Tao, H., Virshup, A. M. & Martínez, T. J. First principles dynamics and minimum energy pathways for mechanochemical ring opening of cyclobutene. *J. Am. Chem. Soc.* **131,** 6377–6379 (2009).

30. Takacs, L. The historical development of mechanochemistry. *Chem. Soc. Rev.* **42,** 7649-7659 (2013).

31. Tsuzuki, T. & McCormick, P. G. Mechanochemical synthesis of nanoparticles. *J. Mater. Sci.* **39,** 5143–5146 (2004)

32. Boldyrev, V. V. & Tkáčová, K. Mechanochemistry of Solids: Past, Present, and Prospects. *J. Mater. Synth. Process.* **8,** 121–132 (2000).

33. Takacs, L. The mechanochemical reduction of AgCl with metals: Revisiting an experiment of M. Faraday. *J. Therm. Anal. Calorim.* **90,** 81–84 (2007).

34. Ling, A. R. & Baker, J. L. XCVI.-Halogen Derivatives of Quinone. Part II.* Derivatives of Quinhydrone. *J. Chem. Soc. Trans.* **63,** 1314-1327 (1893).

35. Bridgman, P. W. Recent Work in the Field of High Pressures. *Rev. Mod. Phys.* **18,** 1–93 (1946).

36. Gaffet, E. & Harmelin, M. Crystal-amorphous phase transition induced by ball-milling in silicon. *J. Common Met.* **157,** 201–222 (1990).

37. Weeber, A. W. & Bakker, H. Amorphization by ball milling. A review. *Phys. B Condens. Matter* **153,** 93–135 (1988).

38. Calka, A. & Radlinski, A. . Universal high performance ball-milling device and its application for mechanical alloying. *Mater. Sci. Eng. A* **134,** 1350–1353 (1991).

39. Oehring, M., Klassen, T. & Bormann, R. The formation of metastable Ti–Al solid solutions by mechanical alloying and ball milling. *J. Mater. Res.* **8,** 2819–2829 (1993).

40. Koch, C. C. Preparation of ‘“amorphous”’ Ni60Nb40 by mechanical alloying. *Appl. Phys. Lett.* **43,** 1017-1019 (1983).

41. Neikov, O. D. *et al. Handbook of Non-Ferrous Metal Powders: Technologies and Applications*. (Elsevier Science, 2009).

42. Liang, J. & Fernández, J. M. Mechanochemistry: One Bond at a Time. *ACS Nano* **3,** 1628–1645 (2009).

43. Neuman, K. C. & Nagy, A. Single-molecule force spectroscopy: optical tweezers, magnetic tweezers and atomic force microscopy. *Nat. Methods* **5,** 491–505 (2008).

44. deCastro, M. J., Fondecave, R. M., Clarke, L. A., Schmidt, C. F. & Stewart, R. J. Working strokes by single molecules of the kinesin-related microtubule motor ncd. *Nat Cell Biol* **2,** 724–729 (2000).

45. Smith, D. E. *et al.* The bacteriophage [phis]29 portal motor can package DNA against a large internal force. *Nature* **413,** 748–752 (2001).

46. Grier, D. G. A revolution in optical manipulation. *Nature* **424,** 810–816 (2003).

47. Charvin, G., Strick, T. R., Bensimon, D. & Croquette, V. Tracking Topoisomerase Activity at the Single-Molecule Level. *Annu. Rev. Biophys. Biomol. Struct.* **34,** 201–219 (2005).

48. Strick, T. R., Croquette, V. & Bensimon, D. Single-molecule analysis of DNA uncoiling by a type II topoisomerase. *Nature* **404,** 901–904 (2000).

49. Long, X., Parks, J. W., Bagshaw, C. R. & Stone, M. D. Mechanical unfolding of human telomere G-quadruplex DNA probed by integrated fluorescence and magnetic tweezers spectroscopy. *Nucleic Acids Res.* **41,** 2746–2755 (2013).

50. Chen, H. *et al.* Improved High-Force Magnetic Tweezers for Stretching and Refolding of Proteins and Short DNA. *Biophys. J.* **100,** 517–523 (2011).

51. Danilowicz, C., Greenfield, D. & Prentiss, M. Dissociation of Ligand−Receptor Complexes Using Magnetic Tweezers. *Anal. Chem.* **77,** 3023–3028 (2005).

52. Guttenberg, Z. *et al.* Measuring Ligand−Receptor Unbinding Forces with Magnetic Beads: Molecular Leverage †. *Langmuir* **16,** 8984–8993 (2000).

53. Sharma, D., Cao, Y. & Li, H. Engineering Proteins with Novel Mechanical Properties by Recombination of Protein Fragments. *Angew. Chem. Int. Ed.* **45,** 5633–5638 (2006).

54. Borgia, A., Williams, P. M. & Clarke, J. Single-Molecule Studies of Protein Folding. *Annu. Rev. Biochem.* **77,** 101–125 (2008).

55. Tani, K. & Stoltz, B. M. Synthesis and structural analysis of 2-quinuclidonium tetrafluoroborate. *Nature* **441,** 731–734 (2006).

56. Berkowski, K. L., Potisek, S. L., Hickenboth, C. R. & Moore, J. S. Ultrasound-Induced Site-Specific Cleavage of Azo-Functionalized Poly(ethylene glycol). *Macromolecules* **38,** 8975–8978 (2005).

57. Price, G., West, P. & Smith, P. Control of polymer structure using power ultrasound. *Ultrason. Sonochem.* **1,** S51–S57 (1994).

58. Belova, V., Shchukin, D. G., Gorin, D. A., Kopyshev, A. & Möhwald, H. A new approach to nucleation of cavitation bubbles at chemically modified surfaces. *Phys. Chem. Chem. Phys.* **13,** 8015-8023 (2011).

59. Crum, L. A. Measurements of the growth of air bubbles by rectified diffusion. *J. Acoust. Soc. Am.* **68,** 203-211 (1980).

60. Basedow, A. M. & Ebert, K. H. in *Physical Chemistry* **22,** 83–148 (Springer Berlin Heidelberg, 1977).

61. May, P. A. & Moore, J. S. Polymer mechanochemistry: techniques to generate molecular force via elongational flows. *Chem. Soc. Rev.* **42,** 7497-7506 (2013).

62. Avalos, M. *et al.* Thermal and Sonochemical Studies on the Diels−Alder Cycloadditions of Masked *o* -Benzoquinones with Furans: New Insights into the Reaction Mechanism †. *J. Org. Chem.* **68,** 7193–7203 (2003).

63. Woodward, R. B. & Hoffmann, R. Stereochemistry of Electrocyclic Reactions. *J. Am. Chem. Soc.* **87,** 395–397 (1965).

64. Woodward, R. B. & Hoffmann, R. The Conservation of Orbital Symmetrya. *Angew. Chem. Int. Ed. Engl.* **8,** 781–853 (1969).

65. Grandbois, M. How strong is a covalent bond? *Science* **283,** 1727–1730 (1999).

66. Weder, C. Mechanochemistry: Polymers react to stress. *Nature* **459,** 45–46 (2009).

67. Kauzmann, W. & Eyring, H. The Viscous Flow of Large Molecules. *J. Am. Chem. Soc.* **62,** 3113–3125 (1940).

68. Bell, G. Models for the specific adhesion of cells to cells. *Science* **200,** 618–627 (1978).

69. Dopieralski, P. *et al.* The Janus-faced role of external forces in mechanochemical disulfide bond cleavage. *Nat. Chem.* **5,** 685–691 (2013).

70. Greenberg, M. J. & Moore, J. R. The molecular basis of frictional loads in the in vitro motility assay with applications to the study of the loaded mechanochemistry of molecular motors. *Cytoskelet. Hoboken NJ* **67,** 273–285 (2010).

71. Lele, T. P., Thodeti, C. K. & Ingber, D. E. Force meets chemistry: analysis of mechanochemical conversion in focal adhesions using fluorescence recovery after photobleaching. *J. Cell. Biochem.* **97,** 1175–1183 (2006).

72. Bustamante, C., Chemla, Y. R., Forde, N. R. & Izhaky, D. Mechanical processes in biochemistry. *Annu. Rev. Biochem.* **73,** 705–748 (2004).

73. Hammond, G. S. A correlation of reaction rates. *J. Am. Chem. Soc.* **77,** 334–338 (1955).

74. Leffler, J. E. Parameters for the Description of Transition States. *Science* **117,** 340–341 (1953).

75. Makarov, D. E., Wang, Z., Thompson, J. B. & Hansma, H. G. On the interpretation of force extension curves of single protein molecules. *J. Chem. Phys.* **116,** 7760 (2002).

76. Su, T. & Purohit, P. K. Mechanics of forced unfolding of proteins. *Acta Biomater.* **5,** 1855–1863 (2009).

77. Ikai, A. & Alimujiang, Y. Force–extension curves of dimerized polyglutamic acid. *Appl. Phys. A* **72,** S117–S120 (2001).

78. Zemanová, M. & Bleha, T. Isometric and Isotensional Force-Length Profiles in Polymethylene Chains. *Macromol. Theory Simul.* **14,** 596–604 (2005).

79. Ryckaert, J.-P., Ciccotti, G. & Berendsen, H. J. . Numerical integration of the cartesian equations of motion of a system with constraints: molecular dynamics of n-alkanes. *J. Comput. Phys.* **23,** 327–341 (1977).

80. Paulusse, J. M. J. & Sijbesma, R. P. Reversible mechanochemistry of a Pd(II) coordination polymer. *Angew. Chem. Int. Ed Engl.* **43,** 4460–4462 (2004).

81. Karthikeyan, S., Potisek, S. L., Piermattei, A. & Sijbesma, R. P. Highly Efficient Mechanochemical Scission of Silver-Carbene Coordination Polymers. *J. Am. Chem. Soc.* **130,** 14968–14969 (2008).

82. Grubmüller, H., Heymann, B. & Tavan, P. Ligand binding: molecular mechanics calculation of the streptavidin-biotin rupture force. *Science* **271,** 997–999 (1996).

83. Forti, F., Boechi, L., Estrin, D. A. & Marti, M. A. Comparing and combining implicit ligand sampling with multiple steered molecular dynamics to study ligand migration processes in heme proteins. *J. Comput. Chem.* **32,** 2219–2231 (2011).

84. Lu, H., Isralewitz, B., Krammer, A., Vogel, V. & Schulten, K. Unfolding of Titin Immunoglobulin Domains by Steered Molecular Dynamics Simulation. *Biophys. J.* **75,** 662–671 (1998).

85. Kochhar, G. S., Bailey, A. & Mosey, N. J. Competition between orbitals and stress in mechanochemistry. *Angew. Chem. Int. Ed.* **49,** 7452–7455 (2010).

86. Ribas-Arino, J., Shiga, M. & Marx, D. Unravelling the mechanism of force-induced ring-opening of benzocyclobutenes. *Chem Eur J* **15,** 13331–13335 (2009).

87. Ribas-Arino, J., Shiga, M. & Marx, D. Mechanochemical Transduction of Externally Applied Forces to Mechanophores. *J. Am. Chem. Soc.* **132,** 10609–10614 (2010).

88. Krupička, M., Sander, W. & Marx, D. Mechanical Manipulation of Chemical Reactions: Reactivity Switching of Bergman Cyclizations. *J. Phys. Chem. Lett.* **5,** 905–909 (2014).

89. Stauch, T. & Dreuw, A. Force-Spectrum Relations for Molecular Optical Force Probes. *Angew. Chem. Int. Ed.* **53,** 2759–2761 (2014).

90. Li, W. & Gräter, F. Atomistic evidence of how force dynamically regulates thiol/disulfide exchange. *J. Am. Chem. Soc.* **132,** 16790–16795 (2010).

91. Iozzi, M. F., Helgaker, T. & Uggerud, E. Influence of external force on properties and reactivity of disulfide bonds. *J. Phys. Chem. A* **115,** 2308–2315 (2011).

92. Fowler, S. B. *et al.* Mechanical Unfolding of a Titin Ig Domain: Structure of Unfolding Intermediate Revealed by Combining AFM, Molecular Dynamics Simulations, NMR and Protein Engineering. *J. Mol. Biol.* **322,** 841–849 (2002).

93. Friedrichs, J., Lüssmann, M. & Frank, I. Conservation of orbital symmetry can be circumvented in mechanically induced reactions. *Chemphyschem Eur. J. Chem. Phys. Phys. Chem.* **11,** 3339–3342 (2010).

94. Puchner, E. M. & Gaub, H. E. Force and function: probing proteins with AFM-based force spectroscopy. *Curr. Opin. Struct. Biol.* **19,** 605–614 (2009).

95. Bailey, A. & Mosey, N. J. Prediction of reaction barriers and force-induced instabilities under mechanochemical conditions with an approximate model: a case study of the ring opening of 1,3-cyclohexadiene. *J. Chem. Phys.* **136,** 44102-1-11 (2012).

96. Konda, S. S. M., Brantley, J. N., Bielawski, C. W. & Makarov, D. E. Chemical reactions modulated by mechanical stress: extended Bell theory. *J. Chem. Phys.* **135,** 164103-1-8 (2011).

Chapter 2

Methods

2.1 Introduction

Quantum chemical calculations were performed to investigate the effect of an applied external force, F, on the reaction barriers, $\Delta E^{\ddagger}$'s, for a set of representative unimolecular and bimolecular reactions. The quantum chemical calculations were used to obtain optimized geometries and vibrational frequencies on the force-modified potential energy surface (FMPES). The concept of the potential energy surface (PES) is described in section 2.2. Minima and TS structures can be located on the PES by performing geometry optimizations and transition state (TS) optimizations respectively, which are discussed in section 2.3. Characterizing the nature of structures on the PES can be accomplished by performing vibrational frequency calculations, which are described in section 2.4. The positions of structures on the PES can provide information on various thermodynamics and kinetic properties. Such properties in relation to the energies of structures on the PES are discussed in section 2.5. The effect of F on the PES is modeled using the External Force is Explicitly Included (EFEI) method.[1] The implementation of this method is discussed is section 2.6. The modification of the PES due to the application of F, affects the thermodynamic and kinetic properties, which is described in section 2.7. The energy of a particular structure on the PES can be evaluated using force-fields or quantum chemistry. These methods are discussed in section 2.8. The quantum chemical calculations that are employed in this thesis are based on density functional theory (DFT). The details of DFT are outlined in section 2.9. Section 2.10 describes the various types of basis sets used in the calculation. A basis set superposition error (BSSE) correction is

applied to several of the bimolecular reactions under study. The details of the BSSE corrections are discussed in section 2.11.

2.2 Potential energy surfaces

In computational chemistry, the PES is used to relate the energy of a molecule to its geometry. The concept of the PES is central to understanding the dynamics of a chemical reaction.[2] The simplest example of a PES corresponds to a diatomic. The PES is constructed for a diatomic by calculating the potential energy at various bond distances. Figure 2-1 illustrates a PES calculated for a general carbon-carbon single bond. The potential energy was calculated using a Morse potential, which is of the form

$$V(r) = D_e(1 - e^{-\alpha(r-r_e)})^2 \qquad (2.1)$$

where D_e is the depth of the potential well, $\alpha = \sqrt{k / 2D_e}$ in which k is the force constant for the bond, r is the distance between the two atoms, and r_e is the equilibrium bond length, which corresponds to a value of 1.54 Å in the case of a carbon-carbon single bond. The parameter α determines the width of the potential. The potential energy of the system decreases as r increases until the system reaches the minimum on the PES, which occurs when $r = r_e$. After this point, the potential energy increases until it reaches a plateau at values of r greater than 3.5 Å.

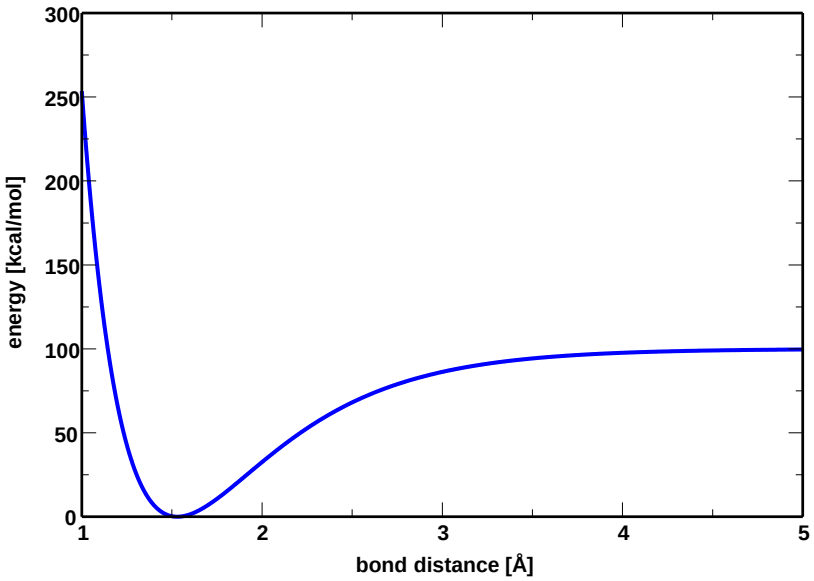

Figure 2-1. Potential energy surface for a carbon-carbon bond calculated using a Morse potential. The minimum on the PES corresponds to the equilibrium bond distance of the carbon-carbon bond length in which r_e = 1.54 Å.

The PES for molecules with more than two atoms is not as simplistic as the case for the diatomic shown in Figure 2-1. For a system with *N* atoms, the molecular geometry can be defined in terms of Cartesian coordinates or internal coordinates. Cartesian coordinates describe each atom in x, y, and z directions. Furthermore, there exists 3*N* Cartesian coordinates for a molecule containing *N* atoms. Internal coordinates refer to those coordinates that are unaffected by the collective translations and rotations of the molecule. For non-linear molecules, three coordinates describe the rotation with respect to three rotational axes and three coordinates describe the translation of molecules in x, y, and z directions. For linear molecules, three coordinates also describe the translational motion, however only two coordinates describe the rotational motion. This is because a rotation of a linear molecule around its own axis leaves the molecule unaffected. Collectively, this yields 3*N*-6 internal coordinates for non-linear molecules and 3*N*-5

internal coordinates for linear molecules. The displacements in Cartesian coordinates affect the kinetic energy whereas changes in internal coordinates alter the potential energy of the system.[3] The PES for a given molecule is constructed by evaluating the energy along each internal coordinate. The PES can therefore be thought of as a hypersurface with dimensions of 3*N*-6 for non-linear molecules and 3*N*-5 for linear molecules. An example of a multidimensional PES for a reaction is the conversion of ozone to iso-ozone. The reaction scheme and calculated PES for the reaction are shown in Figures 2-2a and 2-2b respectively. The PES was obtained for this reaction by systematically varying the O1-O2 bond length and the O2-O1-O3 angle on a grid such that the potential energy was calculated at each set of values. Both ozone and iso-ozone are located at minima on the PES shown in Figure 2-2b. In general, a minimum is defined as a point on the PES where the first derivatives of the energy with respect to atomic positions are zero for all internal coordinates and the second derivatives of the energy with respect to atomic positions are positive in all directions. The minimum energy pathway (MEP) that connects the reactant and the product is known as the reaction coordinate. The highest energy point on the reaction coordinate corresponds to the TS for the reaction. The TS is located at a first-order saddle point on the PES meaning that it is a maximum along the reaction coordinate and minimum along all other internal coordinates. The positions of the reactant, product, and TS, as well as the MEP are shown on the PES in Figure 2-2.

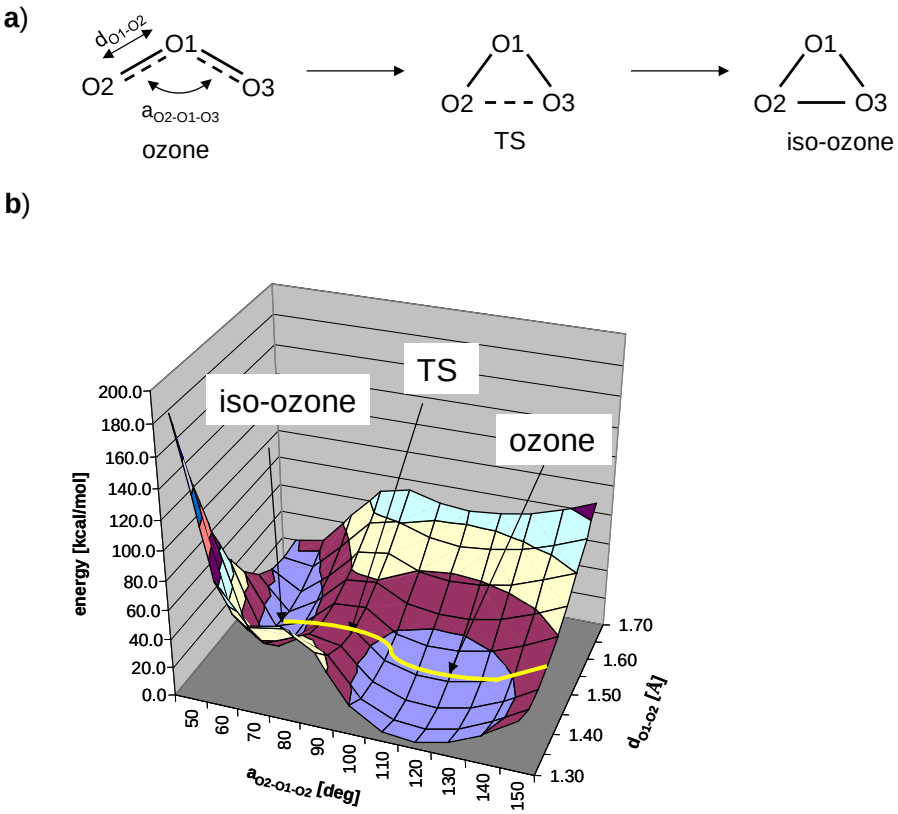

Figure 2-2. a) Reaction scheme for the conversion of ozone to iso-ozone. **(b)** PES for this reaction that was calculated by systematically varying the O2-O1-O3 angle and O1-O2 distance. The minimum energy pathway (MEP) is highlighted in yellow with the two minima and TS structures are labeled on the MEP.

2.3 Geometry and TS optimizations

Minima and the TS on the PES can be located by performing geometry optimizations and TS optimizations respectively. A geometry optimization is one of the most common types of calculation performed in computational chemistry. Locating minima and the TS involves searching for stationary points on the PES. A stationary point is defined as a point on the PES in which the internal forces acting on the nuclei are zero. The basic procedure in a geometry optimization involves providing an initial guess structure of the chemical species of interest i.e. reactant, product, or intermediate, and

iteratively updating the atomic positions until the system reaches a minimum on the PES. In general, there are several minima on the PES. The point on the PES with the lowest energy minimum is referred to as the global minimum while all other minima are known as local minima. Moreover, a geometry optimization does not necessarily lead to the system reaching the global minimum. Instead, the atomic positions are updated from the initial guess structure until the system reaches the nearest local minimum.

A common type of geometry optimization procedure used is the Newton-Raphson method. [4] In the Newton-Raphson method, the geometry is updated according to the expression:

$$\mathbf{q}_{i+1} = \mathbf{q}_i - \mathbf{H}_i^{-1}\mathbf{g}_i \tag{2.2}$$

where $\mathbf{q}_{i+1}$ and $\mathbf{q}_i$ are column vectors containing 3N coordinates that define the molecular geometry for structure i, $\mathbf{g}_i$ is a column vector containing first derivatives of the energy with respect to the 3N coordinates, and $\mathbf{H}_i^{-1}$ is the inverse of a 3N x 3N matrix known as the Hessian. The elements in $\mathbf{H}_i^{-1}$ correspond to the second derivatives of the energy with respect to the 3N coordinates. The first derivatives represent the forces acting on the nuclei and can be calculated analytically by a computational chemistry software package. The second derivatives however are too computationally expensive to be calculated analytically and are typically estimated numerically during the geometry optimization. Eq. (2.2) provides a method for performing geometry optimizations using Cartesian coordinates. This method can also be applied to performing geometry optimizations with internal coordinates. [5] In the case of internal coordinates, the column vectors and matrices

are defined with respect to 3*N*-6 coordinates for non-linear molecules and 3*N*-5 coordinates for linear molecules instead of the 3*N* coordinates.

Once the molecular geometry is updated according to Eq. (2.2), the Hessian is updated using the expression:

$$\left(\frac{\partial^2 E}{\partial q_a q_b}\right) \approx \frac{\Delta(\partial E / \partial q_b)_i}{\Delta q_a} \tag{2.3}$$

where q_a and q_b represent two of the 3*N* Cartesian coordinates. This procedure is repeated until the forces acting on the nuclei and displacements are close to zero. In most computational chemistry codes, the convergence criterion for a geometry optimization is satisfied when the maximum force on the nuclei is less than 4.5×10^{-4} Hartree / Bohr. [6]

A TS optimization is similar to a geometry optimization; however this calculation is used to locate a first-order saddle point instead of a local minimum. A TS optimization is more sensitive to the initial geometry of the molecule than a geometry optimization because the reactants, products, and intermediates are minima along all coordinates whereas the TS is a maximum only along the reaction coordinate and a minimum in all other directions. As such, other types of calculations can be performed prior to a TS optimization to obtain a suitable input geometry. An example of such a calculation is a relaxed scan. In a relaxed scan, an internal coordinate that is relevant to the reaction is scanned over several values while the system is allowed to relax along all other internal coordinates.

2.4 Vibrational frequency calculations

The nature of the stationary points on the PES can be characterized by performing vibrational frequency calculations. A vibrational frequency calculation involves first generating the Hessian, **H**, which is then diagonalized according to the expression:

$$\mathbf{H} = \mathbf{PKP}^{-1} \tag{2.4}$$

where **P** is a square matrix with columns corresponding to normal modes and **K** is a diagonal matrix, in which the diagonal elements represent the force constants. Normal modes are defined as the collective vibrational motions of the atoms in a molecule. The force constants can be related to the vibrational frequencies using the harmonic oscillator approximation for a diatomic:

$$\nu = \frac{1}{2\pi}\left(\frac{k}{\mu}\right)^{1/2} \tag{2.5}$$

where k is the force constant, ν is the frequency, and μ is the reduced mass of the diatomic and determined from the expression:

$$\mu = \left(\frac{m_1 m_2}{m_1 + m_2}\right) \tag{2.6}$$

where m_1 and m_2 are the masses of atoms 1 and 2 respectively in the diatomic. The matrices **P** and **K** are useful for visualizing the normal modes and characterizing the nature of stationary points. For minima, all force constants in **K** are positive, which results in positive frequencies for all normal modes according to Eq. (2.5). For the TS, one of the force constants in **K** is negative whereas all other force constants are positive. A negative force constant leads to an imaginary frequency from Eq. (2.5). The normal mode associated with the imaginary frequency corresponds to the motion along the reaction coordinate.

In addition to characterizing the nature of stationary points, vibrational frequency calculations can be used to simulate infrared spectra and obtain zero-point vibrational energy (ZPVE) corrections to the energies on the PES. As mentioned in the previous section, a geometry optimization involves locating minima on the PES. Details regarding reaction thermochemistry can be accounted for in a geometry optimization from the reactant and product energies at 0 K. As a result, the residual vibrational energy that a molecule possess, known as the zero-point energy [7] is ignored in a geometry optimization. A vibrational frequency calculation accounts for the ZPVE correction by summing the ground state vibrational energies for each normal mode in the molecule according to the expression:

$$E_{ZPVE}(n) = \left(n + 1/2\right) \sum_{i=1}^{3N-6(5)} h\nu_i \qquad (2.7)$$

where E_{ZPVE} is the ZPVE correction to the total energy, n is the vibrational energy level in the molecule, h is Planck's constant, and ν_i is the vibrational frequency for each normal mode. [8]

Vibrational frequency calculations can also be used to estimate thermodynamic corrections to the energies on the PES such as enthalpies and entropies. The change in enthlapy for a reaction, ΔH, can be calculated according to:

$$\Delta H = \Delta U + \Delta(PV) \approx \Delta U \tag{2.8}$$

where ΔU is the change in the internal energy for a reaction, P is the pressure, and V is the volume of the solution. The internal energy, U and the entropy, S for a given system can be calculated from the partition function, which is the key quantity in statistical mechanics.[9] The partition function for a single molecule, q, is evaluated by summing the exponential terms for all possible quantum energy states:[10]

$$q = \sum_{i}^{\text{all states}} e^{-E_i/k_B T} \tag{2.9}$$

where E_i represents the energy associated with the quantum state i, k_B is Boltzmann's constant, and T is the temperature. Different partition functions are associated with translational, rotational, vibrational, and electronic states. The total partition function for a molecule is obtained from the product of the partition functions:

$$q = q_{trans} q_{rot} q_{vib} q_{elec} \tag{2.10}$$

where q_{trans}, $q_{rot,}$ q_{vib}, and q_{elec} are the partition functions for the translational, rotational, vibrational, and electronic quantum states respectively. Furthermore, enthalpy and entropy contributions can be separated into translational, rotational, vibrational, and electronic components. The total enthalpy can be calculated from adding the enthalpy contributions for rotational, vibrational, translational, and electronic states. The same method can be applied to calculate the total entropy. If the molecule is treated as an ideal gas, then known equations from statistical mechanics can be used to calculate the enthlapy and entropy contributions.[8]

2.5 Thermodynamic and kinetic properties

The relative position of the reactants, products, and TS on the PES can provide information regarding the thermodynamic and kinetic properties of a chemical reaction. As mentioned in section 2.4, enthalpic and entropic contributions can be determined from frequency calculations. These contributions can be used to calculate Gibbs free energies, which are typically used in thermochemical experiments. [8] The change in the Gibbs free energy, ΔG, can be estimated from the changes in enthlapy and entropy using the expression:

$$\Delta G = \Delta H - T\Delta S \tag{2.11}$$

where ΔH is the change in enthalpy, ΔS is the change in entropy, and T is the temperature. The change in Gibbs free energy is calculated from the difference between the Gibbs free energy of the products and the reactants. Figure 2-3 illustrates the reaction coordinate on a Gibbs free energy surface for a generic reaction.

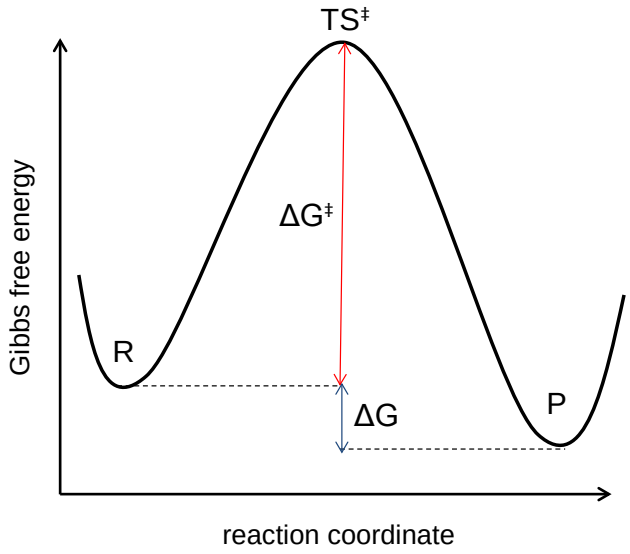

Figure 2-3. A schematic that illustrates the reaction coordinate on a Gibbs free energy surface for a general chemical reaction. The reactants, products, and transition state are indicated with labels *R*, *P*, and *TS* respectively. The change in Gibbs free energy for the reaction and the reaction barrier are represented with the symbols ΔG and $\Delta G^{\ddagger}$ respectively.

The relative Gibbs free energies of the reactants and products can provide information regarding the stability of the system at equilibrium. Assuming the elementary reaction step of R → P is reversible, the equilibrium constant, K_{eq}, can be defined as:

$$K_{eq} = \frac{[P]}{[R]} = e^{-\frac{\Delta G}{RT}} \tag{2.12}$$

where [*R*] and [*P*] are the concentrations of the reactant and product respectively, *T* is the temperature, and *R* is the ideal gas constant and equal to 8.314 J mol^{-1} K^{-1}. Eq. (2.12) provides insight into the thermodynamic details of a chemical reaction.

In addition to thermodynamic properties, the kinetics of a reaction plays a significant role in determining the rates of a reaction. The rate of formation for product *P* can be described by:

$$\frac{d[P]}{dt} = k[R]^n \tag{2.13}$$

where *k* is the rate constant for the reaction involving the conversion of *R* to *P*, and *n* is a stoichiometric coefficient. Several theories can be used to describe the kinetic details of a chemical reaction. The rate constant can be estimated using the Arrhenius equation:

$$k = Ae^{\frac{-\Delta E^{\ddagger}}{RT}} \tag{2.14}$$

where *A* is the Arrhenius pre-exponential factor, *R* is the ideal gas constant, *T* is the temperature, and $\Delta E^{\ddagger}$ is the activation energy. The activation energy is similar to the reaction barrier, which is the potential energy barrier that separates reactant and product minima. In contrast to the reaction barrier, the activation energy is an experimentally derived parameter that depends on the temperature of the system.

Transition state theory (TST)[11] can also be used to describe the kinetic details of a chemical reaction. In TST, it is assumed that the reaction proceeds from one energy

minimum to another via a maximum corresponding to the TS. The motion of the system at the TS along a particular reaction coordinate can be treated as free translational motion and described using kinetic theory. [12] It is also assumed that the TS is in equilibrium with the reactant and described by:

$$K^{\ddagger} = \frac{[TS]^{\ddagger}}{[R]} \tag{2.15}$$

where $[TS]^{\ddagger}$ and $[R]$ are the concentrations of the TS and reactant species respectively, and $K^{\ddagger}$ is the equilibrium constant. The equilibrium constant can be used to estimate the rate of formation of the products according to:

$$\frac{d[P]}{dt} = k^{\ddagger}[TS] = k^{\ddagger}K^{\ddagger}[R] \tag{2.16}$$

where $k^{\ddagger}$ is the rate constant for the step involving the conversion of the reactant to the TS. The equilibrium constant can be related to the Gibbs free energy using the expression:

$$K^{\ddagger} = \frac{k_B T}{h\nu} e^{\frac{-\Delta G^{\ddagger}}{RT}} \tag{2.17}$$

where k_B is Boltzmann's constant, T is the temperature, h is Planck's constant, ν is the frequency of the vibrational mode associated with the motion along the reaction coordinate, R is the ideal gas constant, and $\Delta G^{\ddagger}$ is the reaction barrier on the Gibbs free

energy surface. As shown in Eq. (2.11), the enthalpy and entropy changes can be obtained from the change in Gibbs free energy. As such, Eq. (2.17) can be rewritten in terms of the changes in enthalpy and entropy:

$$K^{\ddagger} = \frac{k_B T}{h\nu} e^{\frac{\Delta S^{\ddagger}}{R}} e^{\frac{-\Delta H^{\ddagger}}{RT}} \tag{2.18}$$

The enthalpy changes in a chemical reaction resemble potential energy barriers. Furthermore, reaction barriers in this thesis are calculated using potential energies.

2.6 Effect of external force on potential energy surfaces

As discussed in chapter 1 section 1.4, there are several theoretical models that have been reported in the literature to simulate mechanochemical conditions. Such models include COnstrained Geometries Simulate External Force (COGEF),[13] Steered molecular dynamics (SMD) simulations,[14] and the External Force is Explicitly Included (EFEI).[1] The EFEI method is used in this thesis to perform quantum chemical calculations under mechanochemical conditions. In the EFEI method, an external force is applied between two atoms or groups in a molecule termed pulling points (PPs). As a result, the potential energy surface on which the molecule moves is modified according to:

$$E(\mathbf{q}, F) = E_0(\mathbf{q}) - FR \tag{2.19}$$

where **q** represents the nuclear coordinate of the atoms in the molecule, F is the magnitude of the applied external force, E_0 is the energy of the structure in the absence of F, and R is the distance between the PPs. The resulting reaction coordinate on the force-modified potential energy surface (FMPES) is illustrated in Figure 2-4. The application of F alters the energy of the reactants, TS, and products, as well as their position along the reaction coordinate. Furthermore, the reactants, TS, and products are located at stationary points on the FMPES.

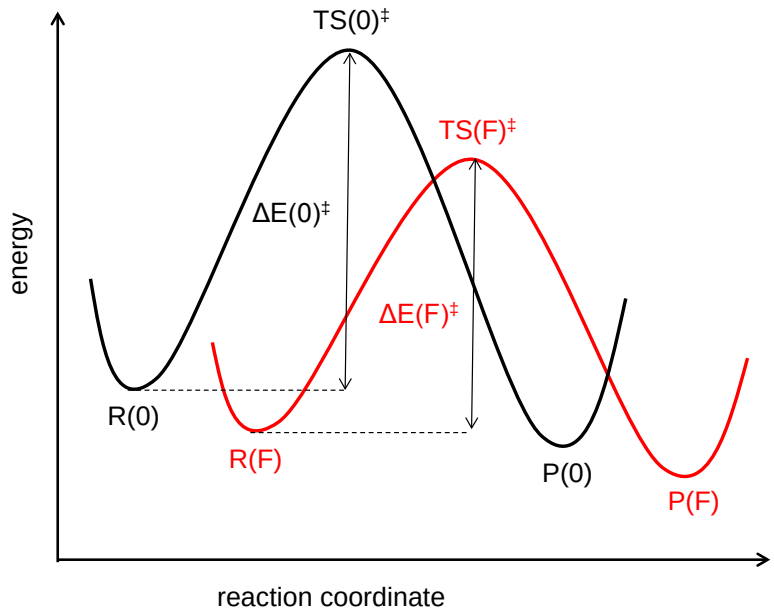

Figure 2-4. A schematic that illustrates the effect of F on the reaction coordinate. The black curve corresponds to the reaction coordinate on the potential energy surface (PES) in the absence of F and the red curve corresponds to the reaction coordinate on the force-modified potential energy surface (FMPES). The labels R(0), TS(0)‡, and P(0) correspond to the reactant, TS, and product respectively on the reaction coordinate in the absence of F. The barrier on the reaction coordinate on the zero-F PES is indicated by the label $\Delta E(0)^{\ddagger}$. The labels R(F), TS(F)‡, and P(F) correspond to the reactant, TS, and product respectively on the reaction coordinate on the FMPES. The barrier on the FMPES is indicated by the label $\Delta E(F)^{\ddagger}$.

The first and second derivatives of Eq. (2.19) can be evaluated with respect to nuclear positions. This allows one to examine features of the FMPES using procedures that are typically employed in quantum chemical calculations such as geometry optimizations, vibrational frequency calculations, intrinsic reaction coordinate calculations, and molecular dynamics simulations. The implementation of the EFEI method in various computational chemistry software packages is outlined in Figure 2-5. The steps involved in the implementation of the EFEI method involve initially selecting the PPs in a molecule that are subjected to *F*. This can be accomplished in several ways. One could select PPs that are fairly intuitive to activate the reaction. For example, the ring opening of cyclobutene involves rupture of a carbon-carbon single bond. Therefore, the substituents attached to the carbon atoms of the scissile bond could be selected as PPs. Predictive models could be used in cases where selection of PPs is not as clear. Chapter 3 describes the model that is used in this thesis to select PPs. Once the PPs have been identified, the vector connecting the PPs is calculated to yield the distance between the PPs, *R*. *F* is then projected along the vector connecting the PPs. The total force acting on the atoms is the sum of the forces acting on the PPs from their position on the PES in the absence of *F* and the components of the force vector. The geometry is then optimized with a new value of *R* and a new energy.

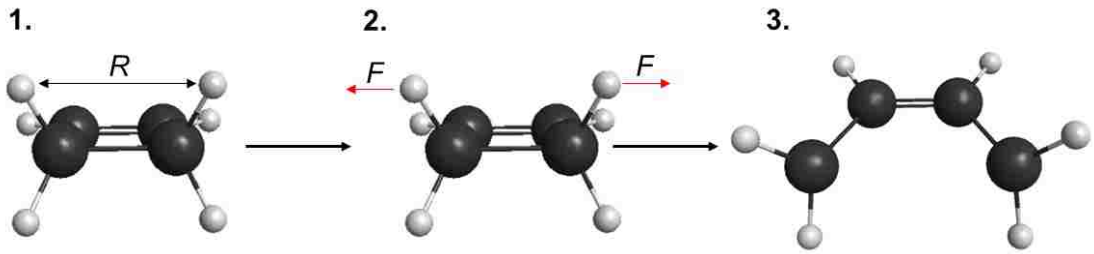

Figure 2-5. The steps involved in the EFEI method. **1.** The vector connecting the PPs is calculated to yield the distance between the PPs, *R*. **2.** The external force, *F* is projected along the vector connecting the PPs. **3.** An optimized geometry is obtained with a new value of *R* and new energy.

Calculations using the EFEI method have shown that the application of *F* can significantly alter the energetics associated with stretching a carbon-carbon bond as shown in Figure 2-6. The energy as a function of carbon-carbon bond length was calculated using Eq. (2.1). The data shown in Figure 2-6 demonstrates that the application of *F* does not significantly affect the energy of the system near the equilibrium bond length. The effect of *F* is more apparent at bond lengths longer than the equilibrium bond length, in which the barrier for the dissociation of the carbon-carbon bond decreases with increased *F*.

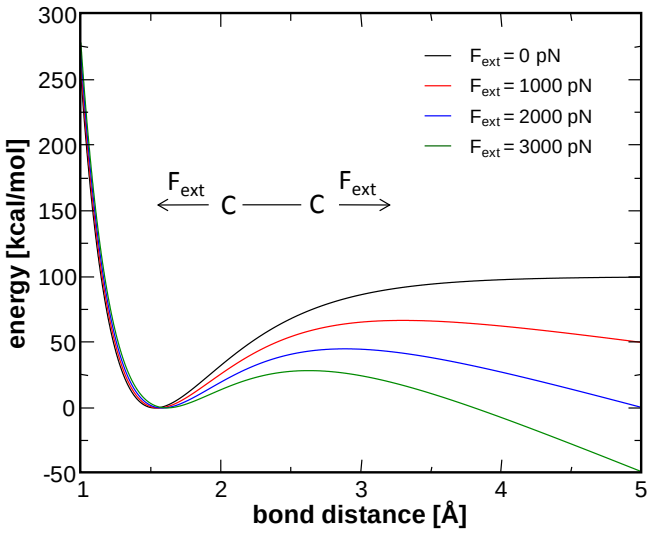

Figure 2-6. Energy as a function of carbon-carbon length at several values of *F*. The energy of the system was calculated using a Morse potential as described in Eq. (2.1). Increasing *F* reduces the barrier for bond dissociation.

2.7 Effect of external force on thermodynamics and kinetic properties of a reaction

Section 2.5 describes how the positions of the reactants, products, and TS on the PES can be used to estimate various thermodynamic and kinetic properties. Under mechanochemical conditions within the EFEI formalism, the PES is modified according to Eq. (2.19) and the positions of the reactants, products, and TS are altered along the reaction coordinate. As such, the thermodynamic and kinetic properties are affected under mechanochemical conditions. Eq. (2.11) describes how the change in Gibbs free energy can be calculated from enthalpy and entropy changes in a reaction. In the absence of *F*, the change in Gibbs free energy upon moving from reactants, *R* to products, *P* can be expressed as:

$$\Delta G = \Delta G^{\circ} + k_B T \ln \frac{[R]}{[P]} \tag{2.20}$$

where $\Delta G°$ is the standard Gibbs free energy change , k_B is Boltzmann's constant, T is the temperature, and $[R]$ and $[P]$ are the concentrations of the reactant and product respectively. The application of F tilts the Gibbs free energy surface along the reaction coordinate in a manner that is analogous to the plot shown in Figure 2-4. The Gibbs free energy surface is altered by an amount that is linearly dependent on the PP distance, R. [15] As such, the change in Gibbs free energy in the presence of F can be expressed as:

$$\Delta G(F) = \Delta G^{\circ} + k_B T \ln \frac{[R]}{[P]} - FR + \Delta G_{\text{stretch}}(F) \tag{2.21}$$

where $\Delta G_{\text{stretch}}(F)$ is the change in Gibbs free energy associated with the shift in minima of reactant and product states on the zero-F PES to the FMPES. At equilibrium, the Gibbs free energy change is zero and thus Eq. (2.21) becomes

$$\Delta G^{\circ} - FR + \Delta G_{\text{stretch}}(F) = -k_B T \ln K_{\text{eq}}$$

(2.22)

where K_{eq} is the equilibrium constant. Eq. (2.22) indicates that the equilibrium constant under mechanochemical conditions depends exponentially on F. Furthermore, the application of F changes the equilibrium of the reaction in a manner that increases or decreases the population of molecules in the reactant and product states.

In addition to altering thermodynamic properties, the application of *F* affects the kinetics of a reaction. The effect of applied *F* on the kinetics of a reaction was first explored by Bell. [16] A theoretical model was developed in that study to understand the adhesion between cells. In Bell's model, the application of *F* lowers the reaction barrier by

$$\Delta E^{\ddagger}(F) = \Delta E^{\ddagger}(0) - FR \tag{2.23}$$

where $\Delta E^{\ddagger}$ (F) is the reaction barrier in the presence of *F* and $\Delta E^{\ddagger}$ (0) is the reaction barrier in the absence of *F*. The effect of *F* on reaction barriers was further explored by Zhurkov and Korsukov. [17] A modified version of Eq. (2.14) was proposed in this study to describe the mechanical degradation of polymers:

$$k(F) = ke^{-(\Delta E^{\ddagger}(0) - W)/RT} \tag{2.24}$$

where *k* (*F*) is the rate constant for reaction in the presence of *F* and *W* is the work performed on the system. The work performed on the system lowers the reaction barrier and thus increases the rate of the reaction.

2.8 Energy evaluation methods

As discussed in section 2.1, constructing the PES for a given molecule allows one to explore the dynamics of a chemical reaction. The energy for a structure on the PES can be evaluated using force-fields or quantum chemical methods.

2.8.1 Force fields

Force-field methods evaluate the energy of a structure as a parametric function of the nuclear coordinates. The parameters that are provided to the function are derived from experiments or higher level computational data. [10] The force-field energy, E_{FF} can be written as a sum of terms that are each associated with altering the molecular geometry in a specific manner:

$$E_{FF} = E_{stretch} + E_{bend} + E_{tors} + E_{vdw} + E_{elec} + E_{cross} \quad (2.25)$$

where $E_{stretch}$ is the energy associated with stretching a bond, E_{bend} corresponds to the energy needed to bend an angle, E_{tors} is the torsional energy required for rotation around a bond, E_{vdw} represents the energy associated with van der Waals interactions, E_{elec} is the energy for electrostatic interactions, and E_{cross} corresponds to the coupling between $E_{stretch,}$ $E_{bend,}$ and E_{tors}.

The starting point for evaluating $E_{stretch}$ is taking a Taylor expansion about the equilibrium bond length, R_0:

$$E(R) = E(R_0) + \frac{dE(R_0)}{dR} + \frac{1}{2!}\frac{d^2E(R_0)}{dR^2}(R-R_0)^2 + ... + \frac{1}{N!}\frac{d^NE(R_0)}{dR^N}(R-R_0)^N \quad (2.26)$$

The first two terms on the right hand side of Eq. (2.26) are zero provided that R_0 corresponds to a potential energy of zero as shown in Figure 2-1. Truncating Eq. (2.26) after the first non-zero term yields:

$$E(R) = \frac{1}{2}k(R - R_0)^2 \tag{2.27}$$

where k corresponds to the second derivative of the potential energy with respect to R. Eq. (2.27) is equivalent to the potential energy in Hooke's law in which k is the force constant for the spring. The practical use of Eq. (2.27) in force-field methods is sufficient for bond lengths near the potential energy minimum, however, is limited as the system progresses to values of R greater than R_0. Eq. (2.27) predicts that the potential energy associated with stretching a bond approaches infinity for values of R greater than R_0, which is not realistic for a diatomic.[18] The potential energy of a diatomic calculated using a Morse potential as shown in Figure 2-1 plateaus at larger values of R, which is a more realistic model for stretching a diatomic. Figure 2-7 illustrates the potential energy calculated for a carbon-carbon single bond using Eq. (2.27) compared with the potential energy calculated using a Morse potential as defined in Eq. (2.1).

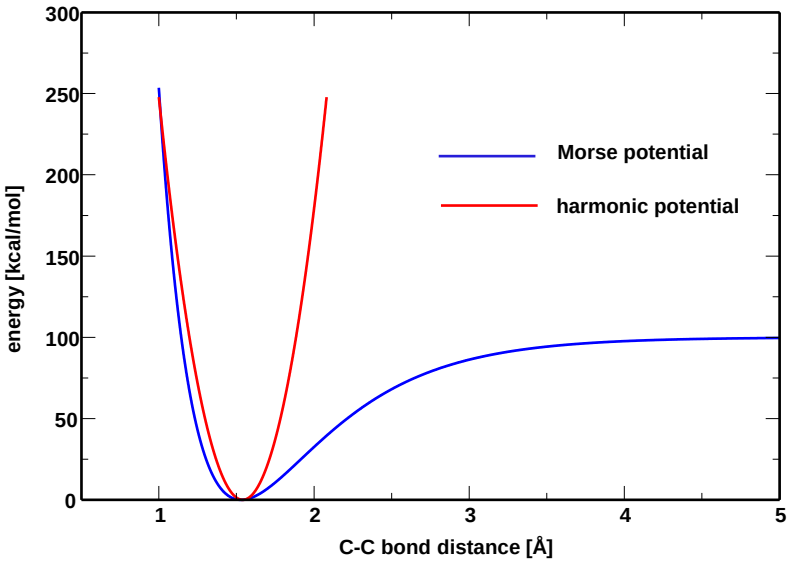

Figure 2-7. Potential energy of a carbon-carbon single bond calculated using a harmonic potential and using a Morse potential. The energy calculated using a harmonic potential approaches infinity at values of R greater than R_0 whereas the energy plateaus when calculated using a Morse potential.

A Morse potential is not typically used in force-field methods because it is more computationally intensive to evaluate an exponential function than a polynomial function. [18] Also, many of the parameters in a Morse potential are not readily accessible from experiments. In practice, higher order terms are employed in the Taylor expansion in Eq. (2.26) to improve the qualitative description of the potential energy of a diatomic. This allows one to accurately describe the potential energy of a diatomic in a manner that is less computationally intensive than using a Morse potential.

The force-field function for evaluating E_{bend} for three atoms in a molecule A, B, and C is

$$E_{\text{bend}}(\theta) = \frac{1}{2}k_{ABC}^{(2)}(\theta-\theta_0)^2 + \frac{1}{2}k_{ABC}^{(3)}(\theta-\theta_0)^3 + \ldots.\frac{1}{2}k_{ABC}^{(N)}(\theta-\theta_0)^N \qquad (2.28)$$

where θ is the angle between the AB and BC bonds, θ_0 is the equilibrium bond angle, and $k_{ABC}^{(N)}$ is the force constant associated with the angle strain for the Nth order in the Taylor expansion. Some of the common force-field methods have an upper bound of $N = 6$ in Eq. (2.28). [18] In the case of torsional rotation, the energy associated with rotation around the B-C bond in a four atom sequence A-B-C-D is given by

$$E_{\text{tors}}(\omega) = \sum_n V_n \cos(n\omega) \tag{2.29}$$

where ω is the torsion associated with rotation around the B-C bond in the A-B-C-D sequence, n is the number of torsions, and V_n is a constant that determines the size of the B-C rotational barrier.

Non-bonding interactions are also accounted for in force-field methods. The energy associated with van der Waals interactions is typically calculated using a Lennard-Jones potential: [19]

$$E_{LJ}(R) = \varepsilon\left[\left(\frac{R_0}{R}\right)^{12} - 2\left(\frac{R_0}{R}\right)^{6}\right] \tag{2.30}$$

where R is the distance between the two non-bonded atoms, R_0 is the distance corresponding to the minimum of energy, and ε is the depth of the minimum. Another part of non-bonding interactions arises from the internal distribution of electrons. The energy associated with such interactions is the electrostatic energy, E_{elec}, and is evaluated using a Coulombic potential:

$$E_{elec}(R_{AB}) = \frac{Q^A Q^B}{R_{AB}} \tag{2.31}$$

where Q^A and Q^B represent point charges of atoms A and B respectively, and R_{AB} corresponds to the distance between the two atoms. Eq. (2.31) is somewhat limited in practical force field applications given that partial atomic charges in a molecule are approximated by point charges.

Overall, the force-field methods provide a means of evaluating the energy for systems consisting of thousands of atoms in a computationally inexpensive manner. One of the main disadvantages of using force-fields in practice is that many of the parameters used are based on specific experimental data. As such, the set of parameters used is only sufficient for a narrow set of chemical systems. Several force-field methods have been developed for particular chemical applications. Examples of force-field methods include AMBER, [20] CHARMM, [21] and MM3.[22] These methods are typically used for organic and biological molecules. Compound containing transition metals are typically treated using VALBOND. [23]

2.8.2 Quantum Chemical Methods

The time-independent Schrödinger equation forms the basis of quantum chemistry and is of the form:

$$\hat{H}\Psi = E\Psi \tag{2.32}$$

where $\hat{H}$ is the Hamiltonian or total energy operator, Ψ is the wave function, and E is the total energy of the system. The wave function is the solution to Eq. (2.32) and is the central quantity in quantum mechanics. If solutions are obtained for Eq. (2.32) without experimental data, the methods are referred to as *ab initio*, which is latin for "from the beginning".[10] Semi-empirical methods, on the other hand combine quantum chemistry with experimental data to calculate the energy of a system. Eq. (2.32) is an eigenvalue equation, in which the wave function is an eigenfunction and the total energy is the eigenvalue. The Hamiltonian operator can be written as a sum of kinetic and potential energy operators for the electrons and the nuclei:

$$\hat{H} = \hat{T}_e + \hat{T}_n + \hat{V}_{ne} + \hat{V}_{ee} + \hat{V}_{nn} \tag{2.33}$$

where $\hat{T}_e$ and $\hat{T}_n$ are the kinetic energy operators for the electrons and nuclei respectively and $\hat{V}_{ne}$, $\hat{V}_{ee}$, and $\hat{V}_{nn}$ are the potential energy operators corresponding to the nuclear-electron attraction, electron-electron repulsion, and nuclear-nuclear repulsion respectively.

The nuclei are viewed as stationary from the perspective of electrons. This is because nuclei are much heavier than electrons and as a result their motion is a lot slower. Furthermore, the electrons can adjust nearly instantaneously to nuclear positions. This notion is known as the Born-Oppenheimer approximation. The Born-Oppenheimer approximation implies that the total wave function can be separated into nuclear and electronic components:

$$\Psi_{\text{tot}}(\mathbf{r},\mathbf{R}) = \Psi_{\text{nuc}}(\mathbf{R})\Psi_{\text{elec}}(\mathbf{r};\mathbf{R}) \tag{2.34}$$

where **R** represents the nuclear coordinates, **r** denotes electronic coordinates, Ψ_{nuc} is the nuclear wave function, and Ψ_{elec} is the electronic wave function. The electronic wave function depends parametrically on the positions of the nuclei. The Born-Oppenheimer approximation is used to construct the PES for a system by solving the electronic Schrödinger equation:

$$\hat{H}_{\text{elec}}\Psi_{\text{elec}}(\mathbf{r};\mathbf{R}) = E_{\text{elec}}\Psi_{\text{elec}}(\mathbf{r};\mathbf{R}) \tag{2.35}$$

where $\hat{H}_{\text{elec}}$ is the electronic Hamiltonian and E_{elec} is the electronic energy. The electronic Hamiltonian is a modification of Eq. (2.33), in which the $\hat{V}_{nn}$ and $\hat{T}_n$ terms are not included. The $\hat{T}_n$ term can be ignored because the nuclei are stationary from the perspective of the electrons. The $\hat{V}_{nn}$ term is treated as a constant and added to the electronic energy.

The electronic Schrödinger equation cannot be solved exactly for systems containing more than one electron. For multi-electron systems, approximate solutions to the electronic Schrödinger equation can be obtained by using the variational principle. The variational principle uses a trial wave function to calculate the energy of the system. The energy of the trial wave function is an upper bound on the energy of the exact wave function and is calculated using the expression:

$$E_{\text{elec}} = \frac{\left\langle \psi^*(\mathbf{r};\mathbf{R}) \middle| \hat{H}_{\text{elec}} \middle| \psi(\mathbf{r};\mathbf{R}) \right\rangle}{\left\langle \psi^*(\mathbf{r};\mathbf{R}) \middle| \psi(\mathbf{r};\mathbf{R}) \right\rangle} \tag{2.36}$$

where ψ and ψ^* are the trial wave function and its complex conjugate respectively. The numerator in Eq. (2.36) corresponds to the expectation value of the electronic energy. The denominator is equal to 1 if the trial wave function is normalized. The trial wave function is selected such that it exhibits the same properties of the exact wave function. Such properties include being single-valued, continuous, and antisymmetric with respect to exchange of any two electrons. The antisymmetry requirement can be met by using a Slater determinant to construct the trial wave function. The rows in a Slater determinant represent electronic coordinates and the columns correspond to single electron wave functions. The single electron wave functions can be thought of as spin orbitals, χ_N, which can be expressed as a product of spatial orbital times a spin function. The spin function is defined as α or β to denote electron spin up or spin down respectively. For the general case of *N* electrons in *N* spin orbitals, the Slater determinant trial wave function is given by:

$$\Psi_{\mathrm{SD}} = \frac{1}{\sqrt{N}} \begin{vmatrix} \chi_1(1)\chi_2(1).....\chi_N(1) \\ \chi_1(2)\chi_2(2).....\chi_N(2) \\ ..... \quad ..... \quad ..... \\ \chi_1(N)\chi_2(N).....\chi_N(N) \end{vmatrix} \tag{2.37}$$

where the index in the bracket corresponds to the electron coordinates. The energy of a spin orbital can be calculated using the Fock equation:

$$\hat{f}\,\chi_i(\mathbf{x}_i) = \varepsilon_i \chi_i(\mathbf{x}_i) \tag{2.38}$$

where χ_i is the spin orbital for the electron *i* with spin coordinates $\mathbf{x}_i$, ε_i is the energy eigenvalue, and $\hat{f}$ is the Fock operator and is the sum of the one-electron, Coulomb, and exchange operators. The one-electron operator can be expressed as:

$$\hat{h}_1 = \left(-\frac{\nabla_1}{2} - \sum_{I=1}^{M} \frac{Z_I}{r_{1I}} \right) \tag{2.39}$$

where *I* is the index for the nuclei, ∇_1 is the Laplacian for electron 1, *M* is the number of nuclei, Z_I is the nuclear charge, and r_{1I} is the electron-nuclear distance. The Coulomb operator is defined as:

$$\hat{J}_2(\mathbf{x}_1) = \int \frac{d\mathbf{x}_2 \left|\chi_2(\mathbf{x}_2)\right|^2}{r_{12}} \tag{2.40}$$

where $\left|\chi_2(\mathbf{x}_2)\right|^2$ is the charge cloud that is the result of an electron with coordinates $\mathbf{x}_2$ occupying χ_2 and r_{12} is the distance between electron 1 and electron 2. The Coulomb operator accounts for the average Coulomb repulsion between electrons in spin orbitals χ_1 and χ_2. The exchange operator acting on the spin orbital χ_1 can be expressed as:

$$\hat{K}_2(\mathbf{x}_1)\chi_1(\mathbf{x}_1) = \left(\int \frac{d\mathbf{x}_2 \chi_2^*(\mathbf{x}_2)\chi_1(\mathbf{x}_2)}{r_{12}} \right) \chi_2(\mathbf{x}_1) \tag{2.41}$$

The exchange operator exchanges the coordinates of the electrons in spin orbitals χ_1 and χ_2. Furthermore, the exchange operator accounts for the Pauli repulsion between electrons 1 and 2.

The spin orbitals that are used to construct the Slater determinant in Eq. (2.37) can be expressed as a linear combination of *K* basis functions.

$$\chi_i(\mathbf{x}) = g(\boldsymbol{\omega}) \sum_{v=1}^{K} c_{vi} \phi_v(\mathbf{r}) \tag{2.42}$$

where φ_v represent the atomic basis functions as a function of spatial coordinates, **r,** c_{vi} are the coefficients that determine the contribution of each basis function to the spin orbital, and g (**ω**) is an artificial spin function that is included to account for the dependence of spatial orbitals on spin coordinates, **ω**. The details of basis functions are discussed in section 2.10. Eq. (2.38) can be expressed in terms of basis functions:

$$\hat{f}\sum_{\nu=1}^{K} c_{\nu i}\phi_{\nu} = \varepsilon_i \sum_{\nu=1}^{K} c_{\nu i}\phi_{\nu}(\mathbf{r}) \tag{2.43}$$

The above eigenvalue equation can be readily solved by conversion into a matrix problem:

$$\mathbf{FC} = \mathbf{SC\varepsilon} \tag{2.44}$$

where **F** is the Fock matrix with elements, $F_{\mu\nu}$ that can be calculated using the expression:

$$F_{\mu\nu} = \int d\mathbf{r}_1 \, \phi_{\mu}^{*}(\mathbf{r}_1) \, \hat{f} \;\; \phi_{\nu} \; (\mathbf{r}_1) \tag{2.45}$$

Each matrix element in **F** indicates how the basis functions φ_{ν} and φ_{μ} contribute to the spin orbital energy, ε. The overlap matrix, **S**, contains elements that have the form of

$$S_{\mu\nu} = \int d\mathbf{r}_1 \, \phi_{\mu}^{*}(\mathbf{r}_1) \; \phi_{\nu} \; (\mathbf{r}_1) \tag{2.46}$$

Each matrix elements represents the spatial overlap between basis functions φ_{ν} and φ_{μ}. The **C** and **ε** terms in Eq. (2.44) represent the matrix of coefficients and diagonal matrix with spin orbital energies along the diagonal respectively. The self-consistent field (SCF) procedure is used to determine the set of coefficients in **C** that yield the lowest energy trial wave function. The SCF procedure involves first guessing the coefficients for the spin orbitals in **C**. This is accomplished by computing the diagonal matrix, **P,** with elements given by

$$P_{\mu\nu} = 2\sum_{i=1}^{N} c^{*}_{\mu i}\, c_{\nu i} \tag{2.47}$$

where N is the number of occupied spin orbitals. The factor of '2' appears before the summation to consider singlet wave functions in which all spin orbitals are doubly occupied.[18] The initial set of coefficients obtained from the density matrix are then used to construct **F,** which is diagonalized to form **C** and **ε** according to Eq. (2.43). A new **P** is formed using the new set of coefficients in **C.** This cycle is repeated until the new **P** is the same as the initial **P.**

Hartree-Fock (HF) and other wave function methods use the SCF procedure to minimize the energy of the system. In the HF method, the trial wave function consists of a single Slater determinant. One of the main issues with using the HF method is that it overestimates the exact ground-state energy. The difference between the HF energy and the ground-state energy obtained for the exact wave function is known as the correlation energy. Electron correlation is treated in an average sense in the HF method. As such, instantaneous electron-electron interactions are not accounted for in the HF method. Improvements to the HF energy can be made using multi-reference wave function methods such as the Complete Active Space Self Consistent Field approach, which is used to capture static correlation. Static correlation occurs in systems with multiple resonance states, in which electrons can avoid each other by occupying such states. Multi-determinant wave function methods such as full configuration interaction and Coupled-cluster theory are used to capture dynamic correlation, in which electrons move to actively avoid other electrons.

2.9 Density functional theory

Wave function based methods beyond HF can accurately describe electron correlation; however several of these methods are computationally expensive. The CCSD(T) method that is used in Coupled-cluster theory is considered the gold standard in *ab inito* quantum chemistry. [24,25] This method, however scales as N^7, in which N represents the size of the system.[26] Density Functional Theory (DFT) provides an improved accuracy over HF at a comparable computational cost. [26] The electron density is the central quantity in DFT as opposed to the wave function. The electron density, $\rho(\mathbf{r})$, is related to the wave function by:

$$\rho(\mathbf{r}) = N\int ...\int \left|\Psi(\mathbf{r})\right|^2 d\boldsymbol{\omega} d\mathbf{x}_2 d\mathbf{x}_3 ... d\mathbf{x}_N \tag{2.48}$$

where N is the number of electrons, $\mathbf{x}$ is the spatial coordinates, and $\boldsymbol{\omega}$ represents the spin coordinates. For a system of N electrons, the wave function depends on four coordinates; $3N$ spatial coordinates and 1 coordinate for electron spin. The electron density on the other hand, depends on three coordinates and is independent on system size. [10]

The foundation of DFT is the idea that there is a fundamental relationship between the ground-state energy and the ground-state electron density. This is known as the first Hohenberg-Kohn theorem.[27] Furthermore, the ground-state energy is a functional of the ground-state electron density. The functional can be separated into components that correspond to the kinetic energy of the electron, $T[\rho]$, electron-nuclear attraction potential term, $E_{Ne}[\rho]$, and the electron-electron repulsion potential term, $E_{ee}[\rho]$:

$$E[\rho] = T[\rho] + E_{ne}[\rho] + E_{ee}[\rho] \tag{2.49}$$

The square brackets indicate that each energy term is a functional of ρ, which is a function of electronic coordinates, **r.** The $E_{ne}[\rho]$ term can be calculated using the Born-Oppenheimer approximation and is given by:

$$E_{ne}[\rho] = -\sum_I \int \frac{Z_I \rho(\mathbf{r})}{|\mathbf{R}_I - \mathbf{r}|} d\mathbf{r} \tag{2.50}$$

where Z_I is the nuclear charge of atom I with nuclear coordinates of **R.** The $E_{ee}[\rho]$ term can be further divided into Coulomb and exchange energies. The classical Coulombic electron-electron interaction can be readily calculated using the electron densities:

$$E_{\text{ee}}^{\text{classical}}[\rho] = \frac{1}{2} \iint \frac{\rho(\mathbf{r}_1)\rho(\mathbf{r}_2)}{|\mathbf{r}_1 - \mathbf{r}_2|} d\mathbf{r}_1 d\mathbf{r}_2 \tag{2.51}$$

where $\mathbf{r}_1$ and $\mathbf{r}_2$ are the coordinates for electrons 1 and 2 respectively, $\rho(\mathbf{r}_1)$ is the electron density associated with electron 1, and $\rho(\mathbf{r}_2)$ is the electron density associated with electron 2. As in the case of the HF method, the $E_{\text{ee}}^{\text{classical}}[\rho]$ term accounts for the Coulombic repulsion in an average sense and does not take into account instantaneous electron-electron interactions.

Several models have been reported to calculate the $T[\rho]$ term. The Thomas-Fermi (TF) model[28,29] was one of the earliest methods to evaluate the kinetic energy by treating the system as a non-interacting uniform electron gas. The $T[\rho]$ term can be expressed as:

$$T[\rho] = \frac{3}{10}\left(3\pi^2\right)^{2/3} \int \rho^{5/3}(\mathbf{r}) d\mathbf{r} \tag{2.52}$$

Eq. (2.49) can be re-written in terms of the TF model:

$$E[\rho] = \frac{3}{10}(3\pi^2)^{2/3} \int \rho^{5/3}(\mathbf{r}) d\mathbf{r} - \sum_I \int \frac{Z_I \rho(\mathbf{r})}{\left|\mathbf{R}_I - \mathbf{r}\right|} d\mathbf{r} + \frac{1}{2} \iint \frac{\rho(\mathbf{r}_1)\rho(\mathbf{r}_2)}{r_{12}} d\mathbf{r}_1 d\mathbf{r}_2 \tag{2.53}$$

The approximation that the system can be treated as a uniform ideal electron gas is not realistic for actual molecules. The TF energy functional in Eq. (2.53) fails to account for exchange interactions and treats electron repulsion in an average sense as in the case of the HF method. As such, instantaneous electron-electron repulsions are ignored. Another issue with the TF model is the uncertainty associated with expressing the kinetic energy in terms of the density.

Kohn and Sham[30] proposed that it is easier to calculate the kinetic energy if a wave function is used instead of the electron density. Specifically, a Slater determinant wave function that is built up from a set of non-interacting one-electron orbitals termed Kohn-Sham (KS) orbitals is used to represent the ground-state electron density. The electron density in terms of KS orbitals can be expressed as:

$$\rho(\mathbf{r}) = \sum_{i=1}^{N} \chi_i^*(\mathbf{r})\chi_i(\mathbf{r}) \tag{2.54}$$

where χ_i and χ_i^* are the KS orbital for electron *i* and its complex conjugate respectively and *N* is the total number of electrons in the system. The kinetic energy for the non-interacting KS orbitals, which is referred to as the reference system, can be expressed as:

$$T_{\text{rs}} = \sum_{i=1}^{N} \int \chi_i^*(\mathbf{r}) \left(-\frac{\nabla_i^2}{2} \right) \chi_i(\mathbf{r}) d\mathbf{r} \tag{2.55}$$

where T_{rs} is the kinetic energy of the reference system consisting of the non-interacting KS orbitals. Eq. (2.55) does not provide the exact ground state kinetic energy. The exact ground state kinetic energy, T_{exact}, can be calculated from the expression:

$$T_{\text{exact}}[\rho] = T_{\text{rs}}[\rho] + \Delta T[\rho] \tag{2.56}$$

where $\Delta T[\rho]$ is a correction term that accounts for the kinetic energy that is not contained in $T_{\text{rs}}[\rho]$. Eq. (2.49) can be rewritten in terms of Eqs. (2.51) and (2.56):

$$E[\rho] = T_{\text{rs}}[\rho] + E_{\text{ne}}[\rho] + E_{\text{ee}}^{\text{class}}[\rho] + E_{\text{ee}}^{\text{non-class}}[\rho] + \Delta T[\rho] \tag{2.57}$$

where the $E_{ee}^{\text{non-class}}[\rho]$ term accounts for the non-classical exchange and instantaneous electron-electron interactions that are not included in the classical electron-electron energy term, $E_{ee}^{\text{class}}[\rho]$. The first three terms on the right hand side of Eq. (2.57) can be easily calculated using Eqs. (2.50), (2.51), and (2.55). The last two terms however, are not as straightforward to calculate and are grouped together in a term called the exchange-correlation functional, $E_{xc}[\rho]$. As such, Eq. (2.57) can be rewritten as:

$$E[\rho] = T_{rs}[\rho] + E_{ne}[\rho] + E_{ee}^{\text{classsical}}[\rho] + E_{xc}[\rho] \tag{2.58}$$

The development of suitable exchange-correlation (XC) functionals is a significant area of research in modern DFT methods.[31–36] The simplest XC functionals are based on the Local Density Approximation (LDA).[37,38] LDA functionals are based on a uniform electron gas model, in which electrons move on positively charge distribution in space. LDA functionals are typically used in solid state applications for modeling band gaps in semiconductors[39,40] and investigating the electronic structure of metal oxides. [41] Although LDA functionals can be used in the aforementioned studies, it is generally inaccurate for most chemical applications. Furthermore, the electron density in a chemical system is typically not uniform as described in the LDA approximation.

Significant improvements in the accuracy of XC functionals can be achieved by focusing on the extent to which the electron density is changing, i.e. the gradient of the electron density, rather than just the local value of the electron density. [18] This approach is referred to as the generalized gradient approximation (GGA). The addition of the gradient of the electron density in GGA functionals makes these types of functionals suitable to

study changes in electron density, which are typically observed in chemical processes. One of the main issues in the design of GGA functionals is dealing with exchange interactions. A component of the exact exchange energy in the HF method can be added to the GGA functional. These XC functionals are known as hybrid functionals. The GGA and hybrid functionals are used in the majority of DFT calculations.[42–47] Some of the common XC functionals used in practical computational efforts are PBE,[48] BP86, [49,50] BLYP, [49,51] M06-2X,[52] and B3LYP.[51,53] The B3LYP functional is used to perform the quantum chemical calculations in this thesis. The B3LYP functional is a hybrid functional that incorporates Becke's exchange energy,[53] exact exchange from HF, and correlation energy provided from Lee, Yang, and Parker.[51]

2.10 Basis sets

In computational chemistry, basis functions are generally regarded as the building blocks of quantum chemical calculations. The KS orbitals described in section 2.9 can be expressed as a linear combination of basis functions like the spin orbitals in the HF method shown in Eq. (2.42). A linear combination of basis functions forms a basis set. Increasing the number of functions in a basis set generally yields a better representation of the KS orbitals. This section focuses on discussing various types of basis sets with an emphasis on atom-centered basis functions, which are used in the quantum chemical calculations performed in this thesis.

There are two types of atom-centered basis functions that are used in quantum chemical software packages; Slater-type orbitals (STOs)[54] and Gaussian type orbitals (GTOs).[55] STOs have the form of

$$\phi_{\alpha,n,l,m}(r,\theta,\zeta) = NY_{l,m}(\theta,\zeta)r^{n-1}e^{-\alpha r} \tag{2.59}$$

where α is an adjustable parameter, *n* is the principal quantum number, *l* is the angular momentum quantum number, *m* is the magnetic quantum number, *N* is a normalization constant, *r* is the distance between the electrons and the nucleus, and $Y_{l,m}(\theta,\xi)$ are spherical harmonics that are a function of polar coordinates θ and ξ. The exponential dependence on *r* in basis sets containing STOs also occurs in the 1s orbital of the hydrogen atom. STOs exhibit a cusp at the nucleus, which is also consistent with the 1s orbital of the hydrogen atom. In practice, basis sets comprised of STOs are not used because they contain a large number of integrals that cannot be evaluated analytically.

Basis sets comprised of GTOs, however contain integrals that can be readily calculated analytically. GTOs have the form of

$$\phi_{\alpha,n,l,m}(r,\theta,\zeta) = NY_{l,m}(\theta,\zeta)r^{n-1}e^{-\alpha r^2} \tag{2.60}$$

The r^2 term in the exponential indicates that GTOs decay too quickly at values of *r* that are far from the nucleus. Unlike STOs, GTOs do not have a cusp at the nucleus. The differences between STOs and GTOs are illustrated in Figure 2-8.

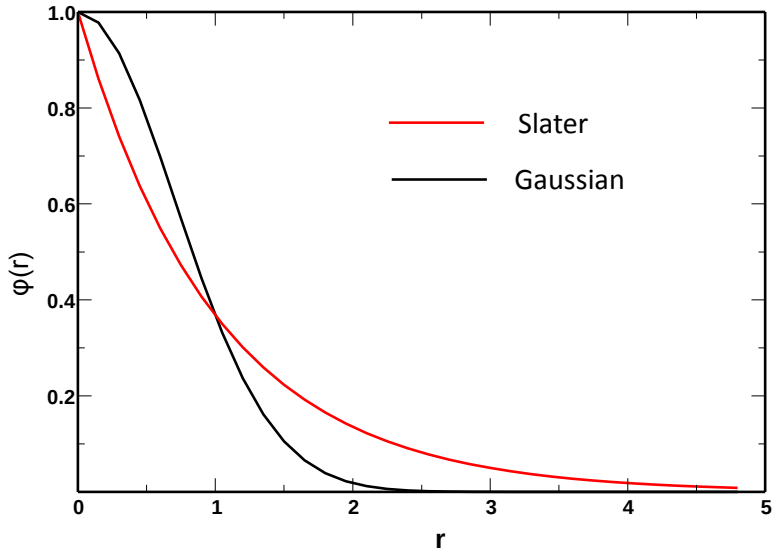

Figure 2-8. Comparison of Gaussian functions and Slater functions, which are used as basis functions in quantum chemical calculations. For simplicity, the parameters in Eqs. (2.58) and (2.59) are set to 1.

GTOs are limited in practice because they do not resemble the decay of the 1s orbital in the hydrogen atom. To overcome this issue with Gaussian functions, contracted Gaussian functions are typically used in practical basis sets. Contracting several GTOs makes the shape of the function closely resemble a STO. Contracted GTOs are obtained from a linear combination of uncontracted GTOs known as primitive GTOs:

$$\gamma = \sum_{i=1}^{G} c_i e^{-\alpha r^2} \tag{2.61}$$

where γ represents the contracted GTO, G is the number of primitive GTOs used in the linear combination, and c_i represents a coefficient that indicates the contribution of each primitive GTO to the contracted GTO basis set.

There are various types of contracted GTO basis sets available in computational chemistry software packages. Examples of such basis sets include the Pople basis sets[56] and the Dunning-Huzinaga basis sets.[57] The discussion in what follows pertains to Pople basis sets because they are used to perform quantum chemical calculations in this thesis.

A Pople basis set has the form *X-YG*, where *X* represents the number of basis functions used to describe the core electrons, *Y* represents the number of basis functions used to describe the valence electrons, and *G* indicates that Gaussian functions are used in this basis set. Two Pople basis sets are used to perform the calculations in this thesis; 6-31G(d,p) and 6-31++G(d,p). Both basis sets are split valence, in which the core electrons are represented by a contraction of six primitive GTOs and the representation of valence electrons is split into two different basis functions. The first basis function describes the inner part of the valence orbitals and consists of a contraction of three primitive GTOs. The second basis function describes the outer part of the valence orbitals and consists of one primitive GTO. The (d,p) term in both basis sets indicates that polarization functions are added to all atoms in the molecule. Polarization functions are Gaussian functions that are of higher angular momentum than the electrons in the atom. The addition of polarization functions allows atoms in a molecule to respond to the distortion of electron clouds in their local environment. In the 6-31G(d,p) basis set, a single set of p-type functions, which is used to represent the distortion due to the presence of p-orbitals, is added to the hydrogen atoms in the molecule. A single set of d-type polarization functions is added to all other atoms, which accounts for the distortion due to the presence of d-orbitals. The '++' terms in the 6-31++G(d,p) are referred to as diffuse functions and represent Gaussian functions that are added to all atoms and decay very slow relative to

the primitive and contracted GTOs. The addition of diffuse functions is significant for chemical problems involving intermolecular interactions such as hydrogen bonding as well as anionic compounds. Many of the chemical reactions explored in this thesis involve weakly bound interactions and anions, therefore diffuse functions are required in the basis set.

2.11 Basis set superposition errors

One of the main challenges with using basis sets in calculations involving bimolecular reactions is dealing with basis set superposition errors. Consider the bimolecular reaction

$$A + B \rightarrow A.B \tag{2.62}$$

where A and B are the respective reactants and A.B is the product. When the reactants are infinitely separated, a set of basis functions are used to describe reactant ‘A’ and another separate set of basis functions are used to describe reactant ‘B’. As A.B is formed, reactant ‘A’ uses extra basis functions from reactant ‘B’ to describe its electronic structure and vice versa. As a result, the number of basis functions increases for the respective component in the product, which leads to an artificial lowering of the energy of the system. The error associated with this phenomenon is known as the basis set superposition error (BSSE).

One of the most common methods for overcoming the BSSE is using the counterpoise method described by Boys and Bernardi.[58] The counterpoise method corrects the interaction energy between the two reacting components in the complex. The uncorrected interaction energy between components 'A' and 'B' can be calculated as:

$$\Delta E_{\text{int}}(A.B) = E_{A.B}^{[A.B]}(A.B) - E_{A}^{[A]}(A) - E_{B}^{[B]}(B) \tag{2.63}$$

where the subscripts indicate the geometry of the chemical species, the superscripts in square brackets represent the basis set used, and the parentheses after the energy terms denote the chemical system of interest. For example, the $E_{A.B}^{[A.B]}(A.B)$ term corresponds to the energy of the A.B complex that is calculated for the A.B geometry and evaluated using the basis set of the complex, i.e. combination of basis set for 'A' and 'B'. The BSSE error associated with the artificial energy stabilization of reactant 'A' in the presence of reactant 'B' in the complex A.B can be estimated using the expression:

$$E_{BSSE}(A) = E_{A}^{[A.B]}(A) - E_{A}^{[A]}(A) \tag{2.64}$$

where the $E_{A}^{[A.B]}(A)$ term represents the energy of the reactant 'A' that is calculated using its geometry and the basis set for the A.B complex. A similar expression can be obtained for the BSSE error associated with reactant 'B':

$$E_{BSSE}(B) = E_{B}^{[A.B]}(B) - E_{B}^{[B]}(B) \tag{2.65}$$

where the $E_B^{[A.B]}(B)$ term represents the energy of the reactant 'B' that is calculated using its geometry and the basis set for the A.B complex. In the counterpoise method, the correction to the BSSE is obtained by subtracting off Eqs. (2.64) and (2.65) from the interaction energy defined in Eq. (2.63). The resulting corrected interaction energy, $\Delta E_{\text{int}}^{CP}(A.B)$, can be expressed as:

$$\Delta E_{\text{int}}^{CP}(A.B) = E_{A.B}^{[A.B]}(A.B) - E_A^{[A.B]}(A) - E_B^{[A.B]}(B) \tag{2.66}$$

The $E_{A.B}^{[A.B]}(A.B)$ term can be evaluated readily from a quantum chemical calculation on the A.B complex. The $E_A^{[A.B]}(A)$ and $E_B^{[A.B]}(B)$ terms, however are not as straightforward to calculate. The $E_A^{[A.B]}(A)$ term is typically evaluated by adding basis functions of reactant 'B' on the atom centers of its component in the complex. The basis functions of reactant 'B' that are added do not take into account the nuclei and electrons of reactant 'B'. As such, these added basis functions are commonly referred to as "ghost functions" while the atoms of reactant 'B' are the "ghost atoms". [59] The same procedure can be applied to calculate the $E_B^{[A.B]}(B)$ term.

The BSSE corrected energies can significantly differ from the uncorrected energies for a particular reaction. A study performed by Simon and colleagues[60] has demonstrated that discrepancies exist between BSSE corrected energies and uncorrected energies for the water dimer complex at various levels of theory. Specifically, differences between the BSSE corrected optimized geometry and the uncorrected optimized geometry for the

water dimer were 0.56 kcal/mol at the HF/D95++(d,p) level of theory, 0.72 kcal/mol at the B3LYP/ D95++(d,p) level of theory, and 1.59 kcal/mol at the MP2/ D95++(d,p) level of theory.

The discrepancies between BSSE corrected values and uncorrected values suggest that correcting the BSSE is necessary to accurately capture the energy of bimolecular systems that involve the formation of complex. Chapters 5 and 6 in this thesis involve bimolecular reactions that proceed via formation of a complex. As such, BSSE corrections are applied to those reactions.

References:

1. Ribas-Arino, J., Shiga, M. & Marx, D. Understanding covalent mechanochemistry. *Angew. Chem. Int. Ed.* **48,** 4190–4193 (2009).

2. Heidrich, D., Kliesch, W. & Quapp, W. *Properties of chemically interesting potential energy surfaces*. (Springer-Verlag, 1991).

3. Wilson, E. B., Decius, J. C. & Cross, P. C. *Molecular vibrations: the theory of infrared and Raman vibrational spectra*. (Dover Publications, 1980).

4. Ypma, T. J. Historical Development of the Newton–Raphson Method. *SIAM Rev.* **37,** 531–551 (1995).

5. Pulay, P. & Fogarasi, G. Geometry optimization in redundant internal coordinates. *J. Chem. Phys.* **96,** 2856-2860 (1992).

6. Ramachandran, K. I., Deepa, G. & Namboori, K. *Computational chemistry and molecular modeling: principles and applications*. (Springer, 2008).

7. Atkins, P. W. & De Paula, J. *Atkins' Physical chemistry*. (Oxford University Press, 2010).

8. Engel, T. & Hehre, W. J. *Quantum chemistry and spectroscopy*. (Pearson/Benjamin Cummings, 2006).

9. Levine, I. N. *Physical chemistry*. (McGraw-Hill, 2009).

10. Jensen, F. *Introduction to computational chemistry*. (Wiley, 1999).

11. Eyring, H. The Activated Complex in Chemical Reactions. *J. Chem. Phys.* **3,** 107-115 (1935).

12. Laidler, K. J. & King, M. C. Development of transition-state theory. *J. Phys. Chem.* **87,** 2657–2664 (1983).

13. Beyer, M. K. The mechanical strength of a covalent bond calculated by density functional theory. *J. Chem. Phys.* **112,** 7307-7312 (2000).

14. Ong, M. T., Leiding, J., Tao, H., Virshup, A. M. & Martínez, T. J. First principles dynamics and minimum energy pathways for mechanochemical ring opening of cyclobutene. *J. Am. Chem. Soc.* **131,** 6377–6379 (2009).

15. Bustamante, C., Chemla, Y. R., Forde, N. R. & Izhaky, D. Mechanical processes in biochemistry. *Annu. Rev. Biochem.* **73,** 705–748 (2004).

16. Bell, G. Models for the specific adhesion of cells to cells. *Science* **200,** 618–627 (1978).

17. Zhurkov, S. N. & Korsukov, V. E. Atomic mechanism of fracture of solid polymers. *J. Polym. Sci. Polym. Phys. Ed.* **12,** 385–398 (1974).

18. Cramer, C. J. *Essentials of computational chemistry: theories and models*. (J. Wiley, 2002).

19. Jones, J. E. On the Determination of Molecular Fields. II. From the Equation of State of a Gas. *Proc. R. Soc. Math. Phys. Eng. Sci.* **106,** 463–477 (1924).

20. Cornell, W. D. *et al.* A Second Generation Force Field for the Simulation of Proteins, Nucleic Acids, and Organic Molecules. *J. Am. Chem. Soc.* **117,** 5179–5197 (1995).

21. Brooks, B. R. *et al.* CHARMM: A program for macromolecular energy, minimization, and dynamics calculations. *J. Comput. Chem.* **4,** 187–217 (1983).

22. Allinger, N. L., Yuh, Y. H. & Lii, J. H. Molecular mechanics. The MM3 force field for hydrocarbons. 1. *J. Am. Chem. Soc.* **111,** 8551–8566 (1989).

23. Cleveland, T. & Landis, C. R. Valence Bond Concepts Applied to the Molecular Mechanics Description of Molecular Shapes. 2. Applications to Hypervalent Molecules of the P-Block. *J. Am. Chem. Soc.* **118,** 6020–6030 (1996).

24. Ramabhadran, R. O. & Raghavachari, K. Extrapolation to the Gold-Standard in Quantum Chemistry: Computationally Efficient and Accurate CCSD(T) Energies for Large Molecules Using an Automated Thermochemical Hierarchy. *J. Chem. Theory Comput.* **9,** 3986–3994 (2013).

25. Sengupta, A., Ramabhadran, R. O. & Raghavachari, K. Breaking a bottleneck: Accurate extrapolation to 'gold standard' CCSD(T) energies for large open shell organic radicals at reduced computational cost. *J. Comput. Chem.* **37,** 286–295 (2016).

26. Koch, W. & Holthausen, M. C. *A chemist's guide to density functional theory*. (Wiley-VCH, 2008).

27. Hohenberg, P. & Kohn, W. Inhomogeneous electron gas. *Phys. Rev.* **136,** B864–B871 (1964).

28. Thomas, L. H. The calculation of atomic fields. *Math. Proc. Camb. Philos. Soc.* **23,** 542-548 (1927).

29. Lieb, E. H. & Simon, B. The Thomas-Fermi theory of atoms, molecules and solids. *Adv. Math.* **23,** 22–116 (1977).

30. Kohn, W. & Sham, L. J. Self-consistent equations including exchange and correlation effects. *Phys. Rev.* **140,** A1133–A1138 (1965).

31. Yanai, T., Tew, D. P. & Handy, N. C. A new hybrid exchange–correlation functional using the Coulomb-attenuating method (CAM-B3LYP). *Chem. Phys. Lett.* **393,** 51–57 (2004).

32. Cohen, A. J., Mori-Sánchez, P. & Yang, W. Development of exchange-correlation functionals with minimal many-electron self-interaction error. *J. Chem. Phys.* **126,** 191109-1-5 (2007).

33. Tozer, D. J. & Handy, N. C. The development of new exchange-correlation functionals. *J. Chem. Phys.* **108,** 2545-2555 (1998).

34. Boese, A. D. & Handy, N. C. New exchange-correlation density functionals: The role of the kinetic-energy density. *J. Chem. Phys.* **116,** 9559-9569 (2002).

35. Boese, A. D. & Martin, J. M. L. Development of density functionals for thermochemical kinetics. *J. Chem. Phys.* **121,** 3405-3416 (2004).

36. Cohen, A. J. & Handy, N. C. Assessment of exchange correlation functionals. *Chem. Phys. Lett.* **316,** 160–166 (2000).

37. Perdew, J. P. & Wang, Y. Accurate and simple analytic representation of the electron-gas correlation energy. *Phys. Rev. B* **45,** 13244–13249 (1992).

38. Vosko, S. H., Wilk, L. & Nusair, M. Accurate spin-dependent electron liquid correlation energies for local spin density calculations: a critical analysis. *Can. J. Phys.* **58,** 1200–1211 (1980).

39. Tran, F. & Blaha, P. Accurate Band Gaps of Semiconductors and Insulators with a Semilocal Exchange-Correlation Potential. *Phys. Rev. Lett.* **102,** 226401-1-4 (2009)
.

40. Kumar, A. & Ahluwalia, P. K. Electronic structure of transition metal dichalcogenides monolayers 1H-MX2 (M = Mo, W; X = S, Se, Te) from ab-initio theory: new direct band gap semiconductors. *Eur. Phys. J. B* **85,** 186 (2012).

41. Nekrasov, I. A., Pavlov, N. S. & Sadovskii, M. V. Consistent LDA' + DMFT approach to the electronic structure of transition metal oxides: Charge transfer insulators and correlated metals. *J. Exp. Theor. Phys.* **116,** 620–634 (2013).

42. Kang, K. Electrodes with High Power and High Capacity for Rechargeable Lithium Batteries. *Science* **311,** 977–980 (2006).

43. Csonka, G. I., Éliás, K. & Csizmadia, I. G. Relative stability of 1C4 and 4C1 chair forms of β-d-glucose: a density functional study. *Chem. Phys. Lett.* **257,** 49–60 (1996).

44. Huang, Y.-W. & Lee, S.-L. Hybrid DFT and hyper-GGA DFT studies of the CO adsorption on Pt nanoclusters: Effects of the cluster size and better CO LUMO description. *Chem. Phys. Lett.* **492,** 98–102 (2010).

45. Nolan, M., Grigoleit, S., Sayle, D. C., Parker, S. C. & Watson, G. W. Density functional theory studies of the structure and electronic structure of pure and defective low index surfaces of ceria. *Surf. Sci.* **576,** 217–229 (2005).

46. Jursic, B. S. Can hybrid DFT methods correctly compute the potential energy surface formic acid dimerization and proton transfer in the formic acid dimer? A comparison of hybrid DFT computed values with experimental and G1, G2, and G2MP2 generated data. *J. Mol. Struct.* **417,** 89–94 (1997).

47. Bauzá, A., Alkorta, I., Frontera, A. & Elguero, J. On the Reliability of Pure and Hybrid DFT Methods for the Evaluation of Halogen, Chalcogen, and Pnicogen Bonds Involving Anionic and Neutral Electron Donors. *J. Chem. Theory Comput.* **9,** 5201–5210 (2013).

48. Ernzerhof, M. & Scuseria, G. E. Assessment of the Perdew–Burke–Ernzerhof exchange-correlation functional. *J. Chem. Phys.* **110,** 5029-5036 (1999).

49. Becke, A. D. Density-functional exchange-energy approximation with correct asymptotic behavior. *Phys. Rev. A* **38,** 3098–3100 (1988).

50. Perdew, J. P. Density-functional approximation for the correlation energy of the inhomogeneous electron gas. *Phys. Rev. B* **33,** 8822–8824 (1986).

51. Lee, C., Yang, W. & Parr, R. G. Development of the Colle-Salvetti correlation-energy formula into a functional of the electron density. *Phys. Rev. B* **37,** 785–789 (1988).

52. Zhao, Y. & Truhlar, D. G. The M06 suite of density functionals for main group thermochemistry, thermochemical kinetics, noncovalent interactions, excited states, and transition elements: two new functionals and systematic testing of four M06-class functionals and 12 other functionals. *Theor. Chem. Acc.* **120,** 215–241 (2008).

53. Becke, A. D. Density-functional thermochemistry. III. The role of exact exchange. *J. Chem. Phys.* **98,** 5648-5652 (1993).

54. Slater, J. C. Atomic Shielding Constants. *Phys. Rev.* **36,** 57–64 (1930).

55. Boys, S. F. Electronic Wave Functions. I. A General Method of Calculation for the Stationary States of Any Molecular System. *Proc. R. Soc. Math. Phys. Eng. Sci.* **200,** 542–554 (1950).

56. R. Ditchfield, W.J. Hehre & J.A. Pople. Self-Consistent Molecular-Orbital Methods. IX. An Extended Gaussian-Type Basis for Molecular-Orbital Studies of Organic Molecules. *J. Chem. Phys.* **54,** 724-728 (1971).

57. Dunning, T. H. Gaussian basis sets for use in correlated molecular calculations. I. The atoms boron through neon and hydrogen. *J. Chem. Phys.* **90,** 1007-1022 (1989).

58. Boys, S. F. & Bernardi, F. The calculation of small molecular interactions by the differences of separate total energies. Some procedures with reduced errors. *Mol. Phys.* **19,** 553–566 (1970).

59. van Duijneveldt, F. B., van Duijneveldt-van de Rijdt, J. G. C. M. & van Lenthe, J. H. State of the Art in Counterpoise Theory. *Chem. Rev.* **94,** 1873–1885 (1994).

60. Simon, S., Duran, M. & Dannenberg, J. J. Effect of Basis Set Superposition Error on the Water Dimer Surface Calculated at Hartree−Fock, Møller−Plesset, and Density Functional Theory Levels. *J. Phys. Chem. A* **103,** 1640–1643 (1999).

Chapter 3

Predicting reaction barriers under mechanochemical conditions

3.1 Introduction

The External Force is Explicitly Included (EFEI) method[1] was used to perform quantum chemical calculations under mechanochemical conditions in this thesis. In this method, an external force, *F*, is applied between two atoms in a molecule that are termed pulling points (PPs). The application of *F* modifies the potential energy surface (PES) on which the molecule moves according to the expression:

$$E(\mathbf{q}, F) = E_0(\mathbf{q}) - FR \tag{3.1}$$

where **q** denotes the nuclear coordinates of the atoms in a molecule, E_0 is the energy of the structure in the absence of *F*, and *R* is the distance between the PPs. As mentioned in section 2.8, the E_0 term can be evaluated using force-fields or *ab initio* methods employing the Born-Oppenheimer approximation. The latter is used in the EFEI calculations reported in this thesis. Eq. (1) provides the energy of a particular structure on the force-modified potential energy surface (FMPES). The thermodynamic and kinetic properties of a reaction, however, involve the relative energies of structures rather than the energy of a particular structure. For instance, the difference in the Gibbs free energies between the products and the reactants are used to calculate ΔG for a reaction. In the context of chemical kinetics, the difference in energies of the reactants and transition state (TS) are used to calculate the reaction barrier, $\Delta E^{\ddagger}$. The effect of applied *F* can alter the

thermodynamic and kinetic properties of a reaction as discussed in section 2.7. This thesis, however, focuses on the kinetics of a reaction under mechanochemical conditions. As such, the Eq. (3.1) can be applied to reactant and TS geometries. Calculating the energy difference between the TS and the reactant using Eq. (3.1) yields:

$$\Delta E^{\ddagger}(F) = \Delta E_0^{\ddagger}(F) - F\Delta R \tag{3.2}$$

where $\Delta E^{\ddagger}(F)$ is the reaction barrier on the FMPES, $\Delta E_{BO}^{\ddagger}(F)$ is the reaction barrier on the Born-Oppenheimer PES, and ΔR is the difference in distance between the PPs as the system progresses from the reactant to the TS.

For a single set of PPs and one value of F, the computational effort for calculating $\Delta E^{\ddagger}(\mathbf{q},F)$ is comparable to the computational cost associated with the calculation of $\Delta E_0^{\ddagger}(\mathbf{q})$. In practical efforts, however, it may be necessary to examine several combinations of PPs at many different values of F to achieve a desired mechanochemical response. As such, the computational cost associated with performing quantum chemical calculations at various values of F for several sets of PPs is significantly greater than Born-Oppenheimer calculations in the absence of F. The challenge in computational mechanochemistry arises from developing models to accurately describe reactions under mechanochemical conditions at a reasonable computational cost.

Bell's model was reported nearly three decades prior to the development of the EFEI method.[2] In Bell's model, the reaction barrier under mechanochemical conditions can be expressed as:

$$\Delta E^{\ddagger}(F) = \Delta E_0^{\ddagger} - F\Delta R_0 \tag{3.3}$$

where $\Delta E_0^{\ddagger}$ is the zero-*F* reaction barrier corresponding to the difference in energies of the zero-*F* reactant and TS structures and ΔR_0 is the change in distance between the PPs upon moving from the reactant to the TS in the absence of *F*. Bell's model is useful for simulating mechanochemical processes because it only requires information of the reactant and TS structures and energies in the absence of *F*, while estimating the changes in $\Delta E^{\ddagger}$ on the FMPES. One of the main drawbacks of Bell's model in practical mechanochemical efforts is that it does not account for the structural changes that occur in reactant and TS under mechanochemical conditions. The tilted PES model, which is discussed in section 1.3, accounts for such structural changes in a limited manner.[3] Specifically, the tilted PES model accounts for structural changes in the reactants and TS that are parallel to the zero-*F* reaction coordinate. This model, however does not account for changes in structure that occur perpendicular to the zero-*F* reaction coordinate. Several models have been reported in the literature to account for such force-induced changes in structure of the reactants and TS. [4–6] A study performed by Bailey and Mosey[4] described the force-induced structural changes by expanding Eq. (3.1) as a 2nd order Taylor series with respect to nuclear coordinates:

$$E(\mathbf{q}_0 + \delta\mathbf{q}, F) = E(\mathbf{q}_0) + \frac{1}{2}\delta\mathbf{q}^T\mathbf{H}_{\text{int}}\delta\mathbf{q} - F(R_0 + \delta R) \tag{3.4}$$

where $\mathbf{q}_0$ corresponds to the nuclear coordinates associated with a stationary point on the Born-Oppenheimer PES, $\delta\mathbf{q}$ represents the changes in the structure of this stationary point as it moves from the Born-Oppenheimer PES to the FMPES, R_0 is the distance between the PPs in the absence of F, and δR is the change in distance between the PPs due to the application of F. All first derivatives of $E(\mathbf{q}_0)$ with respect to nuclear coordinates are zero and are therefore not included in Eq. (3.4). The second derivatives of $E(\mathbf{q}_0)$ with respect to nuclear coordinates are all non-zero and are grouped into the term $\mathbf{H}_{\text{int}}$, which represents the Hessian with respect to internal coordinates. The PP distance, R, corresponds to one of the internal coordinates in $\mathbf{H}_{\text{int}}$. The $\delta\mathbf{q}$ term can be calculated from the expression:

$$\delta\mathbf{q} = \mathbf{CF} \tag{3.5}$$

where $\mathbf{C}$ is the compliance matrix and is calculated from the inverse of the Hessian and $\mathbf{F}$ is a force vector whose components are all zero except for the component that corresponds to the internal coordinate R, which has a magnitude of F. Substituting Eq. (3.5) into Eq. (3.4) yields:

$$E(\mathbf{q}_0 + \delta\mathbf{q}, F) = E(\mathbf{q}_0) - FR_0 - \frac{F^2}{2}C_{RR} \tag{3.6}$$

where C_{RR} is the compliance matrix element associated with R. In general, the compliance matrix elements are reciprocals of the relaxed force constant associated with the internal coordinate. The relaxed force constant, $k_R = 1/C_{RR}$, describes the proportional relationship

between F and δR while accounting for the relaxation of the system along all other internal coordinates. It should be noted in Eq. (3.6) that F is the only component of **F** that is included in the expansion of the FMPES. This is because F is the only non-zero component of **F**, therefore all zero components of **F** are omitted in Eq. (3.6). The estimation of the energy for a stationary point on the FMPES can be applied to reactant and TS geometries. Calculating the energy difference between the TS and reactant geometries using Eq. (3.6) allows one to estimate the $\Delta E^{\ddagger}$ on the FMPES as:

$$\Delta E^{\ddagger}(F) = \Delta E_0^{\ddagger} - F\Delta R_0 - \frac{F^2}{2}\Delta C_{RR} \tag{3.7}$$

where $\Delta E_0^{\ddagger}$ is the reaction barrier in the absence of F. When the calculations are performed using quantum chemical methods, the $\Delta E_0^{\ddagger}$ term corresponds to the reaction barrier on the Born-Oppenheimer PES. The terms ΔR_0 and ΔC_{RR} represent the change in R as the system moves from the reactant to the TS ($R_0^{TS} - R_0^r$) and the change in compliance matrix element associated with R between the TS and reactant ($C_{RR}^{TS} - C_{RR}^r$). The first two terms on the right hand side of Eq. (3.7) are identical to the expression of the reaction barrier under mechanochemical conditions in Bell's model (Eq. 3.3). The last term on the right hand side of Eq. (3.7) accounts for the energy associated with the force-induced structural changes in the reactant and TS geometries.

Eq. (3.7) can be used in practical efforts to examine changes in $\Delta E^{\ddagger}$'s under mechanochemical conditions for a given set of PPs while accounting for structural changes in the reactants and TS. As such, Eq. (3.7) is equivalent to Bell's model in terms

of computational cost, which requires only geometry optimizations and vibrational frequency calculations of the reactants and TS in the absence of *F*. In addition, this model can be used to select a set of PPs in a molecule that elicits a desired mechanochemical response. For instance, one could activate a reaction under mechanochemical conditions by selecting PPs whose distance increases as the system moves from the reactants to the TS ($R_0^{TS} > R_0^r$) and are more compliant in the TS than the reactant ($C_{RR}^{TS} > C_{RR}^r$). Similarly, one could deactivate a reaction by mechanochemical means if the opposite criteria holds true. The application of Eq. (3.7) to predict changes in reaction barriers under mechanochemical conditions is sufficient for a single set of PPs. Examining all possible combinations of PPs in a molecule using this model can be an inefficient process. This is primarily due to calculating the compliance matrix elements that are associated with *R* for the reactant, C_{RR}^r, and the TS, C_{RR}^{TS}. Typically, these compliance matrix elements can be calculated from a plot of ΔR vs. *F* over a small force range, in which ΔR is the difference between the PP separation of the structure at some value of *F* and the structure in the absence of *F*. The slope of this plot corresponds to the reciprocal of the relaxed force constant and hence the compliance matrix element, which is evident from the relationship between *F* and ΔR according to Hooke`s law:

$$F = k_R \Delta R \tag{3.8}$$

where k_R is the relaxed force constant associated with internal coordinate, *R*. Using this procedure to calculate the compliance matrix elements for the reactant and TS associated with all possible sets of PPs can be a laborious processes. This chapter describes a more

computationally efficient approach for computing compliance matrix for all possible combinations of PPs. Section 3.2 discusses the details of this method and its implementation in computational software. The performance of this method is evaluated in section 3.3, in which this method is applied to several chemical reactions to examine changes in reaction barriers, $\Delta E^{\ddagger}$'s under mechanochemical conditions. The results are compared to $\Delta E^{\ddagger}$'s calculated using Eq. (3.2). Section 3.4 describes how this method can be applied to identify structural changes that occur as a result of the application of F. Such changes are known as force-induced instabilities[4] and may alter the reactivity of a particular chemical species. Finally, the future outlook for this approach on a much broader scale is discussed in section 3.5.

3.2 Computing compliance matrix elements for all combinations of PPs

As noted in the previous section, the compliance matrix, **C**, is evaluated by computing the inverse of the Hessian in terms of internal coordinates, $\mathbf{H}_{\text{int}}$**:**

$$\mathbf{C} = \mathbf{H}_{\text{int}}^{-1} \tag{3.9}$$

Several quantum chemical software packages provide $\mathbf{H}_{\text{int}}$ as a part of a vibrational frequency calculation that is performed on a structure defined using a specific set of internal coordinates. The PP distance, R, is not necessarily included in the internal coordinates that define $\mathbf{H}_{\text{int}}$. To obtain compliance matrix elements for all combinations of PPs, it is necessary to generate a unique set of internal coordinates in which R is explicitly included as one the internal coordinates and evaluate $\mathbf{H}_{\text{int}}$ using quantum chemical

calculations for each set of the internal coordinates. A single vibrational frequency calculation can be computationally demanding compared to other quantum chemical calculations such as geometry optimizations. This is primarily due to the evaluation of the second derivatives of the Born-Oppenheimer potential energy in a vibrational frequency calculation, which are more sensitive to numerical errors than the evaluation of first derivatives of the Born-Oppenheimer potential energy in a geometry optimization.[7] Furthermore, it would be computationally prohibitive to repeat this calculation for all possible combinations of PPs in a molecule, which is on the order of $N(N\text{-}1)/2$ with N representing the number of atoms in the molecule. A more computationally efficient approach for obtaining **C** involves computing the second derivatives of the Born-Oppenheimer potential energy with respect to Cartesian coordinates instead of internal coordinates to construct the Hessian in terms of Cartesian coordinates, $\mathbf{H}_{cart}$. $\mathbf{H}_{cart}$ is then transformed into $\mathbf{H}_{int}$ for a given set of internal coordinates that explicitly contain R as one of the internal coordinates.

The first step involved in the transformation from $\mathbf{H}_{cart}$ to $\mathbf{H}_{int}$ is calculating the conversion of Cartesian coordinates to internal coordinates. This is achieved by constructing a matrix **B** of dimensions $3N\text{-}6$ ($3N\text{-}5$ for linear molecules) x $3N$ that transforms a set of Cartesian coordinates, **x**, to a set of internal coordinates, **r,** according to the expression:

$$\mathbf{r} = \mathbf{Bx} \tag{3.10}$$

The above transformation has been used historically to study molecular vibrations as described by Wilson and colleagues. [8] Each element of **B** describes the effect of atomic displacements in Cartesian coordinates on the internal coordinates. Furthermore, the elements of **B** can be divided into specific categories based on the internal coordinate type. As such, elements of **B** are calculated for bond stretching, changes in angles, and changes in torsion. The details for evaluating the elements of **B** for each internal coordinate type are also described by Wilson and colleagues. [8]

The inverse of **B** is more useful in the context of transforming $\mathbf{H}_{cart}$ to $\mathbf{H}_{int}$. The method for using the inverse of **B** to perform this transformation is described by Boatz and Gordon. [9] The transformation can be described as:

$$\mathbf{H}_{int} = (\mathbf{B}^{-1})^{T}\mathbf{H}_{cart}\mathbf{B}^{-1} \tag{3.11}$$

where $\mathbf{B}^{-1}$ is the inverse of **B** and $(\mathbf{B}^{-1})^{T}$ is its transpose. It is worth noting that **B** is not a square matrix and therefore cannot be directly inverted. The approach for computing $\mathbf{B}^{-1}$ reported in the study by Boatz and Gordon[9] involves first calculating a square matrix **G** of dimensions 3*N*-6 x 3*N*-6 for non-linear molecules or 3*N*-5 x 3*N*-5 for linear molecules. The authors expressed **G** in terms of **B** according to**:**

$$\mathbf{G} = \mathbf{B}\mathbf{m}^{-1}\mathbf{B}^{T} \tag{3.12}$$

where $\mathbf{m}^{-1}$ is a 3*N* x 3*N* diagonal matrix in which the diagonal elements represent the reciprocals of the atomic masses and $\mathbf{B}^{T}$ is the transpose of **B**. Taking the inverse of both sides of Eq. (3.12) yields the expression for $\mathbf{B}^{-1}$:

$$\mathbf{B}^{-1} = \mathbf{m}^{-1}\mathbf{B}^{T}\mathbf{G}^{-1} \tag{3.13}$$

where $\mathbf{G}^{-1}$ is the inverse of **G** and can be obtained directly because **G** is a square matrix. The dimensions of $\mathbf{B}^{-1}$ are 3*N* x 3*N*-6 (3*N*-5 for linear molecules). The calculated quantities of $\mathbf{B}^{-1}$ and $\mathbf{H}_{int}$ allow one to use Eq. (3.7) to estimate $\Delta E^{\ddagger}$'s on the FMPES for a specific set of internal coordinates containing *R*.

The work in this chapter of the thesis involved writing a code using the Fortran 90 programming language to generalize this approach for all possible sets of PPs. The first step in the code involved specifying the PPs in the molecule. This was achieved by constructing a Z-matrix, in which *R* was specified as one of the internal coordinates. A Z-matrix is a representation of the geometry of a structure, in which each atom is defined relative to other atoms in the molecule in terms of bond lengths, bond angles, and torsions. [10] Eqs. (3.10) to (3.13) were computed for the molecule with the specified internal coordinates. Each equation was written as a separate module in the code. Once $\mathbf{H}_{int}$ was obtained, **C** was calculated using Eq. (3.9). This was repeated for all possible sets of PPs in a molecule. The code was applied to reactant and TS geometries to yield values of C_{RR}^{r} and C_{RR}^{TS} for all sets of PPs. The information was then used to estimate the barrier on the FMPES for all combinations of PPs according to Eq. (3.7). The implementation of the code is summarized in the flow chart illustrated in Figure 3-1.

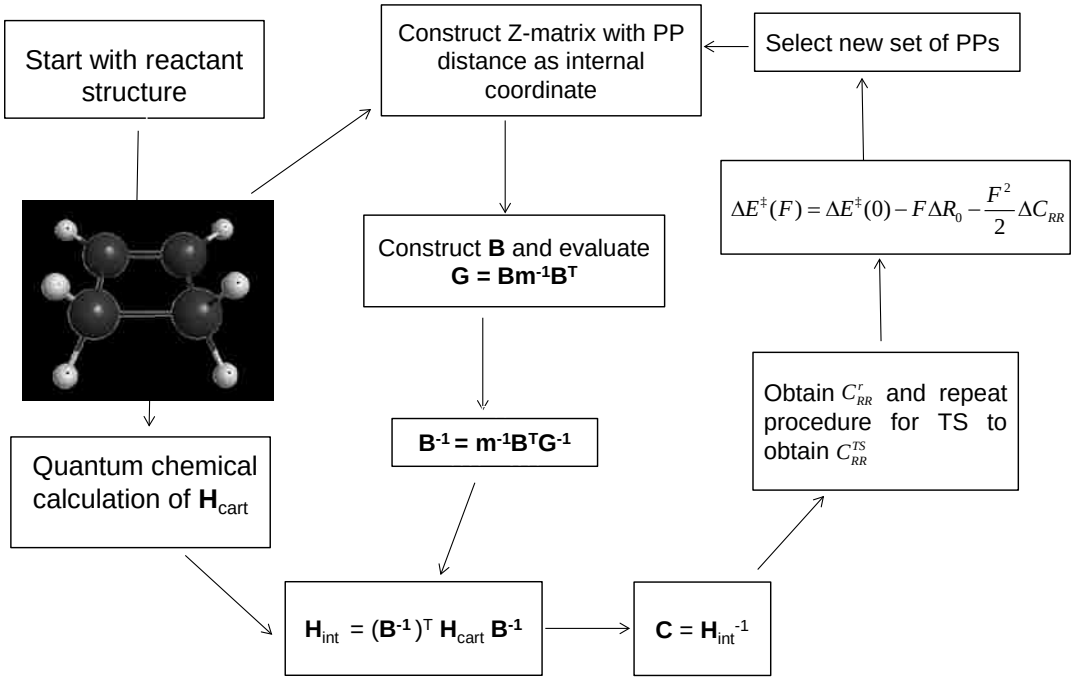

Figure 3-1. A flowchart that illustrates the code to obtain **C** for the reactant and TS in a reaction and estimate the barrier on the force-modified potential energy surface for all possible combinations of PPs in a molecule. The reactant structure shown corresponds to cyclobutene, in which the black and white spheres represent carbon and hydrogen atoms respectively

3.3 Application of the code to chemical reactions

The code discussed in the previous section was used to estimate reaction barriers on the FMPES for the reactions outlined in Figure 3-2. The reactions shown in Figure 3-2 are textbook pericyclic reactions, which are used extensively in organic chemistry.[11–16] Reactions **R1** and **R2** correspond to electrocyclic ring openings of benzocyclobutene and 1,3-hexadiene respectively. These two reactions are governed by the Woodward-Hoffmann (WH) rules[17,18], which dictate the ring opening process on the basis of conservation of orbital symmetry. The WH rules indicate that a conrotatory ring opening

is the thermally allowed pathway for reaction **R1** whereas a disrotatory ring opening is the thermally allowed pathway for reaction **R2.** Conrotatory and disrotatory ring openings refer to methylene groups rotating in the same direction and opposite directions respectively. The thermally allowed pathways are only considered in this work. Several other studies have investigated the formally forbidden pathways under mechanochemical conditions. [19–21] Reactions **R3** and **R4** correspond to sigmatropic shifts that involve the transfer of a hydrogen atom in 1,3-pentadiene and cyclopentadiene respectively. Reaction **R5** is a type of sigmatropic shift that involves a particular electrocyclic rearrangement in 1,5-hexadiene known as a Cope rearrangement.[22]

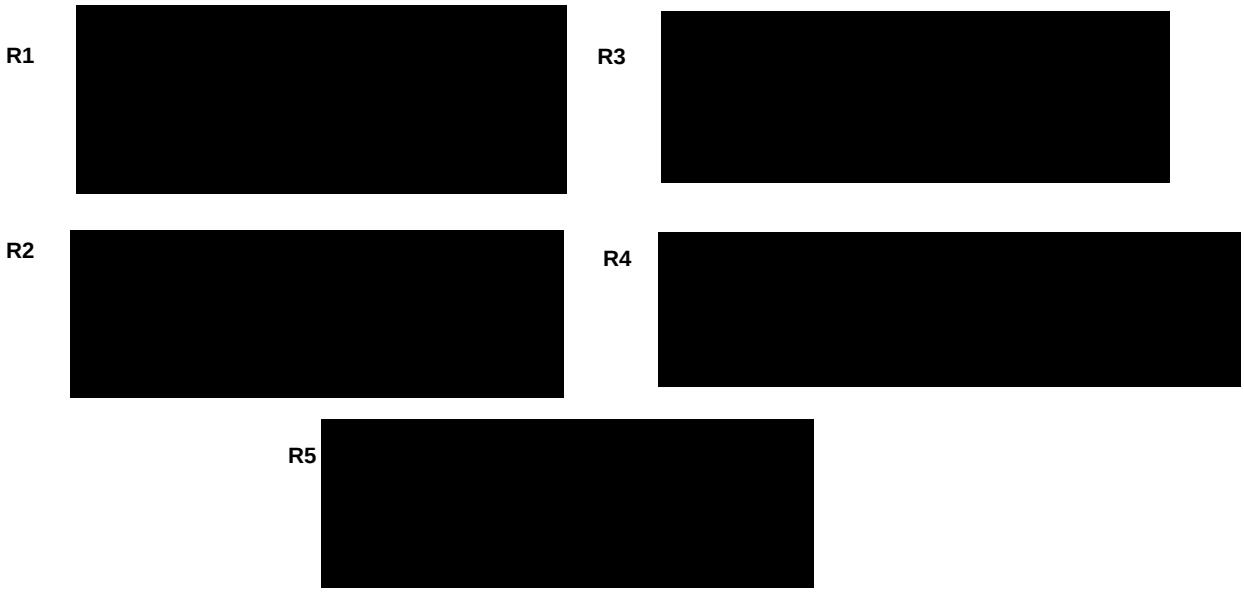

Figure 3-2. Reactions considered in this work. Reactions **R1** and **R2** are electrocyclic ring opening reactions. Reactions **R3-R5** correspond to sigmatropic shifts. Asterisks shown indicate the PPs used in all cases.

The code was applied to reactions **R1** to **R5** to identify a suitable set of PPs. The PPs that resulted in the greatest reduction in the $\Delta E^{\ddagger}$'s with F were selected. These PPs are

indicated with asterisks in the reaction schemes shown in Figure 3-2. The changes in reaction barriers with F that were predicted using Eq. (3.7) were compared to those calculated using quantum chemical methods as shown in Figure 3-3. The quantum chemical calculations were based on density functional theory with the B3LYP exchange-correlation functional [23,24] and the 6-31G(d,p) basis set. The data shown in Figure 3-3 indicate that the $\Delta E^{\ddagger}$-F relationship appears to be significantly different for each reaction. In light of these apparent discrepancies in the force-dependent reaction barriers, a brief discussion for each reaction is presented in what follows. The subsections are divided into ring opening reactions, sigmatropic shifts involving transfer of a hydrogen atom, and the sigmatropic shift involving electrocyclic rearrangement (i.e. reaction **R5**).

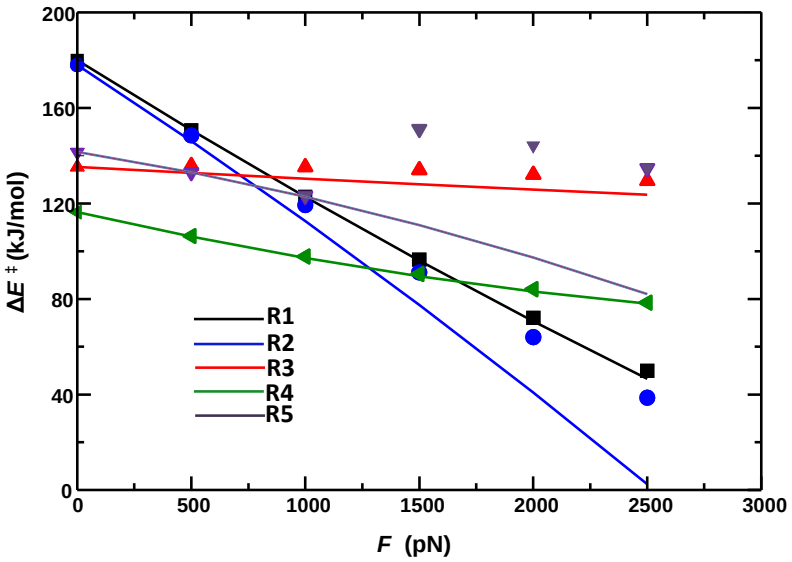

Figure 3-3. $\Delta E^{\ddagger}$ versus F for reactions **R1** to **R5.** The symbols correspond to barriers calculated using the EFEI method and the solid lines represent barriers predicted using Eq. (3.7).

3.3.1 Ring opening reactions

The data shown in Figure 3-3 for reaction **R1** indicates that the $\Delta E^{\ddagger}$'s predicted using Eq. (3.7) and calculated using quantum chemical methods decreased linearly with F. The $\Delta E^{\ddagger}$'s for reaction **R2** also decreased linearly with F. In contrast to reaction **R1**, there was a greater discrepancy between the $\Delta E^{\ddagger}$'s calculated using quantum chemical calculations and predicted using Eq. (3.7) at higher values with F. To make this discrepancy more apparent, the $\Delta E^{\ddagger}$ versus F plots were constructed only for reactions **R1** and **R2** and is shown in Figure 3-4.

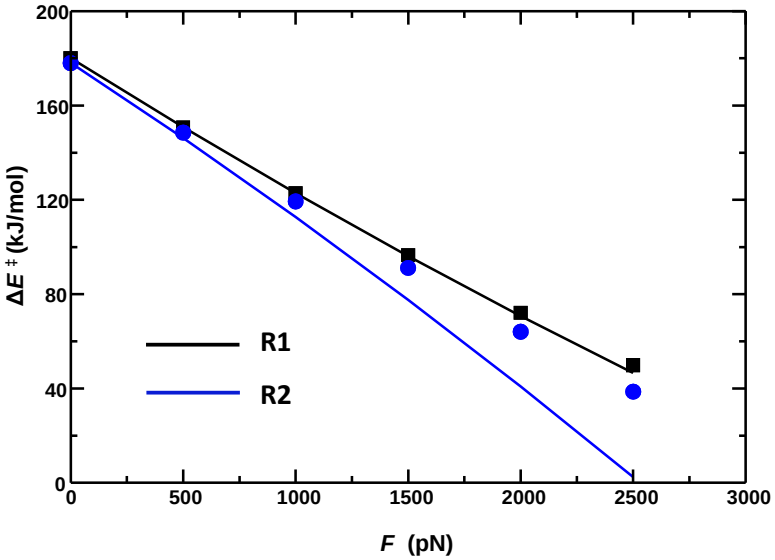

Figure 3-4. $\Delta E^{\ddagger}$ versus F for reactions **R1** and **R2.** The symbols correspond to barriers calculated using the EFEI method and the solid lines represent barriers predicted using Eq. (3.7).

The discrepancy between the $\Delta E^{\ddagger}$'s calculated using quantum chemical methods and predicted using Eq. (3.7) can be attributed to the change in TS structure for reaction **R2** from F = 1000 pN to F = 1500 pN. This change in structure in the TS is illustrated in Figure 3-5. The structural change corresponded to a rotation of the methylene groups

about the carbon-carbon scissile bond. Specifically, the methylene groups are symmetric when F = 1000 pN and asymmetrical when F = 1500 pN.

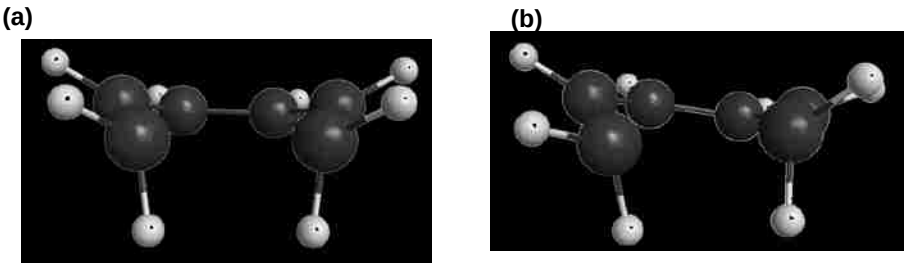

Figure 3-5. Optimized structures of the TS on the FMPES at **a)** F = 1000 pN and **b)** F = 1500 pN for reaction **R2**. The asterisks indicate the PPs in the molecule. The grey and cyan spheres denote carbon atoms and hydrogen atoms respectively.

The structure of the reactant was not affected at higher values of F in a manner that was apparent as in the TS structure. The discrepancy between the $\Delta E^{\ddagger}$'s calculated using quantum chemical methods and predicted using Eq. (3.7) at higher values with F was somewhat expected given that the predictive model outlined in Eq. (3.7) contains information regarding the reactant and TS structures in the absence of F. As such, any structural change in the reactant or TS from their respective structures at F = 0 pN will lead to discrepancies from the predictive model.

3.3.2 Sigmatropic shifts involving hydrogen transfer

The calculated and predicted $\Delta E^{\ddagger}$'s for reactions **R3** and **R4** illustrated in Figure 3-3 slightly decreased with F. The reduction in the $\Delta E^{\ddagger}$'s in these reactions was not as significant compared to reactions **R1** and **R2**. As shown in Figure 3-3, the $\Delta E^{\ddagger}$'s predicted using Eq. (3.7) agreed quite well with those calculated using quantum chemical methods for reaction **R4**. The predicted $\Delta E^{\ddagger}$'s did not agree as well with the calculated $\Delta E^{\ddagger}$'s in

reaction **R3.** To illustrate these discrepancies in a more apparent manner, the $\Delta E^{\ddagger}$ versus F plots were constructed only for reactions **R3** and **R4** and is shown in Figure 3-6.

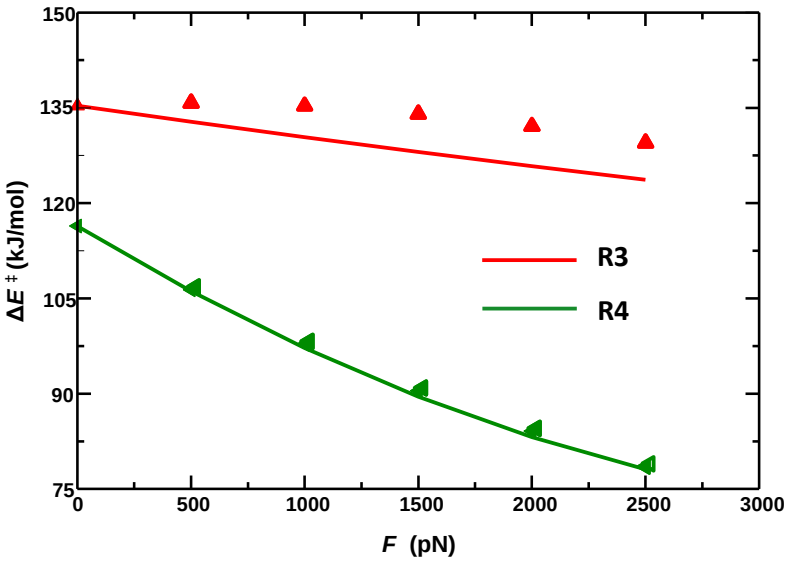

Figure 3-6. $\Delta E^{\ddagger}$ versus F for reactions **R3** and **R4.** The symbols correspond to barriers calculated using the EFEI method and the solid lines represent barriers predicted using Eq. (3.7).

The discrepancy between the predicted $\Delta E^{\ddagger}$'s and calculated $\Delta E^{\ddagger}$'s for reaction **R3** was evident as the system progresses from F = 0 pN to F = 500 pN. This discrepancy can be attributed to a structural change in the reactant. In contrast to reaction **R2**, the structural change in the reactant in reaction **R3** occurred in the predicted structures as calculated using Eq. (3.5) rather than the quantum chemical structures. This structural change is illustrated in Figure 3-7 and involved a rotation around a carbon-carbon bond, in which one of the carbon atoms was bonded to the hydrogen atom involved in the transfer.

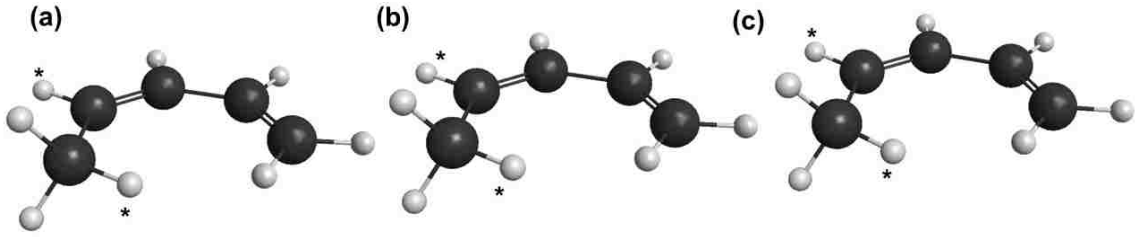

Figure 3-7. Predicted structures using Eq. (3.5) of the reactant for reaction **R3** at **a)** F=0 pN, **b)** F=1000 pN, and **c)** F=2000 pN. The asterisks indicate the PPs in the molecule. The black and white spheres denote carbon and hydrogen atoms respectively.

The predicted structures shown in Figure 3-7 indicate that the application of F to the PPs led to a rotation around the carbon-carbon single bond with the hydrogen atom involved in the transfer moving closer to the adjacent carbon atom at higher values of F. This rotation in the reactant structure was not observed in the quantum chemical structures as shown in Figure 3-8. The differences in the quantum chemical structures and those predicted using Eq. (3.5) can account for the discrepancies observed in their respective $\Delta E^{\ddagger}$'s in Figure 3-6.

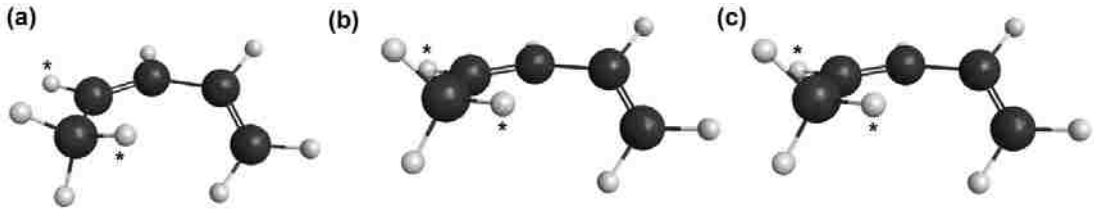

Figure 3-8. Optimized structures of the reactant for reaction **R3** at **a)** F=0 pN, **b)** F=1000 pN, and **c)** F=2000 pN. The asterisks indicate the PPs in the molecule. The black and white spheres denote carbon and hydrogen atoms respectively.

3.3.3 Cope rearrangement of 1,5-hexadiene

The data shown in Figure 3-3 indicate that the greatest discrepancy between the $\Delta E^{\ddagger}$'s calculated using quantum chemical methods and those predicted using Eq. (3.7) was observed in reaction **R5**. The calculated and predicted $\Delta E^{\ddagger}$'s were consistent for values of F between 0 and 1000 pN. A large increase in the calculated $\Delta E^{\ddagger}$'s occurred when F = 1500 pN, which can be attributed to a structural change in the reactant. This structural change from F = 1000 pN to F = 1500 pN is illustrated in Figure 3-9 and corresponded to a rotation around the carbon-carbon scissile bond. The rotation around the carbon-carbon scissile bond was not observed from F = 1000 pN to F = 1500 pN in the structures predicted using Eq. (3.5). As such, the $\Delta E^{\ddagger}$'s predicted using Eq. (3.7) steadily decreased for all values of F.

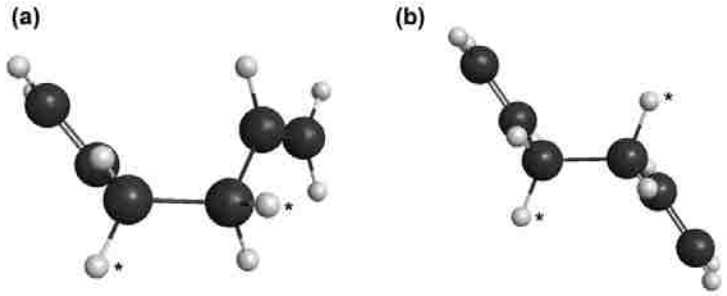

Figure 3-9. Optimized structures of the reactant for reaction **R5** at **a)** F = 1000 pN and **b)** F = 1500pN. The asterisks indicate the PPs in the molecule. The black and white spheres denote carbon and hydrogen atoms respectively.

3.4 Force-induced instabilities

The discrepancies between the $\Delta E^{\ddagger}$'s calculated using quantum chemical methods and predicted using Eq. (3.7) for all reactions outlined in Figure 3-1 can be attributed to structural changes in either the reactant or the TS. The code described in section 3.2 can be

used to identify the value of *F* that leads to a structural change in the reactant or TS without performing geometry optimizations directly on the FMPES. This may be useful from a practical standpoint to identify such force-induced instabilities while limiting the computational effort by performing only quantum chemical calculations of the reactant and TS in the absence of *F*. In some instances, the force-induced instability can alter the nature of the reaction pathway that the system would typically follow in the absence of *F*. For example, the rotation around the carbon-carbon scissile bond in the reactant for reaction **R5** as shown in Figure 3-8 led to the reactant adopting a *trans*-configuration at higher values of *F*. The reaction mechanism associated with the Cope rearrangement of 1, 5-hexadiene, however, requires the reactant to be in a *cis*-configuration. The *trans*-configuration of the reactant may be of significance in other reaction pathways. An important feature of mechanochemistry is the ability to direct chemical systems to follow different reaction pathways than those accessible in the absence of *F*. [4,19,25–27] Therefore, it would be useful to identify when these force-induced instabilities occur in the reactant or TS structures.

A method for identifying the force-induced instabilities without performing quantum chemical calculations directly on the FMPES was described by Bailey and Mosey. [4] In that approach, it was noted that the configuration of a structure in the absence of *F* or at low values of *F* and the configuration of the structure at higher values of *F* in which this force-induced instability occurred are located at two different points along the coordinate associated with the PP distance, *R*. As such, the conversion between these two configurations involves the system moving along *R*. It is important to note that the motion

along R involves changes in the nuclear positions of all atoms in the molecule not just the PPs. The energy for each configuration can be expressed as:

$$E(R) = E_{BO}(\mathbf{q}_0) + \frac{1}{2C_{\mathrm{RR}}}(R - R_0)^2 - FR \tag{3.14}$$

where E_{BO} is the Born-Oppenheimer energy for that particular configuration, C_{RR} is the compliance matrix element associated with R, and R_0 is the PP distance in the absence of F. Eq. (3.14) was applied to the structures of the reactant for reaction **R5** at F = 1000 pN and F = 1500 pN as shown in Figures 3-9a and 3-9b respectively. The resulting plot of $E(R)$ versus R at F = 0 pN is shown in Figure 3-10.

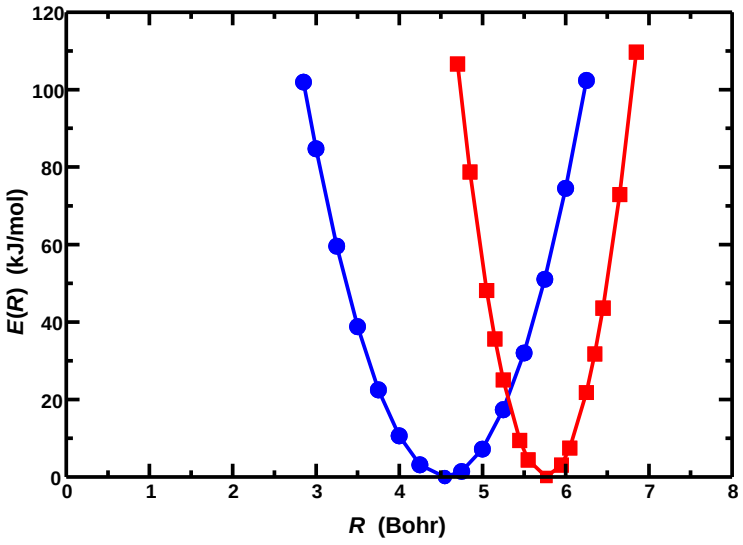

Figure 3-10. Potential energy as a function of PP distance, R, for the configurations of the reactant in reaction **R5**. The blue curve corresponds to using the low force configuration of the reactant shown in Figure 3-9a whereas the red curve corresponds to the high force configuration of the reactant shown in Figure 3-9b. The potential energy was evaluated using Eq. (3.14) at F = 0 pN

The data in Figure 3-10 indicate that the low force structure (Fig. 3-9a), referred to as the initial structure in what follows, and the high force structure (Fig. 3-9b), known as the final structure, are each described with parabolic potential energy profiles. As such, the curves can be used to estimate the change in potential energy associated with the rotation around the carbon-carbon scissile bond as the system moves from the minimum of the initial structure to the minimum of the final structure along *R*. The intersection of the two parabolas occurred at *R*= 5.3 Å. At this point, the system on the initial structure parabola (blue curve) can move onto the final structure parabola (red curve), which would decrease the potential energy as the system reaches the minimum on the final structure parabola. The intersection of the parabolas for the initial and final structures can also be used to estimate the barrier for the reaction involving the rotation around the carbon-carbon scissile bond. The data shown in Figure 3-10 indicate that the barrier for this rotation was approximately 20 kJ/mol whereas the barrier for the rotation reaction calculated using quantum chemical calculations was found to be 10 kJ/mol. The discrepancy between these two values suggests that the intersection of the initial and final structure parabolas is just an approximation and is not reliable for estimating reaction barriers.

The authors in that study (ref. 4) noted that the value of *F* in which the initial structure becomes unstable with respect to the final structure can be determined by solving the quadratic equation:

$$\left[\frac{C_{RR}^{i}}{2C_{RR}^{f}}-\frac{C_{RR}^{i}}{2}\right]F^{2}-\frac{C_{RR}^{i}}{C_{RR}^{f}}\Delta R_{0}F+\frac{1}{2C_{RR}^{f}}\Delta R_{0}^{\,2}+\Delta E_{0}=0 \qquad (3.15)$$

where C_{RR}^{i} and C_{RR}^{f} correspond to the compliance matrix elements for the initial and final structures associated with the internal coordinate, R, and ΔR_0 is the change in R as the system moves from the initial structure to the final structure in the absence of F. The roots of Eq. (3.15) correspond to the values of F and can be solved using the quadratic formula. Solving Eq. (3.15) yields values of F = 1675 pN and F = 7018 pN. The former value is similar to the value of F that led to the structural change in the reactant in the quantum chemical calculations, which occurred when F = 1500 pN. Furthermore, the potential energy of the initial and final structures was calculated using Eq. (3.14) at F = 1675 pN. The resulting plot of $E(R)$ versus R is shown in Figure 3-11 and indicates that the intersection of the parabolas of the initial and final structures occurred at the minimum of the initial structure parabola. As such, it was energetically favorable for the system to move onto the final structure parabola as the system passes the minimum on the initial structure parabola rather than continuing on the potential energy curve of the initial structure. The minimum energies of the initial and final structures in the absence of F were equivalent as shown in Figure 3-9. The application of F shifted the minimum of the final structure parabola to a lower energy relative to the initial structure parabola. This shift in the minima of the two structures accounted for the preference of the final structure of the reactant at higher values of F in the quantum chemical calculations.

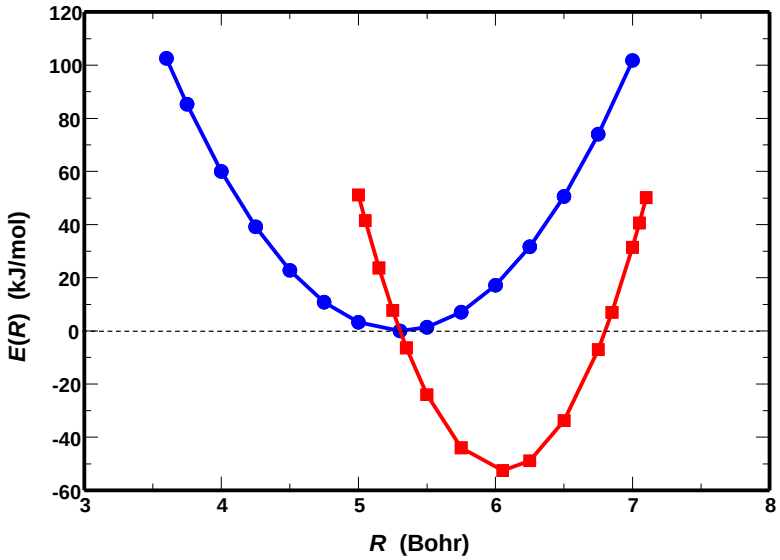

Figure 3-11. Potential energy as a function of PP distance, *R*, for the configurations of the reactant in reaction **R5**. The blue curve corresponds to using the low force configuration of the reactant shown in Figure 3-8a whereas the red curve corresponds to the high force configuration of the reactant shown in Figure 3-8b. The potential energy was evaluated using Eq. (3.14) at F = 1675 pN.

The approach for identifying the force-induced instabilities in reaction **R5** could also be applied to the other reactions outlined in Figure 3-2. One of the main advantages of using this method is that it is computationally inexpensive as only geometry optimizations and vibrational frequency calculations are required for the reactant and TS structures in the absence of F. This approach, however, requires knowledge of key structures that connect the initial and final structures associated with the change in configuration for the reactant or TS. In the case of reaction **R5**, it was somewhat apparent that the initial and final structures were associated with the rotation around the carbon-carbon scissile bond. This might not be the case in other reactions, which would require a more detailed evaluation of the FMPES.

3.5 Summary and outlook

The application of Eq. (3.7) into the code outlined in section 3.2 provides a way to estimate $\Delta E^{\ddagger}$'s on the FMPES for all possible combinations of PPs in a computationally inexpensive manner. This approach is useful in the context of identifying a set of PPs in a molecule that yield a desired mechanochemical response. As such, one can use this code to either activate or deactivate a reaction along particular pathways.

The code was applied to the reactions outlined in Figure 3-2. It was found that the code is able to predict $\Delta E^{\ddagger}$'s under mechanochemical conditions at low values of F when no structural change occurred in either the reactant or TS. Discrepancies between the $\Delta E^{\ddagger}$'s predicted using Eq. (3.7) and those calculated using quantum chemical calculations were observed at higher values of F, in which the application of F altered the structure of the reactant or TS in a configuration that did not coincide with the nature of the reaction mechanism. Such force-induced structural changes can be examined without performing a series of quantum chemical calculations directly on the FMPES by using Eq. (3.5). The value of F that led to the force-induced instability can be identified using the information on the initial and final structures in the absence of F as shown in Eq. (3.15). In the case of reaction **R5**, the value of F that led to the structural change in the reactant shown in Figure 3-8 was F=1675 pN as calculated using Eq. (3.15). This value of F is similar to that identified in the quantum chemical calculations that led to the structural change in the reaction, which occurred when F=1500 pN.

While this code is able to describe changes in the $\Delta E^{\ddagger}$'s under mechanochemical conditions in a manner that is qualitatively consistent with quantum chemical calculations if there is no change in the reactant or TS structure, quantum chemical calculations are

ultimately required to examine key features of the FMPES. In practice, the code can be used in conjunction with quantum chemical calculations to first identify a few possible combinations of PPs that lead to a reduction in $\Delta E^{\ddagger}$ according to Eq. (3.7), and then use these PPs to calculate the $\Delta E^{\ddagger}$'s directly on the FMPES using Eq. (3.2). The code is used in the remaining results chapters in this thesis to identify the set of PPs that are most promising to activate the various chemical reactions.

References:

1. Ribas-Arino, J., Shiga, M. & Marx, D. Understanding covalent mechanochemistry. *Angew. Chem. Int. Ed.* **48,** 4190–4193 (2009).

2. Bell, G. Models for the specific adhesion of cells to cells. *Science* **200,** 618–627 (1978).

3. Bustamante, C., Chemla, Y. R., Forde, N. R. & Izhaky, D. Mechanical processes in biochemistry. *Annu. Rev. Biochem.* **73,** 705–748 (2004).

4. Bailey, A. & Mosey, N. J. Prediction of reaction barriers and force-induced instabilities under mechanochemical conditions with an approximate model: a case study of the ring opening of 1,3-cyclohexadiene. *J. Chem. Phys.* **136,** 44102-1-11 (2012).

5. Konda, S. S. M., Brantley, J. N., Bielawski, C. W. & Makarov, D. E. Chemical reactions modulated by mechanical stress: extended Bell theory. *J. Chem. Phys.* **135,** 164103-1-8 (2011).

6. Kucharski, T. J. & Boulatov, R. The physical chemistry of mechanoresponsive polymers. *J. Mater. Chem.* **21,** 8237–8255 (2011).

7. Pulay, P., Fogarasi, G., Pang, F. & Boggs, J. E. Systematic ab initio gradient calculation of molecular geometries, force constants, and dipole moment derivatives. *J. Am. Chem. Soc.* **101,** 2550–2560 (1979).

8. Wilson, E. B., Decius, J. C. & Cross, P. C. *Molecular vibrations: the theory of infrared and Raman vibrational spectra*. (Dover Publications, 1980).

9. Boatz, J. A. & Gordon, M. S. Decomposition of normal-coordinate vibrational frequencies. *J. Phys. Chem.* **93,** 1819–1826 (1989).

10. Gordon, M. S. Approximate Self-Consistent Molecular-Orbital Theory. VI. INDO Calculated Equilibrium Geometries. *J. Chem. Phys.* **49,** 4643-4650 (1968).

11. Marchand, A. P. & Lehr, R. E. *Pericyclic reactions. Volume II Volume II*. (Elsevier Science : Academic Press, 1977).

12. Poulin, J., Grisé-Bard, C. M. & Barriault, L. Pericyclic domino reactions: concise approaches to natural carbocyclic frameworks. *Chem. Soc. Rev.* **38,** 3092-3101 (2009).

13. Boger, D. L. & Weinreb, S. M. *Hetero Diels-Alder methodology in organic synthesis*. (Academic Press, 1987).

14. Laschat, S. Pericyclic Reactions in Biological Systems—Does Nature Know About the Diels—Alder Reaction? *Angew. Chem. Int. Ed. Engl.* **35,** 289–291 (1996).

15. Carruthers, W. *Cycloaddition reactions in organic synthesis*. (1990).

16. Hendrickson, J. B. The Variety of Thermal Pericyclic Reactions. *Angew. Chem. Int. Ed. Engl.* **13,** 47–76 (1974).

17. Woodward, R. B. & Hoffmann, R. Stereochemistry of Electrocyclic Reactions. *J. Am. Chem. Soc.* **87,** 395–397 (1965).

18. Woodward, R. B. & Hoffmann, R. The Conservation of Orbital Symmetrya. *Angew. Chem. Int. Ed. Engl.* **8,** 781–853 (1969).

19. Kochhar, G. S., Bailey, A. & Mosey, N. J. Competition between orbitals and stress in mechanochemistry. *Angew. Chem. Int. Ed.* **49,** 7452–7455 (2010).

20. Friedrichs, J., Lüssmann, M. & Frank, I. Conservation of orbital symmetry can be circumvented in mechanically induced reactions. *Chemphyschem Eur. J. Chem. Phys. Phys. Chem.* **11,** 3339–3342 (2010).

21. Ong, M. T., Leiding, J., Tao, H., Virshup, A. M. & Martínez, T. J. First principles dynamics and minimum energy pathways for mechanochemical ring opening of cyclobutene. *J. Am. Chem. Soc.* **131,** 6377–6379 (2009).

22. Cope, A. C. & Hardy, E. M. The Introduction of Substituted Vinyl Groups. V. A Rearrangement Involving the Migration of an Allyl Group in a Three-Carbon System [1]. *J. Am. Chem. Soc.* **62,** 441–444 (1940).

23. Becke, A. D. Density-functional thermochemistry. III. The role of exact exchange. *J. Chem. Phys.* **98,** 5648-5652 (1993).

24. Lee, C., Yang, W. & Parr, R. G. Development of the Colle-Salvetti correlation-energy formula into a functional of the electron density. *Phys. Rev. B* **37,** 785–789 (1988).

25. Beyer, M. K. & Clausen-Schaumann, H. Mechanochemistry: the mechanical activation of covalent bonds. *Chem. Rev.* **105,** 2921–2948 (2005).

26. Hickenboth, C. R. *et al.* Biasing reaction pathways with mechanical force. *Nature* **446,** 423–427 (2007).

27. Dopieralski, P. *et al.* On the role of polymer chains in transducing external mechanical forces to benzocyclobutene mechanophores. *J. Mater. Chem.* **21,** 8309–8316 (2011).

Chapter 4

Altering the mechanochemical response of chemical systems through the use of constraints

4.1 Introduction

Quantum chemical calculations typically employ the External Force is Explicitly Included (EFEI) method to simulate mechanochemical conditions.[1] In the EFEI method, an external force of constant magnitude, *F*, is applied between two atoms or groups in a molecule termed pulling points (PPs), which modifies the potential energy surface (PES) according to the expression:

$$E(\mathbf{q}, F) = E_0(\mathbf{q}) - FR \tag{4.1}$$

where $\mathbf{q}$ represents the nuclear coordinates of the atoms in the molecule, E_0 is the energy of the structure in the absence of *F*, and *R* is the distance between the PPs. The effect of *F* on reaction barriers, $\Delta E^{\ddagger}$'s, is of primary interest in this thesis. As such, Eq. (4.1) can be applied to reactant and transition state (TS) geometries. The energy difference between the TS and reactant yields the reaction barrier on the resulting force-modified potential energy surface (FMPES):

$$\Delta E^{\ddagger}(F) = \Delta E_0^{\ddagger}(F) - F\Delta R \tag{4.2}$$

where $\Delta E_0^{\ddagger}(F)$ is the reaction barrier on the Born-Oppenheimer PES and ΔR is the difference in distance between the PPs as the system moves from the reactant to the TS. Performing quantum chemical calculations directly on the FMPES can be computationally demanding for large molecules with several possible combinations of PPs. Specifically, one would have to perform geometry optimizations and vibrational frequency calculations at each value of F for several sets of PPs. Several models have been reported in the literature to estimate the $\Delta E^{\ddagger}$'s on the FMPES while limiting the computational effort.[2–4] Bailey and Mosey[2] have reported an extension of Bell's model[5] to estimate the $\Delta E^{\ddagger}$'s on the FMPES according to the expression:

$$\Delta E^{\ddagger}(F) = \Delta E^{\ddagger}(0) - F\Delta R_0 - \frac{F^2}{2}\Delta C_{RR} \tag{4.3}$$

where $\Delta E^{\ddagger}(0)$ is the reaction barrier in the absence of F, ΔR_0 is the change in distance between PPs upon moving from the reactants to the TS in the absence of F, and ΔC_{RR} is the change in compliance matrix elements associated with R as the system moves from the reactant to the TS. The compliance matrix elements for all internal coordinates comprise the compliance matrix, $\mathbf{C}=\mathbf{H}_{\text{int}}^{-1}$, where $\mathbf{H}_{\text{int}}^{-1}$ is the Hessian in terms of internal coordinates. The C_{RR} term is one of the diagonal elements of **C** and describes the quantitative relationship between F and the change in R in the structure as the system moves from the PES in the absence of F to the FMPES, while accounting for the relaxation along all other internal coordinates. The details of the development of this model are described in section 3.1.

The application of Eq. (4.3) to several pericyclic reactions was explored in section 3.3. It was found that the force-dependent $\Delta E^{\ddagger}$'s predicted using Eq. (4.3) were consistent with those calculated using quantum chemical methods if the reactant or TS does not undergo a significant change in structure that alters its configuration for that particular reaction. The model outlined in Eq. (4.3) contains information on the reactant and TS structures in the absence of *F*. Furthermore, any changes in structure of the reactant or TS in the quantum chemical calculations at higher values of *F* can lead to discrepancies between the calculated $\Delta E^{\ddagger}$'s and those predicted using Eq. (4.3) as was the case for the reactions shown in Figure 3-3 in section 3.3.

The force-induced changes in structures of the reactant or TS may be desirable in some cases as the system may follow different pathways than the typical reaction pathway in the absence of *F*. However, if one aims to activate a reaction along the zero-*F* pathway, it may be necessary to maintain the zero-*F* configurations of the reactant and TS. One way to accomplish this is through the addition of constraints consisting of rings of varying size and chemical composition as well as constraints consisting of intermolecular interactions with other chemical species. The objective of this chapter is to examine the mechanochemical response for a set of representative reactions and identify regions in a molecule in which applying a constraint maintains the zero-*F* reaction configuration of the reactant or TS. Selecting regions in a molecule that are amenable to the addition of a constraint requires one to identify degrees of freedom (DOFs) in a molecule that are most affected by the application of *F*. In some cases, identifying such DOFs is apparent from the structures obtained at various values of *F* from the quantum chemical calculations.

This may not, however, be the case in many other reactions. The general approach to identify the DOFs that are most affected from the application of *F* involves calculating the off-diagonal elements of **C.** The off-diagonal elements of **C** quantify the coupling between *F* applied along *R* and other internal coordinates in the molecule. The addition of constraints to the DOFs that are affected most from the application of *F* alters the strengths of these DOFs and hence the mechanochemical response of the system. In this chapter, quantum chemical calculations employing the EFEI method will be used to calculated the force-dependent $\Delta E^{\ddagger}$'s for a set of representative reactions. The optimized structures obtained from the quantum chemical calculations as well as the zero-*F* reactant and TS compliance matrix elements will be used to identify any force-induced structural changes. Once these force-induced structural changes are identified, constraints of various size and chemical composition will be added to alter the strengths of the DOFs most affected by *F* and hence the mechanochemical response of the system.

4.2 Constraints applied to reactions

Quantum chemical calculations were performed to evaluate the force-dependent ΔE's for the reactions shown in Figure 4-1. All calculations were performed using Kohn-Sham density functional theory[6,7] with a version of the NWChem 6.1 software package[8] that was modified to permit single point molecular energy calculations, geometry optimizations, and vibrational frequency calculations directly on the FMPES. The B3LYP exchange-correlation functional[9,10] was used in conjunction with the 6-31G(d,p) basis set in the calculations for all reactions illustrated in Figure 4-1.

Reaction **R1** corresponds to the Cope rearrangement[11] of 1,5-hexadiene and reactions **R2** and **R3** involve variations of this reaction. In reaction **R2**, ethyl substituents are attached to the carbon atoms of the scissile bond instead of hydrogen atoms. The hydrogen atoms selected as PPs are approximations for long-chain polymers that are typically susceptible to F in experiments. [12–18] Quantum chemical calculations can be computationally demanding for systems with long-chain polymers. As such, replacing hydrogen atoms with ethyl substituents is a better representation of the polymer groups while not significantly increasing the computational cost of the calculation. Reaction **R3** involves replacing the carbon atoms of the scissile bond with nitrogen atoms with ethyl substituents attached to these atoms. Reaction **R3** bridges the gap between reactions **R2** and **R4**, in which reaction **R4** corresponds to an elementary reaction step in the Fischer-Indole synthesis[19,20] with ethyl substituents attached to the nitrogen atoms of the scissile bond. The Cope rearrangement and Fischer-Indole synthesis are used extensively in organic synthesis.[21–29]

The PPs were selected by applying the code outlined in section 3.2 to the reactions shown in Figure 4-1. The code applies Eq. (4.3) to the zero-F reactant and TS geometries of a particular reaction. As such, this code provides insight into which combinations of PPs that F is applied along can lead to an activation of the reaction. Mechanically activating a reaction within the context of Eq. (4.3) can be achieved by selecting PPs that increase in separation as the system moves from the reactants to the TS ($R_0^{TS} > R_0^r$) and are more compliant in the TS than the reactant ($C_{RR}^{TS} > C_{RR}^r$).

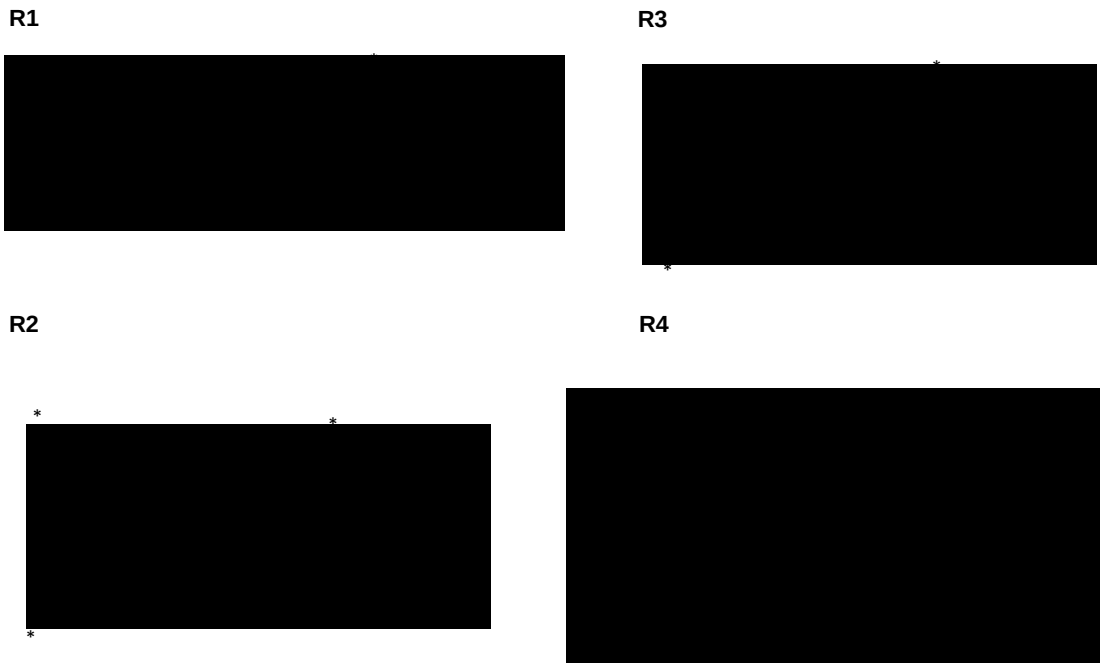

Figure 4-1. Reactions considered in this work. Reactions **R1** through **R3** correspond to variations of the Cope rearrangement of 1,5-hexadiene involving ethyl groups added to the carbon atoms of the scissile bond (reaction **R2**) and replacing the carbon atoms of the scissile bond with nitrogen atoms (reaction **R3**). Reaction **R4** corresponds to an ethyl substituted elementary reaction step in the Fischer-Indole synthesis. The asterisks indicate the pulling points used in all cases.

The force-dependent $\Delta E^{\ddagger}$'s were evaluated for the reactions shown in Figure 4-2. Geometry optimizations and vibrational frequency calculations were performed for the reactant and TS structures for each reaction at each value of F considered. The quantum chemical $\Delta E^{\ddagger}$'s were calculated from the difference in energies of the optimized TS and reactant at each respective value of F. The $\Delta E^{\ddagger}$'s as a function of F were evaluated for reactions **R1** through **R4.** The data show that the $\Delta E^{\ddagger}$'s initially decreased with F for all reactions. A sudden increase in the $\Delta E^{\ddagger}$'s was observed for all reactions. The value of F at which this sudden increase in $\Delta E^{\ddagger}$ occurred was different in each reactant. In light of these apparent discrepancies in the force-dependent $\Delta E^{\ddagger}$'s, detailed analyses are presented for reactions **R1** through **R4**.

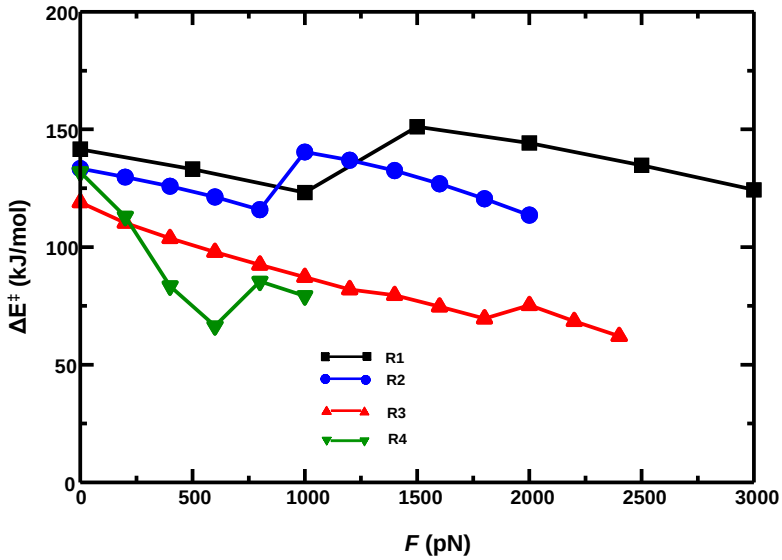

Figure 4-2. $\Delta E^{\ddagger}$ versus F for reactions **R1** through **R4**. The data indicate that $\Delta E^{\ddagger}$ initially decreased at lower values of F and then suddenly increased at a higher value of F for all reactions. The value of F associated with the sudden increase in $\Delta E^{\ddagger}$ was different for all reactions.

4.2.1 R1 Cope re-arrangement of 1,5-hexadiene

The force-dependent $\Delta E^{\ddagger}$'s shown in Figure 4-2 indicate that the sudden increase in the $\Delta E^{\ddagger}$'s occurred when F was increased from 1000 pN to 1500 pN in reaction **R1**. This increase in the $\Delta E^{\ddagger}$'s can be attributed to the structural change in the reactant as shown in Figure 4.3. Specifically, the reactant was in a gauche configuration when $F \leq$ 1000 pN and adopted an anti-configuration when $F >$ 1000 pN.

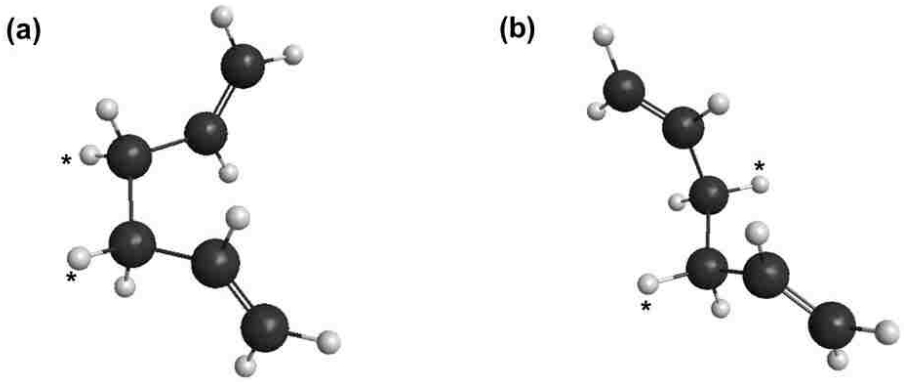

Figure 4-3. Optimized structures of the reactant for reaction **R1** at **a)** F = 1000 pN and **b)** F = 1500 pN. The hydrogen atoms attached to the carbon atoms of the scissile bond were used as pulling points and are shown with asterisks. The black and white spheres represent carbon and hydrogen atoms respectively.

The quantum chemical structures of the reactant shown in Figure 4-3 suggest that the torsion associated with the rotation around the carbon-carbon scissile bond is the DOF that was most affected from the application of F to the PPs. To show this quantitatively, the off-diagonal elements of **C** corresponding to the coupling of R to other internal coordinates were calculated and are displayed in Table 4-1. The angles and torsions listed in Table 4-1 are defined relative to the atomic labels of optimized reactant structure at F=0 pN shown in Figure 4-4.

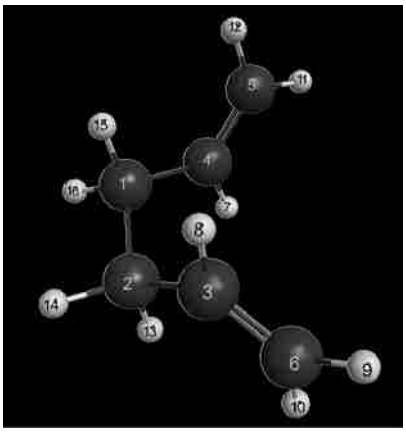

Figure 4-4. Optimized geometry of the reactant for reaction **R1** at F = 0 pN. The black and white spheres denote carbon and hydrogen atoms respectively. The labels on the atoms are used to define the torsions and angles in Table 4-1.

Table 4-1: Off-diagonal elements of **C** of the pulling point distance, *R*, coupled to angles and torsions in the reactant, *q*, in reaction **R1**. The angles and torsions are defined using the atomic labels in Figure 4-4.

Internal coordinate coupled to *R*	C_{Rq} (Hartree/Bohr*Rad)
Torsion defined by atoms 15-1-2-13	-29.79
Torsion defined by atoms 7-4-1-16	-26.35
Torsion defined by atoms 8-3-2-13	-26.49
Angle bend defined by atoms 8-3-2	0.09729
Angle bend defined by atoms 7-4-1	0.6113

The C_{Rq} element was the largest for the coupling between *R* and the torsion defined by atoms 15, 1, 2, and 13, which is associated with the rotation around the carbon-carbon scissile bond. The larger value of C_{Rq} indicates that the torsion associated with the rotation around the carbon-carbon scissile bond was most strongly affected by applying *F* along *R*. Furthermore, hindering this motion through the addition of a constraint can keep the reactant in the configuration necessary to undergo the Cope rearrangement. Ring constraints of varying size were added to the reactant and TS geometries in order to prevent the rotation around the carbon-carbon scissile bond. The force-dependent $\Delta E^{\ddagger}$'s were evaluated for systems ranging from 4 membered rings to 7 membered rings and are shown in Figure 4-5. In all cases, the $\Delta E^{\ddagger}$'s decreased with *F*. Using 4 membered and 5 membered rings, the $\Delta E^{\ddagger}$'s decreased from *F*=0 pN to *F*=1500 pN. The TS for both 4 membered and 5 membered ring constraints were not accessible at values of *F* greater than 1500 pN. The addition of 6 and 7 membered rings to the reactant and TS structures led to a reduction in the $\Delta E^{\ddagger}$'s with *F* over a larger force range than accessible with using 4 and 5 membered rings. The addition of the 7 membered ring resulted in the greatest activation

of the reaction over the force range considered. For all ring constraints, the sudden increase in $\Delta E^{\ddagger}$ was not observed, which can be attributed to the ring constraints preventing the rotation around the carbon-carbon scissile bond in the reactant structure.

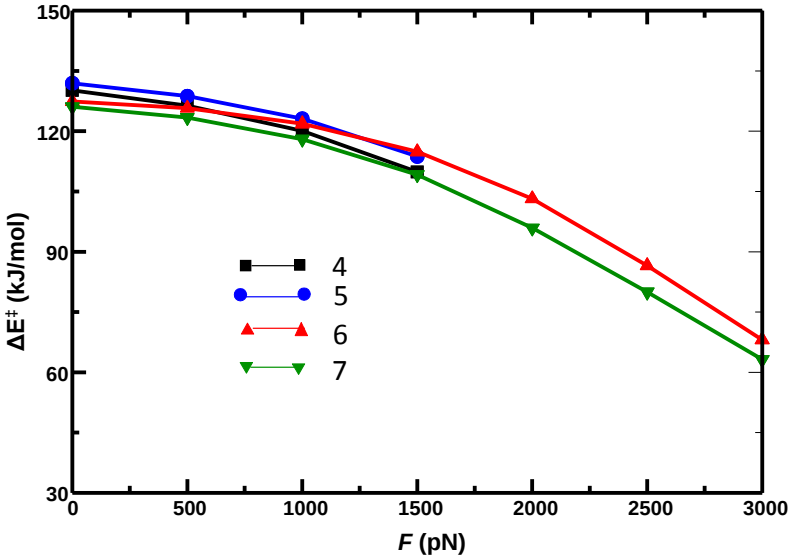

Figure 4-5. $\Delta E^{\ddagger}$ versus F for reaction **R1** with ring constraints of varying sizes added to the reactant and TS structures. The $\Delta E^{\ddagger}$'s decrease with F for all ring constraints. The TS is not accessible at forces greater than 1500 pN when 4 membered and 5 membered ring constraints were used.

The force-dependent $\Delta E^{\ddagger}$'s were evaluated for 7 membered ring constraints with varying chemical compositions. The variations involved replacing the two carbon atoms in the ring with either nitrogen or oxygen atoms. The structures of the reactants at F=0 pN for these systems are displayed in Figures 4-6a and 4-6b respectively with the corresponding calculated $\Delta E^{\ddagger}$'s shown in Figure 4-7. The data show that the calculated $\Delta E^{\ddagger}$'s for the nitrogen substituted 7 membered ring system were similar to the calculated $\Delta E^{\ddagger}$'s with the unsubstituted 7 membered ring. The addition of the oxygen substituted 7 membered ring constraint also led to a reduction in the $\Delta E^{\ddagger}$'s with F, however the TS for this constraint was not accessible at values of F greater than 1500 pN. The inaccessible TS

at values of F greater than 1500 pN refers to those structures on the FMPES that do not contain a single imaginary vibrational mode that corresponds to the motion along the reaction **R1** coordinate.

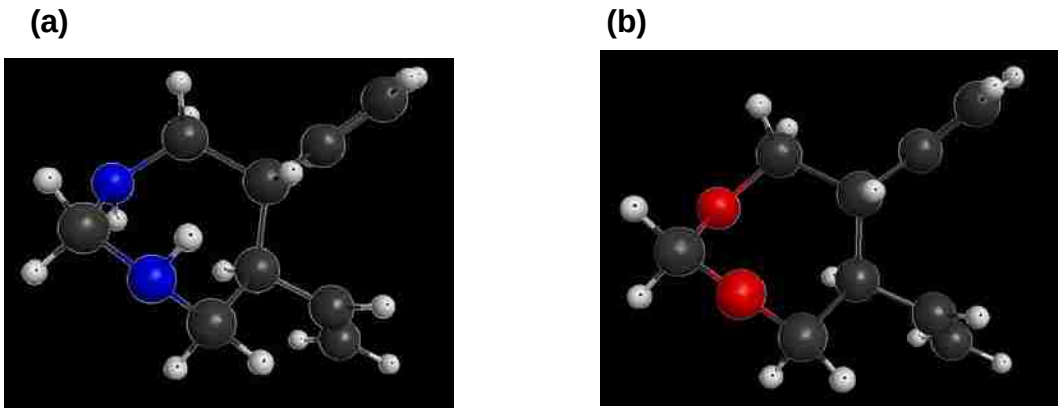

Figure 4-6. Optimized structures of the reactant at F = 0 pN for reaction **R1** with **(a)** 7 membered nitrogen substituted ring constraint and **(b)** 7 membered oxygen ring constraint. The hydrogen atoms attached to the carbon atoms of the scissile bond were selected as pulling points and are indicated with asterisks. The black, white, blue, and red spheres represent carbon, hydrogen, nitrogen, and oxygen atoms respectively.

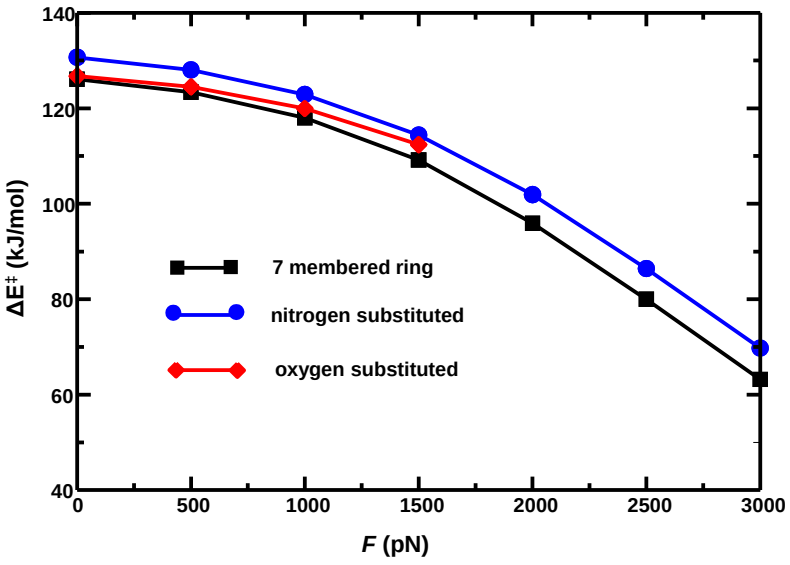

Figure 4-7. $\Delta E^{\ddagger}$ versus F for reaction **R1** with 7 membered ring constraints of varying chemical composition added to the reactant and TS structures. The $\Delta E^{\ddagger}$'s decrease with F for all constraints. The TS is not accessible at values of F greater than 1500 pN when the oxygen substituted 7 membered ring was used.

In addition to using rings to prevent the rotation around the carbon-carbon scissile bond, constraints consisting of interactions with chemical systems were added to the reactant and TS structures in reaction **R1**. The constraints of this type that were considered involve hydrogen bonding to a pyrazole molecule and coordination of cyclopentadiene rings attached to the carbon atoms of the scissile bond to a ruthenium atom. The structures of the reactants for these systems at F = 0 pN are displayed in Figures 4-8a and 4-8b respectively with the changes in the $\Delta E^{\ddagger}$'s with F shown in Figure 4-9. The DFT-D3 dispersion correction[30] was used to calculate the $\Delta E^{\ddagger}$'s for the system constrained through hydrogen bonding with pyrazole. This correction was needed due to the dispersion interactions present within this constraint.

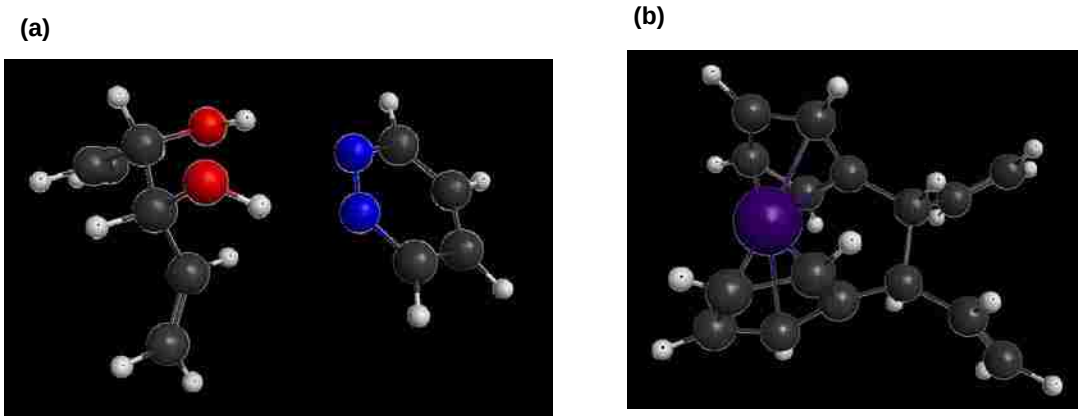

Figure 4-8. Optimized structures of the reactant at F = 0 pN for reaction **R1** with **(a)** hydrogen bonding to pyrazole constraint and **(b)** coordination to a ruthenium atom. The hydrogen atoms attached to the carbon atoms of the scissile bond were selected as pulling points and are indicated with asterisks. The black, white, blue, red, and purple spheres represent carbon, hydrogen, nitrogen, oxygen, and ruthenium atoms respectively.

The data shown in Figure 4-9 indicate that the addition of the constraint involving coordination to a ruthenium atom had the greatest effect in activating reaction **R1**. In the absence of a constraint, reaction **R1** was activated from F = 0 pN to F = 1500 pN prior to

undergoing the rotation around the carbon-carbon scissile bond. The sudden increase in the $\Delta E^{\ddagger}$'s was also observed when the hydrogen bonding constraint was added to the reactant and TS structures. This sudden increase in the $\Delta E^{\ddagger}$'s occurred at the same value of F as in the case of the reaction without a constraint and corresponds to the rotation around the carbon-carbon scissile bond in the reactant. The addition of the constraint involving coordination to a ruthenium atom was a more effective constraint than the hydrogen bonded constraint because it hindered the rotation around the carbon-carbon scissile bond and reduced the $\Delta E^{\ddagger}$'s over a larger force range.

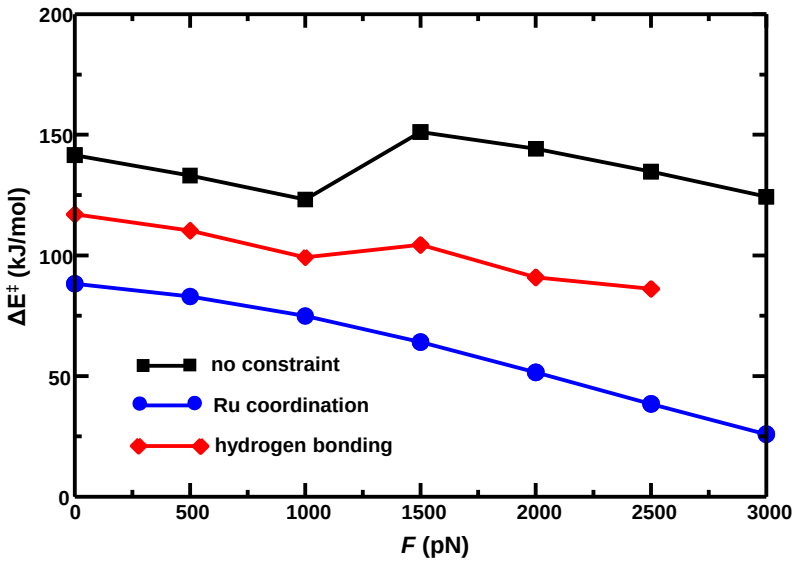

Figure 4-9. $\Delta E^{\ddagger}$ versus F for reaction **R1** with no constraint, coordination to a ruthenium atom constraint, and hydrogen bonding to a pyrazole molecule constraint. The TS was not accessible at values of F greater than 2500 pN when the hydrogen bonding constraint was used.

4.2.2 R2 ethyl substituted Cope re-arrangement of 1,5-hexadiene

The force-dependent $\Delta E^{\ddagger}$'s for reaction **R2** were similar to those calculated for reaction **R1**, in which the $\Delta E^{\ddagger}$'s decreased with F until suddenly increasing at a higher value of F. In the case of reaction **R2**, the increase in the $\Delta E^{\ddagger}$'s occurred when F was increased from 800 pN to 1000 pN. As in the case of reaction **R1**, the sudden increase in the $\Delta E^{\ddagger}$'s for reaction **R2** can be attributed to the rotation around the carbon-carbon scissile bond in the reactant structure as shown in Figure 4-10.

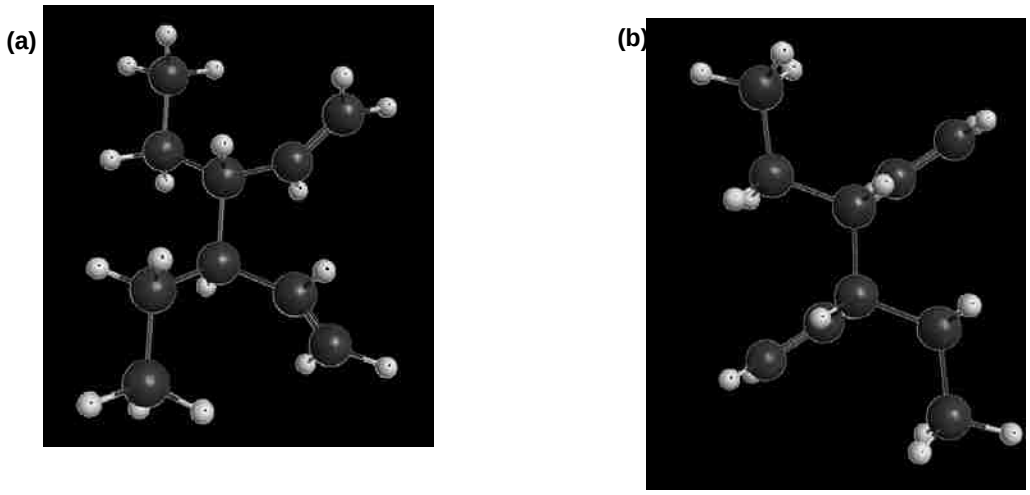

Figure 4-10. Optimized structures of the reactant for reaction **R2** at **a)** F = 800 pN and **b)** F = 1000 pN. The carbon atoms in the attached ethyl groups are used as pulling points and are indicated with asterisks. The black and white spheres represent carbon and hydrogen atoms respectively.

The force-induced structural change in the reactant suggests that this DOF was the most affected from the application of F to the PPs. This assertion was supported by the off-diagonal elements of **C** corresponding to the coupling of R to other internal coordinates as shown in Table 4-2. The torsions listed in Table 4-2 are defined relative to the atomic labels of the optimized reactant structure at F = 0 pN shown in Figure 4-11.

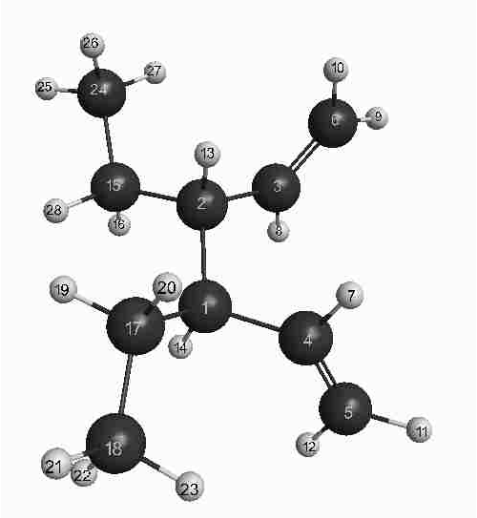

Figure 4-11. Optimized geometry of the reactant for reaction **R2** at F = 0 pN. The black and white spheres denote carbon and hydrogen atoms respectively. The labels on the atoms are used to define the torsions in Table 4-2.

Table 4-2. Off-diagonal elements of **C** of the pulling point distance, R, coupled to angles and torsions in the reactant, q, in reaction **R2**. The torsions are defined using the atomic labels in Figure 4-11.

Internal coordinate coupled to *R*	C_{Rq} (Hartree/Bohr*Rad)
Torsion defined by atoms 14-1-2-13	66.16
Torsion defined by atoms 14-1-17-18	62.19
Torsion defined by atoms 13-2-3-8	34.71
Torsion defined by atoms 20-17-18-22	21.72

The C_{Rq} element was the largest for the coupling between R and the torsion defined by atoms 14, 1, 2, and 13, which corresponds to the rotation around the carbon-carbon scissile bond. The larger value of C_{Rq} indicates that the torsion associated with the rotation around the carbon-carbon scissile bond was most strongly affected by applying F along R. Ring constraints of varying size and chemical composition were added to the reactant and TS geometries in order to prevent the rotation around the carbon-carbon scissile bond. The

force-dependent $\Delta E^{\ddagger}$'s were evaluated for systems ranging from 4 membered rings to 7 membered rings and are shown in Figure 4-12.

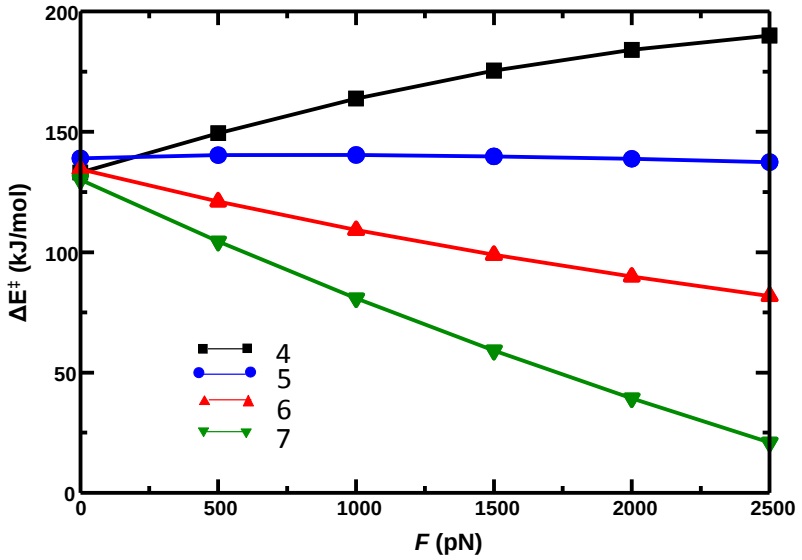

Figure 4-12. $\Delta E^{\ddagger}$ versus F for reaction **R2** with ring constraints of varying sizes added to the reactant and TS structures. The $\Delta E^{\ddagger}$'s increased with F for the 4 membered ring constraint, remained relatively unaffected for the 5 membered ring constraint, and decreased with F for 6 and 7 membered ring constraints.

As in the case of reaction **R1**, the addition of the 7 membered ring constraint led to the greatest reduction in the $\Delta E^{\ddagger}$'s with F for reaction **R2**. Unlike reaction **R1,** the addition of the 4 membered ring constraint led to an increase in the $\Delta E^{\ddagger}$'s for reaction **R2** with F. The $\Delta E^{\ddagger}$'s remained relatively unaffected with F when a 5 membered ring constraint was added to the reactant and TS structures. The results indicated that the size of the constraint can alter the reactivity of reaction **R2** under mechanochemical conditions. The effect of varying the chemical composition of the ring on the $\Delta E^{\ddagger}$'s was examined for the 7 membered ring, given that the addition of this constraint yielded the greatest reduction in the $\Delta E^{\ddagger}$'s with F. As in the case of reaction **R1**, the variations involved replacing the two carbon atoms in the ring with either nitrogen or oxygen atoms (Fig. 4-6). The calculated

$\Delta E^{\ddagger}$'s are shown in Figure 4-13 and indicate that the addition of the nitrogen substituted 7 membered ring yielded force-dependent $\Delta E^{\ddagger}$'s that were nearly identical to those calculated for the unsubstituted 7 membered ring constraint. The addition of the oxygen substituted 7 membered ring constraint to the reactant and TS of reaction **R2** led to a lower $\Delta E^{\ddagger}$ in the absence of F compared to the unsubstituted and nitrogen substituted 7 membered ring constraints. Furthermore, the addition of the oxygen substituted 7 membered ring resulted in the greatest reduction in the $\Delta E^{\ddagger}$'s with F.

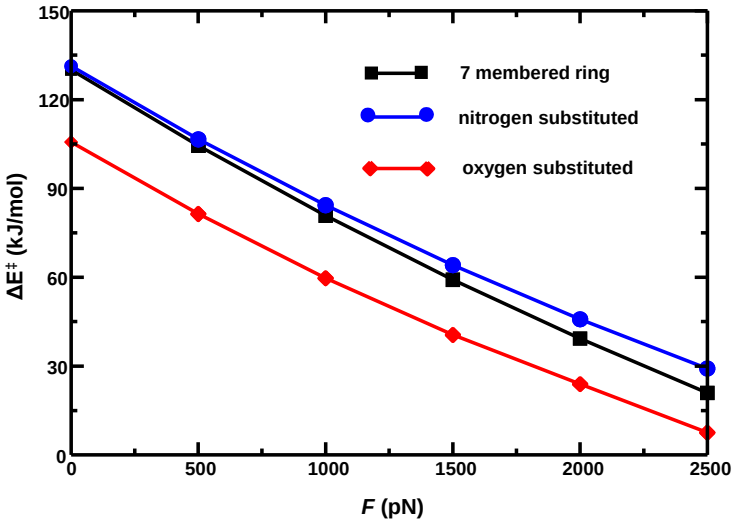

Figure 4-13. $\Delta E^{\ddagger}$ versus F for reaction **R1** with 7 membered ring constraints of varying chemical composition added to the reactant and TS structures. The $\Delta E^{\ddagger}$'s decreased with F for all constraints.

The force-dependent $\Delta E^{\ddagger}$'s were evaluated for reaction **R2** constrained through hydrogen bonding with a pyrazole molecule and coordination of cyclopentadiene rings attached to the carbon atoms of the scissile bond to a ruthenium atom in a similar manner to the structures shown in Figure 4-8. The calculated $\Delta E^{\ddagger}$'s are shown in Figure 4-14. The data indicate that the addition of the ruthenium coordination constraint led to an increase in the $\Delta E^{\ddagger}$'s with F. This was contrary to the data illustrated in Figure 4-9, in which the

addition of the ruthenium coordination constraint resulted in the greatest activation of reaction **R1** under mechanochemical conditions. The addition of the hydrogen bonding constraint to reaction **R2** led to the greatest reduction in the $\Delta E^{\ddagger}$'s with F. The data indicate that the different means of constraining reaction **R2** through interactions with chemical systems resulted in different outcomes for the calculated force-dependent $\Delta E^{\ddagger}$'s.

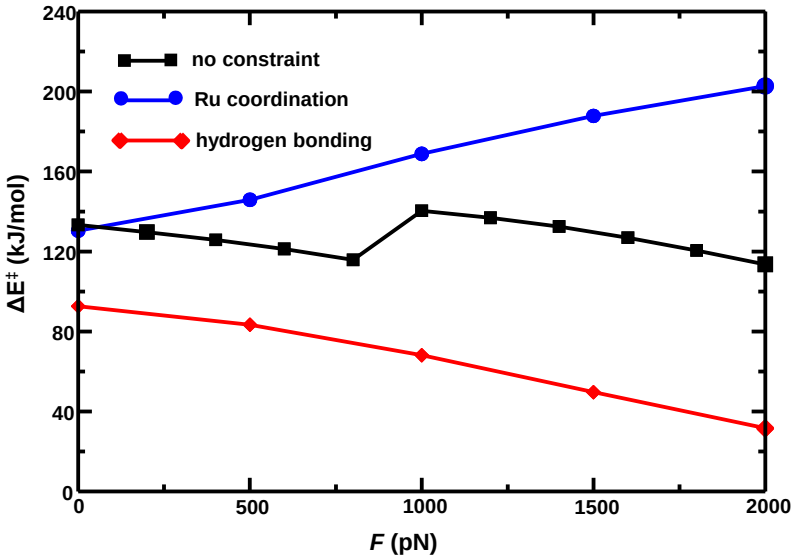

Figure 4-14. $\Delta E^{\ddagger}$ versus F for reaction **R2** with no constraint, coordination of cyclopentadiene rings attached to the carbon atoms of the scissile bond to a ruthenium atom constraint, and hydrogen bonding to a pyrazole molecule constraint.

4.2.3 R3 Nitrogen substituted Cope re-arrangement of 1,5-hexadiene

The sudden increase in the $\Delta E^{\ddagger}$'s occurred at a much higher value of F for reaction **R3** in comparison to reactions **R1** and **R2** as shown in Figure 4-2. The increase in the $\Delta E^{\ddagger}$'s occurred when F was increased from 1800 pN to 2000 pN and corresponded to a change in the TS geometry as opposed to a change in the structure of the reactant, which

was observed for reactions **R1** and **R2**. Specifically, the TS for reaction **R3** underwent a rotation around the nitrogen-nitrogen scissile bond as shown in Figure 4-15.

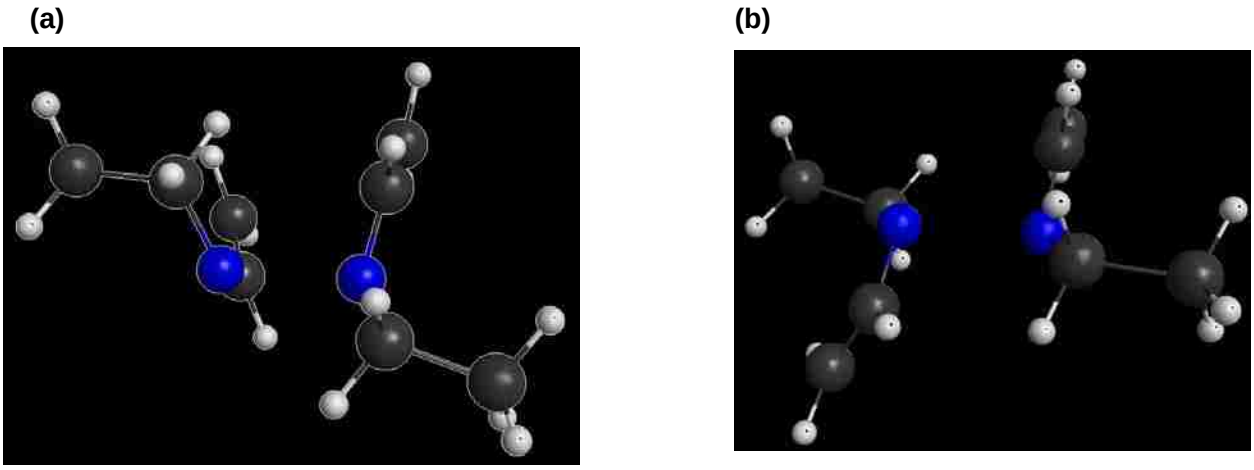

Figure 4-15. Optimized TS structures for reaction **R3** at **(a)** F = 1800 pN and **(b)** F = 2000 pN. The carbon atoms of the attached ethyl group were used as pulling points are indicated with asterisks. The black, white, and blue spheres denote carbon, hydrogen, and nitrogen atoms respectively.

Constraints of varying size and chemical composition were added to reaction **R3** to hinder this force-induced structural change in the TS. The force-dependent $\Delta E^{\ddagger}$'s were evaluated for systems ranging from 4 membered rings to 7 membered rings and are shown in Figure 4-16. As in the case of reactions **R1** and **R2**, the greatest reduction in the $\Delta E^{\ddagger}$'s was achieved when the 7 membered ring constraint was added to the reactant and TS structures of reaction **R3**. The calculated $\Delta E^{\ddagger}$'s in the absence of F was the lowest when a 4 membered ring constraint was used. The nitrogen-nitrogen bond in the reactant structure that contains a 4 membered ring, however, ruptured at values of F greater than 2500 pN as shown in Figure 4-17. As such, the mechanical activation with the addition of a 4 membered ring constraint was limited over a smaller force range compared to larger ring sizes.

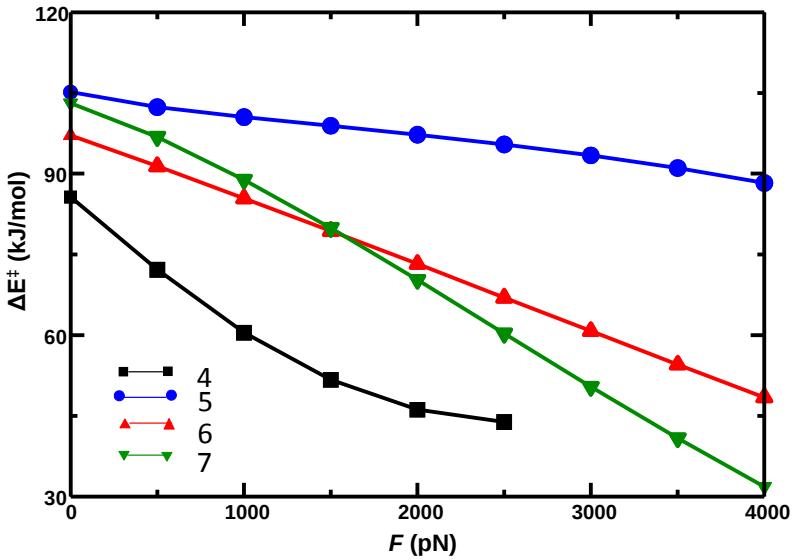

Figure 4-16. $\Delta E^{\ddagger}$ versus F for reaction **R3** with ring constraints of varying sizes added to the reactant and TS structures. The $\Delta E^{\ddagger}$'s decrease with F for all ring constraints. The greatest activation over the force range occurs when the 7 membered ring constraint was applied to the reactant and TS geometries.

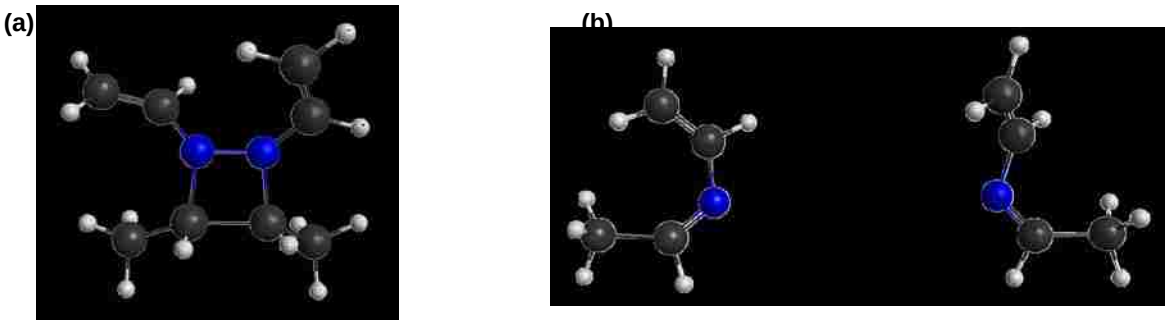

Figure 4-17. Optimized structures of the reactant for reaction **R3** with a 4 membered ring constraint at **(a)** F=2500 pN and **(b)** F=3000 pN. The nitrogen-nitrogen bond dissociated as F was increased from 2500 pN to 3000 pN. The pulling points are shown with asterisks and the black, white, and blue spheres denote carbon, hydrogen, and nitrogen atoms respectively.

Given that the addition of the 7 membered ring yielded the greatest reduction in the $\Delta E^{\ddagger}$'s over the force range, this constraint was used to examine the effect of varying the chemical composition in the ring on the force-dependent $\Delta E^{\ddagger}$'s. The calculated $\Delta E^{\ddagger}$'s for the nitrogen and oxygen substituted constraints are shown in Figure 4-18. The

structures of these substituted 7 membered rings are similar to those shown for reaction **R1** in Figure 4-6 with the carbon atoms of the scissile bond replaced with nitrogen atoms. The data indicate that the $\Delta E^{\ddagger}$ in the absence of F was the largest for the nitrogen substituted 7 membered ring and lowest for the oxygen substituted 7 membered ring. Although the $\Delta E^{\ddagger}$ in the absence of F was the largest in the case of the nitrogen substituted 7 membered ring, the greatest reduction in the force-dependent $\Delta E^{\ddagger}$'s was achieved when this constraint was applied to the reactant and TS geometries.

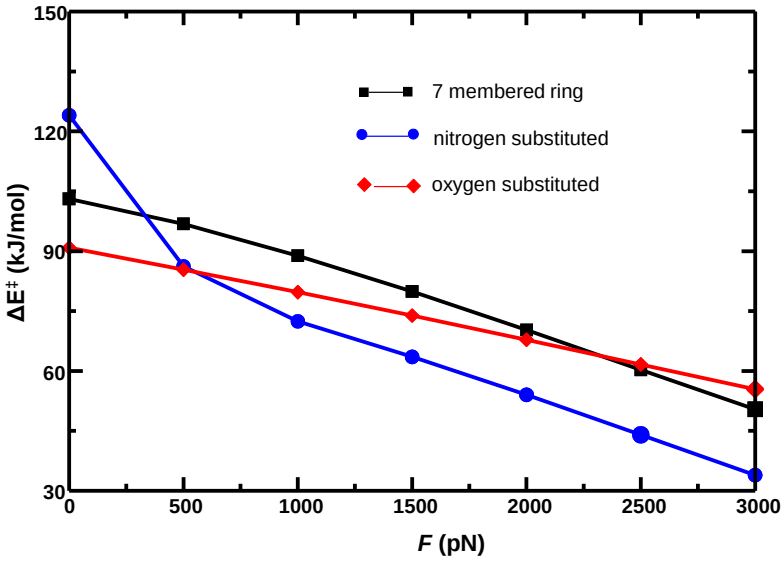

Figure 4-18. $\Delta E^{\ddagger}$ versus F for reaction **R3** with 7 membered ring constraints of varying chemical composition added to the reactant and TS structures. The $\Delta E^{\ddagger}$'s decrease with F for all constraints.

The changes in $\Delta E^{\ddagger}$ with F were also examined for constraints involving hydrogen bonding to a pyrazole molecule and coordination of cyclopentadiene rings attached to the carbon atoms of the scissile bond to a ruthenium atom. The calculated $\Delta E^{\ddagger}$'s for reaction **R3** without a constraint, constrained through hydrogen bonding with a pyrazole molecule,

and constrained through coordination with ruthenium are shown in Figure 4-19. The data indicate that both types of constraints involving interactions with chemical systems led to a greater reduction in the $\Delta E^{\ddagger}$'s than the unconstrained system. The sudden increase in the $\Delta E^{\ddagger}$'s was not observed when both constraints are applied to reaction **R3**.

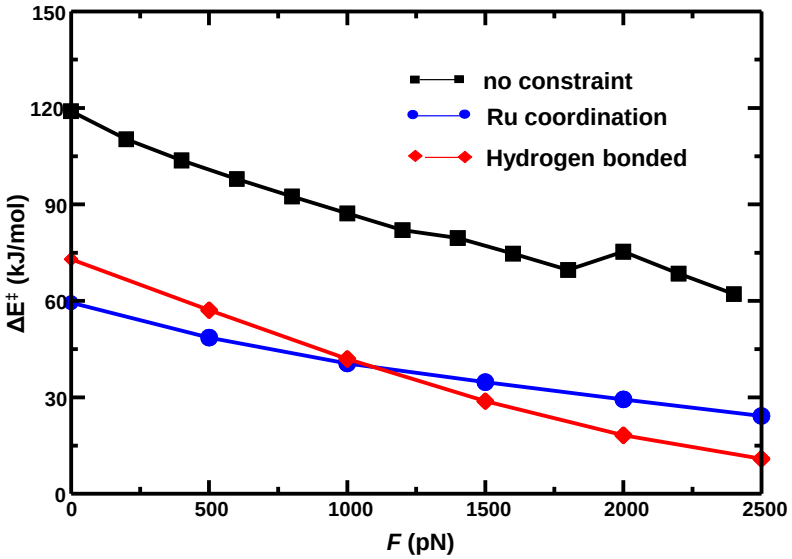

Figure 4-19. $\Delta E^{\ddagger}$ versus F for reaction **R3** with no constraint, coordination of cyclopentadiene rings attached to the carbon atoms of the scissile bond to a ruthenium atom constraint, and hydrogen bonding to a pyrazole molecule constraint.

4.2.4 R4 Elementary reaction step in ethyl substituted Fischer Indole synthesis

The data shown in Figure 4-2 for reaction **R4** indicate that the $\Delta E^{\ddagger}$'s steadily decreased from F = 0 pN to F = 600 pN and then suddenly increased from F= 600 pN to F = 800 pN. The sudden increase in the $\Delta E^{\ddagger}$'s can be attributed to the change in structure of the reactant. Specifically, the reactant was in a gauche configuration when $F \leq 600$ pN and adopted an anti-configuration when $F > 600$ pN. This structural change corresponded to a rotation around the scissile bond in an analogous manner observed for reactions **R1** to **R4.** The $\Delta E^{\ddagger}$'s for reaction **R4** are shown in Figure 4-2 for $F \leq 1000$ pN. The TS for reaction

R4 was inaccessible on the FMPES when F > 1000 pN. Furthermore, the TS structure adopted an anti-configuration with the single imaginary frequency corresponding to a hydrogen transfer between the hydrogen atoms of one of the ethyl groups and the beta carbon of the olefin. The hydrogen transfer competing reaction involved the anti-configurations of the reactant and TS as shown in Figure 4-20.

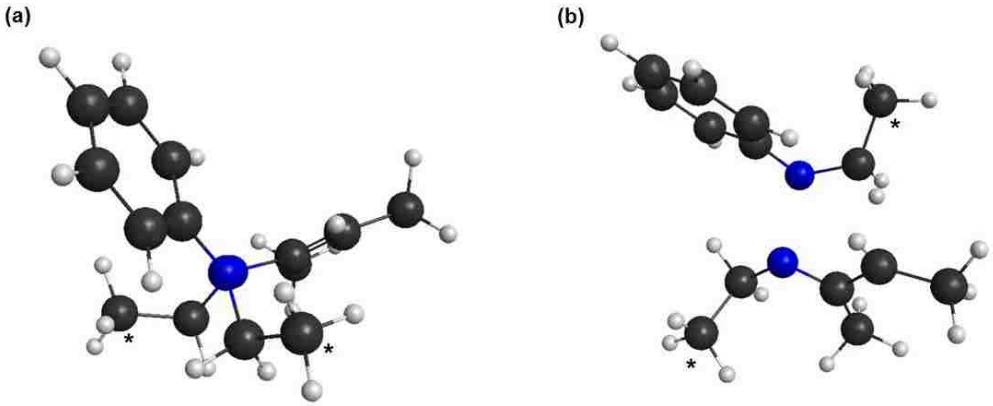

Figure 4-20. Optimized structures of the **(a)** reactant and **(b)** TS for the competing hydrogen transfer reaction at F = 0 pN. The PPs are shown with asterisks and the black, white, and blue spheres denote carbon, hydrogen, and nitrogen atoms respectively.

The calculated $\Delta E^{\ddagger}$'s with F for the hydrogen transfer reaction along with reaction **R4** are shown in Figure 4-21. The data indicate that reaction **R4** was favoured over the competing hydrogen transfer reaction from F=0 pN to F=1000 pN because the $\Delta E^{\ddagger}$'s were lower. However, the TS for reaction **R4** was not accessible when F > 1000 pN. The inaccessible TSs refer to those structures that did not contain a single imaginary vibrational mode corresponding to the motion along reaction coordinate **R4**. As such, the hydrogen transfer reaction was favoured when F > 1000 pN.

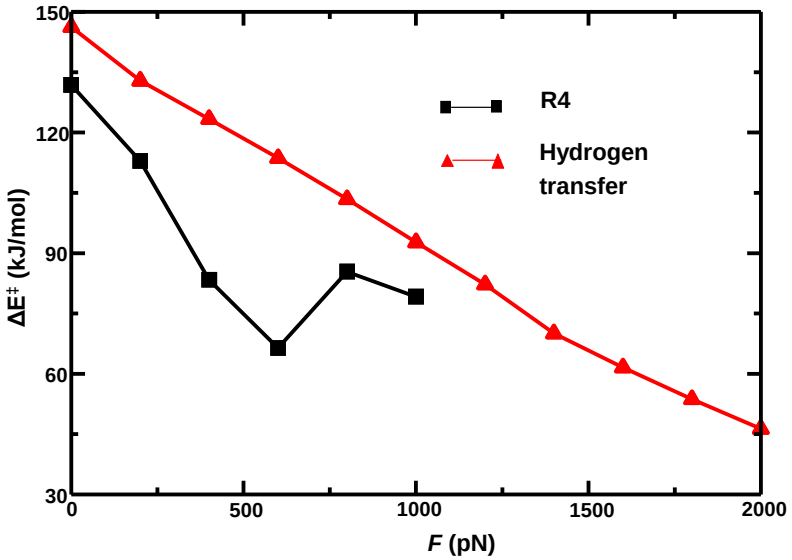

Figure 4-21. $\Delta E^{\ddagger}$ versus F for reaction **R4** and the hydrogen transfer reaction. Reaction **R4** is favoured from F=0 pN to F=1000 pN and the hydrogen transfer reaction is favoured when F > 1000 pN. The TS for reaction **R4** was not accessible at values of F exceeding 1000 pN.

The addition of constaints can be useful in the context of keeping the reactant and TS of reaction **R4** in a reactive state to undergo the elementary reaction step in the Fischer Indole synthesis. Constraints of varying size were added to the reactant and TS structures for both reactions. The calculated force-dependent $\Delta E^{\ddagger}$'s are shown in Figure 4-22. A local minimum could not be located for the anti-configuration of the reactant in the hydrogen transfer reaction when 4 and 5 membered constraints were added. As a result, both these constraints shut off the competing hydrogen transfer reaction. The anti-configuration of the reactant was found to be a local minimum on the PES in the absence of F for the addition of 6 and 7 membered rings. A sudden jump was observed in the calculated $\Delta E^{\ddagger}$'s for the 6 and 7 membered constraints at F = 800 pN and F = 400 pN respectively. In the case of the 7 membered ring constraint, there is a greater reduction in the $\Delta E^{\ddagger}$'s with F for the hydrogen transfer reaction than reaction **R4**. Meanwhile, a greater

activation is achieved for reaction **R4** than the competing hydrogen transfer reaction using a 6 membered ring constraint.

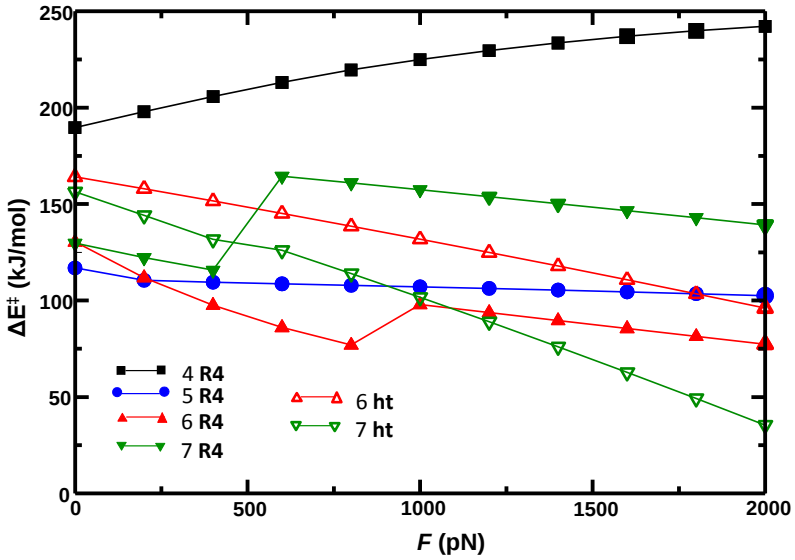

Figure 4-22. $\Delta E^{\ddagger}$ versus F with ring constraints of varying size added to the reactant and TS structures for reaction **R4** (closed symbols) and competing hydrogen transfer reaction (open symbols, **ht**). A local minimum for the reactant could not be located using 4 and 5 membered rings in the competing hydrogen transfer reaction.

Given that the addition of the 6 membered ring constraint yielded the greatest reduction in the $\Delta E^{\ddagger}$'s with F for reaction **R4**, this constraint was used to examine the effect of varying the chemical composition in the ring on the force-dependent $\Delta E^{\ddagger}$'s. The calculated $\Delta E^{\ddagger}$'s for nitrogen and oxygen substituted 6 membered rings are shown in Figure 4-23. The data indicate that the nitrogen and oxygen substituted 6 membered rings resulted in changes in $\Delta E^{\ddagger}$ with F for both reactions that are qualitatively consistent with the unsubstituted 6 membered ring. In all cases, a greater activation with F was achieved for reaction **R4** than the competing hydrogen transfer reaction.

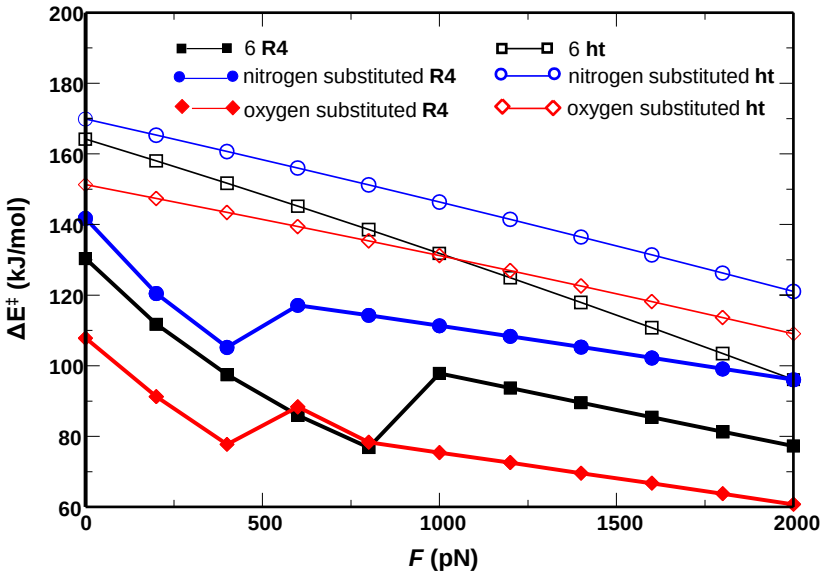

Figure 4-23. $\Delta E^{\ddagger}$ versus F with varying the chemical composition of the 6 membered ring constraint added to the reactant and TS structures for reaction **R4** (closed symbols) and competing hydrogen transfer reaction (open symbols, **ht**)

The changes in $\Delta E^{\ddagger}$ with F for reaction **R4** with constraints involving hydrogen bonding to a pyrazole molecule and coordination of cyclopentadiene rings attached to the carbon atoms of the scissile bond to a ruthenium atom are shown in Figure 4-24. A TS corresponding to the hydrogen transfer reaction could not be located on the PES in the absence of F with the addition of these constraints. The data for reaction **R4** indicate that the addition of the hydrogen bonding and ruthenium coordination constraints affects the force-dependent $\Delta E^{\ddagger}$'s in different ways. The $\Delta E^{\ddagger}$'s increased using the hydrogen bonding constraint from F = 0 pN to F = 1000 pN before decreasing when F > 1000 pN. The TS with this constraint was not accessible on the FMPES at values of F > 2000 pN. The addition of the constraint involving coordination to a ruthenium atom leads to a decrease in the $\Delta E^{\ddagger}$'s with F. The sudden increase in the $\Delta E^{\ddagger}$'s from F = 500 pN to F = 1000 pN can be attributed to the system adopting an anti-configuration from initially existing in a gauche configuration as in the case of reaction **R4** without a constraint. While the addition

of this constraint does not hinder the rotation around the carbon-carbon scissile bond, it allows reaction **R4** to be activated over a larger force range than accessible in the case without a constraint.

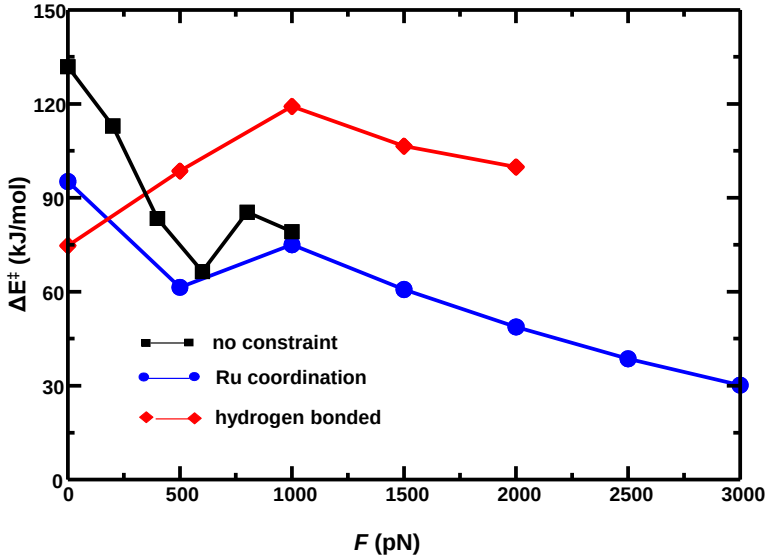

Figure 4-24. $\Delta E^{\ddagger}$ versus F for reaction **R4** with no constraint, coordination of cyclopentadiene rings attached to the carbon atoms of the scissile bond to a ruthenium atom constraint, and hydrogen bonding to a pyrazole molecule constraint.

4.3 Summary

Collectively, the results of the calculations show that the addition of constraints can be used to hinder any force-induced structural changes that the reactant or TS undergo during the course of the reaction. The use of such constraints altered the mechanochemical response of the reactions shown in Figure 4-1 in different ways. Specifically, the use of a 4 membered ring constraint deactivates reactions **R2** and **R4** and activates reactions **R1** and **R3** under mechanochemical conditions. Also, the constraint involving coordination to

a ruthenium atom results in an increase in the $\Delta E^{\ddagger}$'s with F for reaction **R2** and a decrease in the $\Delta E^{\ddagger}$'s with F for reactions **R1**, **R3** and **R4**.

In the case of reaction **R4**, the force-induced changes in the reactant and TS structures results in the system following a competing hydrogen transfer reaction. The nature of the added constraint can influence which of the reaction pathways is more favourable under mechanochemical conditions. The addition of 4 and 5 membered ring constraints shuts off the competing hydrogen transfer reaction because the anti-configuration of the reactant is not a local minimum on the PES calculated in the absence of F. An anti-configuration of the reactant was required for the system to undergo the hydrogen transfer reaction. As well, using constraints involving hydrogen bonding to a pyrazole molecule and coordination to a ruthenium atom shuts off the competing hydrogen transfer pathway because the TS for this reaction is not accessible on the PES calculated in the absence of F.

The results suggest that the addition of constraints can selectively guide systems along particular pathways under mechanochemical conditions. This work may be of general value in the area of mechanoselectivity, in which an applied external force can be used to selectively activate or deactivate reactions along particular pathways.

References:

1. Ribas-Arino, J., Shiga, M. & Marx, D. Understanding covalent mechanochemistry. *Angew. Chem. Int. Ed.* **48,** 4190–4193 (2009).

2. Bailey, A. & Mosey, N. J. Prediction of reaction barriers and force-induced instabilities under mechanochemical conditions with an approximate model: a case study of the ring opening of 1,3-cyclohexadiene. *J. Chem. Phys.* **136,** 44102-1-11 (2012).

3. Konda, S. S. M., Brantley, J. N., Bielawski, C. W. & Makarov, D. E. Chemical reactions modulated by mechanical stress: extended Bell theory. *J. Chem. Phys.* **135,** 164103-1-8 (2011).

4. Kucharski, T. J. & Boulatov, R. The physical chemistry of mechanoresponsive polymers. *J. Mater. Chem.* **21,** 8237–8255 (2011).

5. Bell, G. Models for the specific adhesion of cells to cells. *Science* **200,** 618–627 (1978).

6. Hohenberg, P. & Kohn, W. Inhomogeneous electron gas. *Phys. Rev.* **136,** B864–B871 (1964).

7. Kohn, W. & Sham, L. J. Self-consistent equations including exchange and correlation effects. *Phys. Rev.* **140,** A1133–A1138 (1965).

8. Valiev, M. *et al.* NWChem: A comprehensive and scalable open-source solution for large scale molecular simulations. *Comput. Phys. Commun.* **181,** 1477–1489 (2010).

9. Becke, A. D. Density-functional thermochemistry. III. The role of exact exchange. *J. Chem. Phys.* **98,** 5648-5652 (1993).

10. Lee, C., Yang, W. & Parr, R. G. Development of the Colle-Salvetti correlation-energy formula into a functional of the electron density. *Phys. Rev. B* **37,** 785–789 (1988).

11. Cope, A. C. & Hardy, E. M. The Introduction of Substituted Vinyl Groups. V. A Rearrangement Involving the Migration of an Allyl Group in a Three-Carbon System [1]. *J. Am. Chem. Soc.* **62,** 441–444 (1940).

12. Hickenboth, C. R. *et al*. Biasing reaction pathways with mechanical force. *Nature* **446,** 423–427 (2007).

13. May, P. A. & Moore, J. S. Polymer mechanochemistry: techniques to generate molecular force via elongational flows. *Chem. Soc. Rev.* **42,** 7497-7506 (2013).

14. Beyer, M. K. & Clausen-Schaumann, H. Mechanochemistry: the mechanical activation of covalent bonds. *Chem. Rev.* **105,** 2921–2948 (2005).

15. Price, G., West, P. & Smith, P. Control of polymer structure using power ultrasound. *Ultrason. Sonochem.* **1,** S51–S57 (1994).

16. Ribas-Arino, J., Shiga, M. & Marx, D. Mechanochemical Transduction of Externally Applied Forces to Mechanophores. *J. Am. Chem. Soc.* **132,** 10609–10614 (2010).

17. Paulusse, J. M. J. & Sijbesma, R. P. Ultrasound in polymer chemistry: Revival of an established technique. *J. Polym. Sci. Part Polym. Chem.* **44,** 5445–5453 (2006).

18. Larsen, M. B. & Boydston, A. J. 'Flex-Activated' Mechanophores: Using Polymer Mechanochemistry To Direct Bond Bending Activation. *J. Am. Chem. Soc.* **135,** 8189–8192 (2013).

19. Fischer, E. & Jourdan, F. Ueber die Hydrazine der Brenztraubensäure. *Berichte Dtsch. Chem. Ges.* **16,** 2241–2245 (1883).

20. Fischer, E. & Hess, O. Synthese von Indolderivaten. *Berichte Dtsch. Chem. Ges.* **17,** 559–568 (1884).

21. Van Order, R. B. & Lindwall, H. G. Indole. *Chem. Rev.* **30,** 69–96 (1942).

22. Robinson, B. The Fischer Indole Synthesis. *Chem. Rev.* **63,** 373–401 (1963).

23. Robinson, B. Studies on the Fischer indole synthesis. *Chem. Rev.* **69,** 227–250 (1969).

24. Evans, D. A. & Golob, A. M. [3,3]Sigmatropic rearrangements of 1,5-diene alkoxides. Powerful accelerating effects of the alkoxide substituent. *J. Am. Chem. Soc.* **97,** 4765–4766 (1975).

25. Davies, H. M. L., Dai, X. & Long, M. S. Combined C−H Activation/Cope Rearrangement as a Strategic Reaction in Organic Synthesis: Total Synthesis of (−)-Colombiasin A and (−)-Elisapterosin B. *J. Am. Chem. Soc.* **128,** 2485–2490 (2006).

26. Hughes, D. L. Progress in the Fischer Indole Reaction. A Review. *Org. Prep. Proced. Int.* **25,** 607–632 (1993).

27. Davies, H. M. L. & Lian, Y. The Combined C–H Functionalization/Cope Rearrangement: Discovery and Applications in Organic Synthesis. *Acc. Chem. Res.* **45,** 923–935 (2012).

28. Davies, H. M. L. Tandem cyclopropanation/cope rearrangement: a general method for the construction of seven-membered rings. *Tetrahedron* **49,** 5203–5223 (1993).

29. Knight, S. D., Overman, L. E. & Pairaudeau, G. Synthesis applications of cationic aza-Cope rearrangements. 26. Enantioselective total synthesis of (-)-strychnine. *J. Am. Chem. Soc.* **115,** 9293–9294 (1993).

30. Grimme, S., Antony, J., Ehrlich, S. & Krieg, H. A consistent and accurate ab initio parametrization of density functional dispersion correction (DFT-D) for the 94 elements H-Pu. *J. Chem. Phys.* **132,** 154104-1-19 (2010).

Chapter 5

Effect of sterics on the contribution of mechanical work in activating mechanochemical reactions

5.1 Introduction

The application of an external force, F, to atoms or functional groups in a molecule termed pulling points (PPs) has been shown to lower reaction barriers, $\Delta E^{\ddagger}$'s, for various chemical systems in several experimental and theoretical studies. [1–12] The $\Delta E^{\ddagger}$ under mechanochemical conditions can be described using the External Force is Explicitly Included (EFEI) method: [4]

$$\Delta E^{\ddagger}(F) = \Delta E_0^{\ddagger}(F) - F\Delta R \tag{5.1}$$

where ΔR is the difference in distance between the PPs as the system moves from the reactant to the TS, and $\Delta E^{\ddagger}(F)$ is the reaction barrier on the resulting force-modified potential energy surface (FMPES). The $\Delta E_0^{\ddagger}(F)$ term corresponds to the reaction barrier on the unmodified potential energy surface (PES) and can be calculated using either force-fields or quantum chemical methods, which are described in section 2.8. The latter is used in the EFEI calculations performed in this chapter. Furthermore, the $\Delta E_0^{\ddagger}(F)$ term is obtained from calculating the energy difference between the transition state (TS) and the

reactants on the Born-Oppenheimer PES. Eq. (5.1) can be expressed in terms of the reaction barrier on the Born-Oppenheimer PES, $\Delta E_{\mathrm{BO}}^{\ddagger}$:

$$\Delta E^{\ddagger}(F) = \Delta E_{\mathrm{BO}}^{\ddagger}(F) - F\Delta R \tag{5.2}$$

The force-induced changes in $\Delta E^{\ddagger}$ can be described by expressing Eq. (5.2) into the changes in $\Delta E^{\ddagger}$ relative to the zero-F reaction barrier:

$$\Delta E^{\ddagger}(F) = \Delta E_{\mathrm{BO}}^{\ddagger}(0) + \Delta\Delta E_{\mathrm{BO}}^{\ddagger}(F) - F\Delta R_0 - F\Delta\Delta R(F) \tag{5.3}$$

where $\Delta E_{\mathrm{BO}}^{\ddagger}(0)$ represents the zero-F reaction barrier on the Born-Oppenheimer PES and is calculated from the difference in energies of the zero-F TS and reactant structures. $\Delta\Delta E_{\mathrm{BO}}^{\ddagger}(F)$ represents the change in the Born-Oppenheimer contributions due to the force-induced changes in the reactant and TS structures, ΔR_0 is the change in distance between PPs as the system moves from the zero-F reactant to the zero-F TS, and $\Delta\Delta R$ is the change in ΔR due to the force-induced changes in reactant and TS structures. The use of Eq. (5.3) in practical mechanochemical efforts suggests that $\Delta E^{\ddagger}$ decreases under mechanochemical conditions if the reactants and TS become more similar in structure and if the amount of mechanical work performed on the system increases during the course of the reaction. The former is essentially a Hammond effect,[13] in which the application of F decreases the separation distance between the reactants and TS along the reaction coordinate. Several theoretical studies have shown that the mechanical activation of unimolecular reactions

can be achieved by applying F to a molecule in a manner that decreases the distance between the reactant and TS along the reaction coordinate and hence make the reactant and TS more similar in structure. [4–7,14]

An alternative approach to mechanically activate chemical reactions involves performing sufficient mechanical work to overcome $\Delta E^{\ddagger}$. Specifically, this requires maintaining a positive value of ΔR during the course of the reaction such that the reactants and TS become more dissimilar with F. This notion contrasts with mechanically-induced Hammond effects, in which the application of F causes the reactants and TS to become more similar in structure.

While there are no studies reported in the literature on mechanically activating reactions by targeting the mechanical work term ($-F\Delta R$) in Eq. (5.2) to make the reactant and TS structures more dissimilar, there have been several studies on the effect of the addition of groups that transduce external forces to the reacting species, termed mechanophores,[15] on the mechanical activation of reactions. [3,16–21] For the most part, the mechanophores consisted of polymer chains in a molecule that alter the steric properties of the reactive species. A study performed by Krupicka and Marx has shown that increasing the sterics of the substrate in a S_N2 reaction led to an increase in the $\Delta E^{\ddagger}$'s. [22] Specifically, it was found that the addition of an ethoxide anion as a nucleophile to the ethyl neopentyl ether substrate resulted in an increase in the zero-F $\Delta E^{\ddagger}$ compared to the addition of the ethoxide anion to the less sterically hindered substrate, ethyl propyl ether. The structures of these two substrates are illustrated in Figure 5-1. The $\Delta E^{\ddagger}$'s calculated using both substrates decreased with F. The $\Delta E^{\ddagger}$ in the absence of F is lower in the case of the less sterically hindered substrate ethyl propyl ether than the ethyl neopentyl ether substrate.

The authors in that study attributed the increase in the $\Delta E^{\ddagger}$ for the ethyl neopentyl ether substrate to the increase strain in the TS for this system. The increase strain in the TS was quantified by examining the changes in torsion associated with increasing the sterics of the substrate. Specifically, the authors noted that the torsion for the TS involving the ethyl neopentyl ether substrate was altered compared to the TS with the ethyl propyl ether substrate in a manner that disfavoured nucleophilic attack of the ethoxide anion. The torsion was defined by the four atom labels on the substrate structures illustrated in Figure 5-1.

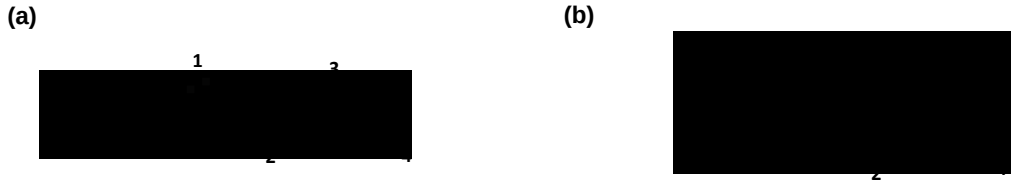

Figure 5-1. Chemical structures of the substrates **(a)** ethyl propyl ether and **(b)** ethyl neopentyl ether used in the S_N2 reaction with the ethoxide anion nucleophile. The labels on the atoms indicate the atoms that define the torsion that is most significantly affected from the increased sterics of the substrate. The nucleophilic attack of the ethoxide anion occurs at carbon atom '2' on the substrate.

The previous study involving the effect of sterics on the mechanical activation of the S_N2 reaction accounted for the differences in the $\Delta E^{\ddagger}$'s based on the structures of the TSs. Furthermore, this study did not investigate the underlying energetics associated with differences in the force-dependent $\Delta E^{\ddagger}$'s for the two reactions. The objective of this chapter is to investigate the effect of sterics on reactions under mechanochemical conditions by examining the changes in the Born-Oppenheimer energy and mechanical work terms for a set of representative chemical reactions.

5.2 Reaction barriers under mechanochemical conditions

Quantum chemical calculations employing the EFEI method[4] were performed to evaluate the force-dependent $\Delta E^{\ddagger}$'s for the reactions shown in Figure 5-2. All calculations were performed using Kohn-Sham density functional theory[23,24] with a version of the NWChem 6.1 software package[25] that was modified to permit single point molecular energy calculations, geometry optimizations, and vibrational frequency calculations directly on the FMPES. The B3LYP exchange-correlation functional[26,27] was used in conjunction with the 6-31G(d,p) basis set for all calculations.

All reactions shown in Figure 5-2 consist of Diels-Alder reactions that proceed via formation of a reactant complex prior to forming the TS. The non-bonding interactions in the reactant complex were treated by using the DFT-D3 dispersion correction.[28] The steric effect involved varying the size of the substituent, X, attached to the diene or dienophile. The substituent was attached to the diene in reactions **R1** and **R2** whereas two substituents were attached to the dienophile in reactions **R3** and **R4**.

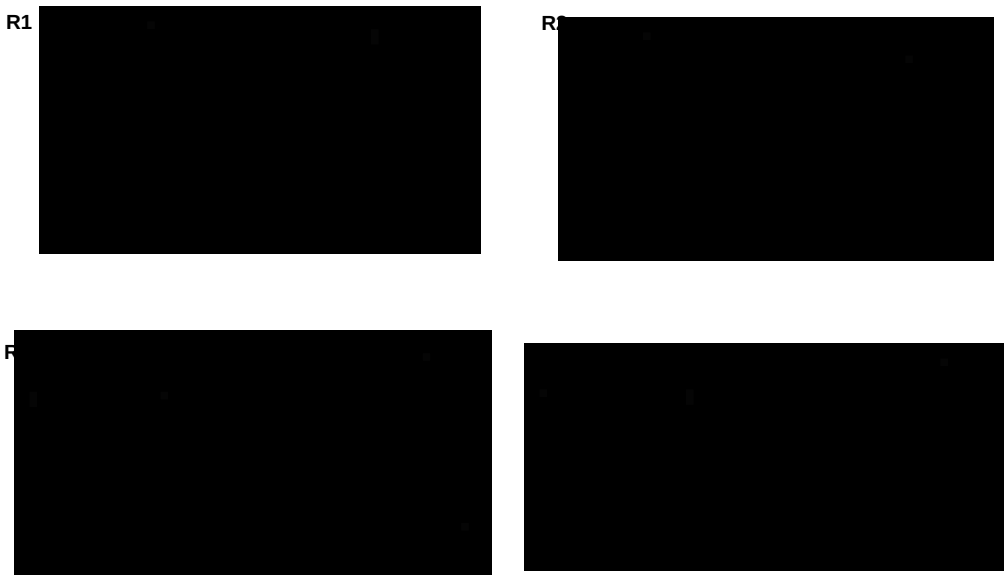

Figure 5-2. Reactions considered in this work. Reactions **R1** and **R2** involve Diels-Alder reactions, in which ethylene is the dienophile and undergoes a cycloaddition with substituted cyclopentadiene and substituted cyclohexene respectively. Reactions **R3** and **R4** involve Diels-Alder reactions in which butadiene undergoes a cycloaddition with substituted cyclopentene and cyclohexene respectively. The 'X' group indicates the substituent added for all reactions. The asterisks indicate the pulling points used in all cases.

The PPs were selected for each reaction by applying the code outlined in chapter 3 section 3.2. The force-dependent $\Delta E^{\ddagger}$'s were evaluated for reactions **R1**-**R4** and are shown in Figure 5-3. The $\Delta E^{\ddagger}$'s were evaluated by calculating the energy difference between the TS and the reactant complex on the FMPES. Substituents of increasing size were added to the reactions such that X=H, CH_3, CF_3, $C(CH_3)_3$, and $C(CF_3)_3$. The data shown in Figure 5-3 indicate that increasing the sterics of the substituent affected the $\Delta E^{\ddagger}$'s for each reaction in different ways. For instance, the zero-F $\Delta E^{\ddagger}$ increased when the sterics of the substituent increased from X = H to X = $C(CF_3)$ in reactions **R1**, **R3**, and **R4.** The zero-F $\Delta E^{\ddagger}$ for reaction **R2**, however was higher when X = H compared to when X = CH_3 and CF_3. The $\Delta E^{\ddagger}$'s for reaction **R1** decreased with F for all substituents in reactions **R1** and

R2. In contrast, the $\Delta E^{\ddagger}$'s remained relatively unaffected with F for all substituents in reaction **R3** and when X = H in reaction **R4.** In light of these apparent discrepancies in the force-dependent $\Delta E^{\ddagger}$'s, detailed analyses are presented in what follows for each reaction.

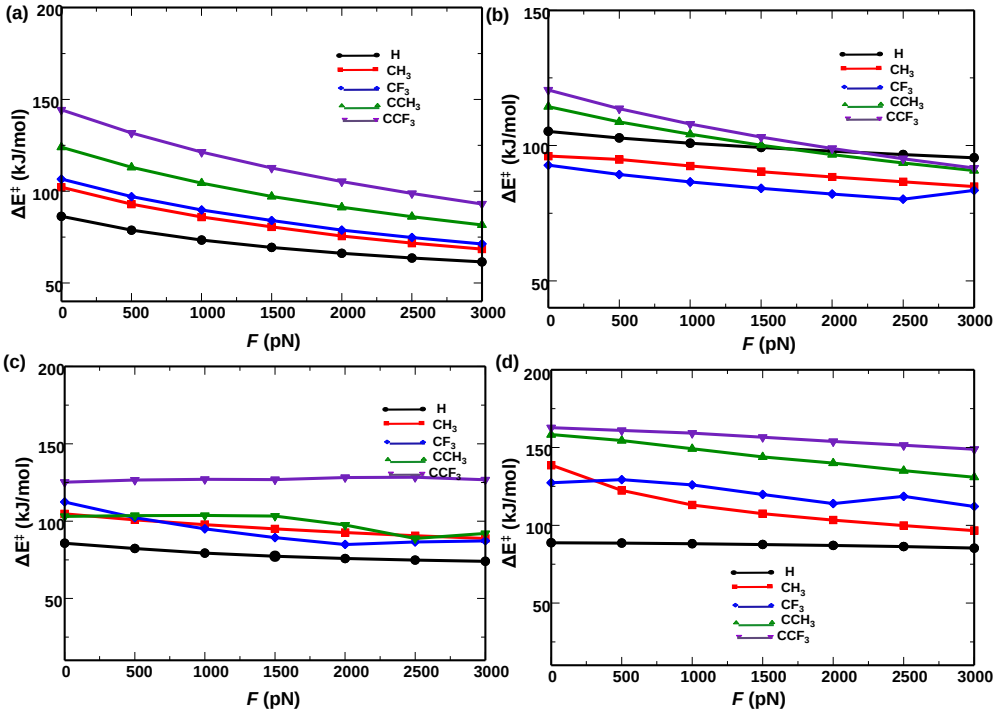

Figure 5-3. $\Delta E^{\ddagger}$ versus F for reactions **(a) R1**, **(b) R2, (c) R3,** and **(d) R4.** The data indicate that $\Delta E^{\ddagger}$ is the highest in the absence of F when X = $C(CF_3)_3$ for all reactions. The changes in $\Delta E^{\ddagger}$ with F for all substituents differs in each reaction.

5.2.1. R1 Diels-Alder reaction of ethylene and substituted cyclopentadiene

The steric effects in reaction **R1** were determined by examining the interaction of the substituent with the cyclopentadiene ring as the system moves from the reactant complex to the TS. The interaction of the substituent with the ring was quantified by evaluating the changes in the angle between the sp^2 carbon atoms in the ring and the carbon-substituent bond, θ, with the sterics of the substituent in the complex and TS. The

changes in θ along with the reactant complex and TS structures are shown in Figure 5-4. The data indicate that θ increased when the sterics of the substituent was increased from X = H to X = $C(CF_3)_3$ in both the reactant complex and the TS.

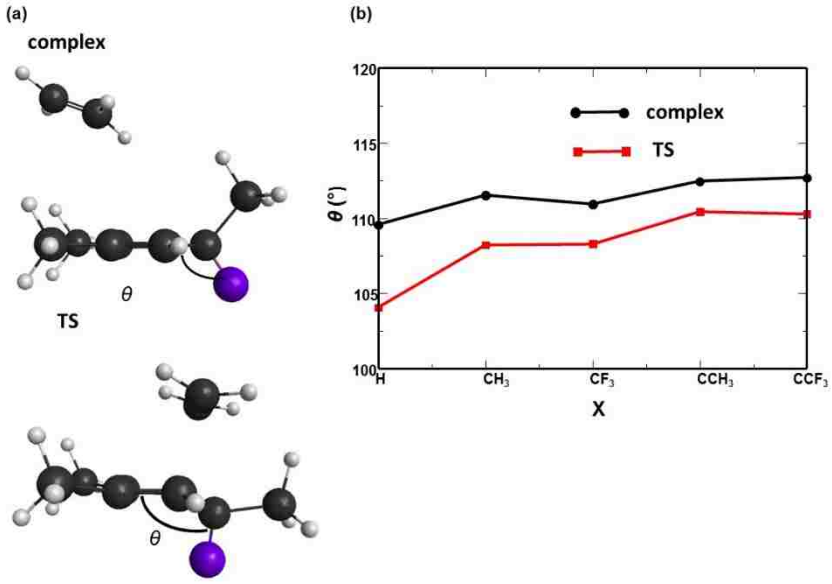

Figure 5-4. (a) Structures of the reactant complex and TS for reaction **R1**. The black, white, and purple spheres denote carbon atoms, hydrogen atoms, and substituents respectively. The angle, θ, is defined between the sp^2 carbon atoms in the ring and the carbon-substituent bond. **(b)** Changes in θ with substituent, X = H, CH_3, CF_3, $C(CH_3)$, and $C(CF_3)$. The data indicate that θ increased as the sterics of the substituent increased.

The force-dependent $\Delta E^{\ddagger}$'s for reaction **R1** shown in Figure 5-3 indicate that increasing the sterics of the substituent led to an increase in the $\Delta E^{\ddagger}$ in the absence of F. Furthermore, the data show that force-dependent $\Delta E^{\ddagger}$'s in reaction **R1** are the lowest when X = H. While the least sterically hindered substituent resulted in the lowest force-dependent $\Delta E^{\ddagger}$'s, the greatest reduction in the zero-F $\Delta E^{\ddagger}$ was achieved when X = $C(CF_3)_3$ as illustrated from the plot of the changes in $\Delta E^{\ddagger}$ with F with respect to the zero-F $\Delta E^{\ddagger}$, $\Delta\Delta E^{\ddagger}$, as a function of F shown in Figure 5-5.

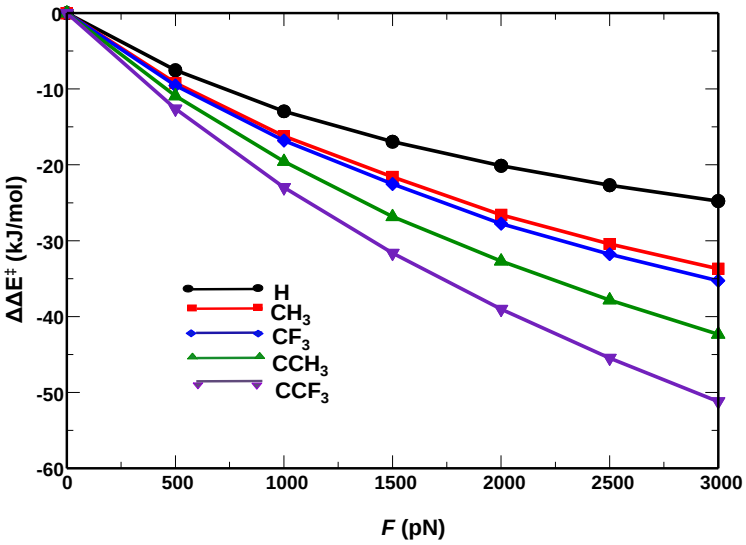

Figure 5-5. $\Delta\Delta E^{\ddagger}$ versus F for reaction **R1**. The data indicate that increasing the sterics of the substituent resulted in a greater reduction in $\Delta E^{\ddagger}$ with F.

The effect of sterics on the force-dependent $\Delta E^{\ddagger}$'s was further investigated by evaluating changes in the contributions of the Born-Oppenheimer energy terms and the mechanical work terms with F. The contributions from the changes in the Born-Oppenheimer energy, $\Delta\Delta E_{BO}^{\ddagger}$, are shown in Figure 5-6a. The data indicate that $\Delta\Delta E_{BO}^{\ddagger}$ steadily became more negative and increased in magnitude with F for all substituents. This result indicates that the Born-Oppenheimer energy had a greater contribution in the reduction of the $\Delta\Delta E^{\ddagger}$'s as F was increased. Furthermore, the greater contribution of $\Delta\Delta E_{BO}^{\ddagger}$ suggests that the reactant and TS became more similar in structure with F. In addition, the magnitude of the $\Delta\Delta E_{BO}^{\ddagger}$ term increased as the sterics of the substituent increased. Similarly, the magnitude of the contributions from the changes in the mechanical work performed on the system, $-F\Delta\Delta R$, also increased as the sterics of the substituent increased (Fig. 5-6b). In the case of X = H, the contributions from the $\Delta\Delta E_{BO}^{\ddagger}$ term to the mechanical activation of reaction **R1** were greater than the contributions from

the $-F\Delta\Delta R$ term when $F > 2500$ pN. For all other substituents, the contributions from the $-F\Delta\Delta R$ term were greater than the contributions from the $\Delta\Delta E_{BO}^{\ddagger}$ term at all values of F. The discrepancy between the magnitudes of $-F\Delta\Delta R$ and $\Delta\Delta E_{BO}^{\ddagger}$ was more significant with the more sterically hindered substituents.

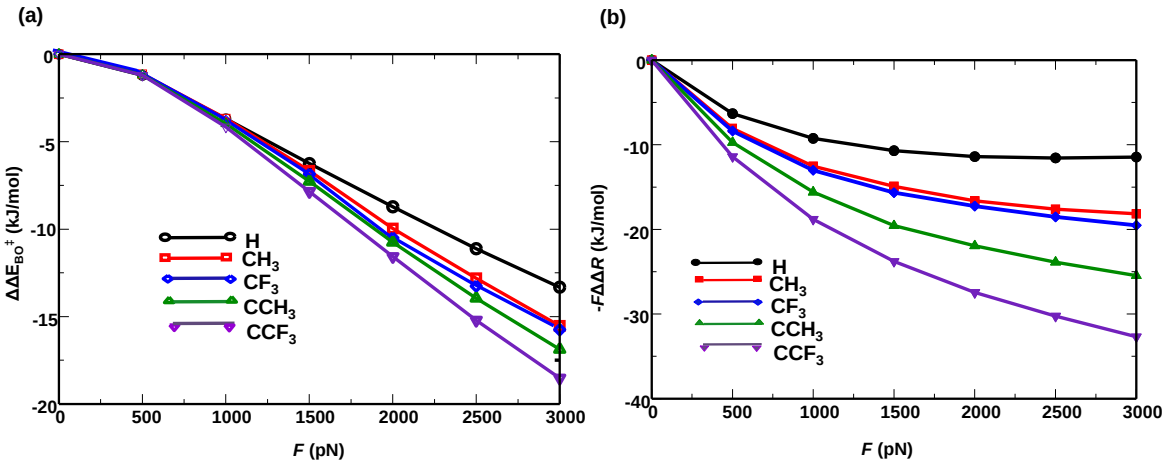

Figure 5-6. Contributions of the **(a)** Born-Oppenheimer energy and **(b)** mechanical work components to the changes in $\Delta\Delta E^{\ddagger}$ with F. The data indicate that $\Delta\Delta E_{BO}^{\ddagger}$ and $-F\Delta\Delta R$ decreased with F for all substituents. Increasing the sterics of the substituent resulted in an increase in magnitude of $\Delta\Delta E_{BO}^{\ddagger}$ and $-F\Delta\Delta R$ for all values of F.

The data shown in Figure 5-6 suggests that the mechanical work contribution to the mechanical activation of reaction **R1** was greater than contributions from the changes in the Born-Oppenheimer energy as the sterics of the substituent was increased. The mechanical work contribution can be interpreted from the changes in R with F in the reactant complex and TS structures along with the force-dependent values of ΔR. The force-induced changes in R and ΔR are illustrated in Figures 5-7a and 5-7b respectively. The data shown in Figure 5-7a indicate that R increased with F in both the complex and the TS with R in the complex being greater than R in the TS for all values of F. It was found that the value of R in the complex and the TS decreased with increased sterics of the

substituent. The decrease in *R* with the sterics of the substituent was more signifcant in the complex compared to the TS. Furthermore, the force-dependent values of *R* in the TS were nearly identical for all substituents.

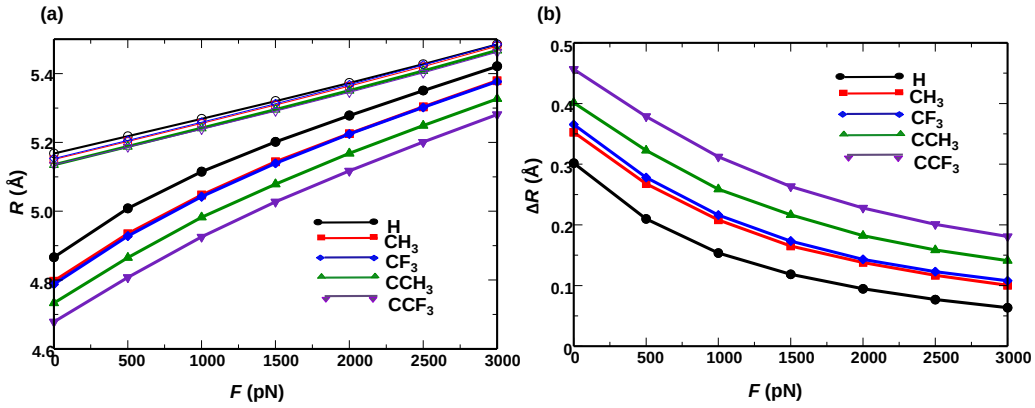

Figure 5-7. (a) Changes in pulling point distance, *R*, with *F* for the complex (closed symbols) and for the TS (open symbols) and **(b)** Δ*R* versus *F* for reaction **R1**. The data indicate that *R* in the complex and TS increased with *F* and Δ*R* decreased with *F* for all substituents.

The data shown in Figure 5-7b indicate that Δ*R* decreased with *F* for all substituents. The value of Δ*R* increased as the sterics of the substituent was increased for all values of *F*. The increase in Δ*R* with the sterics of the substituent suggests that the more sterically hindered substituents increased the mechanical work performed on the system according to Eqs. (5.2) and (5.3).

5.2.2. R2 Diels-Alder reaction of ethylene and substituted cyclohexadiene

The force-dependent $\Delta E^{\ddagger}$'s for reaction **R2** shown in Figure 5-3b exhibited a similar behaviour as the $\Delta E^{\ddagger}$'s for reaction **R1**, in which the $\Delta E^{\ddagger}$'s decreased with *F* for all substituents. In contrast to reaction **R1**, the force-dependent $\Delta E^{\ddagger}$'s were lower when X = CH_3 and CF_3 than X= H. In both reactions **R1** and **R2**, the highest $\Delta E^{\ddagger}$'s were obtained for

the most sterically hindered substituent, X = $C(CF_3)_3$. To examine the steric effect in reaction **R2**, the changes in the angle between the sp^2 carbon atoms in the ring and the carbon-substituent bond, θ, with the sterics of the substituent in the complex and TS were evaluated. The structures of the complex and the TS for reaction **R2** along with the changes in θ with substituent size are shown in Figures 5-8a and 5-8b respectively.

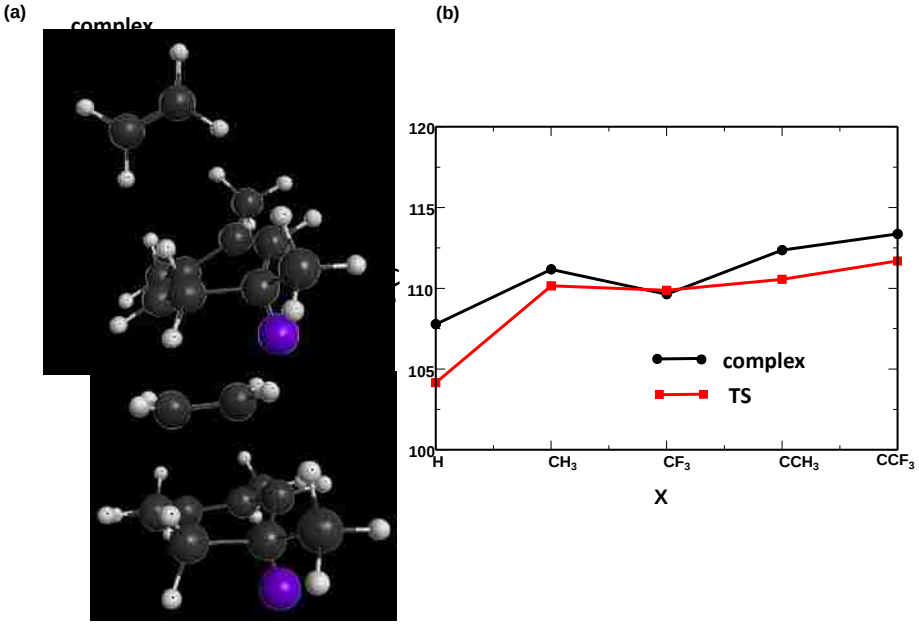

Figure 5-8 (a) Structures of the reactant complex and TS for reaction **R2**. The black, white, and purple spheres denote carbon atoms, hydrogen atoms, and substituents respectively. The angle, θ, was defined between the sp^2 carbon atoms in the ring and the carbon-substituent bond. **(b)** Changes in θ with substituent, X = H, CH_3, CF_3, $C(CH_3)_3$, and $C(CF_3)_3$. The data indicate that θ increased as the sterics of the substituent increased.

The structures of the complex and TS shown in Figure 5-8a involved the substituent added to the same carbon atom as the methyl group. Another configuration involved the substituent added to the neighbouring carbon atom as illustrated in Figure 5-9a. In both configurations, the dienophile was added to the top and bottom of the diene as shown in Figures 5-9b and 5-9c respectively. The configuration that yielded the lowest zero-F $\Delta E^{\ddagger}$ was used to calculate the force-dependent $\Delta E^{\ddagger}$'s in Figure 5-3b.

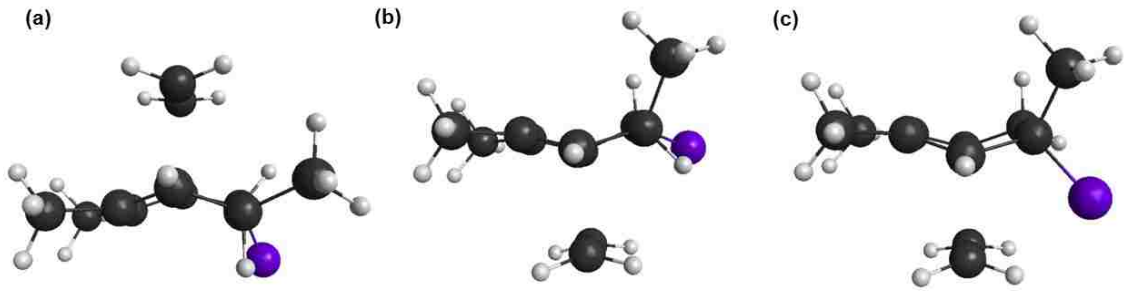

Figure 5-9. Configurations of the TS in reaction **R2**, in which ethylene was added to substituted cyclohexadiene from **(a)** the top with the substituent attached to the neighbouring carbon atom of the methyl group, **(b)** the bottom with the substituent attached to the neighbouring carbon of the methyl group, and **(c)** the bottom with substituent attached to the same carbon atom as the methyl group. The black, white, and purple spheres denote carbon atoms, hydrogen atoms, and the substituent respectively.

The data shown in Figure 5-8b indicate that θ increased in the reactant complex and the TS as the sterics of the substituent was increased from X = H to X = $C(CF_3)_3$ in a similar manner as the data for reaction **R1** (Fig. 5-4b). The steric effect of the substituent on the mechanical activation of reaction **R2** was further investigated by evaluating $\Delta\Delta E^{\ddagger}$, as a function of F shown in Figure 5-10.

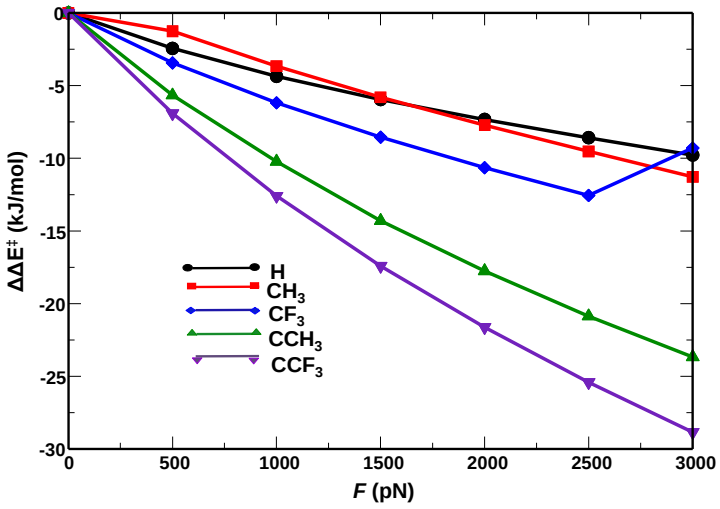

Figure 5-10. $\Delta\Delta E^{\ddagger}$ versus F for reaction **R2**. The data indicate that increasing the sterics of the substituent resulted in a greater reduction in the $\Delta\Delta E^{\ddagger}$ with F.

The data in Figure 5-10 indicate that increasing the sterics of the substituent led to a greater reduction in $\Delta\Delta E^{\ddagger}$ with F, which is consistent with the data obtained for reaction **R1** (Fig. 5.5). In the case of X = CF_3, an increase in $\Delta\Delta E^{\ddagger}$ was observed when F was increased from 2500 pN to 3000 pN. The results obtained for the force-dependent $\Delta E^{\ddagger}$'s and $\Delta\Delta E^{\ddagger}$'s were further interpreted by evaluating the changes in the Born-Oppenheimer energy and the changes in mechanical work that occurred under mechanochemical conditions. The changes in $\Delta\Delta E_{BO}{}^{\ddagger}$ and $-F\Delta\Delta R$ with F are shown in Figure 5-11.

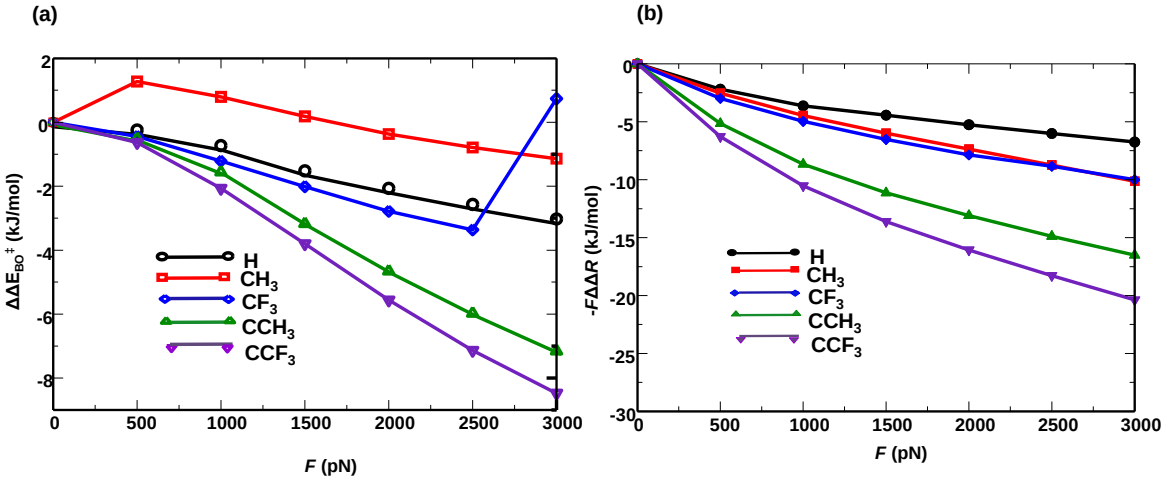

Figure 5-11. Contributions of the **(a)** Born-Oppenheimer energy and **(b)** mechanical work components to the changes in $\Delta\Delta E^{\ddagger}$ with F. The magnitude of both $\Delta\Delta E_{BO}{}^{\ddagger}$ and $-F\Delta\Delta R$ increased with increased sterics of the substituent.

The data shown in Figure 5-11a indicate that $\Delta\Delta E_{BO}{}^{\ddagger}$ increased in magnitude with F when X = H, CH_3, $C(CH_3)_3$, and $C(CF_3)_3$. In the case of X = CF_3, a sudden jump in $\Delta\Delta E_{BO}{}^{\ddagger}$ was observed when F was increased from 2500 pN to 3000 pN. In fact, the value of $\Delta\Delta E_{BO}{}^{\ddagger}$ adopted a positive value when F = 3000 pN. The adoption of a positive value of $\Delta\Delta E_{BO}{}^{\ddagger}$ when F = 3000 pN was consistent with the force-dependent $\Delta E^{\ddagger}$'s and $\Delta\Delta E^{\ddagger}$'s shown in Figures 5-3b and 5-10, which also adopted positive values when F was increased

from 2500 pN to 3000 pN. The data shown in Figure 5-11b indicate that $-F\Delta\Delta R$ increased in magnitude with F for all substituents. The value of $-F\Delta\Delta R$ did not increase as F was increased from 2500 pN to 3000 pN.

Collectively, the data shown in Figure 5-11 indicate that the increase in $\Delta E^{\ddagger}$ was entirely due to the change in the Born-Oppenheimer energy as F was increased from 2500 pN to 3000 pN. The significant increase in $\Delta\Delta E_{BO}^{\ddagger}$ can be attributed to a change in structure of the reactant complex or TS. The optimized structures of the reactant complex and the TS at F = 2500 pN and F = 3000 pN are shown in Figure 5-12. The conformation of the complex was altered while the TS structure remained relatively unaffected as F was increased from 2500 pN to 3000 pN.

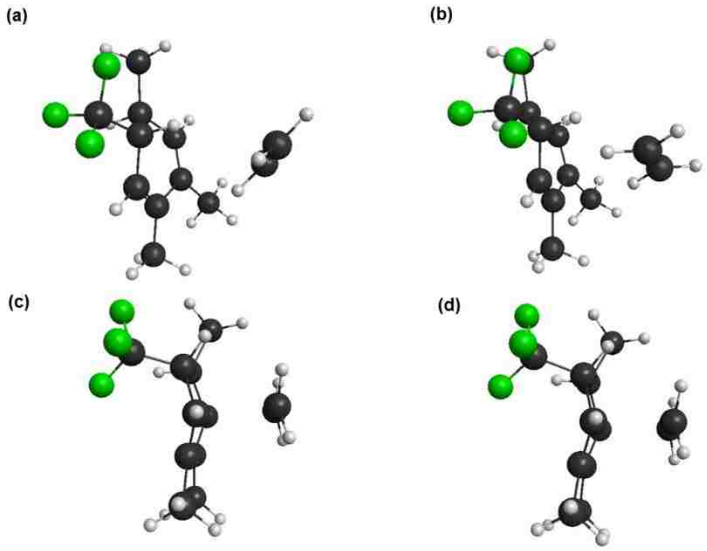

Figure 5-12. Optimized structures of the reactant complex in reaction **R2** when X = CF_3 at **(a)** F=2500 pN and **(b)** F=3000 and the TS at **(c)** F=2500 pN and **(d)** F=3000 pN. The black, white, and green spheres denote carbon, hydrogen, and fluorine atoms respectively.

The data shown in Figure 5-11 indicate that the force-dependent values of $-F\Delta\Delta R$ and $\Delta\Delta E_{BO}^{\ddagger}$ increased in magnitude with sterics of the substituent for all values of F. The mechanical work contribution to the activation of reaction **R2** was greater than the contribution from the changes in the Born-Oppenheimer energy as the sterics of the substituent was increased. The mechanical work contribution to the activation of reaction **R2** was further investigated by evaluating the changes in R with F in the reactant and TS structures as well as the force-dependent values of ΔR. The changes in R in the reactant and TS as well as ΔR with F are shown in Figures 5-13a and 5-13b respectively.

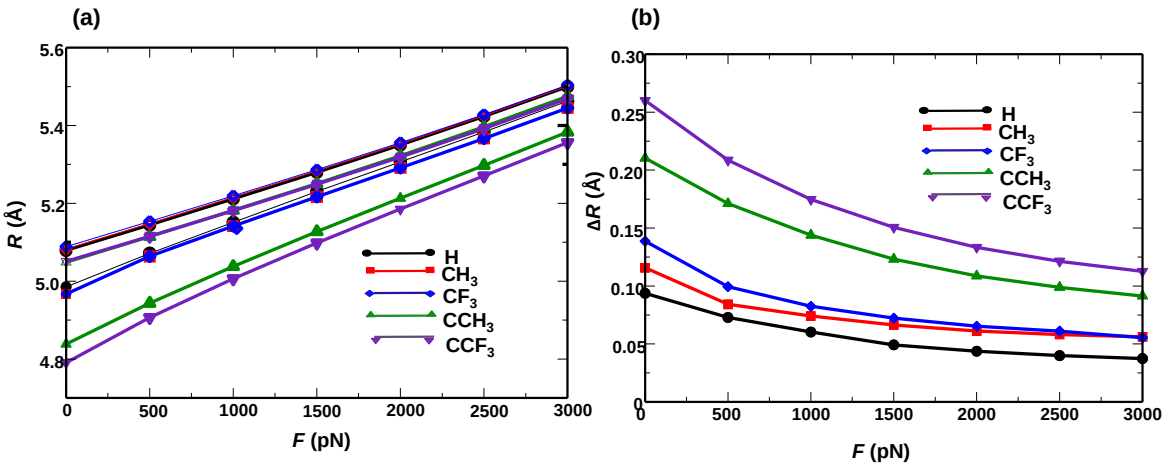

Figure 5-13. (a) Changes in R with F for the complex (closed symbols) and for the TS (open symbols) and **(b)** ΔR versus F for reaction **R2.** The value of R in the complex and the TS increased with F and ΔR decreased with F for all substituents.

The data shown in Figure 5-13a indicate that R increased with F in the reactant complex and TS for all substituents. The value of R decreased with increased sterics of the substituent in both the reactant complex and the TS. The reduction in R with increased sterics of the substituent was more significant in the reactant complex than the TS. The data shown in Figure 5-13b indicate that ΔR decreased with F for all substituents. As in

the case of reaction **R1**, the value of ΔR increased as the sterics of the substituent was increased for all values of F. The larger value of ΔR suggested a greater amount of mechanical work performed on the system, which led to a reduction in $\Delta E^{\ddagger}$ according to Eqs. (5.2) and (5.3). As such, the more sterically hindered substituents in reaction **R2** resulted in a greater amount of mechanical work performed on the system.

5.2.3. R3 Diels-Alder reaction of 1,3-butadiene and substituted cyclopentene

The steric effect in reaction **R3** was investigated by adding substituents of varying size to substituted cyclopentene. Four different configurations were considered, in which 1,3-butadiene was added to substituted cyclopentene from the left or right in an *exo* or *endo* arrangement. The four configurations of the TS are shown in Figure 5-14. The configuration that resulted in the lowest zero-F $\Delta E^{\ddagger}$ was used to calculated the force-dependent $\Delta E^{\ddagger}$'s shown in Figure 5-3c.

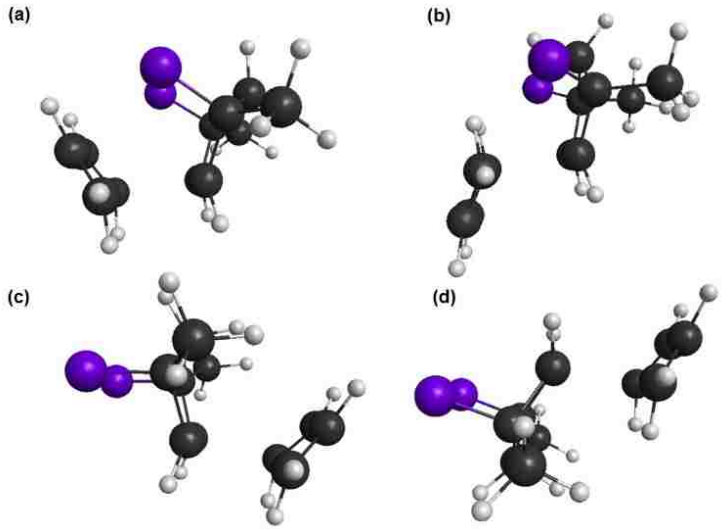

Figure 5-14. Configurations of the TS in reaction **R3**, in which 1,3-butadiene was added to substituted cyclopentene from **(a)** left of the diene in an *endo* configuration, **(b)** left of the diene in an *exo* configuration, and **(c)** right of the diene in an *endo* configuration, and **(d)** right of the diene in an *exo* configuration. The black, white, and purple spheres denote carbon atoms, hydrogen atoms, and the substituent respectively.

The interaction of the substituents with the cyclopentene ring was examined by calculating the changes in the angle between the sp^2 carbon atoms in the ring and the carbon-substituent bond, θ, with the sterics of the substituent in the complex and TS. The structures of the complex and the TS for reaction **R3** along with the changes in θ with substituent size are shown in Figures 5-15a and 5-15b respectively. The data shown in Figure 5-15b indicate that θ increased in the reactant complex and the TS as the sterics of the substituent was increased from X = H to X = $C(CF_3)_3$ in a similar manner as the data for reactions **R1** and **R2**.

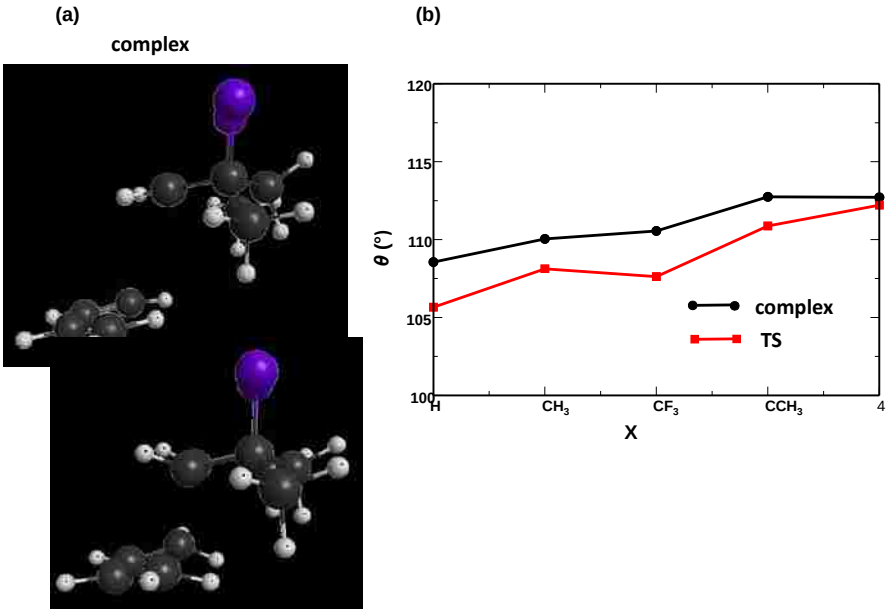

Figures 5-15. (a) Structures of the reactant complex and TS for reaction **R3**. The black, white, and purple spheres denote carbon atoms, hydrogen atoms, and substituents respectively. The angle, θ, is defined between the sp^2 carbon atoms in the ring and the carbon-substituent bond. **(b)** Changes in θ with substituent, X = H, CH_3, CF_3, $C(CH_3)_3$, and $C(CF_3)_3$. The data indicate that θ increased as the sterics of the substituent increased.

The $\Delta E^{\ddagger}$'s for reaction **R3** shown in Figure 5-3c remained relatively unaffected with increased F for all substituents. The force-dependent $\Delta E^{\ddagger}$'s increased with increased sterics of the substituent. The steric effect of the substituent on the mechanical activation of reaction **R3** was further investigated by evaluating the changes in $\Delta\Delta E^{\ddagger}$ with F . The resulting plot of $\Delta\Delta E^{\ddagger}$ versus F is shown in Figure 5-16 and appears qualitatively different than the force-dependent $\Delta\Delta E^{\ddagger}$'s for reactions **R1** and **R2**. The data for reactions **R1** and **R2** shown in Figures 5-5 and 5-10 respectively indicate that $\Delta\Delta E^{\ddagger}$ decreased with F for all substituents. The data for reaction **R3** indicate that the $\Delta\Delta E^{\ddagger}$'s decreased for all values of F when X = H or X = CH_3. In the case of X = CF_3, the $\Delta\Delta E^{\ddagger}$'s decreased from F = 0 pN to F = 2000 pN and then increased from F = 2500 pN to F = 3000 pN. The addition of the more sterically hindered substituents, X = $C(CH_3)_3$ and X = $C(CF_3)_3$, yielded values of

$\Delta\Delta E^{\ddagger}$ that remained relatively unaffected from F = 0 pN to F = 1500 pN. At values of F > 1500 pN, the $\Delta\Delta E^{\ddagger}$'s decreased when X = $C(CH_3)_3$ and slightly increased when X = $C(CF_3)_3$.

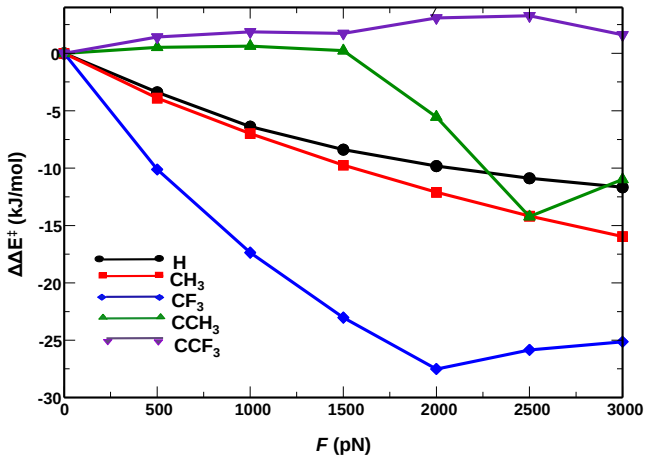

Figure 5-16. $\Delta\Delta E^{\ddagger}$ versus F for reaction **R3**. The data shows that varying the sterics of the substituents affected the force-dependent $\Delta\Delta E^{\ddagger}$'s in different ways.

The discrepancies between the force-dependent $\Delta\Delta E^{\ddagger}$'s with varying substituents were investigated by evaluating the changes in $\Delta\Delta E_{BO}^{\ddagger}$ and $-F\Delta\Delta R$ with F as shown in Figures 5-17a and 5-17b respectively. The data shown in Figure 5-17a indicate that $\Delta\Delta E_{BO}^{\ddagger}$ slightly decreased with F when X = H, CH_3, and CF_3. In the case of X = $C(CH_3)_3$, the $\Delta\Delta E_{BO}^{\ddagger}$'s slightly increased from F = 0 pN to F = 1500 pN. A large increase, approximately 30 kJ/mol, in $\Delta\Delta E_{BO}^{\ddagger}$ was observed when F was increased from 1500 pN to 2000 pN. The $\Delta\Delta E_{BO}^{\ddagger}$'s decreased when F > 2000pN.

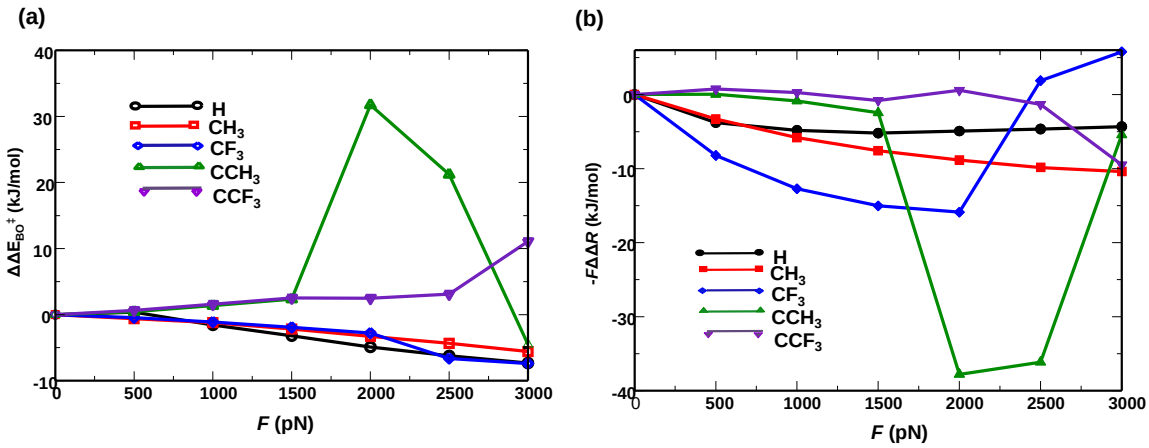

Figure 5-17. Contributions of the **(a)** Born-Oppenheimer energy and **(b)** mechanical work components to the changes in $\Delta\Delta E^{\ddagger}$ with F. The data indicate that varying the sterics of the substituent affected the force-dependent $\Delta\Delta E_{BO}{}^{\ddagger}$ and $-F\Delta\Delta R$ terms in different ways.

The large increase in $\Delta\Delta E_{BO}{}^{\ddagger}$ in the case of X = $C(CH_3)_3$ from F = 1500 pN to F = 2000 pN can be attributed to a change in a structure of the TS as shown in Figure 5-18a. Specifically, the structural change in the TS involved a rotation around the carbon-substituent bond. The rotation around the carbon-substituent bond was not as apparent in the reactant complex as illustrated in the structures in Figure 5-18b. The structural change in the TS and the reactant complex were quantified by evaluating the changes in torsion associated with the rotation, φ, around the carbon-substituent bond. The changes in φ with F in both the reactant complex and TS are shown in Figure 5-18c and were consistent with the structures illustrated in Figures 5-18a and 5-18b, in which the rotation around the carbon-substituent bond was affected more significantly in the TS than the complex when F was increased from 1500 pN to 2000 pN. The effect of applied F on the rotation around the carbon-substituent bond in the TS was evident from the significant decrease in φ from F = 2500 pN to F =3000 pN. An increase in $\Delta\Delta E_{BO}{}^{\ddagger}$ was also observed in the case of X = $C(CF_3)_3$ from F = 2500 pN to F = 3000 pN. The increase in $\Delta\Delta E_{BO}{}^{\ddagger}$ can be attributed to

the structural change in the reactant complex in a similar manner to reaction **R2** when X = CF_3 as illustrated in Figure 5-12.

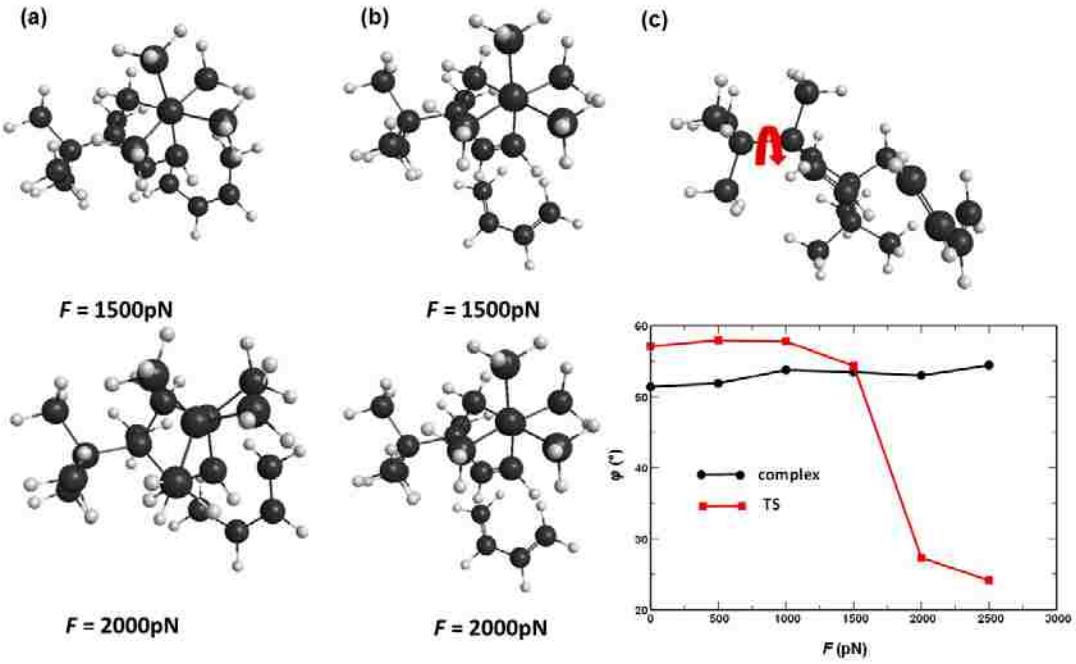

Figure 5-18. Optimized structures for reaction **R3** when X = CH_3 of the **(a)** complex and **(b)** TS at F=1500 pN and F=2000 pN from the perspective of the carbon-substituent bond. The black and white spheres denote carbon and hydrogen atoms respectively. **(c)** Changes in the torsion associated with the rotation around the carbon-substituent bond, φ, with F in the complex and the TS. The data indicate that φ remains relatively unaffected with F in the complex and significantly decreased from F=1500 pN to F =2000 pN in the TS.

The large increase in $\Delta\Delta E_{BO}^{\ddagger}$ when X = $C(CH_3)_3$ from F=1500 pN to F=2000 pN was compensated by the $-F\Delta\Delta R$ term adopting large negative values as shown in Figure 5-17b. As such, the overall $\Delta E^{\ddagger}$'s in Figure 5-3c remained relatively unaffected with F. For the substituents X = H, CH_3, $C(CF_3)_3$, $-F\Delta\Delta R$ slightly increased in magnitude as F was increased from 0 pN to 2500 pN. A more signifcant increase in magnitude of $-F\Delta\Delta R$ was observed as F was increased from 2500 pN to 3000 pN when X = CCF_3. The adoption of larger negative values of $-F\Delta\Delta R$ from F = 2500 pN to F = 3000 pN was compensated

by large positive values of $\Delta\Delta E_{BO}^{\ddagger}$ when F was increased from 2500 pN to 3000 pN as shown in Figure 5-17a. In the case of X = CF_3, $-F\Delta\Delta R$ became slightly more negative from F = 0 pN to F = 2000 pN prior to increasing to adopt positive values from F = 2000 pN to F = 2500 pN. The adoption of positive $-F\Delta\Delta R$ values from F = 2000 pN to F = 2500 pN can be attributed to a structural change in the reactant complex in a similar manner as in the case of X = CH_3 illustrated in Figure 5-18a. The increase in $-F\Delta\Delta R$ was not compensated by a significant decrease in $\Delta\Delta E_{BO}^{\ddagger}$ as illustrated in Figure 5-17a. As such, the increase in $\Delta E^{\ddagger}$'s and $\Delta E^{\ddagger}$'s when X = CF_3 from F = 2000 pN to F = 2500pN in Figures 5-3c and 5-16 respectively can be attributed entirely to the contribution of the changes in mechanical work performed on the system.

The contributions from the changes in mechanical work performed on the system were further investigated by evaluating the changes in R with F in the reactant complex and TS structures as well as the force-dependent values of ΔR. The changes in R in the complex and TS as well as ΔR with F are shown in Figures 5-19a and 5-19b respectively.

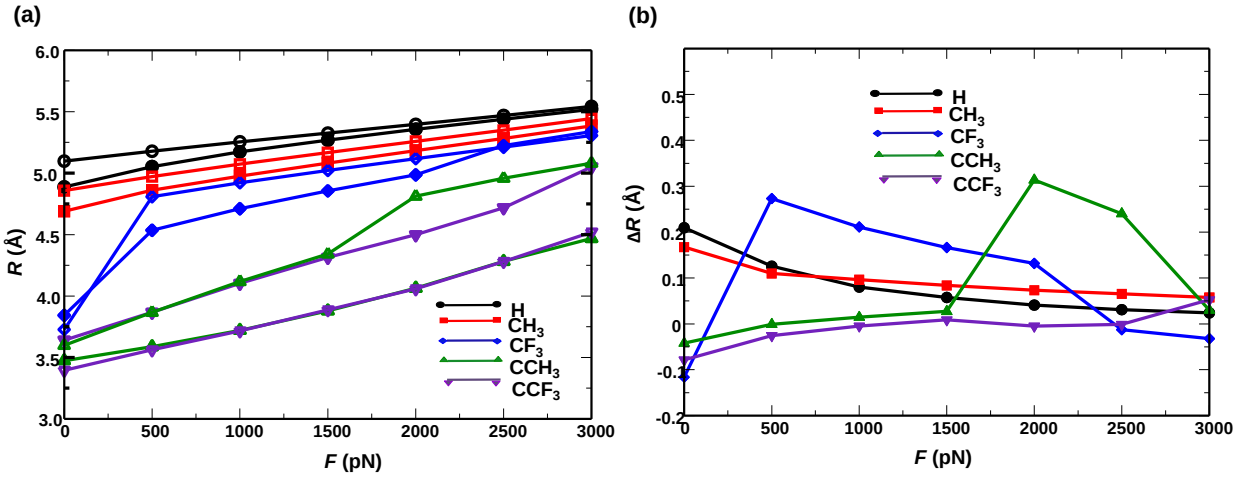

Figure 5-19. (a) Changes in R with F for the complex (closed symbols) and for the TS (open symbols) and **(b)** ΔR versus F for reaction **R3.** The value of R in the complex and the TS increased with F for all substituents. Varying the sterics of the substituents affects the force-dependent ΔR values in different ways.

The data shown in Figure 5-19a indicate that R increased with F in the reactant complex and the TS for all substituents. The value of R decreased with increased sterics of the substituent in the reactant complex and TS for all substituents. The reduction in R was more significant in the complex than the TS. The data shown in Figure 5-19b indicate that ΔR slightly decreased with F when X = H and CH_3 and slightly increased with F when X = CCF_3. In the case of X = CF_3, ΔR increased from F = 0 pN to F = 500 pN and then decreased when F > 500 pN. An increase in ΔR from F = 0 pN to F = 500 pN suggested an increase in mechanical work performed on the system according to Eq. (5.2). In the case of X = CCH_3, ΔR slightly decreased from F = 0 pN to F = 1500 pN. As F was increased from 1500 pN to 2000 pN, a more significant increase in ΔR was observed. The ΔR term decreased at values of F > 2000pN. The sudden increase in ΔR from F = 1500 pN to F = 2000 pN was consistent with $-F\Delta\Delta R$ values increasing in magnitude and becoming more negative as illustrated in Figure 5-17b. Similarly, the decrease in ΔR at values of F > 2000 pN can be attributed to the $-F\Delta\Delta R$ values decreasing in magnitude and becoming more positive.

5.2.4. R4 Diels-Alder reaction of 1,3-butadiene and substituted cyclohexene

As in the case of reaction **R3**, four possible configurations resulted from the addition of substituents of varying size to substituted cyclohexene. These configurations are shown in Figure 5-20 and involved 1,3-butadiene adding from the left or right in an *exo* or *endo* manner. The configuration that resulted in the lowest zero-F $\Delta E^{\ddagger}$ was used to calculate the force-dependent $\Delta E^{\ddagger}$'s in Figure 5-3d. The interaction of the substituents

with the cyclohexene ring was examined by calculating the changes in the angle between the sp^2 carbon atoms in the ring and the carbon-substituent bond, θ, with the sterics of the substituent in the complex and TS. The structures of the complex and the TS for reaction **R4** along with the changes in θ with substituent size are shown in Figures 5-21a and 5-21b respectively. The data shown in Figure 5-21b indicate that θ increased in the reactant complex and the TS as the sterics of the substituent was increased from X = H to X = $C(CF_3)_3$ in a similar manner as the data for reactions **R1, R2**, and **R3**.

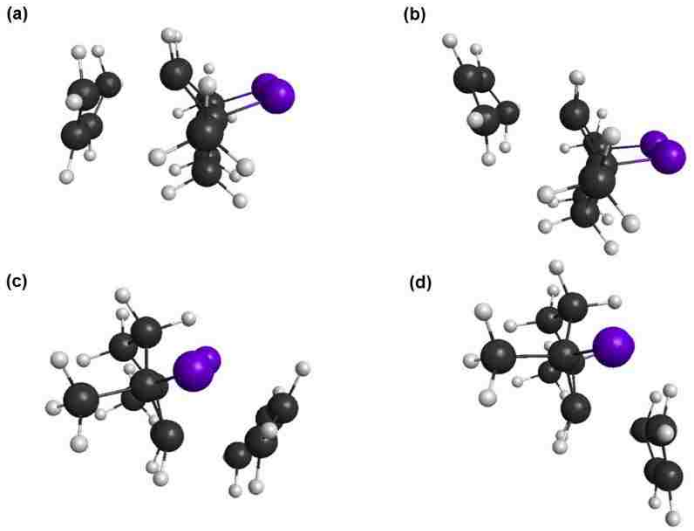

Figure 5-20. Configurations of the TS in reaction **R4**, in which 1,3-butadiene was added to substituted cyclohexene from **(a)** left of the diene in an *endo* configuration, **(b)** left of the diene in an *exo* configuration, and **(c)** right of the diene in an *endo* configuration, and **(d)** right of the diene in an *exo* configuration. The black, white, and purple spheres denote carbon atoms, hydrogen atoms, and the substituent respectively.

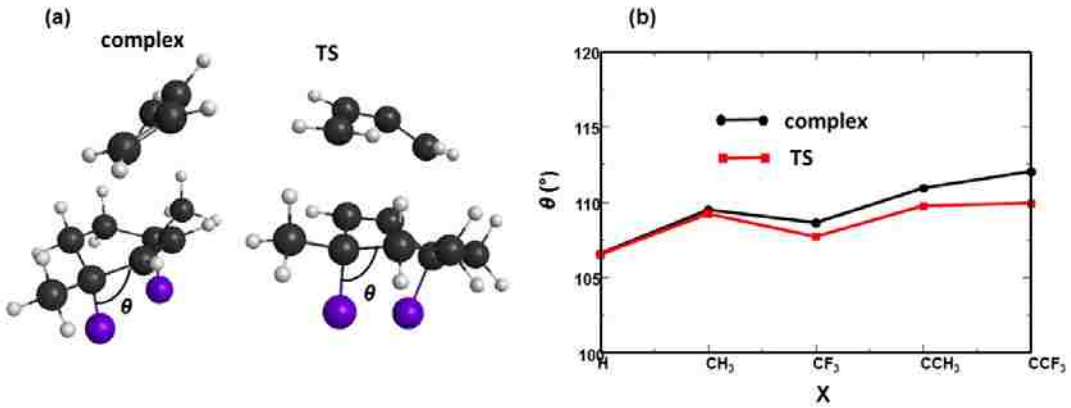

Figure 5-21. (a) Structures of the reactant complex and TS for reaction **R4**. The black, white, and purple spheres denote carbon atoms, hydrogen atoms, and substituents respectively. The angle, θ, is defined between the sp^2 carbon atoms in the ring and the carbon-substituent bond. **(b)** Changes in θ with substituent, X = H, CH_3, CF_3, CCH_3, and CCF_3. The data indicate that θ increased as the sterics of the substituent increased.

The force-dependent $\Delta E^{\ddagger}$'s shown for reaction **R4** in Figure 5-3d increased with increased sterics of the substituent. The $\Delta E^{\ddagger}$'s decreased with F when X = CH_3, $C(CH_3)_3$, and $C(CF_3)_3$. In the case of X = CF_3, the $\Delta E^{\ddagger}$'s decreased from F = 0 pN to F = 2000 pN and then slightly increased as F was increased from 2000 pN to 2500 pN. The $\Delta E^{\ddagger}$'s remained relatively unaffected with F when X = H. The steric effect of the substituent on the mechanical activation of reaction **R4** was further investigated by evaluating the changes in $\Delta\Delta E^{\ddagger}$ with F. The resulting plot of $\Delta\Delta E^{\ddagger}$ versus F is shown in Figure 5-22 and indicate that $\Delta\Delta E^{\ddagger}$ increased in magnitude with F for all substituents. The force-dependent $\Delta\Delta E^{\ddagger}$'s were the largest in magnitude when X = CH_3. Similar to the plot of $\Delta E^{\ddagger}$ versus F shown in Figure 5-3d, the $\Delta\Delta E^{\ddagger}$'s increased from F = 2000 pN to F = 2500 pN when X = CF_3.

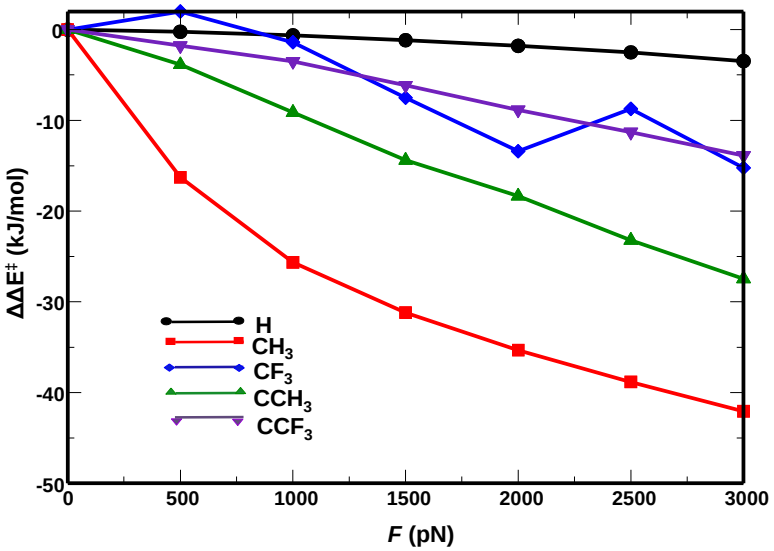

Figure 5-22. $\Delta\Delta E^{\ddagger}$ versus F for reaction **R4**. The data indicate that $\Delta\Delta E^{\ddagger}$ decreased with F for all substituents.

The changes in $\Delta\Delta E^{\ddagger}$ with F were further investigated by evaluating the changes in $\Delta\Delta E_{BO}{}^{\ddagger}$ and $-F\Delta\Delta R$ under mechanochemical conditions as shown in Figure 5-23. The data indicate that the sterics of the substituent affected the force-dependent $\Delta\Delta E_{BO}{}^{\ddagger}$'s in different ways. In the case of X = H, $C(CH_3)_3$, and $C(CF_3)_3$, $\Delta\Delta E_{BO}{}^{\ddagger}$ remained relatively unaffected with F. The $\Delta\Delta E_{BO}{}^{\ddagger}$'s decreased with F when X = CH_3 and increased when X = CF_3. A signifcant increase in the $\Delta\Delta E_{BO}{}^{\ddagger}$'s was observed when X = CF_3 as F was increased 2000 pN to 2500 pN. This increase in the $\Delta\Delta E_{BO}{}^{\ddagger}$'s can be attributed to a change in structure of the reactant complex as shown in Figure 5-24.

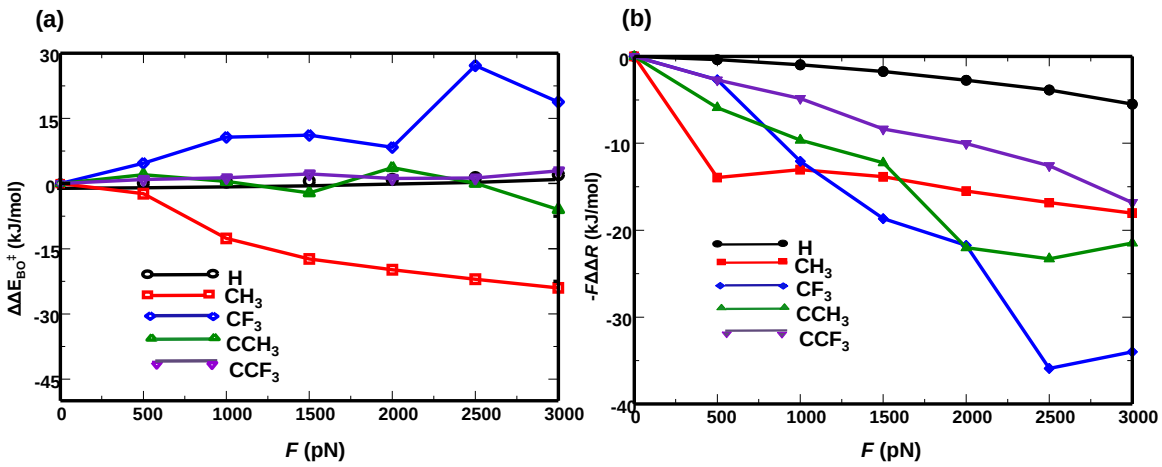

Figure 5-23. Contributions of the **(a)** Born-Oppenheimer energy and **(b)** mechanical work components to the changes in $\Delta\Delta E^{\ddagger}$ with F. The data indicate that varying the sterics of the substituent affected the force-dependent $\Delta\Delta E_{BO}{}^{\ddagger}$ and $-F\Delta\Delta R$ terms in different ways.

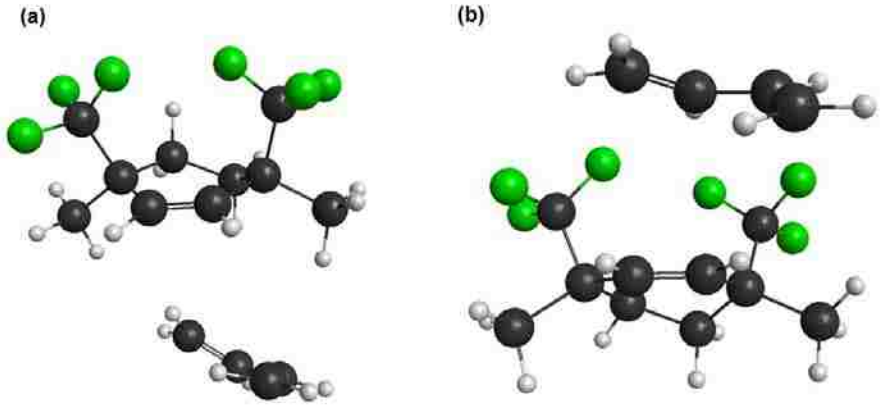

Figure 5-24. Optimized structures of the reactant complex in reaction **R4** when X=CF_3 at **(a)** F = 2500 pN and **(b)** F = 3000 pN. The black, white, and green spheres denote carbon, hydrogen, and fluorine atoms respectively.

The$-F\Delta\Delta R$ term increased in magnitude with F for all substituents with the greatest increase in $-F\Delta\Delta R$ observed when X = CF_3. The adoption of large negative values of $-F\Delta\Delta R$ at higher values of F compensated for the adoption of $\Delta\Delta E_{BO}{}^{\ddagger}$ positive values in the case of X = CF_3 as illustrated in Figure 5-23a. In the case of X = CH_3, $-F\Delta\Delta R$ was larger in magnitude than $\Delta\Delta E_{BO}{}^{\ddagger}$ from F = 500 pN to F = 1000 pN and smaller in magnitude at values of F > 3000 pN. The contributions from the mechanical work

performed on the system were further investigated by evaluating the changes in R in the reactant complex and TS as well as the force-dependent changes in ΔR. The changes in R and ΔR with F are shown in Figures 5-25a and 5-25b respectively.

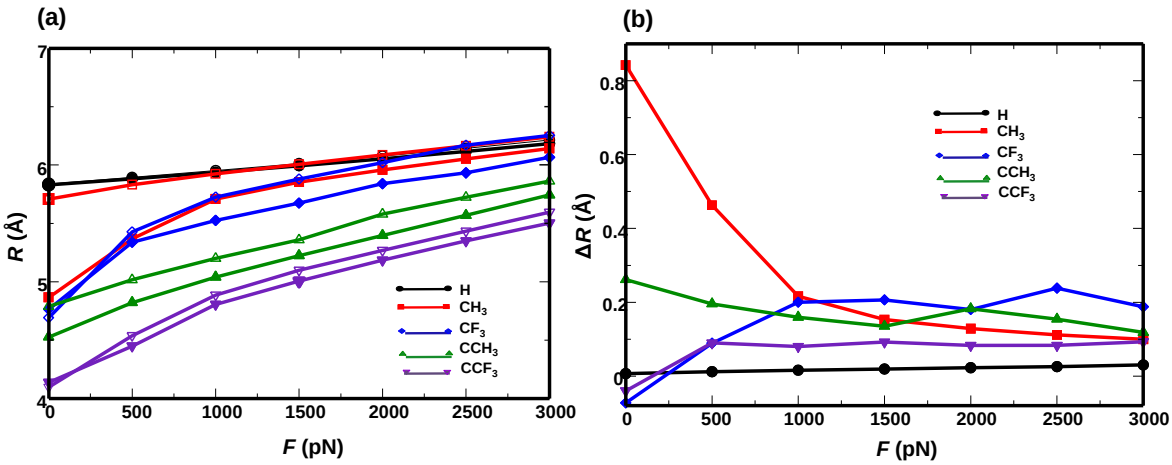

Figure 5-25. (a) Changes in R with F in the complex (closed symbols) and for the TS (open symbols) and **(b)** ΔR versus F for reaction **R4.** The value of R in the complex and the TS increased with F. Varying the sterics of the substituent affects the force-dependent values of ΔR in different ways.

The data shown in Figure 5-25a indicate that R increased with F in the complex and in the TS for all substituents. The value of R decreased with increased sterics of the substituent in both the complex and TS. The data shown in Figure 5-25b indicate that ΔR remained relatively unaffected with F when X = H. An increase in ΔR was observed from F = 0 pN to F = 500 pN when X = $C(CF_3)_3$. However, ΔR remained relatively unaffected at values of F > 500 pN. In the case of X = CF_3, ΔR increased from F = 0 pN to F = 1000 pN, remained fairly constant from F = 1000 pN to F = 2000 pN, and increased from F = 2000 pN to F = 3000 pN. In contrast, ΔR decreased from F = 0 pN to F = 1000 pN, remained fairly constant from F = 1000 pN to F = 2000 pN, and then decreased from F = 2000 pN to F = 3000 pN. The force-dependent values of $-F\Delta\Delta R$ shown in Figure 5-23b

also exhibited contrasting results in the cases of X = CF_3 and X = $C(CH_3)_3$. In the case of X = CH_3, ΔR decreased with F. The reduction in ΔR with F was more significant at low forces (F < 1000 pN), which is consistent with the force-dependent values of $-F\Delta\Delta R$ shown in Figure 5-23b.

5.3 Summary

Overall, the results demonstrate that the sterics of the substituent can influence the mechanical activation of reactions by affecting the contributions from the changes in the Born-Oppenheimer energy and mechanical work in different ways. In the case of reaction **R1**, increasing the sterics of the substituent resulted in greater reductions in $\Delta E^{\ddagger}$ and $\Delta\Delta E^{\ddagger}$ under mechanochemical conditions. This reduction in $\Delta\Delta E^{\ddagger}$ with F was supported by the changes in the contributions of $\Delta\Delta E_{BO}{}^{\ddagger}$ and $-F\Delta\Delta R$ with F. The data shown in Figure 5-6 indicate that increasing the sterics of the substituent increased the magnitude of $\Delta\Delta E_{BO}{}^{\ddagger}$ and $-F\Delta\Delta R$ for all values of F. The values of $-F\Delta\Delta R$ were more significantly affected with the sterics of the substituent than the values of $\Delta\Delta E_{BO}{}^{\ddagger}$. This result suggests that the mechanical activation of reaction **R1** with sterically hindered substituents was largely driven by the amount of work that was performed on the system during the course of the reaction. Furthermore, the convergence of reactant and TS structures through contributions from $\Delta\Delta E_{BO}{}^{\ddagger}$ were rendered secondary to the amount of work performed on the system for the more sterically hindered substituents. The increase in mechanical work performed on the system with sterics of the substituent was further supported by the force-dependent values of ΔR shown in Figure 5-7b, in which increasing the sterics of the substituent resulted in a larger value of ΔR under mechanochemical conditions. A larger

ΔR value corresponds to an increased mechanical work contribution on the system according to Eqs. (5.2) and (5.3). The results for reaction **R2** were similar to those obtained for reaction **R1**, in which increasing the sterics of the substituent resulted in the $\Delta\Delta E^{\ddagger}$, $\Delta\Delta E_{BO}{}^{\ddagger}$, and $-F\Delta\Delta R$ terms becoming more negative with F. In reaction **R2**, however, an increase in $\Delta\Delta E^{\ddagger}$ and $\Delta\Delta E_{BO}{}^{\ddagger}$ was observed from F = 2500 pN to F = 3000 pN when X = CF_3. The sudden increase in $\Delta\Delta E^{\ddagger}$ and $\Delta\Delta E_{BO}{}^{\ddagger}$ was attributed to a change in structure of the reactant complex illustrated in Figure 5-12.

For reaction **R3**, it was found that increasing the sterics of the substituent did not result in a greater mechanical activation. In fact, the substituent X = CF_3, which is intermediate in terms of sterics for all the substituents considered, resulted in the greatest reduction in $\Delta\Delta E^{\ddagger}$ with F as shown in Figure 5-16. The contributions from $-F\Delta\Delta R$ were greater than the contributions from $\Delta\Delta E_{BO}{}^{\ddagger}$ to the mechanical activation of **R3** when X = CF_3 (Fig. 5-17). In the case of X = CCH_3, which is more sterically hindered than CF_3, the contributions from $-F\Delta\Delta R$ were greater than CF_3 at values of $F \geq$ 2000pN. The changes in ΔR with F shown in Figure 5-19b were consistent with the force-dependent values of $-F\Delta\Delta R$, in which ΔR was the largest from F = 500 pN to F = 1500 pN when X = CF_3 and from F = 2000 pN to F = 3000 pN when X = $C(CH_3)_3$. The adoption of large negative values of $-F\Delta\Delta R$ in CCH_3 was compensated from the adoption of large positive values of $\Delta\Delta E_{BO}{}^{\ddagger}$ at values of $F \geq$ 2000pN. As such, the overall mechanical activation of reaction **R3** was greater in the case of X = CF_3 than X = $C(CH_3)_3$.

In reactions **R1**, **R2**, and **R3**, it was found that the contributions from $-F\Delta\Delta R$ were greater than the contributions from $\Delta\Delta E_{BO}{}^{\ddagger}$ for nearly all substituents. The exception occurred in reaction **R1**, in which $\Delta\Delta E_{BO}{}^{\ddagger}$ was more negative and larger in magnitude than

$-F\Delta\Delta R$ when X=H at F = 3000pN. In reaction **R4**, $-F\Delta\Delta R$ was larger in magnitude than $\Delta\Delta E_{BO}^{\ddagger}$ when X=H, CF_3, $C(CH_3)_3$, and $C(CF_3)_3$ for all values of F. In the case of X = CH_3, which resulted in the greatest reduction in $\Delta\Delta E^{\ddagger}$ with F, $-F\Delta\Delta R$ was larger in magnitude than $\Delta\Delta E_{BO}^{\ddagger}$ from F = 500 pN to F = 1000 pN and smaller in magnitude from F = 1500 pN to F = 3000 pN. This result suggests that the contributions from the changes in mechanical work are significant to the mechanical activation of reaction **R4** when X = CH_3 at low forces and the contributions from the changes in the Born-Oppenheimer energy are significant at higher forces. The changes in ΔR with F are consistent with this notion, in which ΔR is the largest when X = CH_3 in the absence of F and then significantly decreased as F was increased. The lower values of ΔR indicate less mechanical work performed on the system as described by Eqs. (5.2) and (5.3).

As a whole, the results demonstrate that varying the sterics of the substituent can influence the mechanical activation of reactions by controlling the contributions from the mechanical work performed on the system and the contributions from the changes in the Born-Oppenheimer energy. It was found that the optimal size of the substituent for increasing the mechanical work contribution depended on the nature of the reaction. In the case of reactions **R1** and **R2**, the substituent was added to the ring that acted as the diene. Increasing the sterics of the substituent resulted in larger mechanical work performed on the system, which in turn led to a lower overall reduction in $\Delta E^{\ddagger}$ under mechanochemical conditions. Meanwhile, the substituents were added to the ring that acted as the dienophile in reactions **R3** and **R4**. As such, increasing the sterics of the substituent did not lead to larger work performed on the system. The largest amount of mechanical work and reduction in $\Delta\Delta E^{\ddagger}$ with F occurred when X = CF_3 for reaction **R3.** In reaction **R4,** the

reduction in $\Delta\Delta E^{\ddagger}$ with F was most significant when X = CH_3 by the contributions from the changes in mechanical work at low forces and contributions from the changes in Born-Oppenheimer energy at higher forces.

References:

1. Beyer, M. K. The mechanical strength of a covalent bond calculated by density functional theory. *J. Chem. Phys.* **112,** 7307-7312 (2000).

2. Beyer, M. K. & Clausen-Schaumann, H. Mechanochemistry: the mechanical activation of covalent bonds. *Chem. Rev.* **105,** 2921–2948 (2005).

3. Ribas-Arino, J., Shiga, M. & Marx, D. Mechanochemical transduction of externally applied forces to mechanophores. *J. Am. Chem. Soc.* **132,** 10609–10614 (2010).

4. Ribas-Arino, J., Shiga, M. & Marx, D. Understanding covalent mechanochemistry. *Angew. Chem. Int. Ed.* **48,** 4190–4193 (2009).

5. Kochhar, G. S. & Mosey, N. J. Differences in the Abilities to Mechanically Eliminate Activation Energies for Unimolecular and Bimolecular Reactions. *Sci. Rep.* **6,** 23059-1-9 (2016).

6. Kochhar, G. S., Bailey, A. & Mosey, N. J. Competition between orbitals and stress in mechanochemistry. *Angew. Chem. Int. Ed.* **49,** 7452–7455 (2010).

7. Ong, M. T., Leiding, J., Tao, H., Virshup, A. M. & Martínez, T. J. First principles dynamics and minimum energy pathways for mechanochemical ring opening of cyclobutene. *J. Am. Chem. Soc.* **131,** 6377–6379 (2009).

8. Huang, Z. & Boulatov, R. Chemomechanics with molecular force probes. *Pure Appl. Chem.* **82,** 931-951 (2010).

9. Tian, Y., Kucharski, T. J., Yang, Q.-Z. & Boulatov, R. Model studies of force-dependent kinetics of multi-barrier reactions. *Nat. Commun.* **4,** (2013).

10. Davis, D. A. *et al.* Force-induced activation of covalent bonds in mechanoresponsive polymeric materials. *Nature* **459,** 68–72 (2009).

11. Bailey, A. & Mosey, N. J. Prediction of reaction barriers and force-induced instabilities under mechanochemical conditions with an approximate model: a case study of the ring opening of 1,3-cyclohexadiene. *J. Chem. Phys.* **136,** 44102-1-11 (2012).

12. Hickenboth, C. R. *et al.* Biasing reaction pathways with mechanical force. *Nature* **446,** 423–427 (2007).

13. Hammond, G. S. A correlation of reaction rates. *J. Am. Chem. Soc.* **77,** 334–338 (1955).

14. Ribas-Arino, J., Shiga, M. & Marx, D. Mechanochemical Transduction of Externally Applied Forces to Mechanophores. *J. Am. Chem. Soc.* **132,** 10609–10614 (2010).

15. Potisek, S. L., Davis, D. A., Sottos, N. R., White, S. R. & Moore, J. S. Mechanophore-linked addition polymers. *J. Am. Chem. Soc.* **129,** 13808–13809 (2007).

16. Tian, Y. & Boulatov, R. Quantum-Chemical Validation of the Local Assumption of Chemomechanics for a Unimolecular Reaction. *ChemPhysChem* **13,** 2277–2281 (2012).

17. Dopieralski, P. *et al.* On the role of polymer chains in transducing external mechanical forces to benzocyclobutene mechanophores. *J. Mater. Chem.* **21,** 8309–8316 (2011).

18. Larsen, M. B. & Boydston, A. J. 'Flex-Activated' Mechanophores: Using Polymer Mechanochemistry To Direct Bond Bending Activation. *J. Am. Chem. Soc.* **135,** 8189–8192 (2013).

19. Kryger, M. J., Munaretto, A. M. & Moore, J. S. Structure–mechanochemical activity relationships for cyclobutane mechanophores. *J. Am. Chem. Soc.* **133,** 18992–18998 (2011).

20. Kean, Z. S., Niu, Z., Hewage, G. B., Rheingold, A. L. & Craig, S. L. Stress-Responsive Polymers Containing Cyclobutane Core Mechanophores: Reactivity and Mechanistic Insights. *J. Am. Chem. Soc.* **135,** 13598–13604 (2013).

21. Chen, Y. *et al.* Mechanical Activation of Mechanophore Enhanced by Strong Hydrogen Bonding Interactions. *ACS Macro Lett.* **3,** 141–145 (2014).

22. Krupička, M. & Marx, D. Disfavoring Mechanochemical Reactions by Stress-Induced Steric Hindrance. *J. Chem. Theory Comput.* **11,** 841–846 (2015).

23. Hohenberg, P. & Kohn, W. Inhomogeneous electron gas. *Phys. Rev.* **136,** B864–B871 (1964).

24. Kohn, W. & Sham, L. J. Self-consistent equations including exchange and correlation effects. *Phys. Rev.* **140,** A1133–A1138 (1965).

25. Valiev, M. *et al.* NWChem: A comprehensive and scalable open-source solution for large scale molecular simulations. *Comput. Phys. Commun.* **181,** 1477–1489 (2010).

26. Becke, A. D. Density-functional thermochemistry. III. The role of exact exchange. *J. Chem. Phys.* **98,** 5648-5652 (1993).

27. Lee, C., Yang, W. & Parr, R. G. Development of the Colle-Salvetti correlation-energy formula into a functional of the electron density. *Phys. Rev. B* **37,** 785–789 (1988).

28. Grimme, S., Antony, J., Ehrlich, S. & Krieg, H. A consistent and accurate ab initio parametrization of density functional dispersion correction (DFT-D) for the 94 elements H-Pu. *J. Chem. Phys.* **132,** 154104-1-19 (2010).

Chapter 6

Differences in the Abilities to Mechanically Eliminate Activation Energies for Unimolecular and Bimolecular Reactions

6.1 Introduction

Chapters 4 and 5 investigated the application of an external force, *F*, to two atoms or groups in a molecule termed pulling points (PPs) in a set of representative unimolecular and bimolecular reactions respectively. The reaction barriers, $\Delta E^{\ddagger}$'s, for the reactions in chapters 4 and 5 under mechanochemical conditions were calculated using the External Force is Explicitly Included (EFEI) method:[1]

$$\Delta E^{\ddagger}(F) = \Delta E^{\ddagger}_{\mathrm{BO}}(F) - F\Delta R \tag{6.1}$$

where $\Delta E^{\ddagger}_{\mathrm{BO}}(F)$ is the reaction barrier on the Born-Oppenheimer potential energy surface, ΔR is the change is distance between the PPs as the system progresses from the reactant to the transition state (TS), and $\Delta E^{\ddagger}(F)$ is the reaction barrier on the resulting force-modified potential energy surface (FMPES). Eq. (6.1) suggests that $\Delta E^{\ddagger}(F)$ is reduced if $\Delta E^{\ddagger}_{\mathrm{BO}}(F)$ is lowered and if there is a large amount of mechanical work performed on the system such that $\Delta R > 0$. The latter effect was investigated in chapter 5, in which the addition of sterically hindered substituents to Diels-Alder reactions increased the mechanical work performed on the system, and therefore led to a reduction in the $\Delta E^{\ddagger}$'s

under mechanochemical conditions. The $\Delta E_{\mathrm{BO}}^{\ddagger}(\mathbf{q})$ term is affected by the changes in the structures of the reactant and TS. The reduction in $\Delta E_{\mathrm{BO}}^{\ddagger}(\mathbf{q})$ under mechanochemical conditions is essentially a Hammond effect, [2] in which $\Delta E_{\mathrm{BO}}^{\ddagger}(\mathbf{q})$ decreases as the reactants and TS become more similar in structure. Experimental techniques such as atomic force microscopy,[3,4] molecular force probes, [5–7] and sonication[8–13] have made it possible to activate reactions by mechanically altering reactant and TS structures.[4,14–18]

Several theoretical studies have demonstrated that the application of F can lower $\Delta E^{\ddagger}$'s for unimolecular reactions by decreasing the distance between the reactants and TS along the reaction coordinate. [19–21] Additional theoretical studies of unimolecular reactions occurring under mechanochemical conditions have shown that it is possible to eliminate $\Delta E^{\ddagger}$ by applying sufficiently large F. [1,22–24] The elimination of $\Delta E^{\ddagger}$ under mechanochemical conditions can be achieved through a convergence of reactant and TS structures, which is evident from studies of force-induced ring opening reactions. [19–21] $\Delta E^{\ddagger}$ plays a significant role in reaction kinetics, therefore the ability to eliminate $\Delta E^{\ddagger}$ may apply to unimolecular reactions in a broader context. In general, the reactant and TS in unimolecular reactions are separated by a finite distance along the zero-F reaction coordinate, Furthermore, it should be possible in principle to eliminate $\Delta E^{\ddagger}$ under mechanochemical conditions if the reactant and TS structures can sustain sufficiently large forces.

The ability to eliminate $\Delta E^{\ddagger}$ under mechanochemical conditions in bimolecular reactions is not as straightforward as in the case of unimolecular reactions. This is particularly true if the bimolecular reactions involve reacting species that are infinitely

separated. The infinite distance between the reactants and TS along the reaction coordinate hinders the convergence of these structures under mechanochemical conditions. As such, the lack of convergence of reactant and TS structures limits the ability to mechanically eliminate $\Delta E^{\ddagger}$ according to Hammond`s postulate. [2] Several bimolecular reactions, such as those studied in chapter 5, contain elementary reaction steps that involve the reaction proceeding from a reactant complex to the TS. In those cases, the reactant and TS structures may converge under mechanochemical conditions because there exists a finite distance that separates the complex and TS along the reaction coordinate.

The objective of this chapter is to address whether differences exist in the abilities to mechanically eliminate $\Delta E^{\ddagger}$ in unimolecular and bimolecular reactions in light of the aforementioned distinctions in each case. The limitations that exist in the ability to eliminate $\Delta E^{\ddagger}$ for each type of reaction will be investigated if such differences exist between unimolecular and bimolecular reactions. Quantum chemical calculations employing the EFEI method[1] are performed to examine how the $\Delta E^{\ddagger}$'s for a set of representative unimolecular and bimolecular reactions are affected by F. All calculations were performed using Kohn-Sham density functional theory[25,26] with a version of the NWChem 6.1 software package[27] that was modified to permit single point molecular energy calculations, geometry optimizations, and vibrational frequency calculations directly on the FMPES. The B3LYP exchange-correlational functional[28,29] was used in conjunction with the 6-31G(d,p) basis set for all calculations. The force-induced changes in the $\Delta E^{\ddagger}$'s are interpreted in terms of changes in the reactant and TS structures along their respective positions along the reaction coordinate.

6.2 Unimolecular reactions

The force-dependent reactant and TS structures were evaluated for the unimolecular reactions shown in Figure 6-1. Reaction **U1** corresponds to the electrocyclic ring opening of cyclobutene, which involves cleavage of a carbon-carbon single bond. Reaction **U2** involves a Berry pseudorotation[30] of PF_5, in which the axial fluorine atoms are exchanged with the equatorial fluorine atoms. Reactions **U3** and **U4** involve rotations of biaryl systems that contain fluorine atoms bonded to the aromatic rings in a *cis*-configuration in reaction **U3** and in a *trans*-configuration in reaction **U4**.

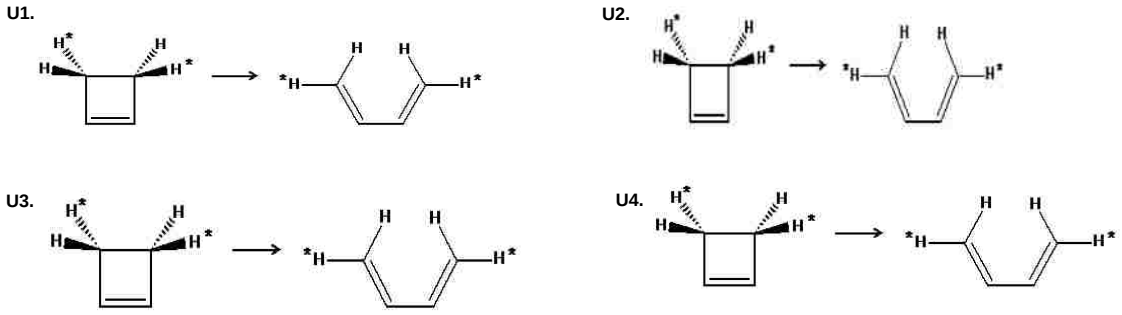

Figure 6-1. Unimolecular reactions considered in this work. The pulling points in each reaction are indicated using asterisks.

The force-dependent $\Delta E^{\ddagger}$'s were evaluated for the unimolecular reactions shown in Figure 6-1. The $\Delta E^{\ddagger}$'s were plotted versus $1/F$ to illustrate the effect of the $\Delta E^{\ddagger}$'s tending toward zero at large forces. The data is shown in Figure 6-2a and indicate that the $\Delta E^{\ddagger}$'s approached zero with increasing F, with $\Delta E^{\ddagger}$ reaching values below 0.15 kcal/mol at the highest values of F considered in each reaction. The force-dependent $\Delta E^{\ddagger}$'s were interpreted by evaluating the root-mean-squared (RMS) atomic displacements, Δx_{RMS}, as the system progressed from the reactant to the TS. The force-dependent Δx_{RMS} values are

shown in Figure 6-2b and indicate that increasing F led to a reduction in Δx_{RMS} for all reactions. The reduction in the Δx_{RMS} values suggests that the similarity of the reactant and TS structures increased with F. The similarity in reactant and TS structures in conjunction with the decrease in the $\Delta E^{\ddagger}$'s with F was consistent with Hammond's postulate.[2] The values of Δx_{RMS} calculated at the highest F considered were nearly zero for reactions **U1** and **U2**, which was consistent with these reactions being effectively barrierless. In reactions **U3** and **U4**, however, the Δx_{RMS} values did not appear to approach zero at high F. This result was inconsistent with the $\Delta E^{\ddagger}$'s for these reactions, which tended towards zero at the highest values of F considered. The behavior associated with the Δx_{RMS} values for reactions **U3** and **U4** at high F was a result of evaluating the structural similarities of the reactant and TS using Cartesian coordinates. Specifically, the progression from the reactant to the TS in both these reactions involved rotation around the central carbon-carbon single bond of the biaryl system. The torsion associated with the rotation around the carbon-carbon scissile bond changed from 10.3° in the reactant to 13.0° in the TS. This change in torsion was relatively small, yet involved large changes in the Cartesian positions of the atoms located far from the carbon-carbon single bond rotational axis.

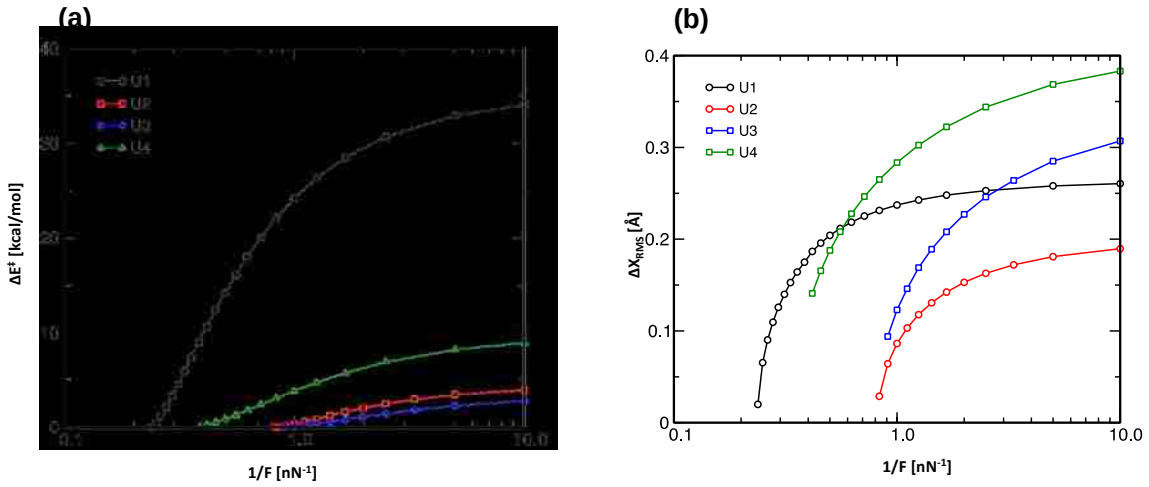

Figure 6-2. (a) $\Delta E^{\ddagger}$ versus $1/F$ and **(b)** Δx_{RMS} versus $1/F$ for the reactions **U1-U4**. The data indicate that $\Delta E^{\ddagger}$ and Δx_{RMS} approached zero at high values of F. [31]

The force-induced convergence of the reactant and TS shown in Figure 6-2b was further investigated by evaluating the displacements of these species parallel to the zero-F minimum energy pathway, S_0 known as Hammond effects and perpendicular to S_0 termed anti-Hammond effects. The procedure for evaluating such Hammond and anti-Hammond effects involved first computing S_0 via an intrinsic reaction coordinate calculation. A stationary point i.e. a reactant or TS, that was optimized on the FMPES for that reaction was selected and the Δx_{RMS} values between the structure of that stationary point and each structure along S_0 were calculated. The structure, j, along S_0 that resulted in the lowest value of Δx_{RMS} was identified to be most similar to the stationary point. This value of Δx_{RMS}, termed $\Delta x_{\perp}^{RMS}$, was used to quantify the displacement of the stationary point perpendicular to S_0. The displacement of the stationary point parallel to S_0 was quantified by calculating the root-mean squared difference between the structure j and the zero-F reactant termed $\Delta x_{\parallel}^{RMS}$. The manner in which the quantities $\Delta x_{\perp}^{RMS}$ and $\Delta x_{\parallel}^{RMS}$ were calculated is described in what follows for the specific example of the TS in reaction **U1** at

F = 3000 pN. The optimized structure of the TS in reaction **U1** at F=3000 pN was used as the reference point, i, relative to the structures, j, along S_0. The root-mean-squared (RMS) differences in the structures i and j were quantified using the expression:

$$\Delta x_{i-j}^{RMS} = \sqrt{\frac{\sum_{k=1}^{3N} (x_k^j - x_k^i)^2}{3N}} \tag{6.2}$$

where $3N$ represents the Cartesian coordinates for the N atoms in the system, x_k^j is the value of the kth atomic position for the structure j along the S_0, and x_k^i is the value of the kth atomic position for the reference structure, i. A plot of Δx_{i-j}^{RMS} versus j is shown in Figure 6-3. The data indicate the value of Δx_{i-j}^{RMS} was the lowest for structure j = 369 along S_0, which suggests that this structure was most similar to i. The value of Δx_{i-j}^{RMS} in which j = 369 corresponds to the value of $\Delta x_{\perp}^{RMS}$ was used to quantify the displacement of the stationary point perpendicular to S_0. The displacement of the stationary point parallel to S_0 was quantified by $\Delta x_{\parallel}^{RMS}$, which was obtained from RMS differences between the atomic positions of structure j = 369 along S_0 and the zero-F reactant (j = 0). For the specific example of the TS at F = 3000 pN, the displacement of the reactant in the direction of the TS can be achieved by the zero-F reactant moving an amount $\Delta x_{\parallel}^{RMS}$ parallel to S_0 to reach the structure j = 369 and then moving an amount $\Delta x_{\perp}^{RMS}$ perpendicular to S_0 in the direction towards the structure, i.

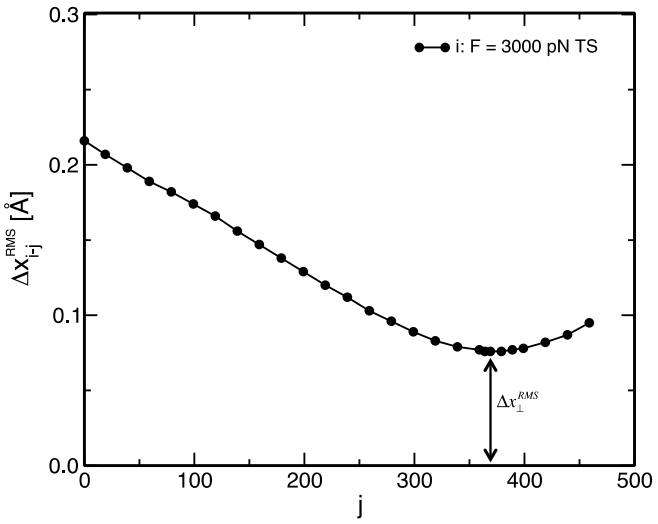

Figure 6-3. Δx_{i-j}^{RMS} versus *j* along S_0 for reaction **U1** using the TS at F = 3000 pN as the reference structure, *i*. The index *j* on the x-axis corresponds to the structures along S_0 with the zero-F reactant located at j = 0 and the zero-F TS located at j = 459. The minimum of Δx_{i-j}^{RMS} corresponds to j = 369 and was used to quantify the displacement perpendicular to S_0, $\Delta x_{\perp}^{RMS}$.[31]

The procedure for evaluating $\Delta x_{\parallel}^{RMS}$ and $\Delta x_{\perp}^{RMS}$ was repeated for the stationary points in the reactions **U1**-**U4** for all values of F considered. The convergence of reactant and TS structure was described by plotting $\Delta x_{\parallel}^{RMS}$ versus $\Delta x_{\perp}^{RMS}$ for all reactions at all values of F as illustrated in Figure 6-4. The data indicate that the force-induced convergence of the reactant and TS structures was achieved through a combination of Hammond and anti-Hammond effects. In the cases of reactions **U1** and **U2**, the application of F shifted the positions of both the reactant and TS in a manner that resulted in changes in $\Delta x_{\parallel}^{RMS}$ and $\Delta x_{\perp}^{RMS}$. As such, the convergence of the reactant and TS structures in reactions **U1** and **U2** involved movements parallel and perpendicular to S_0. The data for reactions **U3** and **U4**, however, show that the reactant shifted parallel and perpendicular to

S_0 while the TS structure did not move parallel to S_0 at all under mechanochemical conditions. In particular, only the $\Delta x_{\perp}^{RMS}$ values were affected by the application of F in the TS structures in reactions **U3** and **U4**. This result can be attributed to the nature of the reactions associated with the rotation of the biaryl systems. Specifically, the torsion associated with the rotation around the central carbon-carbon single bond is 180° in both TS structures. As such, the shift in the TS parallel to S_0 in the direction of the reactant would require the PPs to move closer together. Given that F was applied along the vector connecting the PPs, such changes in the TS structures would require mechanical work to be performed against F and therefore did not occur.

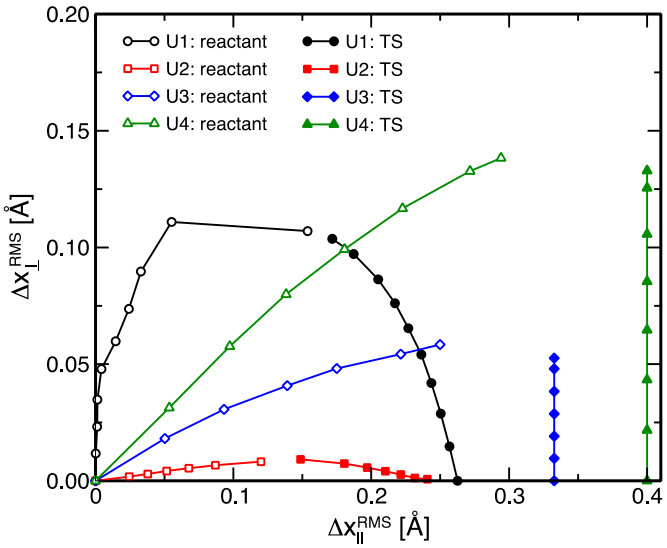

Figure 6-4. Force-induced shifts in the reactant and TS structures for reactions **U1**-**U4**. Changes in $\Delta x_{\parallel}^{RMS}$ indicate movements parallel to the zero-F reaction coordinate, S_0, whereas changes in $\Delta x_{\perp}^{RMS}$ indicate movements perpendicular to S_0. Open symbols designate reactant structures and closed symbols denote TS structures optimized a different values of F. Reactant and TS structures obtained at higher F lie further from the origins from each curve. [31]

6.3 Bimolecular Reactions

The force-dependent reactant and TS structures were evaluated for the bimolecular reactions shown in Figure 6-5. Reactions **B1** and **B2** correspond to S_N2 reactions that involve the formation of a reactant complex. Both reactions involve chloromethane as a substrate and chloride as a nucleophile in reaction **B1** and ammonia as a nucleophile in reaction **B2**. Reactions **B3**, **B4**, and **B5** correspond to cycloaddition reactions that proceed via formation of a reactant complex in reactions **B3** and **B4** and involve infintely separated reacting species in reaction **B5**. Reactions **B3** and **B5** are Diels-Alder reactions that involve cyclopentadiene and maleic anhydride as the reactants in the case of reaction **B3** and ethylene and butadiene as reactants in the case of reaction **B5**. Reaction **B4** is another type of cycloaddition that involves a nitrone and ethylene as the reacting species. The 6-31++G(d,p) basis set was used for the bimolecular reactions instead of the 6-31G(d,p) basis set employed for the unimolecular reactions. The '++' terms denote diffuse functions that were added to account for the non-bonding interactions present in the reactant complexes and TS structures. In the case of reaction **B5**, the reactants were found to be infinitely separated given the level of theory used in the quantum chemical calculations and the force-dependent $\Delta E^{\ddagger}$'s were corrected for basis set superposition errors using the counterpoise method. The details of basis set superposition errors and the counterpoised method are described in section 2.11. A dispersion correction could be added to the quantum chemical calculations, which may result in the formation of a reactant complex in the case of reaction **B5**. However, it was necessary to examine several types of

bimolecular reactions including those involving infinitely separated reagents. As such, no dispersion correction was added for any of the bimolecular reactions.

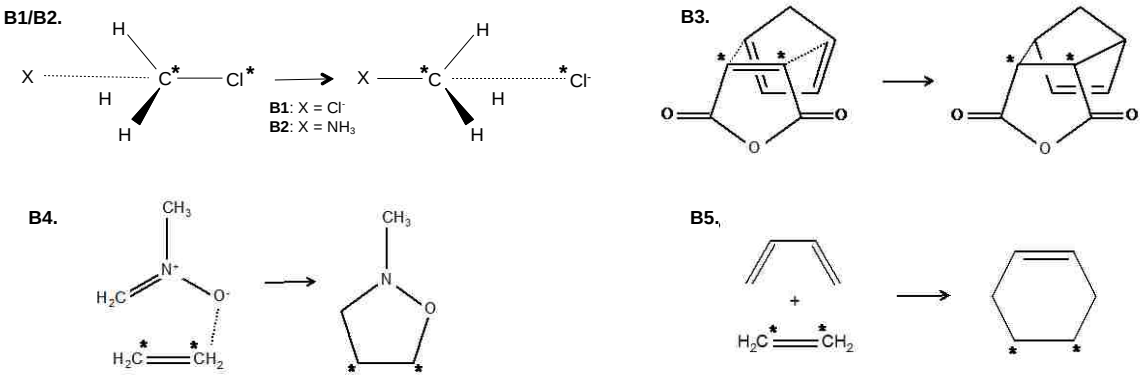

Figure 6-5. Bimolecular reactions considered in this work. The pulling points in each reaction are indicated using asterisks.

6.3.1 Barriers and Structures

The force-dependent $\Delta E^{\ddagger}$'s were evaluated for reactions **B1**-**B4** and shown in Figure 6-6a. As in the case of the unimolecular reactions, the $\Delta E^{\ddagger}$'s were plotted versus $1/F$ to illustrate the $\Delta E^{\ddagger}$'s approaching zero at large F. For reactions **B1**-**B3**, $\Delta E^{\ddagger}$ was below 0.25 kcal/mol at the highest F that could be supported by the TS. The $\Delta E^{\ddagger}$'s for reactions **B4** and **B5** did not reach zero at the highest values of F considered. The lowest values of the $\Delta E^{\ddagger}$'s calculated for these reactions were 2.3 kcal/mol and 6.9 kcal/mol respectively. Although the $\Delta E^{\ddagger}$'s for reactions **B4** and **B5** reached non-zero values at the highest values of F, the trends in the data suggest that the $\Delta E^{\ddagger}$'s should reach zero at a finite value of F for both reactions. While this notion is reasonable for reaction **B4,** which can be thought of in a similar manner to a unimolecular reaction because the reactants formed a complex along the reaction coordinate, it is inconsistent for reaction **B5** with

infinitely separated reactants. As discussed in section 6.1, the ability to eliminate $\Delta E^{\ddagger}$ requires the convergence of reactant and TS structures. This convergence is not possible when the reactants are infinitely separated as in the case of reaction **B5**. The inconsistency between the trends in the data for reaction **B5** in Figure 6-6b and the requirement for the elimination of $\Delta E^{\ddagger}$ was investigated by evaluating the force-induced changes in the reactant and TS structures. The data is shown in Figure 6-6b and indicate that the application of F shifted the complex and TS closer to one another by movements parallel ($\Delta x_{\parallel}^{RMS}$) and perpendicular ($\Delta x_{\perp}^{RMS}$) to S_0 for reactions **B1**-**B3**. The changes in $\Delta x_{\parallel}^{RMS}$ and $\Delta x_{\perp}^{RMS}$ with F were relatively symmetric for the complex and TS in reactions **B1** and **B3**. In the case of reaction **B2**, the force-induced changes in the TS structure were greater than the complex. The data shown for reaction **B4** indicate that the force-induced structural changes in the complex were dominated by $\Delta x_{\perp}^{RMS}$ such that the complex was shifted almost entirely perpendicular to S_0. As such, the force-induced convergence of the complex and TS was achieved through movements of the TS parallel and perpendicular to S_0. In the case of reaction **B5**, the TS shifted towards the reactant as F was increased. The reactants, however, remained infinitely far away from the TS with increasing F.

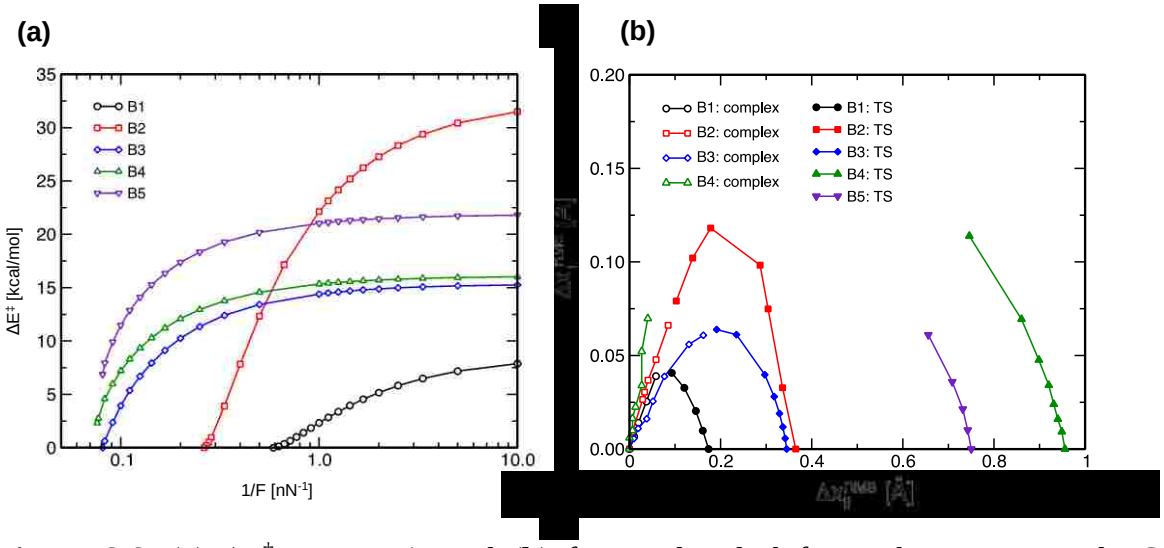

Figure 6-6. (a) $\Delta E^{\ddagger}$ versus $1/F$ and **(b)** force-induced shifts in the reactant and TS structures for reactions **B1**-**B5**. Changes in $\Delta x_{\parallel}^{RMS}$ indicate movements parallel to the zero-F reaction coordinate, S_0, whereas changes in $\Delta x_{\perp}^{RMS}$ indicate movements perpendicular to S_0. Open symbols designate reactant structures and closed symbols denote TS structures optimized a different values of F. Reactant and TS structures obtained at higher F lie further from the origins from each curve. [31]

6.3.2 Contributions to Barriers

The changes in the $\Delta E^{\ddagger}$'s for reactions **B1**-**B5** were further interpreted by representing the $\Delta E^{\ddagger}$'s as a sum of a term associated with the structural and electronic changes that occur within each reacting species as the system progressed from the reactants to the TS known as the change in the deformation energy, ΔE_{def}, and another term that corresponds to the change in the interaction energy between the reacting components as the system moves from the reactants to the TS, ΔE_{int}. The change in the deformation energy under mechanochemical conditions can be expressed as:

$$\Delta E_{\text{def}}(F) = E_{\text{BO}}^{\text{A}}(\mathbf{x}_{\text{TS}}) + E_{\text{BO}}^{\text{B}}(\mathbf{x}_{\text{TS}}) - E_{\text{BO}}^{\text{A}}(\mathbf{x}_{\text{r}}) + E_{\text{BO}}^{\text{B}}(\mathbf{x}_{\text{r}}) - F(R_{\text{TS}} - R_{\text{r}}) \qquad (6.3)$$

where A and B denote each of the reacting components, $\mathbf{x}_{TS}$ and $\mathbf{x}_r$ represent the nuclear coordinates of the TS and reactants respectively, and R_{TS} and R_r are the distances between the PPs in the TS and reactant respectively. Once ΔE_{def} is calculated, ΔE_{int} can be obtained using the expression:

$$\Delta E_{int}(F) = \Delta E^{\ddagger}(F) - \Delta E_{def}(F) \tag{6.4}$$

In general, $\Delta E_{def} > 0$ for bimolecular reactions where A and B are infinitely separated reactants. This is because the infinitely separated reactants adopt their respective minimum energy structures. Therefore, any deformation of those structures will lead to an increase in their respective energies. In bimolecular reactions that proceed via formation of a complex, ΔE_{def} is evaluated as the sum of the energies associated with deforming each reacting component from their respective structures in the reactant complex. However, each reacting species is not in its minimum energy configuration in the reactant complex. Furthermore, it is possible that the deformation of the reacting components upon moving from the reactant complex to the TS leads to a reduction in ΔE_{def}. It is reasonable to assume, however, that the structure of each reacting species is more similar to its isolated structure in the reactant complex than it is in the TS, given that the infinitely separated reactants are closer to the reactant complex along S_0 than the TS. As such, it is reasonable to assume that $\Delta E_{def} > 0$ even if the bimolecular reactions proceed via formation of a complex. This notion is supported from the data in Figure 6-7, which show the values of E_{def} relative to the structures along S_0 for reactions **B1-B5**. In all cases, the value of E_{def}

was larger in the TS than the reactants, which resulted in $\Delta E_{def} > 0$.

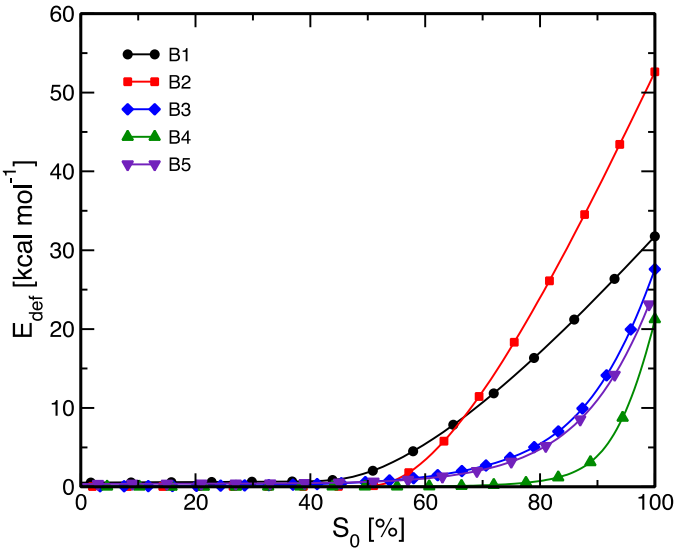

Figure 6-7. E_{def} versus S_0 for reactions **B1**-**B5**. The values of E_{def} are calculated relative to the infinitely separated reactants. That data indicate that E_{def} is greater in the TS than the reactants for all reactions. Note that S_0 has been plotted from 0 to 100 % where the reactants reside at 0 % and the TSs reside at 100 %. [31]

The values of ΔE_{def} and ΔE_{int} are plotted versus F for reactions **B1**-**B5**. The data is shown in Figure 6-8 and indicate that ΔE_{def} is positive and ΔE_{int} is negative at low values of F for all reactions. For reactions **B1**-**B3**, ΔE_{def} was increased and ΔE_{int} was decreased monotonically with F such that these quantities approached zero from opposite sides. The force-induced changes in ΔE_{def} and ΔE_{int} in reactions **B4** and **B5** are similar to those observed in reactions **B1**-**B3**, however, increasing F to the highest values considered in

reactions **B4** and **B5** caused ΔE_{int} to become positive without ΔE_{def} reaching zero.

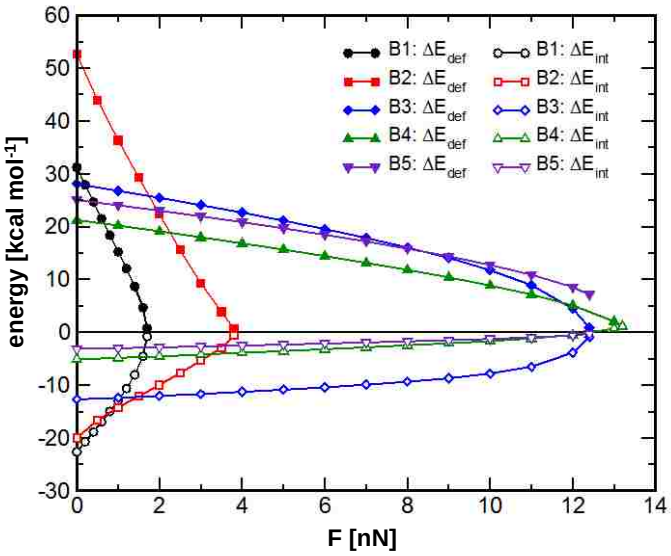

Figure 6-8. ΔE_{def} and ΔE_{int} versus F for reactions **B1**-**B5**. The data indicate that ΔE_{def} decreased and ΔE_{int} increased with F.[31]

The steady reductions in ΔE_{def} with F in these reactions indicate that the reactants and TS become increasingly similar in structure as F was increased. The similarity in the structure between the reactant complex and TS with F was illustrated in Figure 6-9 for the example of reaction **B1** at F = 0 pN and F = 2000 pN.

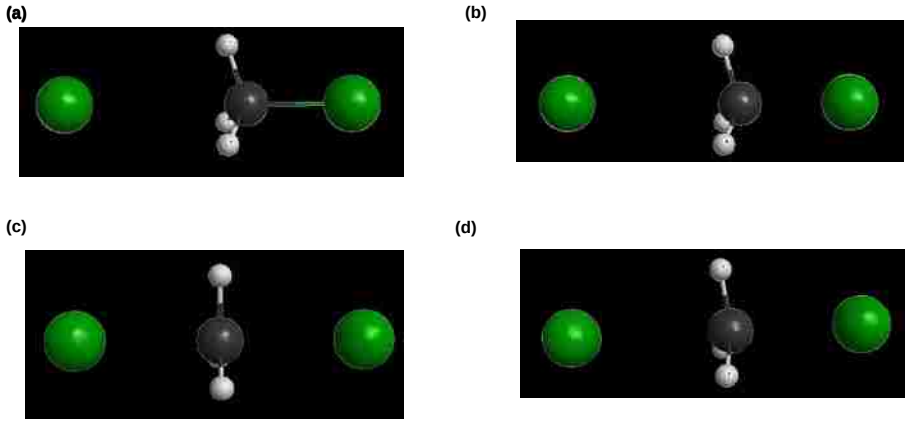

Figure 6-9. Optimized structures of the complex at **(a)** F=0 pN and **(b)** F=2000 pN and the TS at **(c)** F=0 pN and **(d)** F=2000 pN. The complex and TS were more similar in structure at higher values of F. The black, white, and green spheres denote carbon, hydrogen, and fluorine atoms respectively.

The adoption of positive values of ΔE_{int} in reactions **B4** and **B5** suggests that the interactions between the reacting species stabilized the reactant complex and infinitely separated reactants respectively than the TS at higher values of F. According to Eq. (6.4), a positive value of ΔE_{int} indicates that $\Delta E^{\ddagger} > 0$. As such, reactions **B4** and **B5** should not become barrierless with increasing F, despite the trends in the force-dependent $\Delta E^{\ddagger}$'s for these reactions shown in Figure 6-8. As a whole, the data in Figure 6-8 indicate that maintaining a negative or zero value of ΔE_{int} was necessary to eliminate $\Delta E^{\ddagger}$ for the bimolecular reactions. The data in Figures 6-6b and 6-8 suggest that ΔE_{int} remained negative or zero if the reactant complex was shifted parallel to S_0, which was observed in reactions **B1-B3**. In reactions **B4** and **B5**, the reactant complex and the infinitely separated reactants did not move parallel to S_0. As a result, ΔE_{int} adopted positive values, despite significant shifts in the TSs for these reactions parallel to S_0. The differences in ΔE_{int} for the various bimolecular reactions were further investigated by examining the changes in the interaction energy between the two reacting components, E_{int}, as the system moved

along S_0. The data is shown in Figure 6-10 and indicate that E_{int} increased steadily as the system progressed from the reactants to the TS prior to reaching a maximum and then decreased as the system was closer to the TS. The maximum in E_{int} can be attributed to the repulsion between the valence electrons of the two reacting components without a sufficiently large stabilization due to bonding or attractive electrostatic interactions between these species. In all reactions, E_{int} was lower in the TS than in the reactants. ΔE_{int}, however, is a relative quantity that is affected by the changes in reactant and TS structures that occur parallel to S_0. Furthermore, ΔE_{int} can become positive if the TS is shifted parallel to S_0 in the direction of the reactants without a significant shift in the reactants parallel to S_0 towards the TS.

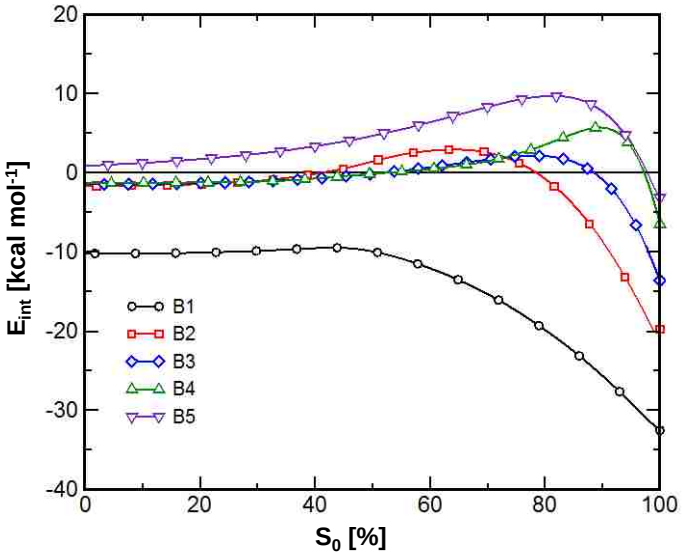

Figure 6-10. E_{int} versus S_0 for reactions **B1**-**B5**. The values of E_{int} are calculated relative to the infinitely separated reactants. Note that S_0 has been plotted from 0 to 100 % where the reactants reside at 0 % and the TSs reside at 100 %. The data indicate that E_{int} increased as the system progressed from the reactant towards the TS before reaching a maximum and then decreased closer to the TS for all reactions. [31]

The data shown in Figure 6-10 highlight the notion that the reactant must undergo a force-induced change in structure that directs it towards the TS for the reaction to become barrierless. Those plots were obtained using structures along S_0. Analogous plots can be obtained using reactant and TS structures along reaction coordinates at different values of F. As an example, the changes in E_{int} were evaluated along reaction coordinates at different values of F for reactions **B3** and **B4**. In each case, E_{int} was calculated relative to the infinitely separated reactants. The positions of the structures along the reaction coordinate at each value of F were plotted at its position parallel to S_0 using the calculated values of $\Delta x_{\parallel}^{RMS}$. The data for reaction **B3** is shown in Figure 6-11a and indicate that E_{int}-S_0 curves obtained at values of $F \leq 9000$ pN exhibited similar behaviour to the E_{int}-S_0 curve shown in Figure 6-10, in which E_{int} increased as the system progressed from the reactants to the TS before reaching a maximum and then decreased closer to the TS. The maximum value of E_{int} decreased with F. As well, increasing F shifted the position of the maximum closer to the reactant. The E_{int}-S_0 curve obtained at F=12000 pN did not contain a maximum because the reactant complex was shifted parallel to S_0 to a point where the changes in the separation of the reacting components no longer dominated the movement along S_0. The disappearance of the maximum of E_{int} at the highest value of F ensured that ΔE_{int} remained negative at high values of F.

The data for reaction **B4** is shown in Figure 6-11b and indicate that the E_{int}- S_0 curves exhibited similar behaviour for all values of F. As in the case of reaction **B3**, the maximum value of E_{int} decreased with F and its position was shifted parallel to S_0 towards the reactants with increasing F. As well, the value of E_{int} at the TS increased with F. This increase in E_{int} for the TS indicates that ΔE_{int} will become positive at higher values of F as

illustrated in Figure 6-8. Furthermore, the E_{int}-S_0 curves calculated for reaction **B4** were consistent with the notion that force-induced movements of the TS parallel to S_0 alone was not sufficient for $\Delta E^{\ddagger} = 0$.

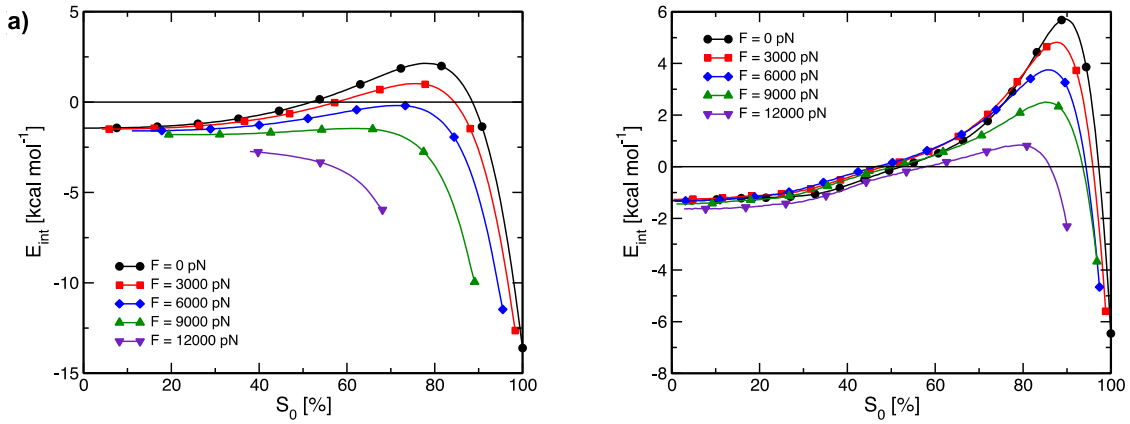

Figure 6-11. E_{int} versus S_0 for the series of structures along reaction coordinates at different values of F for reactions **(a) B3** and **(b) B4**. In all cases, E_{int} was calculated relative to the isolated reactants. The positions of the structures along S at each value of F were plotted relative to their locations parallel to S_0. Note that S_0 has been plotted from 0 to 100 % where the reactants reside at 0 % and the TSs reside at 100 %.[31]

6.3.3 Structural changes along S_0

The requirement that the reactants must move toward the TS along S_0 to eliminate $\Delta E^{\ddagger}$ for the reactions **B1**-**B5** was based on the assumption that the features of the E_{int}-S_0 curves illustrated in Figures 6-10 and 6-11 can be generalized for common classes of bimolecular reactions occurring under mechanochemical conditions. The general features of the E_{int}-S_0 curves can be understood by investigating the structural changes that occur as the system progresses from the reactants to the TS along S_0. Such structural changes correspond to the change in the separation of the reacting species and the deformation of

the internal structures of the reacting components. The contributions from each of these structural changes were evaluated from the changes in the atomic coordinates of each structure, *j*, along S_0 relative to the reactants, *r*, and were used to calculate the total structural change according to the expression:

$$\Delta x_{tot}^{j} = \sum_{i=1}^{3Nt} \left| \mathbf{x}_i^j - \mathbf{x}_i^r \right| \tag{6.5}$$

deformation of the reacting species:

$$\Delta x_{def}^{j} = \sum_{A=1}^{2} \sum_{i=1}^{N_I} \left| \mathbf{x}_{i,A}^j - \mathbf{x}_{i,A}^r \right| \tag{6.6}$$

and change in separation of the reaction species:

$$\Delta x_{sep}^{j} = \Delta x_{tot}^{j} - \Delta x_{def}^{j} \tag{6.7}$$

where the index *i* runs over the number of atomic coordinates in the system, the index *I* runs over the two reacting components, N_t is the total number of atoms in the system, N_I is the number of atoms in the reacting component, *I*, $\mathbf{x}_i^j$ and $\mathbf{x}_i^r$ denote the Cartesian coordinates of all the atoms present in the structure *j* and reactant respectively, and $\mathbf{x}_{i,A}^j$ and $\mathbf{x}_{i,A}^r$ represent the Cartesian coordinates of the atoms in the reacting component *A* in the structure *j* and the reactants respectively. The rates at which Δx_{sep} and Δx_{def} changed along

S_0 were evaluated and the resulting plots are shown in Figure 6-12. The data indicate that changes in Δx_{sep} dominated near the reactants whereas Δx_{def} dominated closer to the TS in all reactions. The region at which Δx_{sep} dominated led to steric and electrostatic repulsion between the valence electrons in the reacting components, which resulted in an increase in E_{int}. As the system progressed to the region where Δx_{def} dominated, valence bonding occurred between the reacting species, which resulted in a reduction in E_{int}. Furthermore, the arguments above regarding the changes in ΔE_{int} were based on force-induced changes in structure that occurred parallel to S_0. The data shown in Figure 6-6b, however, indicate that the reactants and TSs for the various bimolecular reactions were shifted perpendicular to S_0 as well. In fact, such anti-Hammond effects contributed to the reduction in ΔE_{def} towards zero as well as the adoption of positive values in ΔE_{int} at higher values of F in reactions **B4** and **B5**. These anti-Hammond effects, however, were not sufficiently large to render the requirement that the reactant must move parallel to S_0 to achieve a barrierless bimolecular reaction.

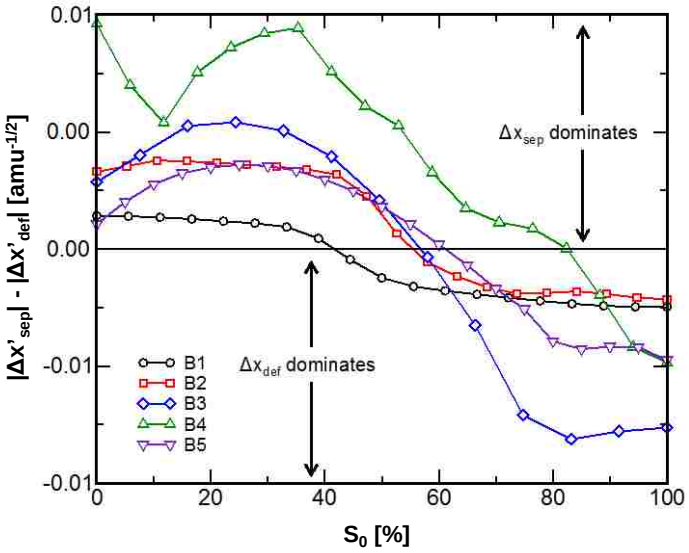

Figure 6-12. Difference in rates at which Δx_{sep} and Δx_{def} change along S_0 for reactions **B1-B5**. The rates at which Δx_{sep} and Δx_{def} change are denoted by $\Delta x'_{sep}$ and $\Delta x'_{def}$ respectively. Note that S_0 has been plotted from 0 to 100 % where the reactants reside at 0 % and the TSs reside at 100 %. The data indicate that Δx_{sep} dominated near the reactants whereas Δx_{def} dominated closer to the TS.[31]

6.3.4 Coupling between *F* and S_0

The significance of the force-induced changes in structure of the reactants in a manner that led to movement parallel to S_0 in eliminating $\Delta E^{\ddagger}$ was most apparent in reactions **B3** and **B4**. Both these reactions are pericyclic cycloadditions that proceed via formation of a complex, yet the discrepancies in the force-induced changes in the reactant complex for these reactions suggest that the nuclear degrees of freedom (DOFs) in these complexes couple to F in different ways. The coupling between the nuclear DOFs and F was examined by evaluating the overlap between F and S_0 and determining the directions in which the atomic positions in the reactant complexes change due to the application of

F. The overlap between *F* and S_0 was evaluated by calculating the tangent to S_0 at each point, *i*, along S_0 according to the expression:

$$\boldsymbol{\tau}_i = \frac{\mathbf{x}_{i+1} - \mathbf{x}_i}{\left|\mathbf{x}_{i+1} - \mathbf{x}_i\right|} + \frac{\mathbf{x}_i - \mathbf{x}_{i-1}}{\left|\mathbf{x}_i - \mathbf{x}_{i-1}\right|} \tag{6.8}$$

where $\boldsymbol{\tau}_i$ represent the tangent to S_0 at point *i* and is normalized using the procedure outlined by Henkelman and Jónsson:[32]

$$\hat{\boldsymbol{\tau}} = \frac{\boldsymbol{\tau}_i}{\left|\boldsymbol{\tau}_i\right|} \tag{6.9}$$

The normalized vector, $\hat{\mathbf{R}} = \mathbf{R}_i / \left|\mathbf{R}_i\right|$, along which *F* was applied was then projected onto $\boldsymbol{\tau}_i$ at each point along S_0. The overlap between $\hat{\mathbf{R}}$ and $\hat{\boldsymbol{\tau}}$ was calculated at each point along S_0 for reactions **B3** and **B4**. The resulting plot is shown in Figure 6-13 and indicates that the overlap between $\hat{\mathbf{R}}$ and $\hat{\boldsymbol{\tau}}$ was nearly zero at the reactant complex and increased as the system progressed toward the TS. This result was consistent with the ability to apply *F* in a manner that moved the TS parallel to S_0 for both reactions, however the data suggests that the direct overlap between $\hat{\mathbf{R}}$ and $\hat{\boldsymbol{\tau}}$ was not responsible for the movement of the reactant complex parallel to S_0, which was necessary to eliminate $\Delta E^{\ddagger}$. Furthermore, the movements of the reactant complexes along S_0 are dictated by the manner in which the application of *F* affects other nuclear DOFs in the complexes instead of the direct coupling between $\hat{\mathbf{R}}$ and $\hat{\boldsymbol{\tau}}$. The changes in other nuclear DOFs due to the application of *F*

were evaluated by examining the coupling between the vector defining the PP distance, **R**, and those nuclear DOFs. This coupling was evident from the structures of the reactant complexes for reactions **B3** and **B4** illustrated in Figure 6-13. The arrows in the zero-*F* reactant complexes indicate the magnitude and directions of the force-induced structural changes with longer arrows corresponding to larger force-induced motions. The arrows in the reactant complex for reaction **B3** pointed toward each other, which indicate that *F* will shift the reacting species closer to one another in a manner that is consistent with motion along S_0. It was found that the coupling between **R** and the other nuclear DOFs in the reactant complex caused the carbon-carbon distances associated with the two σ bonds formed in the products to change at a rates of -2.3×10^{-2} Å/nN. In contrast, the arrows on the reactant complex in reaction **B4** did not point toward one another, which was required for movement parallel to S_0. Furthermore, the carbon-oxygen and carbon-carbon distances associated with the product formation changed at rates of -1.9×10^{-3} Å/nN and -2.2×10^{-3} Å/nN respectively.

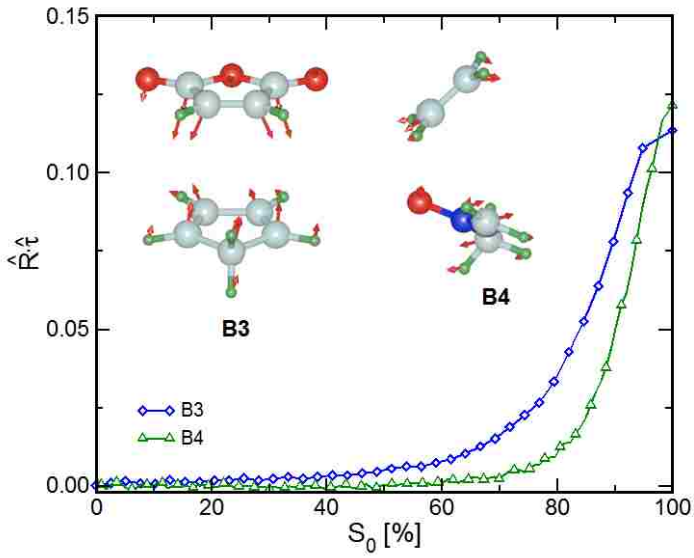

Figure 6-13. Overlap between $\hat{\mathbf{R}}$ and $\hat{\boldsymbol{\tau}}$ for the reactant complexes in reactions **B3** and **B4**. Note that S_0 has been plotted from 0 to 100 % where the reactants reside at 0 % and the TSs reside at 100 %. The data indicate that the coupling was nearly zero for the reactant complexes and increased as the system moved closer to the TS in both reactions. The zero-*F* structures of the reactant complexes for both reactions are shown with the red arrows indicating the force-induced motions of atoms in those structures, with longer arrows indicating larger motions.[31]

In a general sense, the ability to apply *F* in a manner that shifts the reactant along S_0 towards the TS can be investigated by examining the molecular compliance matrix, **C**,[33–35] which is obtained from the inverse of Hessian in terms of internal coordinates, $\mathbf{H}_{\text{int}}$. Specifically, one can use $\hat{\boldsymbol{\tau}}$ to identify which nuclear DOFs are most affected as the system follows S_0 starting from the reactant geometry. Once the relevant nuclear DOFs are determined, the compliance matrix elements that couple **R** to other DOFs can be used to quantify the displacement of the system along S_0 under mechanochemical conditions. This approach can also be used in the context of identifying PPs in a molecule that lead to force-induced changes in the reactants along S_0 in the direction towards the TS.

6.4 Summary

As a whole, the results in this chapter demonstrate that $\Delta E^{\ddagger}$ can be eliminated under mechanochemical conditions through a combination of Hammond and anti-Hammond effects that cause the reactant and TS structures to converge. The abilities to mechanically induce structural convergence between the reactant and TS are fundamentally different in unimolecular and bimolecular elementary reactions.

In principle, unimolecular elementary reactions can become barrierless under mechanochemical conditions if the reactant, TS, or both these species are shifted along S_0. While the data shown in Figure 6-2 indicate that $\Delta E^{\ddagger}$ was rendered to zero for the reactions **U1-U4**, the PPs and values of F used in the quantum chemical calculations may not be accessible from an experimental standpoint.

In the case of the bimolecular reactions studied, the coupling between F and the nuclear DOFs in the molecule associated with the movement of the reactants towards the TS was necessary to eliminate $\Delta E^{\ddagger}$ irrespective of the force-induced changes in the TS. This coupling was not possible for reaction **B5** because the reactants were infinitely separated. As a result, no sets of PPs in the molecule would exist in which applying F along the vector connecting the PPs would shift the reactants along S_0 in a direction towards the TS though force-induced reductions in Δx_{sep}. Therefore, it is not possible to mechanically eliminate $\Delta E^{\ddagger}$ for bimolecular reactions with infinitely separated reagents without changing the underlying mechanism. For reactions **B1**-**B4**, which involve the formation a reactant complex, there exists a finite distance that separates the complex and TS along S_0. The finite distance along S_0 between the reactant and TS negates the

requirement for these bimolecular reactions to have a non-zero $\Delta E^{\ddagger}$. In the cases of reactions **B1-B3**, the application of F shifted the reactant complex parallel to S_0 towards the TS. The shift in the reactant complexes for these reactions occurred due to the coupling between F and the nuclear DOFs that are aligned with S_0. This coupling ensured that the reactions retained zero or negative values of ΔE_{int} under mechanochemical conditions, which resulted in an elimination of $\Delta E^{\ddagger}$. In reaction **B4**, the interactions between the reacting components did not lead to sufficient coupling between F and the nuclear DOFs that are aligned with S_0. As a result, the system relied on force-induced changes in the TS structure to achieve structural convergence of the reactant complex and TS. The force-induced changes that shifted the TS parallel to S_0 towards the reactant led to the TS adopting structures that resulted in an increase in ΔE_{int} without a reduction in ΔE_{def} at higher values of F as illustrated in Figure 6-8. The adoption of positive values of ΔE_{int} without a signifcant decrease in ΔE_{def} led to a non-zero $\Delta E^{\ddagger}$ at high F in reaction **B4.** The results for the bimolecular reactions that involve formation of a reactant complex suggest that the movement of the TS along S_0 alone was not sufficient to eliminate $\Delta E^{\ddagger}$, which is possible for unimolecular reactions. The elimination of $\Delta E^{\ddagger}$ in bimolecular reactions requires sufficient coupling between F and the DOFs in the reactant complex aligned with S_0 such that the complex was shifted along S_0 towards the TS.

References

1. Ribas-Arino, J., Shiga, M. & Marx, D. Understanding covalent mechanochemistry. *Angew. Chem. Int. Ed.* **48,** 4190–4193 (2009).

2. Hammond, G. S. A correlation of reaction rates. *J. Am. Chem. Soc.* **77,** 334–338 (1955).

3. Kreuzer, H. J., Payne, S. H. & Livadaru, L. Stretching a Macromolecule in an Atomic Force Microscope: Statistical Mechanical Analysis. *Biophys. J.* **80,** 2505–2514 (2001).

4. Kersey, F. R., Yount, W. C. & Craig, S. L. Single-molecule force spectroscopy of bimolecular reactions: system homology in the mechanical activation of ligand substitution reactions. *J. Am. Chem. Soc.* **128,** 3886–3887 (2006).

5. Yang, Q.-Z. *et al.* A molecular force probe. *Nat. Nanotechnol.* **4,** 302–306 (2009).

6. Huang, Z. & Boulatov, R. Chemomechanics with molecular force probes. *Pure Appl. Chem.* **82,** 931-951 (2010).

7. Lenhardt, J. M. & Craig, S. L. Mechanochemistry: Force probes in a bottle. *Nat. Nanotechnol.* **4,** 284–285 (2009).

8. Basedow, A. M. & Ebert, K. H. in *Physical Chemistry* **22,** 83–148 (Springer Berlin Heidelberg, 1977).

9. Price, G., West, P. & Smith, P. Control of polymer structure using power ultrasound. *Ultrason. Sonochem.* **1,** S51–S57 (1994).

10. Berkowski, K. L., Potisek, S. L., Hickenboth, C. R. & Moore, J. S. Ultrasound-Induced Site-Specific Cleavage of Azo-Functionalized Poly(ethylene glycol). *Macromolecules* **38,** 8975–8978 (2005).

11. Hickenboth, C. R. *et al.* Biasing reaction pathways with mechanical force. *Nature* **446,** 423–427 (2007).

12. Avalos, M. *et al.* Thermal and Sonochemical Studies on the Diels−Alder Cycloadditions of Masked *o* -Benzoquinones with Furans: new Insights into the Reaction Mechanism. *J. Org. Chem.* **68,** 7193–7203 (2003).

13. Koda, S. Ultrasonic degradation of water-soluble polymers. *Polymer* **35,** 30–33 (1994).

14. Beyer, M. K. & Clausen-Schaumann, H. Mechanochemistry: the mechanical activation of covalent bonds. *Chem. Rev.* **105,** 2921–2948 (2005).

15. Kryger, M. J., Munaretto, A. M. & Moore, J. S. Structure–mechanochemical activity relationships for cyclobutane mechanophores. *J. Am. Chem. Soc.* **133,** 18992–18998 (2011).

16. Klukovich, H. M., Kouznetsova, T. B., Kean, Z. S., Lenhardt, J. M. & Craig, S. L. A backbone lever-arm effect enhances polymer mechanochemistry. *Nat. Chem.* **5,** 110–114 (2012).

17. Piermattei, A., Karthikeyan, S. & Sijbesma, R. P. Activating catalysts with mechanical force. *Nat. Chem.* **1,** 133–137 (2009).

18. Davis, D. A. *et al.* Force-induced activation of covalent bonds in mechanoresponsive polymeric materials. *Nature* **459,** 68–72 (2009).

19. Ong, M. T., Leiding, J., Tao, H., Virshup, A. M. & Martínez, T. J. First principles dynamics and minimum energy pathways for mechanochemical ring opening of cyclobutene. *J. Am. Chem. Soc.* **131,** 6377–6379 (2009).

20. Kochhar, G. S., Bailey, A. & Mosey, N. J. Competition between orbitals and stress in mechanochemistry. *Angew. Chem. Int. Ed.* **49,** 7452–7455 (2010).

21. Konda, S. S. M. *et al.* Molecular catch bonds and the anti-Hammond effect in polymer mechanochemistry. *J. Am. Chem. Soc.* **135,** 12722–12729 (2013).

22. Ribas-Arino, J., Shiga, M. & Marx, D. Mechanochemical Transduction of Externally Applied Forces to Mechanophores. *J. Am. Chem. Soc.* **132,** 10609–10614 (2010).

23. Ribas-Arino, J., Shiga, M. & Marx, D. Unravelling the mechanism of force-induced ring-opening of benzocyclobutenes. *Chem Eur J* **15,** 13331–13335 (2009).

24. Dopieralski, P. *et al.* On the role of polymer chains in transducing external mechanical forces to benzocyclobutene mechanophores. *J. Mater. Chem.* **21,** 8309–8316 (2011).

25. Kohn, W. & Sham, L. J. Self-consistent equations including exchange and correlation effects. *Phys. Rev.* **140,** A1133–A1138 (1965).

26. Hohenberg, P. & Kohn, W. Inhomogeneous Electron Gas. *Phys. Rev.* **136,** B864–B871 (1964).

27. Valiev, M. *et al.* NWChem: A comprehensive and scalable open-source solution for large scale molecular simulations. *Comput. Phys. Commun.* **181,** 1477–1489 (2010).

28. Becke, A. D. Density-functional thermochemistry. III. The role of exact exchange. *J. Chem. Phys.* **98,** 5648-5652 (1993).

29. Lee, C., Yang, W. & Parr, R. G. Development of the Colle-Salvetti correlation-energy formula into a functional of the electron density. *Phys. Rev. B* **37,** 785–789 (1988).

30. Berry, R. S. Correlation of Rates of Intramolecular Tunneling Processes, with Application to Some Group V Compounds. *J. Chem. Phys.* **32,** 933-938 (1960).

31. Kochhar, G. S. & Mosey, N. J. Differences in the Abilities to Mechanically Eliminate Activation Energies for Unimolecular and Bimolecular Reactions. *Sci. Rep.* **6,** 23059-1-9 (2016).

32. Henkelman, G. & Jónsson, H. Improved tangent estimate in the nudged elastic band method for finding minimum energy paths and saddle points. *J. Chem. Phys.* **113,** 9978–9985 (2000).

33. Bailey, A. & Mosey, N. J. Prediction of reaction barriers and force-induced instabilities under mechanochemical conditions with an approximate model: a case study of the ring opening of 1,3-cyclohexadiene. *J. Chem. Phys.* **136,** 44102-1-11 (2012).

34. Grunenberg, J., Streubel, R., von Frantzius, G. & Marten, W. The strongest bond in the universe? Accurate calculation of compliance matrices for the ions N_2H^+, HCO^+, and HOC^+. *J. Chem. Phys.* **119,** 165-169 (2003).

35. Kucharski, T. J. & Boulatov, R. The physical chemistry of mechanoresponsive polymers. *J. Mater. Chem.* **21,** 8237–8255 (2011).

Chapter 7

Conclusions and Future Work

The use of mechanical stress to alter the reactivity of chemical systems, an approach termed mechanochemistry, has gained significant interest in recent years. [1–8] This interest has been largely driven by advances in experimental techniques such as atomic force microscopy,[9–12] molecular force probes, [3,13,14] optical and magnetic tweezers, [9,15–18] and sonochemical methods.[19–23] These methods have been used to activate chemical reactions involving rupture of covalent bonds[7,21,24–26] and selectively guide systems along particular reaction pathways. [13,19,27] These experimental findings have prompted significant research from a theoretical perspective to understand the interplay between mechanical stress and chemical reactivity. [2,8,28–31]

The application of mechanical stresses to chemical systems can alter the thermodynamic and kinetic properties of the reaction. This thesis focusses on understanding the effect of F on the kinetics of a reaction, particularly changes in the reaction barrier, $\Delta E^{\ddagger}$, that occur under mechanochemical conditions. To gain such insight, quantum chemical calculations employing the External Force is Explicitly Included (EFEI) method[29] were used to evaluate the force-dependent $\Delta E^{\ddagger}$'s for a set of representative chemical reactions. The EFEI method models isotensional conditions in mechanochemical experiments by applying a constant external force of magnitude, F, to two atoms or groups in a molecule termed pulling points (PPs). The application of F modifies the potential energy surface (PES) on which the molecule moves, which alters $\Delta E^{\ddagger}$ according to the expression:

$$\Delta E^{\ddagger}(F) = \Delta E_{\mathrm{BO}}{}^{\ddagger}(F) - F\Delta R \tag{7.1}$$

where ΔR is the distance between the PPs as the system progressed from the reactants to the transition state (TS), and $\Delta E_0{}^{\ddagger}(F)$ is the reaction barrier on the Born-Oppenheimer PES. The computational effort associated with an EFEI calculation is comparable to a Born-Oppenheimer calculation for a single set of PPs and one value of *F*. However, it may be necessary to examine several combinations of PPs at multiple values of *F* for mechanochemical processes. Performing such calculations would require more computational effort than a Born-Oppenheimer calculation. A previous model was developed by Bailey and Mosey to predict changes in $\Delta E^{\ddagger}$ that occur under mechanochemical conditions using the optimized zero-*F* reactant and TS structures. [32] In the context of this model, the reaction barrier on the force-modified PES can be expressed as:

$$\Delta E^{\ddagger}(F) = \Delta E_0{}^{\ddagger} - F\Delta R_0 - \frac{F^2}{2}\Delta C_{RR} \tag{7.2}$$

where ΔR_0 and ΔC_{RR} are the differences in distance between PPs and compliance matrix elements associated with the PP distance, *R*, respectively as the system progresses from the reactants to the TS in the absence of *F*. The compliance matrix, **C**, is obtained from the inverse of the Hessian in terms of internal coordinates, $\mathbf{H}_{\mathrm{int}}$.

Eq. (7.2) provides an estimation of $\Delta E^{\ddagger}$ under mechanochemical conditions for a single set of PPs. Chapter 3 described a computationally efficient approach for extending

Eq. (7.2) to examine the changes in $\Delta E^{\ddagger}$'s with F for all possible combinations of PPs. The $\Delta E^{\ddagger}$'s predicted from this model were compared to the $\Delta E^{\ddagger}$'s calculated at each value F in the quantum chemical methods for a set of representative pericyclic reactions. It was found that predicted $\Delta E^{\ddagger}$'s yielded results that were qualitatively consistent with the calculated $\Delta E^{\ddagger}$'s if the reactant or TS does not undergo a significant change in structure with F. Ultimately, quantum chemical calculations are needed to examine the full structural and electronic changes that occur in the reactant and TS under mechanochemical conditions. The code outlined in chapter 3 can be used in conjunction with quantum chemical calculations to first identify a few possible sets of PPs that elicit a desired mechanochemical response and then use these PPs in the quantum chemical calculations performed using Eq. (7.1)

Chapter 4 focused on applying constraints of varying size and chemical composition to prevent such force-induced structural changes in the reactant or TS. The force-dependent $\Delta E^{\ddagger}$'s were evaluated for a set of unimolecular reactions involving bond rupture of carbon-carbon and nitrogen-nitrogen single bonds. The results of the calculations demonstrated that the addition of certain ring constraints hindered the force-induced structural changes in the reactant or TS for these reactions. The size of constraint had a noticeable effect on the force-dependent $\Delta E^{\ddagger}$'s, which varied in the studied reactions. In reactions **R1** and **R3** in chapter 4, which correspond to the Cope re-arrangement[33] of 1,5-hexadiene and a variation of this reaction with the carbon atoms of the scissile bond replaced with nitrogen atoms that are attached to ethyl substituents respectively, the addition of a 4 membered ring constraint led to a reduction in the $\Delta E^{\ddagger}$'s with F in both these reactions. Conversely, the addition of this constraint resulted in an

increase in the $\Delta E^{\ddagger}$'s with F in reactions **R2** and **R4** in chapter 4, which corresponded to another variation of the Cope re-arrangement with ethyl groups attached to the carbon atoms of the scissile bond and an elementary reaction step in the Fischer-Indole synthesis[34,35] respectively. Non-bonding types of constraints including coordination to a ruthenium complex and hydrogen bonding to pyrazole were also added to the various reactions. As in the case of the ring constraints, the addition of non-bonding constraints affected the reactions in different ways. For example, the addition of the constraint involving coordination to a ruthenium complex resulted in an increase in the $\Delta E^{\ddagger}$'s with F for reaction **R2** and a decrease in the $\Delta E^{\ddagger}$'s with F for reactions **R1**, **R3** and **R4**. Reaction **R4** was a unique case, in which the force-induced rotation around the nitrogen-nitrogen scissile bond in the reactant and TS structure led to the system following a competing hydrogen transfer reaction. The nature of the added constraint influenced which of the reaction pathways was more favorable under mechanochemical conditions. In fact, the addition of 4 and 5 membered ring constrains shut off the competing hydrogen transfer reaction because the configuration of the reactant needed to undergo the hydrogen transfer reaction was not a local minimum on the Born-Oppenheimer PES. In addition, the constraints involving coordination to a ruthenium complex and hydrogen bonding to pyrazole also shut off the competing hydrogen transfer reaction because first-order saddle points corresponding to the TSs for these reactions could not be located on the Born-Oppenheimer PES.

While the data shown in chapter 4 was obtained for a narrow set of unimolecular reactions, the results are of value in a broader context for using constraints to prevent force-induced changes in reactant and TS structures such that a reaction can be activated

over a larger force range or even using the constraint to deactivate a reaction along a particular reaction pathway under mechanochemical conditions. The latter is used in the area of a mechanochemical selectivity, which has gained signifcant interest in recent years.[19,36–38]

The results presented in chapter 5 demonstrated that the sterics of substituents added to various bimolecular reactions influenced the force-dependent $\Delta E^{\ddagger}$'s by affecting the contributions from the changes in the Born-Oppenheimer energy, $\Delta\Delta E_{BO}^{\ddagger}$ and changes in mechanical work, $-F\Delta\Delta R$ in different ways. In reactions **R1** and **R2** in chapter 5, which corresponded to Diels-Alder reactions involving the addition of ethylene to substituted pentadiene and substituted hexadiene respectively, the increased sterics of the substituent added to the dienes led to an increase in magnitudes of $\Delta\Delta E_{BO}^{\ddagger}$ and $-F\Delta\Delta R$ with F. This increase in magnitudes of the force-dependent $\Delta\Delta E_{BO}^{\ddagger}$ and $-F\Delta\Delta R$ values with sterics of the substituent resulted in an overall reduction in the $\Delta E^{\ddagger}$'s. Furthermore, the values of $-F\Delta\Delta R$ were more significantly affected with the increased sterics of the substituent than the $\Delta\Delta E_{BO}^{\ddagger}$ values. This result suggests that the convergence of reactant and TS structures through contributions from $\Delta\Delta E_{BO}^{\ddagger}$ were rendered secondary to the amount of mechanical work performed on the system for the more sterically hindered substituents. In reactions **R3** and **R4** in chapter 5, which involved Diels-Alder reactions of 1,3-butadiene adding to substituted cyclopentene and substituted cyclohexene respectively, increasing the sterics of the substituent added to the dienophiles did not lead to a greater reduction in the $\Delta E^{\ddagger}$'s. The greatest reductions in $\Delta E^{\ddagger}$ and $\Delta\Delta E^{\ddagger}$ with F were observed when X = CF_3 in reaction **R3**, which was intermediate in size for all the substituents considered As in the cases of reactions **R1** and **R2**, the contributions from $-F\Delta\Delta R$ were greater than the contributions

from $\Delta\Delta E_{BO}^{\ddagger}$ to the mechanical activation of **R3.** The greatest reduction in the $\Delta E^{\ddagger}$'s with F in reaction **R4** was achieved for the substituent CH_3, which is not as sterically hindered as the other substituents considered. For this substituent, the $-F\Delta\Delta R$ values were larger in magnitude than the $\Delta\Delta E_{BO}^{\ddagger}$ values from F = 500 pN to F = 1000 pN and smaller in magnitude from F = 1500 pN to F = 3000 pN. As a whole, the results presented in chapter 5 indicate that the sterics of attached substituents to chemical systems influence the underlying energy terms associated with the $\Delta E^{\ddagger}$'s under mechanochemical conditions.

Chapters 4 and 5 examined the force-dependent $\Delta E^{\ddagger}$'s for a set of unimolecular and bimolecular reactions. The differences in the abilities to mechanically eliminate the $\Delta E^{\ddagger}$'s in unimolecular and bimolecular reactions were investigated in chapter 6. It was found that unimolecular reactions can become barrierless under mechanochemical conditions if the reactant, TS, or both these species are shifted along the zero-F reaction coordinate such that these structures converge. In bimolecular reactions, however, the $\Delta E^{\ddagger}$'s can be eliminated if there is sufficient coupling between F and the other nuclear degrees of freedom (DOFs) in the reactants that drive the reactants along the zero-F reaction coordinate in the direction of the TS. This coupling is not possible for bimolecular reactions with infinitely separated reactants, therefore the $\Delta E^{\ddagger}$'s cannot be eliminated these reaction under mechanochemical conditions without changing the underlying mechanism. Furthermore, the mechanical elimination of the $\Delta E^{\ddagger}$'s in bimolecular reactions is only possible for the reactants that form a complex. The force-dependent $\Delta E^{\ddagger}$'s for bimolecular reactants were represented as a term associated with the structural and electronic changes that occur within each reacting species as the system progressed from the reactants to the TS known as the change in the deformation energy,

ΔE_{def}, and another term that corresponds to the change in the interaction energy between the reacting components as the system moves from the reactants to the TS, ΔE_{int}. The coupling between F and the other nuclear DOFs in the reactant complex ensured that the reactions retained a zero or non-negative value of ΔE_{int}, which was necessary to eliminate $\Delta E^{\ddagger}$. In bimolecular reactions that relied on movements of the TS along the zero-F reaction coordinate without a significant force-induced change in the reactant complex structure, the TS adopted structures that led to an adoption of positive values of ΔE_{int} at high F without a reduction in ΔE_{def}, which ultimately resulted in non-zero $\Delta E^{\ddagger}$'s. Highlighting the importance of the coupling of F to other nuclear DOFs in the reactant complex may be of value of a practical standpoint in the development of reactive units that are susceptible to external mechanical stress termed mechanophores[39–41] as well as the selection of PPs in a molecule. Furthermore, demonstrating the limitations of the ability to mechanically eliminate $\Delta E^{\ddagger}$ for bimolecular reactions is of fundamental value.

Overall, the results presented in this thesis further enhanced the understanding of the interplay between mechanical stresses and chemical reactivity. The effect of F on the kinetics of reactions was investigated by performing quantum chemical calculations to evaluate force-dependent $\Delta E^{\ddagger}$'s for various unimolecular and bimolecular reactions. The results in this thesis highlight the fundamental aspects of mechanochemistry as well as the applications of mechanochemistry through the design of mechanophores, which was shown through additions of constraints and substituents to chemical systems.

Future work in the area of theoretical mechanochemistry may involve simulations of systems that are more amenable to applied mechanical stress in experiments. In experiments involving mechanochemistry such as sonication, the molecules under study

are typically long-chain polymers. [20,22,23] Quantum chemical calculations performed on long-chain polymers for several sets of PPs at different values of F may be computationally demanding. As a starting point, one can perform quantum chemical calculations for systems with smaller chain functional groups and examining the force-dependent $\Delta E^{\ddagger}$'s with increasing chain size. In addition, it will be desirable to advance the current models for simulating mechanochemical conditions (EFEI and COGEF) to include the chemical tethers required to deliver a large force to a molecule. The long-chain polymers that are typically studied in mechanochemical experiments may be investigated computationally by using QM/MM models. Such models are able to describe larger systems than those discussed in this thesis. This may be of value for investigating solid-state applications of mechanochemistry such as applying external forces or stresses to molecules attached to a solid surface.

Future efforts may also focus on examining a wider range of chemical reactions typically used in the synthetic industry. A prominent feature of mechanochemistry is the ability to use an applied external force to bias reactions along a particular pathway. This approach, termed mechanoselectivity, was described in the sonochemical experimental study[19] and the computational studies[31,36] for the ring opening of cyclobutene along conrotatory and disrotatory pathways. While ring opening reactions are significant in organic chemistry, it would be interesting to investigate biasing other reaction pathways under mechanochemical conditions. An example is chiral mechanoselectivity, in which an external force may selectively guide the system along a pathway that leads to the formation of one enantiomer over the other.

References

1. Beyer, M. K. & Clausen-Schaumann, H. Mechanochemistry: the mechanical activation of covalent bonds. *Chem. Rev.* **105,** 2921–2948 (2005).

2. Ribas-Arino, J. & Marx, D. Covalent Mechanochemistry: Theoretical Concepts and Computational Tools with Applications to Molecular Nanomechanics. *Chem. Rev.* **112,** 5412–5487 (2012).

3. Lenhardt, J. M. & Craig, S. L. Mechanochemistry: Force probes in a bottle. *Nat. Nanotechnol.* **4,** 284–285 (2009).

4. Rosen, B. M. & Percec, V. Mechanochemistry: A reaction to stress. *Nature* **446,** 381–382 (2007).

5. Piermattei, A., Karthikeyan, S. & Sijbesma, R. P. Activating catalysts with mechanical force. *Nat. Chem.* **1,** 133–137 (2009).

6. Seidel, C. A. M. & Kühnemuth, R. Mechanochemistry: molecules under pressure. *Nat. Nanotechnol.* **9,** 164–165 (2014).

7. Liang, J. & Fernández, J. M. Mechanochemistry: One Bond at a Time. *ACS Nano* **3,** 1628–1645 (2009).

8. Kochhar, G. S., Heverly-Coulson, G. S. & Mosey, N. J. in *Polymer Mechanochemistry* (ed. Boulatov, R.) **369,** 37–96 (Springer International Publishing, 2015).

9. Neuman, K. C. & Nagy, A. Single-molecule force spectroscopy: optical tweezers, magnetic tweezers and atomic force microscopy. *Nat. Methods* **5,** 491–505 (2008).

10. Rief, M., Gautel, M., Oesterhelt, F., Fernandez, J. M. & Gaub, H. E. Reversible unfolding of individual titin immunoglobulin domains by AFM. *Science* **276,** 1109–1112 (1997).

11. Puchner, E. M. & Gaub, H. E. Force and function: probing proteins with AFM-based force spectroscopy. *Curr. Opin. Struct. Biol.* **19,** 605–614 (2009).

12. Kreuzer, H. J., Payne, S. H. & Livadaru, L. Stretching a Macromolecule in an Atomic Force Microscope: Statistical Mechanical Analysis. *Biophys. J.* **80,** 2505–2514 (2001).

13. Yang, Q.-Z. *et al.* A molecular force probe. *Nat. Nanotechnol.* **4,** 302–306 (2009).

14. Huang, Z. & Boulatov, R. Chemomechanics with molecular force probes. *Pure Appl. Chem.* **82,** 931-951 (2010).

15. Moffitt, J. R., Chemla, Y. R., Smith, S. B. & Bustamante, C. Recent Advances in Optical Tweezers. *Annu. Rev. Biochem.* **77,** 205–228 (2008).

16. Grier, D. G. A revolution in optical manipulation. *Nature* **424,** 810–816 (2003).

17. Stauch, T. & Dreuw, A. Force-Spectrum Relations for Molecular Optical Force Probes. *Angew. Chem. Int. Ed.* **53,** 2759–2761 (2014).

18. Wang, M. D., Yin, H., Landick, R., Gelles, J. & Block, S. M. Stretching DNA with optical tweezers. *Biophys. J.* **72,** 1335–1346 (1997).

19. Hickenboth, C. R. *et al.* Biasing reaction pathways with mechanical force. *Nature* **446,** 423–427 (2007).

20. Basedow, A. M. & Ebert, K. H. in *Physical Chemistry* **22,** 83–148 (Springer Berlin Heidelberg, 1977).

21. Colarusso, P. & Serpone, N. Sonochemistry II.—Effects of ultrasounds on homogeneous chemical reactions and in environmental detoxification. *Res. Chem. Intermed.* **22,** 61–89 (1996).

22. Koda, S. Ultrasonic degradation of water-soluble polymers. *Polymer* **35,** 30–33 (1994).

23. Price, G., West, P. & Smith, P. Control of polymer structure using power ultrasound. *Ultrason. Sonochem.* **1,** S51–S57 (1994).

24. Avalos, M. *et al.* Thermal and Sonochemical Studies on the Diels−Alder Cycloadditions of Masked *o* -Benzoquinones with Furans: New Insights into the Reaction Mechanism †. *J. Org. Chem.* **68,** 7193–7203 (2003).

25. Klukovich, H. M., Kean, Z. S., Iacono, S. T. & Craig, S. L. Mechanically Induced Scission and Subsequent Thermal Remending of Perfluorocyclobutane Polymers. *J. Am. Chem. Soc.* **133,** 17882–17888 (2011).

26. Kryger, M. J. *et al.* Masked Cyanoacrylates Unveiled by Mechanical Force. *J. Am. Chem. Soc.* **132,** 4558–4559 (2010).

27. Cravotto, G. & Cintas, P. Forcing and Controlling Chemical Reactions with Ultrasound. *Angew. Chem. Int. Ed.* **46,** 5476–5478 (2007).

28. Tian, Y., Kucharski, T. J., Yang, Q.-Z. & Boulatov, R. Model studies of force-dependent kinetics of multi-barrier reactions. *Nat. Commun.* **4,** 1-10 (2013).

29. Ribas-Arino, J., Shiga, M. & Marx, D. Understanding covalent mechanochemistry. *Angew. Chem. Int. Ed.* **48,** 4190–4193 (2009).

30. Beyer, M. K. The mechanical strength of a covalent bond calculated by density functional theory. *J. Chem. Phys.* **112,** 730-7312 (2000).

31. Ong, M. T., Leiding, J., Tao, H., Virshup, A. M. & Martínez, T. J. First principles dynamics and minimum energy pathways for mechanochemical ring opening of cyclobutene. *J. Am. Chem. Soc.* **131,** 6377–6379 (2009).

32. Bailey, A. & Mosey, N. J. Prediction of reaction barriers and force-induced instabilities under mechanochemical conditions with an approximate model: a case study of the ring opening of 1,3-cyclohexadiene. *J. Chem. Phys.* **136,** 44102-1-11 (2012).

33. Cope, A. C. & Hardy, E. M. The Introduction of Substituted Vinyl Groups. V. A Rearrangement Involving the Migration of an Allyl Group in a Three-Carbon System [1]. *J. Am. Chem. Soc.* **62,** 441–444 (1940).

34. Fischer, E. & Hess, O. Synthese von Indolderivaten. *Berichte Dtsch. Chem. Ges.* **17,** 559–568 (1884).

35. Fischer, E. & Jourdan, F. Ueber die Hydrazine der Brenztraubensäure. *Berichte Dtsch. Chem. Ges.* **16,** 2241–2245 (1883).

36. Kochhar, G. S., Bailey, A. & Mosey, N. J. Competition between orbitals and stress in mechanochemistry. *Angew. Chem. Int. Ed.* **49,** 7452–7455 (2010).

37. Friedrichs, J., Lüssmann, M. & Frank, I. Conservation of orbital symmetry can be circumvented in mechanically induced reactions. *Chemphyschem Eur. J. Chem. Phys. Phys. Chem.* **11,** 3339–3342 (2010).

38. May, P. A. & Moore, J. S. Polymer mechanochemistry: techniques to generate molecular force via elongational flows. *Chem. Soc. Rev.* **42,** 7497-7506 (2013).

39. Potisek, S. L., Davis, D. A., Sottos, N. R., White, S. R. & Moore, J. S. Mechanophore-linked addition polymers. *J. Am. Chem. Soc.* **129,** 13808–13809 (2007).

40. Dopieralski, P. *et al.* On the role of polymer chains in transducing external mechanical forces to benzocyclobutene mechanophores. *J. Mater. Chem.* **21,** 8309–8316 (2011).

41. Larsen, M. B. & Boydston, A. J. 'Flex-Activated' Mechanophores: Using Polymer Mechanochemistry To Direct Bond Bending Activation. *J. Am. Chem. Soc.* **135,** 8189–8192 (2013).